The Development and Fabrication of Silicon Carbide Based Metal Oxide Semiconductor Gas Sensors for Automotive Applications

SIDDALL, RYAN,JAMES

The Development and Fabrication of Silicon Carbide Based Metal Oxide Semiconductor Gas Sensors for Automotive Applications

Ryan James Siddall

A thesis submitted in fulfilment of requirements for the degree of Doctor of Philosophy

Department of Engineering, University of Durham

July 2024

Abstract

The detection of gases in hazardous environments has been a subject of great interest due to the number of potential applications. Vehicle and volcano emission monitoring, space exploration and nuclear waste management could all make use of sensitive and selective gas sensors. Traditional silicon based electronic systems have poor resilience in harsh environments and struggle to operate at temperatures in excess of 150°C. Silicon carbide (SiC) is an alternative material from which temperature-stable sensors can be fabricated. The wide band gap, strong silicon to carbon bonding, and low intrinsic carrier concentration make it a suitable candidate for these devices. SiC based metal oxide semiconductor capacitors have been successfully deployed as hydrogen, oxygen, methane and hydrogen sulfide sensors in the past, however there are still issues around selectivity, as cross-analyte sensitivity occurs, leading to the need for sensor arrays.

In order to ensure compliance with the continuously iterated European legislation on diesel engine emissions, a selective, temperature-stable, real-time sensor could be employed to monitor levels of nitrogen oxide (NOx) emissions. In this study, metal oxide semiconductor (MOS) capacitors were fabricated, comprising a material with a high-dielectric constant (high-κ), and a noble metal layer as the catalytic gate material. Previously, devices based on hafnium oxide (HfO_2) and titanium dioxide (TiO_2) have shown sensitivity to hydrogen and oxygen at high temperatures, therefore, in this work, the fabrication process for these devices was built upon to target NOx.

Tungsten oxide (WO_3) has previously shown sensitivity towards NOx and was incorporated as the dielectric material of the device, with a study carried out to find the optimum tungsten deposition and oxidation conditions. It was concluded that DC sputtering of 50 nm of tungsten metal and subsequent oxidation in air at 500°C for 10 minutes produces a uniform film of WO_3, suitable for use as the dielectric layer of a capacitor.

Platinum was chosen as the gate metal due to its ability to catalytically decompose gases. It has been shown in the past, that a porous gate metal layer can encourage interaction of gases such as ammonia and NOx. Therefore, a study was carried out to optimise the platinum deposition conditions in order to incorporate

porosity into the film. Alteration of the sputter power and argon pressure was carried out and it was found that sputtering at 50 W with an argon pressure of 140 mTorr incorporated a suitable level of porosity into the metal.

Devices comprising HfO_2, TiO_2, ZrO_2 and WO_3 as the dielectric layer were fabricated, and their capacitance-voltage (C-V) and conductance-voltage (G-V) characteristics were extracted. Sensor behaviour in the presence of H_2, O_2 and NO was examined. It was found that device response varies depending on the identity of the dielectric material. ZrO_2 devices demonstrate a temperature dependant response, showing no sensitivity at room temperature, but displaying a visible shift in characteristics at 573 K. We have also shown for the first time that a Pt/WO_3/SiO_2/4H-SiC device demonstrates sensitivity to NO at 573K.

A Pt/TiO_2/SiO_2/4H-SiC device was exposed to different organic solvents and the C-V characteristics were monitored, in order to determine more information about the mechanism of response. A significant relationship between magnitude of response, and solvent dipole moment was discovered, leading to the hypothesis that traps in the dielectric layer drive device response.

In conclusion, this work has built upon previous demonstration of SiC based MOS capacitor gas sensors comprising HfO_2 and TiO_2 as dielectric materials. We have demonstrated the use of a Pt/ZrO_2/SiO_2/4H-SiC device as an oxygen sensor and a Pt/WO_3/SiO_2/4H-SiC device as a nitric oxide (NO) sensor, for the first time. Combining these devices into a sensor array would lead to a system capable of selectively targeting specific analyte gases in high temperature environments, such as a diesel exhaust engine.

For Lauren, Evie, Ted and my Parents.
Thank you for always supporting me.

Acknowledgements

I would primarily like to thank my supervisor Professor Alton Horsfall for taking a chance on a humble chemist and providing me with the opportunity to carry out this work. His continued guidance, support and friendship, throughout what has been a very non-traditional and fragmented PhD, will always be remembered and appreciated.

Thanks must go to Dr. Konstantin Vasilevskiy of Newcastle University for his device fabrication and cleanroom etiquette advice, which was essential in the realisation of this work.

I would like to thank Littelfuse for their support in this work, specifically Brian Johnson who is extremely knowledgeable and has taught me a lot. Also, Dr. Marc Debliquy and Dr. Driss Lahem from the University of Mons for their work in device testing.

I must recognise the contribution of my PhD groups at Newcastle University and Durham University who made my experience an enjoyable one. In particular, Dr. Amy Peters - her support as a friend and colleague was essential in keeping me sane in the transition between academic institutions!

My friends have been extremely supportive throughout the years, and I'm very grateful for their candour, humour, and hours spent in the pub. A huge thank you should go to my Nana for setting me on my career path at an early age by gifting me my first chemistry set and continually inspiring me to be inquisitive and try new things. The love and comfort from her, and my other grandparents, has helped shape me into the person I am today.

I would like to thank my parents for their unwavering support throughout my studies. Nothing I have achieved, or will achieve in the future, would be possible without them, and I am eternally grateful for the sacrifices that they have made for me. I hope I make them proud.

Finally, the love and support of my fiancée, Lauren, has kept me going through the toughest of times and she is my rock. As I sit here writing these acknowledgements, holding our baby daughter, it serves as a reminder of how far we have come together. This is for you and Evie.

Contents

Chapter 1

Introduction

Over the past two decades the number of vehicles on the road has doubled, therefore the need to be able to accurately monitor the concentration of pollutant gases in automotive systems is greater than ever. Ever-changing legislation continually demands a reduction in maximum allowable levels of gaseous releases from vehicles in an effort to improve air quality and reduce the rate of global warming. The impact of carbon dioxide (CO_2) on the ozone layer has been well documented and the level of atmospheric CO_2 has steadily increased in line with technological advancement [1, 2, 3]. CO_2 alone is not responsible for climate change with methane (CH_4), chlorofluorocarbons (CFCs) and nitrogen oxides (NOx) also contributing. Since 1993, European (Euro) emission standards have been enforced to define acceptable limits for engine emissions with tighter restrictions for each introduced iteration. Since the introduction of the first Euro standard (Euro 1), the maximum value of allowable NOx and particulate matter (PM) emission has reduced by over 95% and 97% respectively, as summarised in Table 1.1 [4]. These margins stress the need for a reliable and accurate sensor system capable of quantitatively monitoring the concentration of exhaust gases from the moment the engine is engaged.

Currently, yttria stabilised zirconium based sensors (Lambda sensors) are used to monitor oxygen concentrations with the intention of calculating the efficiency of the catalytic converter [5]. However, these devices are ineffective as pollutant monitors as they do not begin to operate until the engine environment heats to a temperature of around 300°C, and zirconium ions become conductive. Heaters have reduced this operational time from minutes to seconds, but issues still persist. Before heating to an adequate temperature is achieved, water droplets form on the surface of the sensor, interfering with sensitivity. This renders the device ineffective as a comprehensive emission monitor. A NOx sensor released by NGK in 2008 builds upon the design of the lambda sensor and removes any oxygen ions remaining after combustion to selectively target NOx [6]. This device is still based on conductive zirconia, so experiences the same temperature related issues. Lost time is a critical

drawback to employing these devices in pollution monitoring applications, as the accuracy of the sensor would be compromised due to the high rate of pollution production in the first few seconds after ignition.

A solution to overcome the issues of current automotive sensors is the development of a temperature independent sensor system which can be placed in close proximity to the combustion chamber. This device would need to be stable in the extreme environment of an engine as the released exhaust gas has a temperature of around 500-700°C [7]. Discrimination between a mixture of gases (oxygen, carbon dioxide, nitrous oxides and sulfur dioxide) is also necessary as these are all present within the engine. Existing metal-oxide-semiconductor structures based on silicon have shown to be effective gas sensors, however silicon devices are limited to operation below 200°C. Semiconductors with higher bandgap values than silicon are more stable at elevated temperatures as the thermal generation of carriers is orders of magnitude lower. Gallium nitride and diamond have wide bandgap values of 3.4 and 5.6 eV respectively, however processing limitations prevent these materials from being used industrially. The processability of silicon carbide (SiC) is a lot more advanced, as this material can be integrated into established silicon processing methods. The advantage of this ease of fabrication, as well as a wide bandgap of 3.23 eV, makes 4H-SiC a natural material candidate for high temperature devices [8]. The temperature and chemical resilience of a silicon carbide-based sensor allows positioning considerably closer to the engine itself. This feature will provide an accurate picture of pollutant generation, and engine combustion can also be monitored, making real-time data capture a possibility.

Euro Standard	**Date Enforced**	**NOx (g/kWh)**	**PM (g/kWh)**
Euro 1	1993	8.0	0.36
Euro 2	1996	7.0	0.15
Euro 3	2001	5.0	0.10
Euro 4	2006	3.5	0.02
Euro 5	2009	2.0	0.02
Euro 6	2014	0.46	0.01

Table 1.1: Euro standards legislation history [4]

The critical material properties of a semiconductor that is suitable for high temperature applications include a high bandgap value, low intrinsic carrier concen-

tration (n_i), high thermal conductivity and a high carrier mobility. The electrical properties of common semiconductors are outlined in Table 2.1 [9]. It can be seen from this table that diamond is the most suitable material for these applications, however as previously alluded to, there are processing limitations which prevent this. Diamond substrates are commercially available, however due to significant expense, research and development is difficult. The material hardness and the chemical inertness of diamond also demands novel fabrication processes to be developed. Furthermore, diamond lacks a native oxide which is a feature often required in semiconductor devices [10]. At 300 K, 4H-SiC has a wide bandgap (3.23 eV), low intrinsic carrier concentration (10^{-8} cm^{-3}), high thermal conductivity (5 W cm^{-1} K), and reasonable electron and hole mobility (1000 and 120 cm^2/Vs, respectively). These properties, coupled with advanced processing makes 4H-SiC the substrate of choice for MOS capacitor sensors for use in extreme environments.

Chapter 2 reviews the current literature on state of the art silicon carbide gas sensors, considering the material properties of silicon carbide, the operation of the metal oxide semiconductor structure and a comprehensive review of gas sensing results published in the scientific literature. The chapter reports on the challenges of uniquely identifying the component gases in mixtures using sensors that are unable to fully discriminate due to their operating principles.

Chapter 3 thoroughly describes experimental investigation of the gas sensing response of silicon carbide based gas sensors with a particular focus on the porosity of the catalytic metal gate and the fabrication of the dielectric film. The chapter details the first experimental investigation in to the integration of ZrO_2 and WO_3 dielectrics into silicon carbide gas sensors. As well as the optimisation of the process conditions to realise a sensor array to enable discrimination between different gas species in a mixture.

Chapter 4 details the solvent sensing performance of the silicon carbide based gas sensors and identifies that the passivation of charge traps in the dielectric is the dominant mechanism that describes the overall response. This supports the hypothesis that the enhanced response for titanium based dielectrics in comparison to those based on either hafnium or zirconium is related to the passivation of oxygen vacancies in the dielectric, that arise from the manufacturing process. The testing of these devices when exposed to solvents is novel and this experimental plan was designed to discover more information about the mechanism of interaction between these devices and analytes.

Chapter 5 describes the operation of the sensors in representative gases found in an automotive exhaust system. The outcomes show that the zirconium based sensor is highly stable when operated in high temperature applications. In contrast, the leakage current of the tungsten based devices is too high at 300°C limiting the

suitability of this for the realisation of a sensor array for automotive applications.

Chapter 6 summarises the key findings of the thesis and identifies further areas of study to support the long term development of sensors for pollution detection.

Bibliography

[1] Joan E. Rosenfield, Anne R. Douglass, and David B. Considine. "The impact of increasing carbon dioxide on ozone recovery". In: *Journal of Geophysical Research: Atmospheres* 107 (D6 Mar. 2002), ACH 7-1-ACH 7–9.

[2] Richard S Stolarski et al. "Impact of future nitrous oxide and carbon dioxide emissions on the stratospheric ozone layer". In: *Environmental Research Letters* 10 (3 Mar. 2015), p. 034011.

[3] B. Ekwurzel et al. "The rise in global atmospheric CO2, surface temperature, and sea level from emissions traced to major carbon producers". In: *Climatic Change* 144 (4 Oct. 2017), pp. 579–590.

[4] DieselNet.com. *Emission Standards: Europe: Cars and Light Trucks.* {EmissionStandards} Reference. 2018. URL: `https://www.dieselnet.com/standards/eu/ld.php#test`.

[5] Hiroyuki Kaneko et al. "Performance of a miniature zirconia oxygen sensor with a Pd–PdO internal reference". In: *Sensors and Actuators B: Chemical* 108 (1–2 2005), pp. 331–334.

[6] NGK. *Bringing the world's first high-precision NOx sensor to market — NEWS — NGK INSULATORS, LTD.* 2008. URL: `https://www.ngk-insulators.com/en/news/20080611_9229.html`.

[7] Dennis P. Nolan. *Fire fighting pumping systems at industrial facilities.* Gulf Professional Publishing, 2017.

[8] Stephen E. Saddow and Anant (Anant K.) Agarwal. *Advances in silicon carbide processing and applications.* Vol. 2. Artech House, 2004.

[9] Carl-Mikael. Zetterling. *Process technology for silicon carbide devices.* Institution of Engineering and Technology, 2002.

[10] Chris J.H. Wort and Richard S. Balmer. "Diamond as an electronic material". In: *Materials Today* 11 (1-2 Jan. 2008), pp. 22–28.

Chapter 2

Literature Review

2.1 Diesel Engines

Diesel engines operate differently to gasoline engines as they do not make use of spark plugs to ignite the air/fuel mixture. To generate power, the cylinders of the engine compress the air and then inject a pre-determined quantity of diesel fuel to initiate combustion [1, 2]. This operating principle is based on Boyle's law and Charles' law which outline relationships between volume, pressure and temperature. Boyle's law states that the pressure of a fixed amount of gas is inversely proportional to its volume at a constant temperature. Charles' law states that the volume of a fixed amount of gas is directly proportional to its temperature at constant pressure [3]. Therefore, as a piston compresses air, the volume is decreased, pressure is increased and the temperature rises to a sufficient value to enable ignition. In other words, diesel engines use heat to release the chemical energy stored within the diesel fuel. As a result of these high temperatures, unwanted pollutants are often formed such as nitrogen oxides, carbon monoxide, unburned hydrocarbons and particulate matter.

Other less harmful products are also emitted including oxygen, nitrogen, water vapour and carbon dioxide. As a proportion of total diesel emissions, the harmful pollutants make up less than one percent, but this is still much greater than the Euro 6 legislation permits. In theory, the complete combustion of diesel fuel (hydrocarbon based) would only release carbon dioxide and water, however there are influences within the engine that which prevent complete combustion. Imperfect air/fuel ratio, variations in engine temperature and timing of ignition all contribute to the generation of pollutants. NOx pollution arises from the presence of nitrogen poisons, provided by ambient N_2 gas and nitrogen containing impurities found within the diesel fuel. The ratio of these pollutants in exhaust gas is outlined in Figure 2.1 [4].

Controls are put in place to limit the release of harmful products from the en-

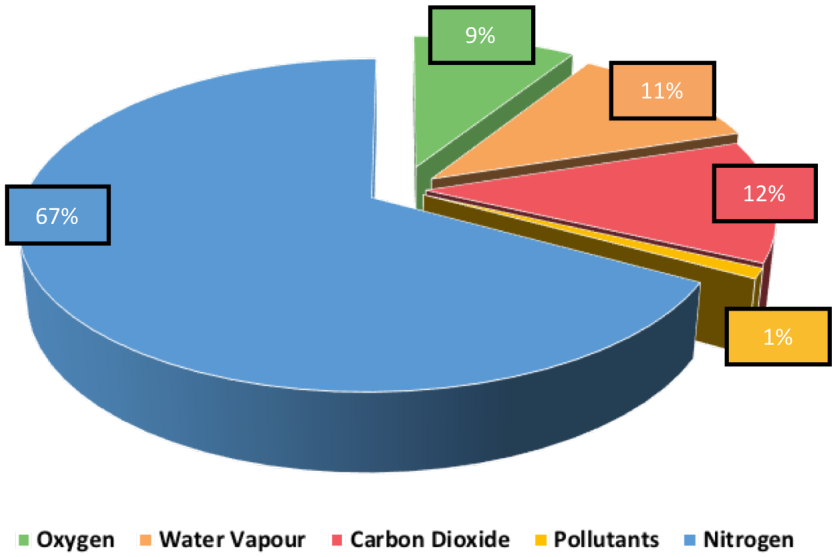

Figure 2.1: Components of Diesel Emissions - 1% of pollutants include hydrocarbons, NOx, sulphur dioxide, and particulate matter

gine. Exhaust gas recirculation (EGR) and selective catalytic reduction (SCR) are both methods used to reduce the levels of NOx emissions from exhaust gases. The purpose of EGR is to limit the concentration of NOx produced within the combustion chamber. In this method, a portion of the exhaust gas is taken, cooled, and recirculated back into the chamber, reducing the amount of fresh air intake. This reduces the amount of nitrogen in the chamber which can react with oxygen to form NOx. The additional exhaust gas can also absorb some of the heat energy produced in the chamber, reducing the peak cylinder temperature. As NOx can only form at high temperatures, this temperature reduction helps to prevent the formation of nitrogen oxides [5, 6, 7].

Selective catalytic reduction (SCR) systems actively target NOx, and chemically reduce these compounds to harmless products. Urea, a liquid reducing agent, is injected into the exhaust stream of the diesel engine and breaks down via thermal decomposition into ammonia and isocyanic acid, above 180°C. The ammonia reacts with the NOx, in the presence of a catalyst within a specific temperature range, to form N_2 and H_2O and these are expelled through the exhaust pipe of the vehicle. The temperature required for this reaction depends on the catalyst used, for example, alumina based catalysts are effective at temperatures in excess of 500°C, whereas copper containing zeolites can work at temperatures below 300°C [8]. A schematic representation of this process is shown in Figure 2.2. The major reaction in SCR is nitric oxide (NO) reduction by ammonia, driven by the presence of excess oxygen. A real time, temperature stable NOx sensor can be employed to improve the efficiency of this system. Placing a device downstream of the reduction catalyst would mean NOx concentration can be recorded, allowing constant regulation and

tuning of urea injection via a closed loop feedback system [9]

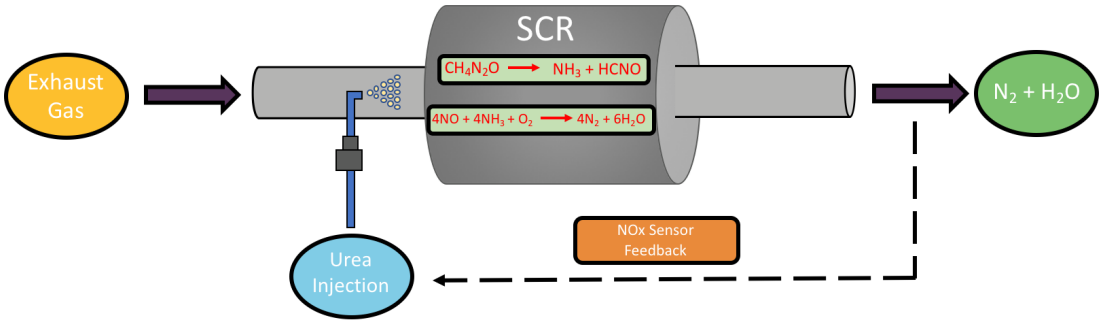

Figure 2.2: Selective catalytic reduction schematic

These systems contribute to the reduction of pollutant emissions to meet increasingly restrictive legislative standards. More focus is put on the reduction of NOx and particulate matter, as these cause the most damage to human health [10]. While it is well documented that CO_2 is a prominent greenhouse gas, it is naturally present in air and does not adversely affect health, meaning controls are not as stringent. In fact, harmful carbon monoxide is converted into carbon dioxide via the catalytic converter. European emission standards have continually evolved since the conception of Euro 1 legislation in 1993, becoming more strict with each iteration. The allowable emissions of NOx and particulate matter has decreased by 95% and 97% respectively from 'Euro 1' to 'Euro 6'. Figure 2.3 summarises the evolution of the legislation for the reduction of NOx and particulate matter [11]. These fine margins highlight the applicability of a real-time NOx sensor which can ensure that pollution reduction systems are working effectively.

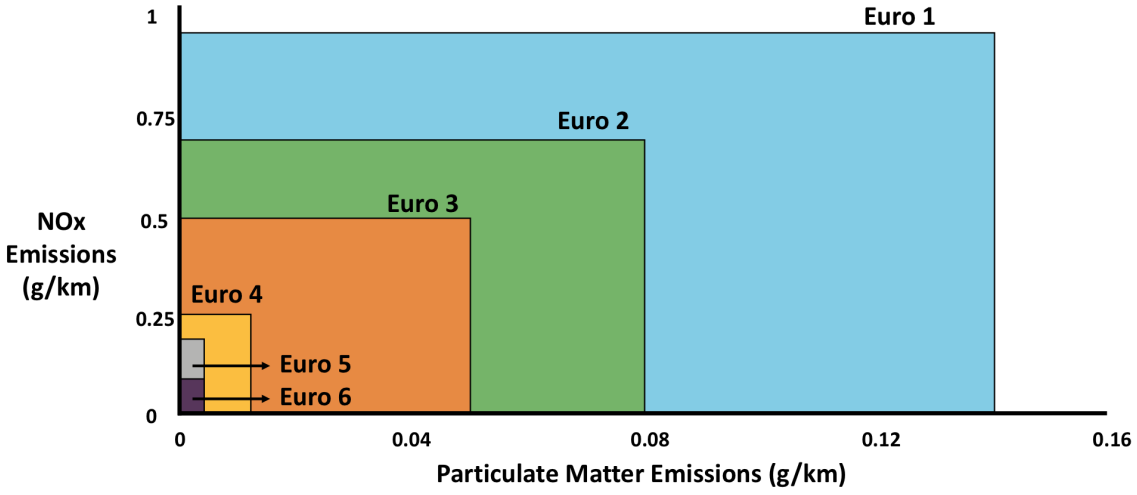

Figure 2.3: Effects of euro legislation on allowable PM and NOx emissions for light commercial vehicles - Based on data from [11]

2.1.1 Nitrogen Oxides

Nitrogen oxides is a term used to classify chemical compounds made up of nitrogen and oxygen atoms. In an automotive context, NOx refers to nitric oxide (NO) and nitrogen dioxide (NO_2) that are products of combustion. Principally it is NO that is produced in an engine, but this can readily react with ozone to form NO_2 once released into the atmosphere. There are three mechanisms that result in NOx formation during combustion, these are prompt, fuel and thermal (Zeldovich) [12].

Prompt

The prompt mechanism produces NOx as a result of the reaction between unburned fuel hydrocarbons and atmospheric nitrogen. This occurs typically at the beginning of the combustion process, with nitrogen reacting with carbon-based radicals from fuel. Nitrogen containing species such as HCN, NH, and CN are formed which are readily oxidised into NO, contributing to the NOx concentration [13, 14]. These reactions are outlined below.

$$\mathrm{CH_2 + N_2 \longrightarrow HCN + NH}$$
$$\mathrm{CH + N_2 \longrightarrow HCN + N}$$
$$\mathrm{C + N_2 \longrightarrow CN + N}$$

This mechanism does not contribute significantly to NOx levels, as temperatures and pressures quickly increase beyond those favorable and another mechanism dominates. The rate limiting step of this reaction is the interaction between N_2 and unburned hydrocarbons. Over time the engine heats up and there are fewer unburned hydrocarbons, making this reaction less favourable. NOx formed via this mechanism is more prominent if the engine is operating with excess air (lean mode) due to the extra atmospheric nitrogen [15].

Fuel

The fuel mechanism occurs when fuel bound nitrogen reacts with atmospheric oxygen. The contribution to overall NOx levels is dependent on the amount of nitrogen chemically bound in the combustion fuel. Nitrogen radicals such as ammonia, amines and cyanides are formed, and these compounds are subsequently oxidised to produce NOx. While diesel fuels do contain nitrogen compounds, these levels are relatively low, which prevents this mechanism from being the dominant mechanism contributing to NOx pollution [12].

Thermal (Zeldovich)

The thermal mechanism is responsible for producing the majority of the NOx pollution in a diesel engine and it was first proposed by the Russian scientist Yakov Borisovich Zeldovich in 1947 [16].

In an engine, it is principally the high temperature that is responsible for the formation of NOx, as nitrogen present in the engine is oxidised as a result of excess heat energy. The chemical equations for these reactions are outlined below [10].

$$N_2 + O \rightleftharpoons NO + N\cdot$$

$$N\cdot + O_2 \rightleftharpoons NO + O$$

$$N\cdot + OH \rightleftharpoons NO + H$$

The first step of the reaction makes use of the thermal energy within the engine to break the very strong N_2 triple bond (945 kJ/mol) [17]. Temperatures need to be in excess of 1500 K in order to achieve this. NO and an N radical are formed, which can go on and react with oxygen and hydroxyl groups present within the engine. The formation of nitrogen oxides depends on the engine temperature, the A/F ratio and the amount of time that gases are exposed to favorable reaction conditions [10, 18]. Controls can then be instigated which use this information to reduce NOx pollutant levels. Exhaust gas recirculation, for example, aims to reduce the peak temperature and lower the A/F ratio by recycling exhaust gas back into the cylinder to absorb some of the heat energy, ultimately reducing the concentration of NOx formed [19].

2.2 Existing Automotive Sensors

2.2.1 Automotive Oxygen Sensor

Existing automotive gas sensing technologies include a solid-state electrochemical sensor based on a yttria stabilised zirconia element and platinum electrodes [20]. This sensor is responsible for detecting oxygen concentration within an engine and ensuring that efficient performance and pollution control is achieved. Engines typically have two oxygen sensors, positioned pre and post-catalytic converter. The former is used to monitor combustion efficiency and the latter is used to check operation of the catalytic converter. Known as lambda sensors, these devices use two platinum electrodes to measure the difference in oxygen partial pressure inside and outside of the test environment, generating a voltage which can be used to find the oxygen concentration. With respect to this work, it is worth noting that Lambda sensors are currently used in vehicles to detect NOx emissions, so devices produced need to present an improvement in selectivity, sensitivity and reliability.

A schematic of this is shown in Figure 2.4 [21]. Although generally used in gasoline engines to monitor the A/F ratio, these sensors are often employed in diesel engines as primitive NOx sensors [22]. These sensors were not wholly suitable, however, due to the inability to discriminate between NO_x and other oxygen containing species.

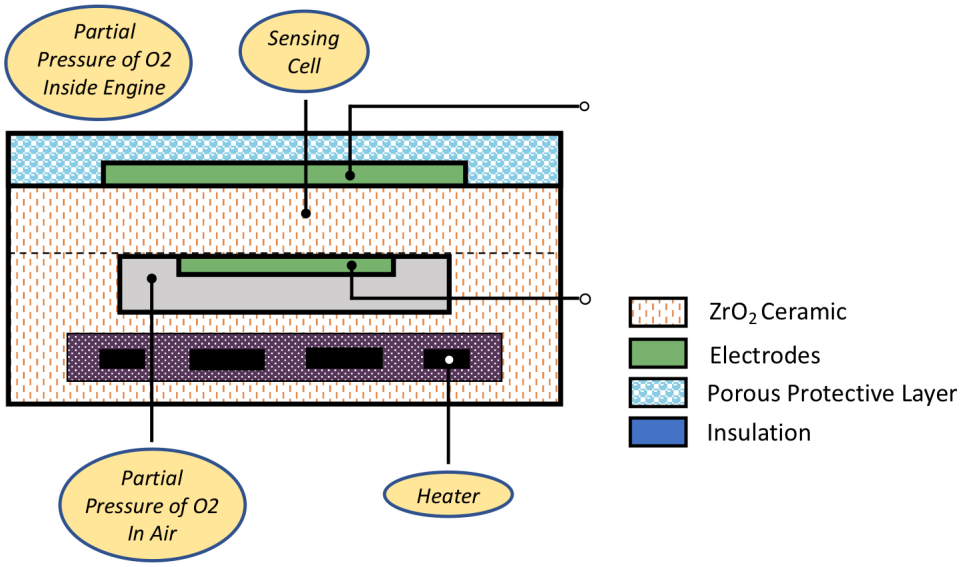

Figure 2.4: Schematic of a lambda oxygen sensor

The operating principle of lambda sensors is based on the Nernst equation and is essentially the relationship of oxygen partial pressures inside and outside of the engine as shown by equation 2.1.

$$V = \frac{RT}{4F} \ln \frac{P\,O_{2\ \text{Air}}}{P\,O_{2\ \text{Engine}}} \tag{2.1}$$

V is the voltage response of the sensor (V), R the ideal gas constant (8.314 J/K/mol), T the temperature (K), 4 represents the number of electrons transferred in the electrochemical cell, F is the Faraday constant (96485 C/mol) and $PO_{2\ \text{Engine}}$ and $PO_{2\ \text{Air}}$ are the partial pressures of oxygen inside and outside of the engine respectively.

An operating temperature in excess of 300°C is required as below this the zirconium ceramic cannot conduct oxygen ions [23]. To satisfy this, modern lambda sensors are designed with a built-in heating system to quickly reach the required operating temperature, allowing data collection to begin more quickly after engine ignition. There are still issues with this system, as mentioned previously, as water droplets can form on the sensor surface before the desired temperature is reached.

These sensors provide the engine control unit (ECU) of the vehicle with real-time oxygen concentrations every second, allowing rapid manipulation of the A/F

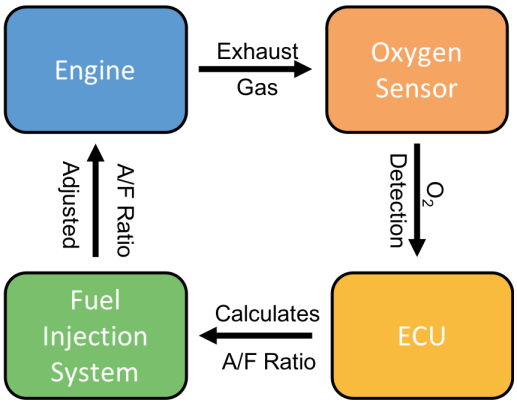

Figure 2.5: Schematic of closed loop feedback

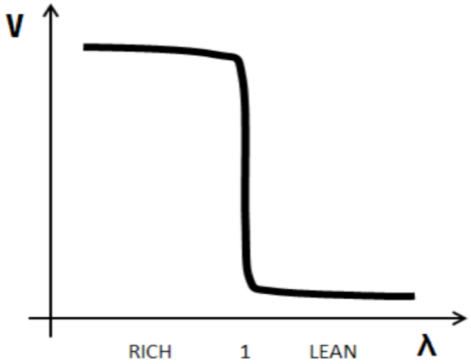

Figure 2.6: Electrical response of a stoichiometric lambda sensor

ratio. If the engine is running lean, i.e. an excess of oxygen in the engine which is described in terms of $\lambda < 0$, more fuel will be injected to restore the A/F balance and increase λ to a value > 1. Conversely, if the engine is deficient of oxygen and running rich, fuel injection will be reduced. This ensures that the combustion engine is running as efficiently as possible. As can be seen in Figures 2.5 and 2.6, when the engine is operating under lean conditions the voltage, and therefore sensor output is lowered. However under rich conditions, a voltage increase occurs. This closed loop feedback control is essential for efficient engine performance, as it restores the A/F ratio towards the stoichiometric value at which the combustion cycle is most efficient [24].

2.2.2 NOx Sensor

A high precision sensor based on zirconium oxide and platinum to monitor nitrogen oxide concentrations in diesel exhaust emissions was brought to market by NGK in 2008 [25]. Due to the developments in European regulations, the ability to detect and reduce the quantities of harmful pollutants, such as NOx emitted in exhaust gas is essential. Whilst this device reduces the NOx measurement error by 30% from previous sensors, the levels of sensitivity required to satisfy Euro 6 legislation can not be achieved. Therefore, a two-chamber system, utilising the properties of conductive zirconia, is employed to assist exhaust gas purifiers present in diesel engines [26, 27]. Previously, lambda oxygen sensors were used to predict NOx concentrations, however these were unable to accurately distinguish oxygen ions generated directly from NOx from other combustion products and free oxygen. Selective catalytic reduction systems are commonplace in diesel automotives and rely on accurate NOx sensors for their efficient operation. Consequently, sensor devices are placed downstream of the reduction catalyst providing NOx concentration data, enabling constant regulation via a closed feedback loop.

Figure 2.7 shows a schematic of the two-chamber system. In chamber 1 oxygen ions move through the zirconia under the influence of the applied voltage. In chamber 2, the voltage change generated is proportional to the concentration of oxygen ions present, similar to the operation of the lambda oxygen sensor. In chamber one, O_2 is pumped out and all combustible gases which remain are combusted. The catalytic properties of the electrode convert NO_2 into NO and pump it into chamber 2, where it is broken down into N_2 and O_2 at the platinum electrode. The quantity of O_2 can then be detected, and this is proportional to the amount of NOx present in the exhaust gas. The detection of this concentration will generate an electronic signal which is fed to the ECU. This will then be used to optimise the selective catalytic reduction process (Figure 2.7) [28, 29].

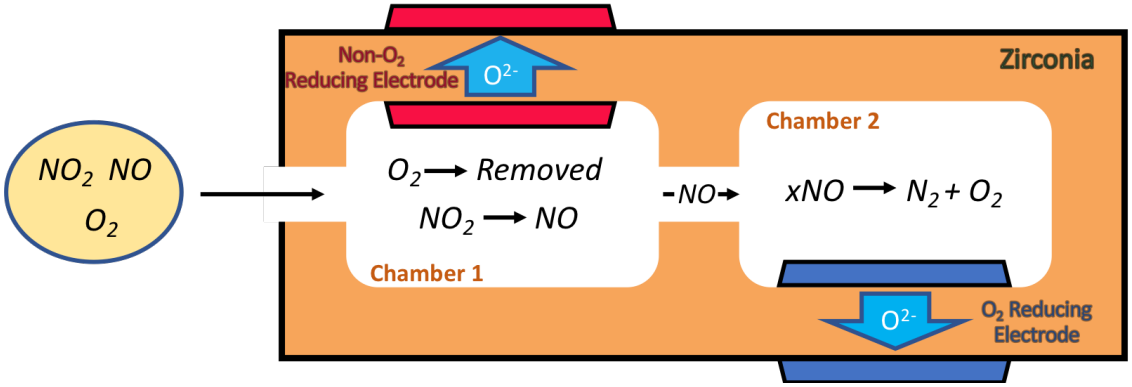

Figure 2.7: NOx sensor schematic adapted from [25]

The zirconia and platinum electrodes in each chamber operate identically to those of a conventional lambda sensor, but it is the removal of exhaust gas oxygen in chamber 1 which allows accurate NOx concentrations to be determined. Incorporation of reduction catalysts within the sensor also ensures that only the correct NOx concentration is detected and sent to the ECU.

However, this sensor system is not without its limitations. As the design is similar to that of a lambda sensor and makes use of conductive zirconia, it does not begin collecting data as soon as the engine is engaged. A temperature of at least 300°C is needed to allow the zirconium ions to become conductive, and allow the sensor to begin working. The engine usually takes around 3-4 minutes to warm to the appropriate temperature, however heater systems can be installed to reduce this to around 2 minutes. As well as this cold start issue, there are also selectivity concerns to be considered. The sensor relies on pre-treatment of the exhaust gas to remove any oxygen from the mixture to ensure that only NOx is detected. Over time, exhaust gas pre-treatment systems can become less effective due to the build up of poisons, therefore the sensor would be providing inaccurate readings to the ECU

which will incorrectly alter the A/F ratio, reducing engine efficiency. This further reinforces the need for a sensor system that is operational upon engine ignition and selective towards the desired analytes only.

2.3 Silicon Carbide

Silicon carbide is a IV-IV compound semiconductor and is a mechanically and electronically resilient material. The wide bandgap of silicon carbide, chemical and radiation tolerance, high material hardness and ability to cope in excessive electric fields makes it a suitable candidate for application in extreme environments [30, 31]. SiC based electronic devices have been deployed in harsh conditions of high radiation, high temperature as well as chemically corrosive environments, with minimal effect on performance. Traditional silicon devices are unable to cope with these conditions, this is why industries such as automotive, nuclear, military and aerospace have turned to SiC technology over the past few decades.

Other wide bandgap semiconductors such as diamond and gallium nitride have been investigated as potential substrates for hostile environment electronics, however SiC technology has progressed more rapidly. SiC can be seamlessly transitioned into already established silicon fabrication techniques and it is the existence of a thermally growable silicon dioxide (SiO_2) layer which aids this transition. 6" SiC substrates with high quality epitaxial layers are commercially available and can be purchased as either n-type or p-type to suit device requirements. These features, coupled with comfortable operation at high voltages and high switching frequencies, have allowed SiC technology to progress from laboratory operation, to commercially available devices.

Within the field of power electronics there are a range of structures that have been developed on SiC, such as Schottky diodes, MOSFET/JFET switches, radiation detectors and gas sensors [32]. In terms of gas sensors, high temperature operation is key as potential applications include monitoring of industrial processes, nuclear storage and combustion efficiency. Using silicon carbide provides this temperature resilience, therefore the failure of a device operated in an exhaust may be dominated by limitations in the packaging, rather than the device itself. This is an area of active research worldwide and is beyond the scope of this thesis.

2.3.1 Silicon Carbide History

The discovery of silicon carbide is credited to Jans Jakob Berzelius in 1824 when he proposed the existence of a covalent bond between silicon and carbon [33, 34]. However it was 67 years later before the basis of a commercial process was established

by Eugene. G. Acheson in 1891, as the result of a failed experiment. Acheson's attempt to react aluminium silicate with carbon powder produced a substance containing lustrous aggregates of silicon carbide, which he named 'carborundum'. The fundamental principles of this reaction are still upheld in the electric batch furnace process used to make silicon carbide [35, 36]. Silicon dioxide and coke (carbon) are combined at 1500-2500°C which produces the desired silicon carbide and a by-product of carbon monoxide.

$$\mathrm{SiO_2} + 3\,\mathrm{C} \longrightarrow \mathrm{SiC} + 2\,\mathrm{CO}$$

The production of different silicon carbide polytypes depends on the temperature of the Acheson furnace, as well as the presence of any impurities. β-SiC forms at around 1500 °C, but at higher temperatures of 2500°C α-SiC dominates. The 6H polytype of SiC is produced when the reaction proceeds without the influence of impurities. However, upon the addition of aluminium, the product changes to 4H SiC. Silicon carbide is a naturally occurring compound, but examples of this are very rare. The first instance of its natural discovery was 2 years after Acheson's experiments, in 1893 by Nobel Prize winning chemist Dr Henri Moissan. SiC grains were identified upon investigation of the Diablo Canyon iron meteorite in Arizona and the mineral was named Moissanite after the discoverer [37].

In 1907, Henry Round applied a voltage across a crystal of SiC and observed the emission of light as a result; this is widely accepted as the first example of a light emitting diode (LED) [38, 39]. Up until this use in electronics, it was mainly the physical properties of silicon carbide which were exploited. The high hardness of the material made it a leading candidate for use in machinery and abrasive applications. The Acheson production process produces non-uniform, low-purity samples which are suitable for these physical applications, however a more refined process is required when producing SiC for electronics. In 1955, the Lely sublimation process was invented to produce more uniform crystals from which electronic devices can be created more easily. The Lely process is not as sophisticated as the more recently discovered chemical vapour deposition (CVD) technique as, even though good quality crystals can be produced, the sizes can be irregular and no polytype control is possible [40].

2.3.2 Properties of Silicon Carbide

Silicon based electronics are widely established for a variety of applications such as transistors and integrated circuits, however the intrinsic material properties of silicon limit operation to temperatures below 175°C. Significant research has been undertaken to find semiconductor materials capable of functioning at higher temperatures. Ideal candidates to overcome this challenge are wide bandgap semiconductors which

have intrinsic properties more suited to operation at elevated temperatures. While theoretically wide bandgap materials are suitable for this application, in practice there are difficulties faced such as a lack of readily available substrates, increased expense as well a lack of reproducibility. Therefore, the development of wide bandgap electronics has been subject to intense research over the last few decades, with SiC device efficiency and high temperature performance being key goals [41, 42].

The stability of SiC at high temperatures stems from its intrinsic material properties such as wide bandgap and high thermal conductivity, which vary from polytype to polytype. Furthermore, the existence of a thermally growable native oxide allows easy transition into established silicon fabrication processes. These features make SiC a promising material for electronic devices capable of operating at high temperatures.

2.3.3 Polytypes

Silicon carbide is a IV-IV compound formed as a result of a strong covalent bond (447 kJ/mol) between atoms of silicon and carbon in a stoichiometric ratio of 1:1 [17]. In order to fill the valence bands of the two atoms, a tetrahedral structure makes up the basic building block of all crystalline forms of silicon carbide (Figure 2.8). The distance between the carbon and silicon atoms is 1.89Å, and between the carbon atoms is 3.08Å [43]. It is the stacking and arrangement of these individual tetrahedra which determines the polytype of the material.

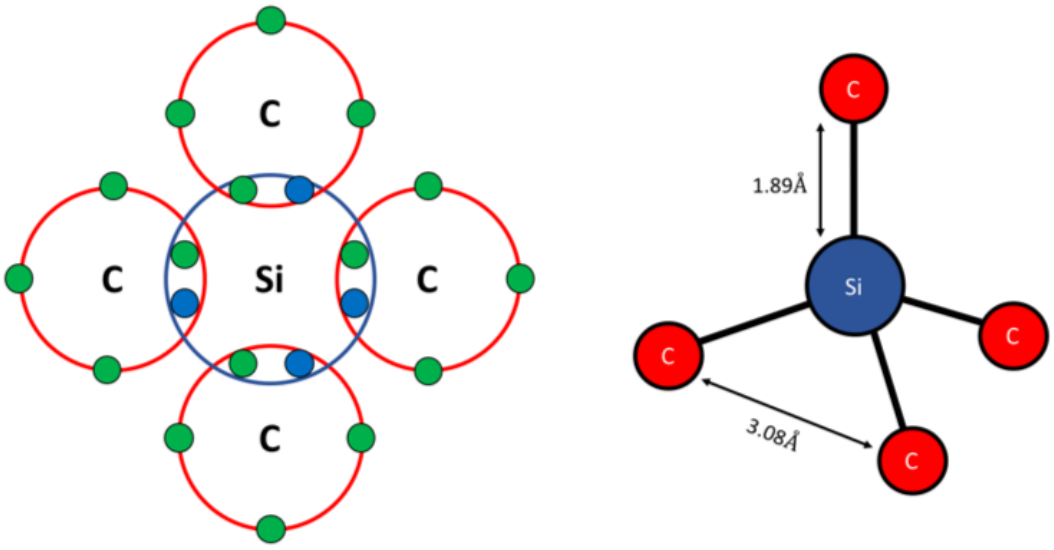

Figure 2.8: Silicon Carbide Valence Diagram and Tetrahedron

Unlike many other semiconductors, SiC exists in a number of crystalline forms, each with different properties. Polymorphism is the phenomenon where the same

chemical compound exists in more than one crystallographic arrangement, with these individual arrangements known as polymorphs. In SiC and other close packed structures, one-dimensional polymorphism can arise and is known as polytypism. Here, individual polytypes arise from the variation in stacking arrangements of crystallographic planes. There are over 200 known polytypes of SiC, each with different physical and electronic properties [44, 45].

Over 200 different polytypes have been discovered to date, but only a select number have suitable properties to be used in electronic applications. The most common nomenclature used to identify these polytypes is Ramsdell notation in which the names are self-descriptive. The integer indicates the number of bilayers in the stacking sequence and the letter (C, R or H) refers to the symmetry present in the structure. Fundamentally, all silicon carbide polytypes are based on three structures which are cubic, rhombohedral and hexagonal, represented by the letters C, R and H respectively [46]. 3C, 4H and 6H are the most common polytypes used in fabrication, with 4H and 6H being commercially available in bulk wafers with epitaxial layers. Out of these polytypes, 4H-SiC is preferred as it offers the most advantageous electronic properties i.e. the widest bandgap, lowest intrinsic carrier concentration, lowest mobility anisotropy and highest carrier mobility [47].

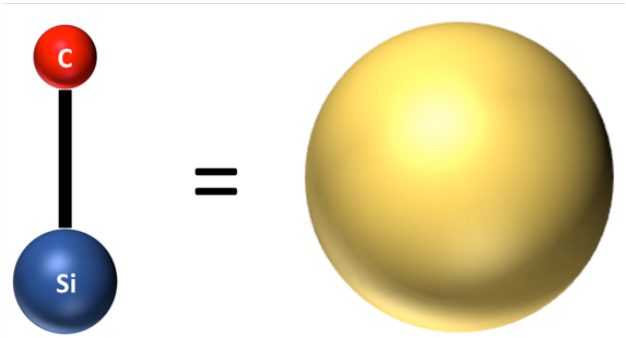

Figure 2.9: Silicon-Carbon bond represented as a sphere used in hexagonal close packing

To understand the arrangement of different crystal types, hexagonal close packing can be considered, by replacing the Si-C pair with a sphere, as shown in Figure 2.9. Hexagonal close packing arises when layers of these spheres overlay one another, but not directly, this is shown schematically in Figure 2.10. For example, if one layer is considered to be in arrangement A, the following layer can only form in arrangement B or C. This rule applies for all three arrangements. A layer of B or C can only be followed by A/C or A/B respectively [45].

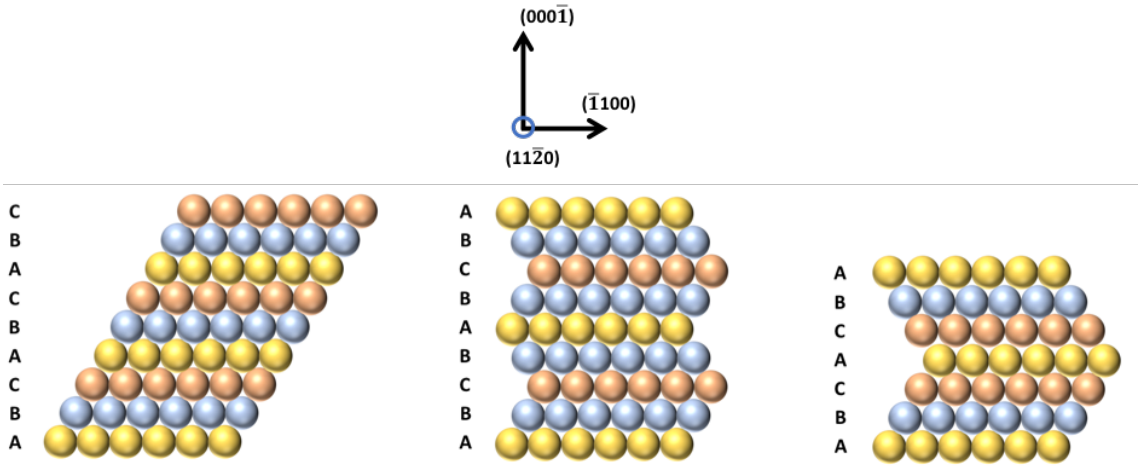

Figure 2.10: Schematic of hexagonal close packing

The 2D and 3D stacking sequences of 3C, 4H and 6H SiC are shown in Figures 2.10 and 2.11 [48]. 3C-SiC has the stacking sequence of ABCABC, with the repeating sequence of three letters indicating a cubic arrangement. 4H-SiC and 6H-SiC have the sequences ABCBABCB and ABCACBABCACB respectively. This self-descriptive Ramsdell notation for 4H-SiC details that there are four Si-C bilayers in the repeating unit and indicates that the crystal has a hexagonal structure. These structures are shown from the side view, or (11$\bar{2}$0) direction, as shown in Figure 2.12.

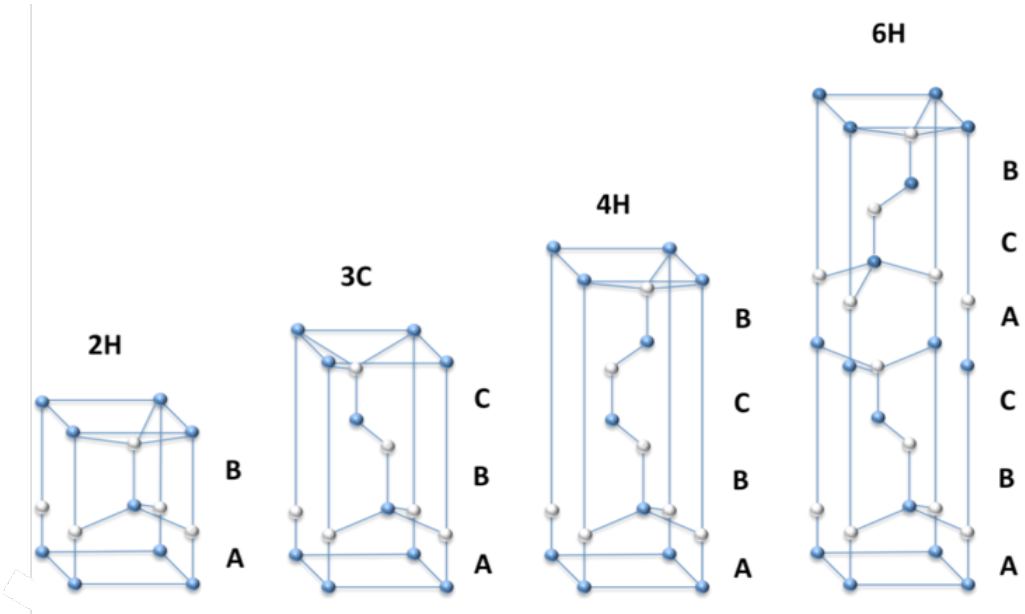

Figure 2.11: SiC Polytypes [48]

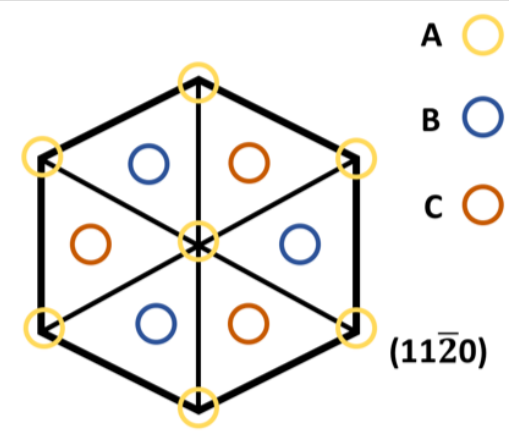

Figure 2.12: Representational view of 11$\bar{2}$0 plane

2.3.4 Wide Bandgap

The bandgap of a material is what determines whether the material is a conductor, an insulator or a semiconductor. The bandgap is the energy difference between the valence band (VB) and the conduction band (CB) of a material. Conduction occurs when charge carriers exist in VB or the CB[49].

A material is usually an insulator if it has a bandgap in excess of 4 eV, as this value is considered to be too high for the material to act as a semiconductor (with the exception of diamond) [50]. Silicon has a relatively low bandgap of 1.12 eV, whereas commercially available 4H-SiC has a bandgap value of 3.23 eV (See Figure 2.13).

The bandgap of a material is related to operation at elevated temperatures, generally the wider the bandgap, the more functional the material is at high temperatures [51]. For intrinsic semiconductors, at lower temperatures the material does not have sufficient energy to conduct (i.e. transfer electrons from the VB to the CB), therefore it remains an insulator. However at higher temperatures, the system has more energy, enabling electrons to flow to the CB which generates an electron-hole pair. The more energy that a system has, the more electron-hole pairs are generated, increasing conductivity. If the gap between the VB and the CB is small, less thermal energy is needed for carriers to be promoted to the conduction band (electrons) or valence band (holes), which limits operational temperature. More energy will be needed for electron flow if the bandgap is large, therefore allowing the material to withstand higher temperatures before conduction occurs. This explains why traditional silicon electronics break down at temperatures in excess of 200°C and why silicon carbide electronics can withstand higher temperatures [52].

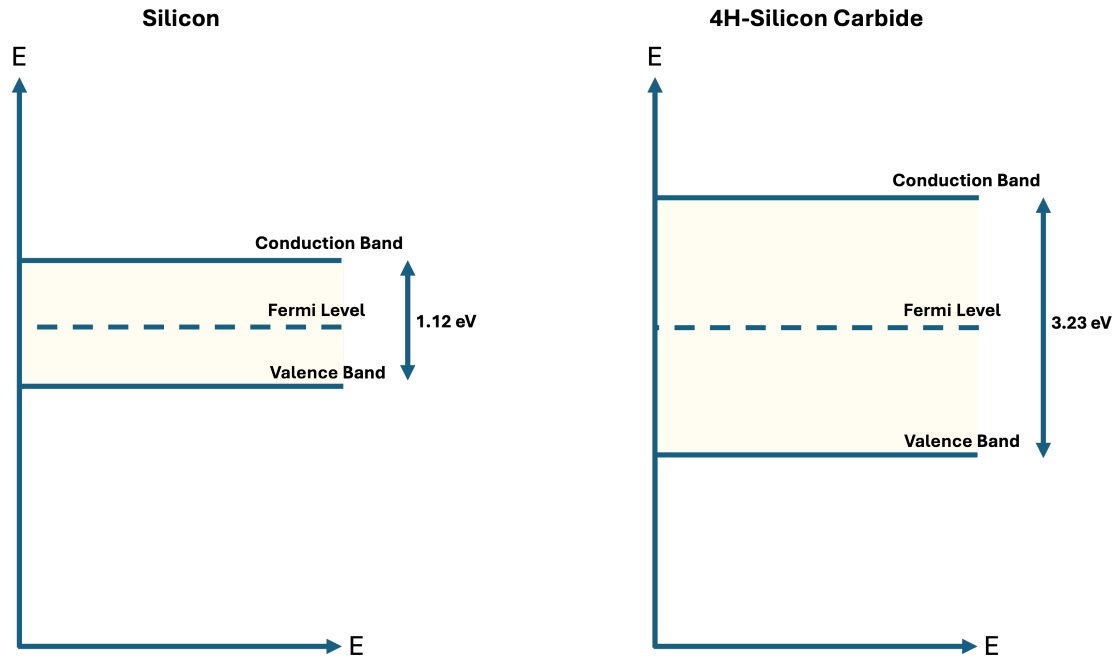

Figure 2.13: Energy band diagrams for silicon and 4H-silicon carbide, illustrating the variation in bandgap

2.3.5 Fermi Level and Doping

The Fermi level is the energy at which the probability of finding an electron is 50% when the system is at absolute zero in temperature. This is an indication of the likelihood that a charge carrier is occupying the valence or conduction band. The Fermi energy is an important parameter that influences the electronic characteristics of semiconductor devices and can be altered by the levels of doping within the substrate.

Intrinsic semiconductors are defined as a highly pure crystal of semiconductor material. For intrinsic silicon carbide, the fermi level is found in the middle of the bandgap between the valance and conduction bands, as there is an equal chance of a charge carrier occupying these bands. Doping is a way to increase the conductivity of semiconductors by increasing the density of free charge carriers within the system [53]. If we consider a silicon lattice for simplicity, every silicon atom is bonded to four other silicon atoms to fill the valence shell with electrons (structurally, this formation of silicon is not strictly representative, but it is used to illustrate the concept). Each silicon has four electrons in its valence shell, so if an atom of silicon is replaced with an atom of phosphorous (with five valence electrons), this leaves one spare electron free to move around the lattice, leaving behind a positive charge on the phosphorous atom. This phosphorous atom is termed as a donor as it donates an electron to the

conduction band of the crystal, increasing the concentration of electrons, shifting the fermi level towards the conduction band - n-type doping. A schematic representation of n-type doping is shown in Figure 2.14, where a phosphorous atom replaces a silicon atom in the lattice.

For p-type doping, an electron acceptor such as boron (with three valence electrons) is added to the lattice, the missing electron is captured elsewhere in the crystal, leaving the boron negatively charged and increasing the number of holes in the valence band [54].

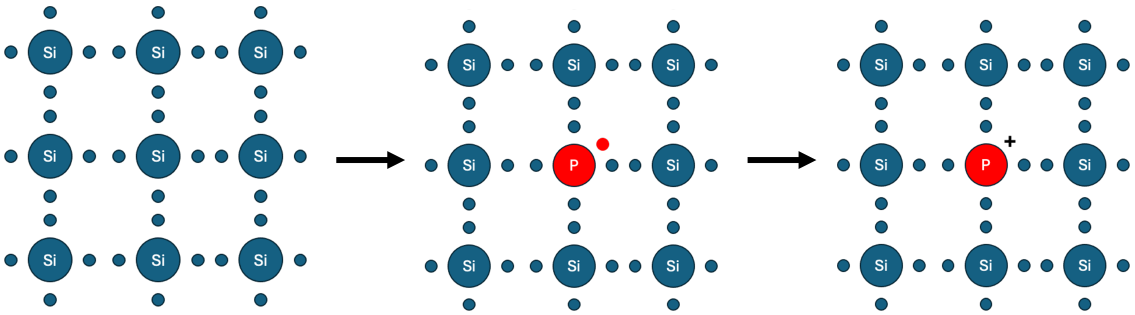

Figure 2.14: Schematic representation of phosphorous (n-type) doping in silicon

If the semiconductor is doped with n-type materials, additional electrons are added to the system shifting the fermi level closer to the conduction band. The amount that this is shifted depends on the concentration of dopant added. Conversely, if p-type dopants are added, the Fermi level shifts downwards towards the valence band, as more holes are added to the substrate. A schematic representation of this is shown in Figure 2.15

2.3.6 Intrinsic Carrier Concentration

Control of the local free carrier concentration in semiconductor electronics is vital to device operation and behaviour can be controlled by the introduction of dopant impurities into desired regions of a device [31, 55]. It is important that these carriers are prominent enough to control conduction within the system in order to satisfy device requirements. These dopants are not the only carriers present however, as semiconductor materials possess a standard number of thermally generated electrons and holes, known as the intrinsic carrier concentration. It is important for the number of dopant carriers to exceed the number of intrinsic carriers, as this allows a device to function as engineered. If there are more intrinsic carries than dopant carriers, electrical conductivity will be governed by the intrinsic carriers and the device will fail. For effective high temperature operation, it is beneficial for a semiconductor to have a low intrinsic carrier concentration. This is due to the exponential relationship between intrinsic carrier concentration and temperature, where

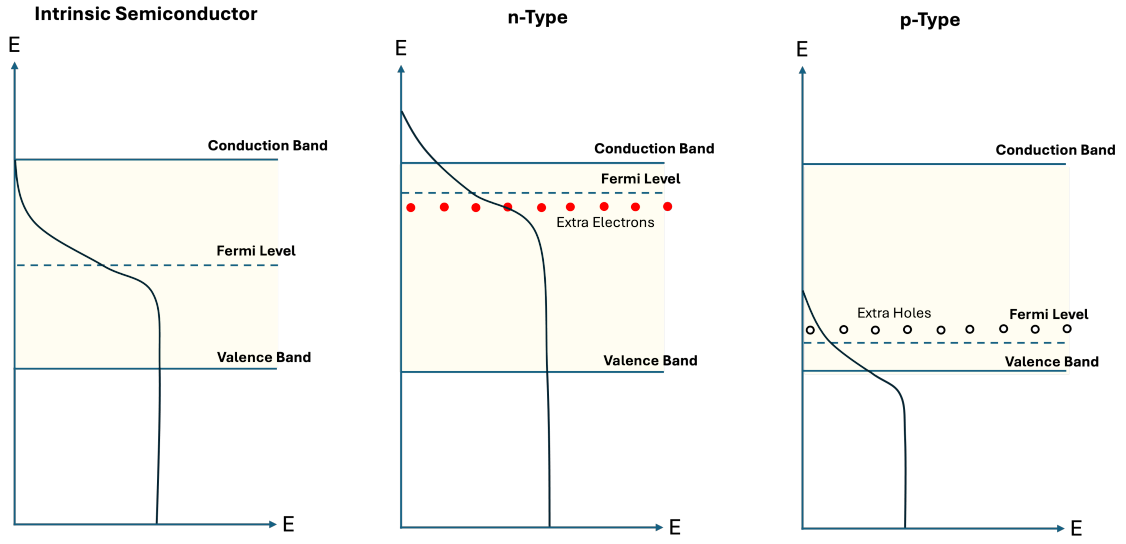

Figure 2.15: Schematic representation of energy bands for an intrinsic semiconductor, n-type doping and p-type doping

an increase in temperature results in a greater number of carriers [56]. A graphical representation of this relationship is shown in Figure 2.16.

The intrinsic carrier concentration can be determined from the following empirical equations:

$$N_i = \sqrt{N_c N_v}\ e^{\left(\frac{E_g}{-2k_B T}\right)} \tag{2.2}$$

$$N_c = 3.25 \times 10^{15}\ T^{\frac{3}{2}} \tag{2.3}$$

$$N_v = 4.80 \times 10^{15}\ T^{\frac{3}{2}} \tag{2.4}$$

$$E_g = E_g(0) - 6.5 \times 10^{-4}\ \left(\frac{T^2}{T + 1300}\right) \tag{2.5}$$

where N_c and N_v are the density of states in the conduction and valence bands respectively, E_g the bandgap of the semiconductor, k_B is Boltzmann's constant and T the temperature [57, 58].

The data in Table 2.1 show that at 300 K (taken to be room temperature), both Si and SiC have an intrinsic carrier concentration of approximately 10^{10} cm^{-3} and 10^{-8} cm^{-3} respectively. The carrier concentration in doped regions of SiC usually lies between 10^{14}-10^{17} cm^{-3}. As the temperature is increased above 300 K however, the intrinsic carrier concentration increases, resulting in more intrinsic carriers than

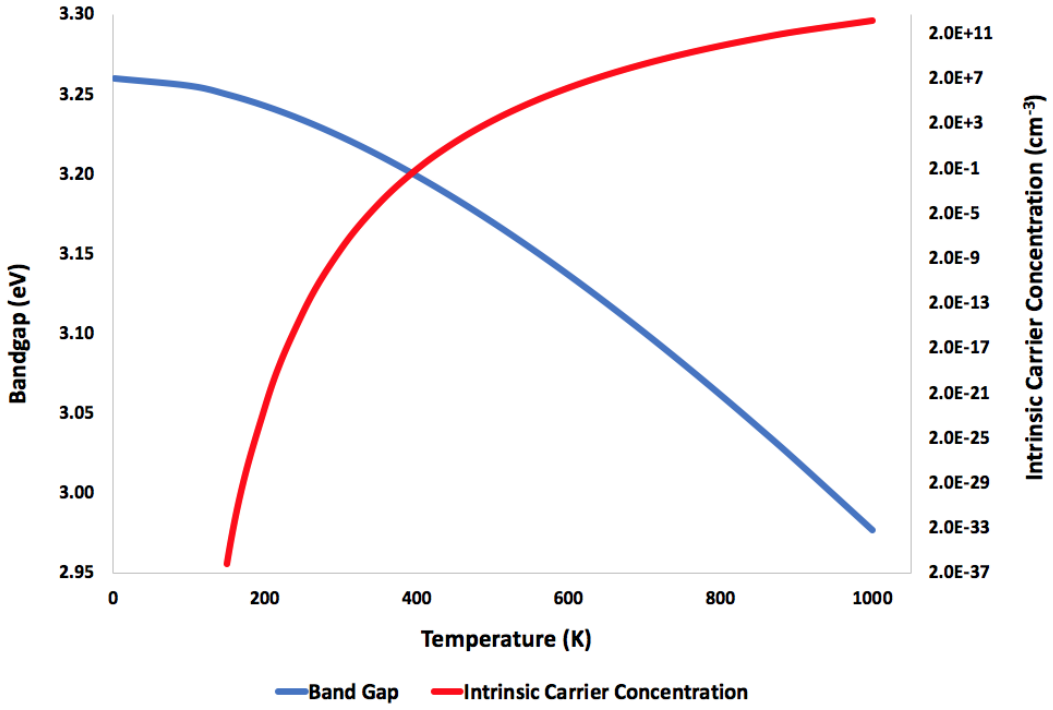

Figure 2.16: Bandgap and intrinsic carrier concentration variation of 4H-SiC with temperature

dopants. In lighter doped regions, conductivity is therefore controlled by intrinsic carriers, resulting in device breakdown.

At around 800 K, SiC has an intrinsic carrier concentration of around 10^{10} cm^{-3}, similar to the value of Si at room temperature. The thermal carrier generation of SiC at elevated temperatures is comparable to that of Si at room temperature, making SiC a good material for high temperature electronics.

		Unit	3C-SiC	4H-SiC	6H-SiC	Si	Ge	GaAs
Bandgap	(E_g)	eV	2.40	3.26	3.00	1.12	0.66	1.43
Breakdown Critical Field	(E_c)	Mv/cm	2.00	2.20	2.60	0.25	0.10	0.30
Electron Mobility	(μ_n)	cm^2/Vs	1000	1000	500	1350	3900	8500
Hole Mobility	(μ_p)	cm^2/Vs	40	120	80	480	1900	400
Electron Drift Velocity		cm/s	-	$2x10^{-7}$	-	$1x10^{-7}$	-	$1x10^{-7}$
Intrinsic Carrier Concentration	(n_i)	cm^{-3}	10	10^{-8}	10^{-6}	10^{10}	10^{13}	10^6
Permittivity	(ε_r)	-	9.7	10.0	10.0	11.9	16.0	13.1
Thermal Conductivity	(κ)	W/cm K	5.0	5.0	5.0	1.5	1.6	0.6

Table 2.1: Bulk properties of common semiconductors at 300 K [59]

2.4 Metal Oxide Semiconductor Capacitors

The metal-oxide-semiconductor capacitor comprises a gate metal, an insulating dielectric layer and a semiconductor substrate. In the case of high temperature gas sensors, the gate is usually a noble metal with catalytic properties, the oxide is a combination of a thin SiO_2 layer and a high-κ dielectric, and the semiconductor substrate is silicon carbide. In terms of a traditional capacitor, the metal acts as one plate of the capacitor, and the doped semiconductor acts as the other. The MOS capacitor behaves as two distinct capacitors connected in series both contributing to the overall capacitance value, these are the oxide capacitance (C_{ox}) and semiconductor capacitance (C_s). A schematic representation of this is shown in Figure 2.17.

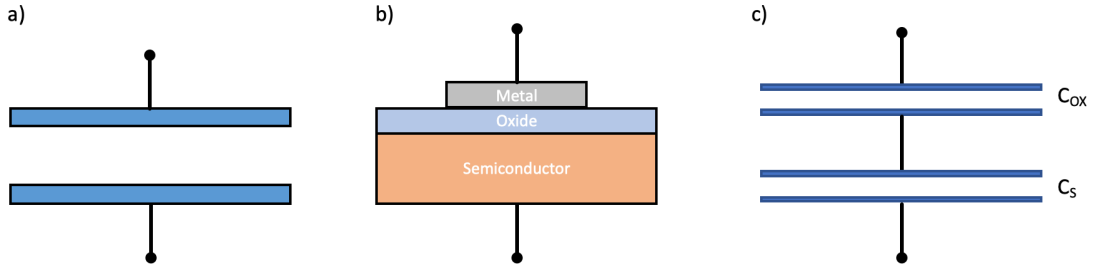

Figure 2.17: Schematic of a) parallel plate capacitor b) Metal oxide semiconductor capacitor and c) Representation of C_{ox} and C_s acting as two capacitors in series

In order to overcome the low band offset between SiC and high–κ dielectrics, the device should include a 20 nm interfacial layer of SiO_2 (Figure 2.18). This offset arises from the bandgap value of 4H-SiC (3.26 eV) and the bandgap value of high-κ oxides which are typically in the range of 5–7 eV. Without the presence of the SiO_2 layer, leakage currents are typically three orders of magnitude higher than equivalent devices which have a SiO_2 layer, and the breakdown voltage is significantly lower, especially at high temperatures. For devices using HfO_2 as the high-κ dielectric layer it has been shown that the value of the valance bend offset can be increased from 1.5 eV to 2.2 eV with the inclusion of a thin SiO_2 layer, ultimately reducing leakage current [60].

The energy band diagram of the MOS capacitor under flatband conditions is shown schematically in Figure 2.19. E_0 represents the vacuum level, E_F the Fermi level and E_C and E_V are the conduction and valence bands respectively. The work function of the metal and semiconductor (Φ_M and Φ_S) is the energy difference between the Fermi level and the vacuum level and these are equal at the flatband condition. χ_I and χ_s are the electron affinity of the insulator and semiconductor, which is the energy difference between the conduction band and the vacuum level [61].

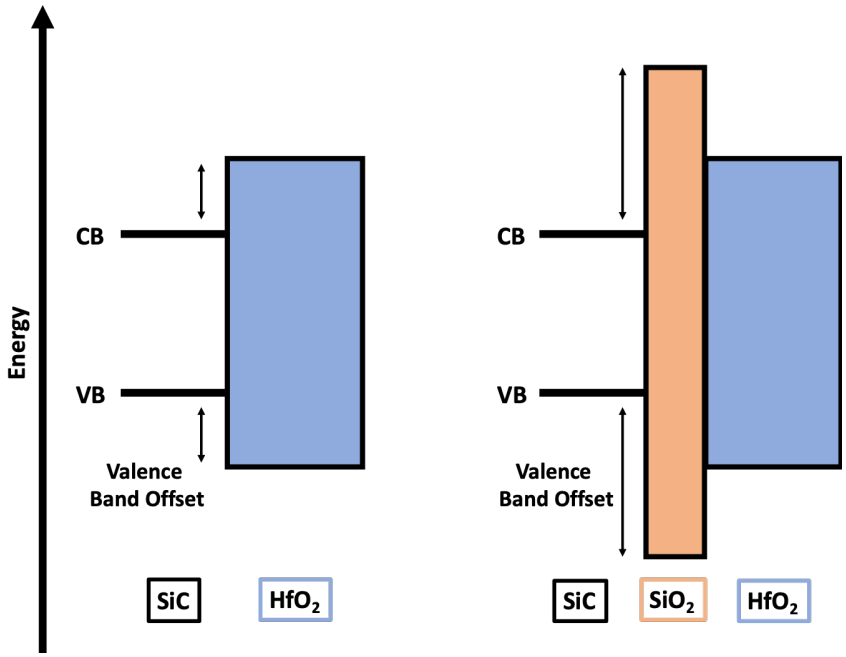

Figure 2.18: Energy band diagrams of SiC/HfO_2 and $SiC/SiO_2/HfO_2$ outlining valance band offset

Shifts in the C–V curve of the capacitor on exposure to gas species are used to determine the sensor response when exposed to chemical species, so it is important to understand the physics that results in the observed characteristics. A typical C-V trace comprises three separate regions; accumulation, depletion and inversion. A schematic capacitance-voltage characteristic for an n-type curve is shown in Figure 2.20. The figure shows the typical high frequency curve for an n–type capacitor with deep depletion observed at negative bias. Because of the low minority carrier concentration in silicon carbide, typically 1×10^{-8} cm^{-3} at room temperature, low frequency characteristics do not show evidence of inversion and the characteristics are identical to those taken at high frequencies, as shown in the figure. At high forward bias, the capacitance becomes saturated and does not show a voltage dependence, this is the accumulation region.

An important parameter that can be extracted from the C–V data is the flatband voltage, denoted by V_{FB}. Under equilibrium conditions, the flatband voltage is equal to the difference in work function between the metal and the semiconductor. Shift in this parameter is used to determine the response of the sensor to gas exposure.

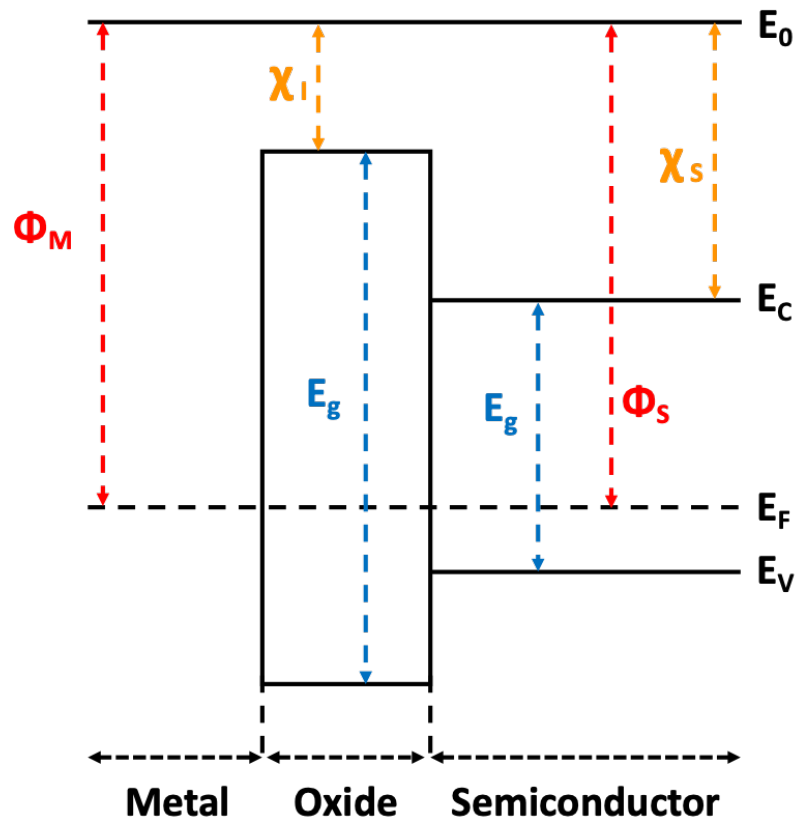

Figure 2.19: Energy band diagram of an ideal p-type MOS capacitor under equilibrium conditions

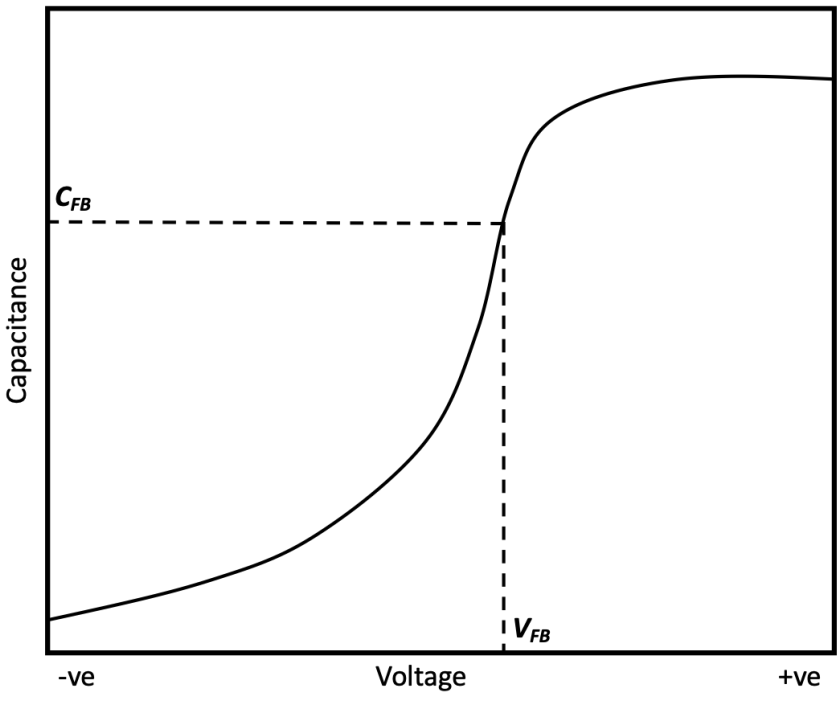

Figure 2.20: Schematic of an ideal MOS capacitor CV curve

2.4.1 Accumulation

For an n-type device, accumulation occurs when a positive bias is applied to the gate metal, attracting electrons and forming an accumulation layer at the semiconductor-oxide interface. It is the insulating nature of the oxide that prevents these charges from moving to the conduction band in the oxide and subsequently into the gate contact. The positive bias lowers the fermi level of the metal with respect to the vacuum level, and causes downward band bending as can be seen in Figure 2.21. In the accumulation region, the measured capacitance is equal to the oxide capacitance (C_{ox}). If the gate metal is considered to be one electrode of a parallel capacitor, the electron layer at the semiconductor-oxide interface can be considered to be the second, leaving the insulating oxide layer in between. Therefore, the total capacitance per unit area of the device in accumulation mode only arises from the oxide capacitance [61]. This is shown in Equation 2.6,

$$C_{ox} = \frac{\varepsilon_0 \varepsilon_{ox}}{t_{ox}} \tag{2.6}$$

where ε_0 is the permittivity of free space (8.854×10^{-14} F cm^{-2}), and the relative permittivity of the silicon dioxide dielectric, $\varepsilon_r = 3.9$.

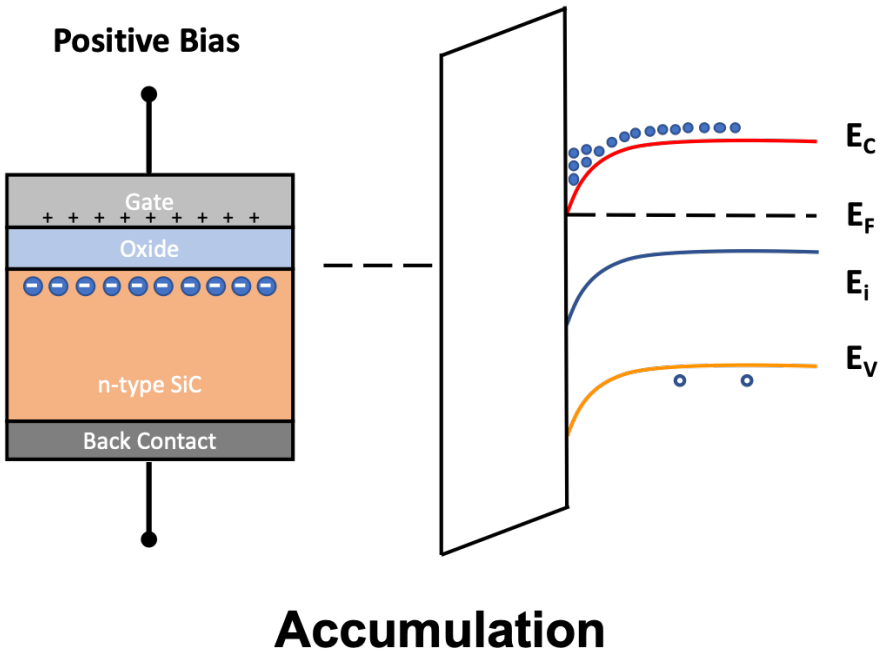

Figure 2.21: Schematic representation of a MOS capacitor in accumulation mode

2.4.2 Depletion

As the voltage becomes slightly negative with respect to flatband voltage, electrons are repelled from the oxide to the SiC interface, resulting in the formation of a volume with no free charge, forming a depletion region. This raises the fermi level of the gate, resulting in upward band bending as shown in Figure 2.22. This depletion region increases in size until a maximum width is reached (W_{max}). The total capacitance now includes a contribution from the semiconductor capacitance.

Following Figure 2.17c, the total capacitance (C_T) can be calculated from Equation 2.7, where C_{ox} is the oxide capacitance and C_s is the semiconductor capacitance (Equation 2.8).

$$\frac{1}{C_T} = \frac{1}{C_{ox}} + \frac{1}{C_s} \tag{2.7}$$

$$C_s = \frac{\varepsilon(SiC)\,\varepsilon_0}{W_D} \tag{2.8}$$

The depletion width, W_{dep}, can be determined using Equation 2.9.

$$W_{dep} = \sqrt{\frac{2\,\varepsilon_s\,\varepsilon_0\,\psi_s}{q\,N_A}} \tag{2.9}$$

where, ε_{SiC} is the relative permittivity of the silicon carbide, q the electron charge, N_D the donor concentration, and ψ_s the surface potential, which is related to the applied bias at the gate contact.

The maximum depletion width can be determined using Equation 2.10. This parameter describes the transition between the depletion and the deep depletion regions in the C–V characteristics. This is a temperature dependent variable, as described using Equation 2.10

$$W_{max} = \sqrt{\frac{4\,\varepsilon_s\,\varepsilon_0\,k_B\,T\,\ln\frac{N_A}{n_i}}{q^2\,N_A}} \tag{2.10}$$

where k_B is Boltzmann's constant, T the temperature, and n_i the intrinsic carrier concentration.

2.4.3 Inversion

Inversion occurs when a large negative bias is applied to the gate, attracting minority carriers from the bulk semiconductor, for n-type SiC, holes are the minority carriers. This forms an inversion layer at the semiconductor-oxide interface where the minority carrier concentration exceeds the dopant concentration. Upward band bending is seen, causing the valence band to approach the fermi level, resulting in

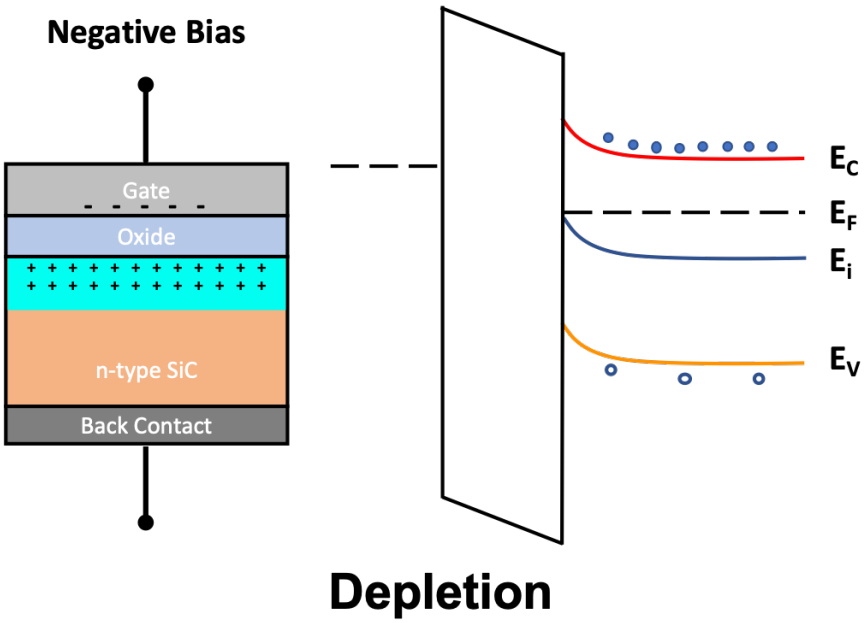

Figure 2.22: Schematic representation of a MOS capacitor in depletion mode

an increased hole concentration at semiconductor oxide interface (Figure 2.23). As the intrinsic carrier concentration of SiC is so low, for the gas sensors produced for this work, inversion is not observed.

2.4.4 Deep Depletion

In contrast to silicon based devices, silicon carbide MOS capacitors do not show evidence of inversion, due to the low intrinsic carrier concentration, n_i, of the material. Instead of inversion, deep depletion is observed. Due to the low n_i, no minority carriers are present, so the capacitance continues to decrease, with a characteristic similar to that observed in the depletion region, regardless of the magnitude of the negative bias applied. The concentration of minority carriers (holes) is linked to n_i, as well as the dopant concentration N_D in the relationship outlined in Equation 2.11.

$$p = \frac{n_i^2}{N_D} \tag{2.11}$$

As the intrinsic carrier concentration of 4H-SiC is around 10^{-8} cm^{-3}, and the dopant concentration is around 10^{16} cm^{-3}, the concentration of minority carriers (as calculated from Equation 2.11) is approximately 10^{-32} cm^{-3}. This number is so small, it is considered negligible, meaning in reality that no minority carriers are attracted from the bulk SiC to form an inversion layer.

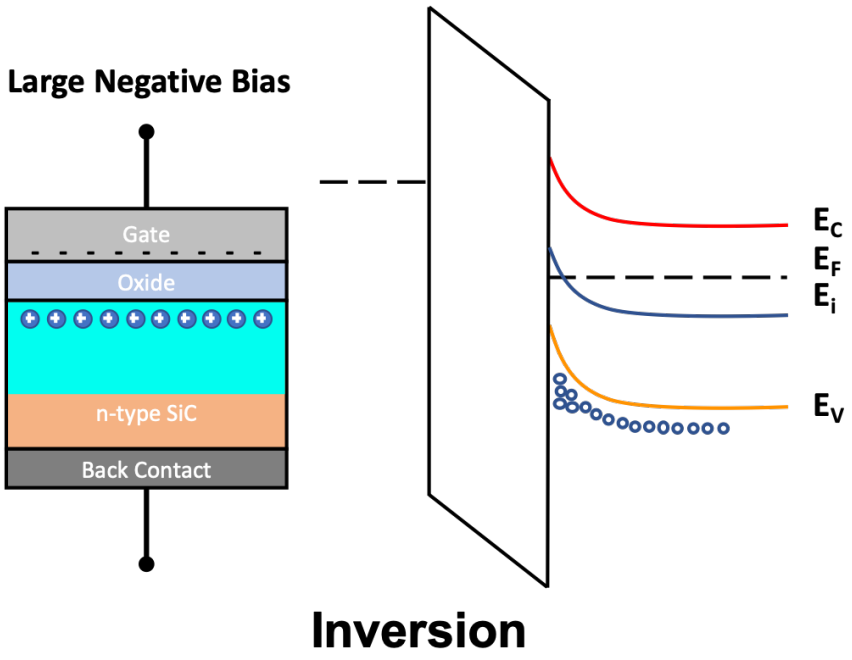

Figure 2.23: Schematic representation of a MOS capacitor in weak inversion mode

2.4.5 Origin of Traps in MOS Capacitors

Traps are important features of MOS devices and understanding how they arise is important to allow mitigation or manipulation of these to control device performance.

Bulk traps exist in the SiC substrate itself and arise for various reasons. These traps can alter device characteristics such as breakdown voltage and leakage current, and therefore impact the reliability of the device as a long term, reliable gas sensor. Defects, or crystal dislocations, can occur in the chemical vapour deposition growth of SiC wafers, leading to bulk traps in the substrate. These defects arise due to thermal stress as a result of the high temperatures needed for formation or steric stress experienced in the SiC lattice. These traps can also be generated during device processing when dopants are introduced (ion implantation) [62, 63, 64].

Traps can also arise at the interface between silicon carbide and silicon dioxide. These traps can form at multiple points during the fabrication of MOS Capacitors. High temperature oxidation of the SiC substrate to form SiO_2 can lead to defects in the oxide layer, incorporating fixed or mobile traps. Further processing of the devices, such as the deposition and oxidation of other dielectric layers can also give rise to interface traps [65]. Fixed traps are charges trapped in the SiO_2 layer and are immobile. They can influence electrical properties, but the concentration of these is constant irrespective of the applied voltage to the device. Traps introduced as a result of device processing tend to be mobile and are affected by the levels of applied voltage and can move within the oxide layer in response to an electric field. The

applied electric field causes mobile charges to move towards the SiC/SiO_2 interface, this will affect electrical characteristics such as flatband voltage and can contribute to the levels of leakage current and ultimately cause premature breakdown [66]. Therefore, it is important to try and reduce the concentration of these interface traps by controlling the temperature and speed of oxidation, as well as potentially annealing devices after oxidation [67].

2.5 Gas Sensors

Traditionally, a sensor system is made up of a receptor and a transducer. The receptor is a material that when exposed to a measurand induces a detectable change in its own properties. It is the role of the transducer to take this change and transform it into a measurable electronic signal known as the response. In terms of gas sensors, the measurand is the gas molecules and the response is usually an electrical output, such as a change in capacitance or resistance.

Semiconductor gas sensors have been widely investigated over the past few decades as it is an attractive prospect to combine the material and electrical properties of semiconductors with the requirements of gas sensors, such as small size and high sensitivity. Semiconductor materials can provide analyte selectivity and sensitivity as well as providing resilience to harsh environments. Established semiconductor processing also allows devices to be made physically smaller than conventional gas sensors based on optical detection methods, as well as the potential to manufacture in bulk, offering significant reductions in cost.

There are a number of device structures which have demonstrated sensitivity to a number of gas species. Sensitivity arises from the interaction between the catalytic metal and the gas analyte, with the first example of hydrogen sensitivity to a metal-oxide system being reported in 1975 [68]. This metal-oxide system can be incorporated into a variety of structures to fit electronic requirements including Schottky diodes, field effect transistors (MOSFET) and MOS capacitors. Figure 2.24 shows the structure of these devices and the observable shift in their electronic characteristics upon exposure to hydrogen gas.

2.5.1 Schottky Diode Sensors

Schottky diodes are made up of a metal contact deposited onto a lightly doped semiconductor, forming a Schottky contact at the interface. The inclusion of a thin interfacial oxide layer between metal and semiconductor improves the stability and reproducibility, as well as reducing the leakage current under reverse bias conditions at high temperatures [33, 70, 71]. Interfacial layers in Schottky diodes usually have

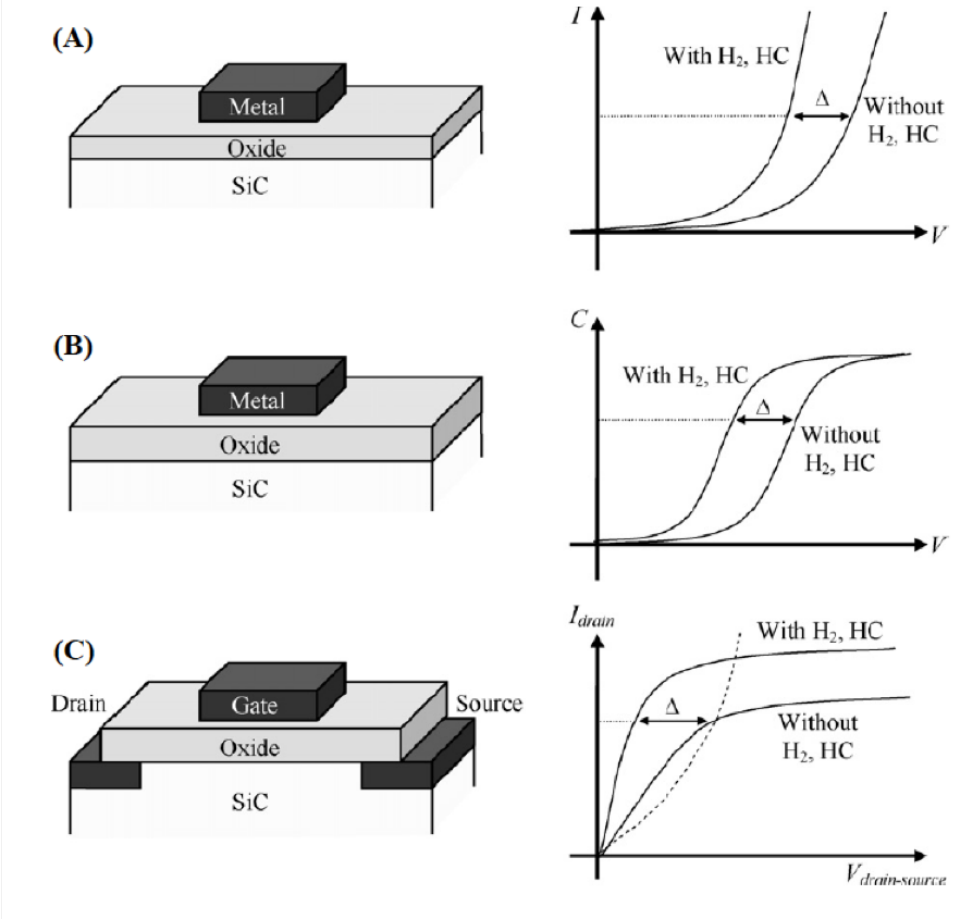

Figure 2.24: The structure and hydrogen response of a (A) Schottky diode (B) MOS capacitor (C) MOSFET [69]

an equivalent oxide thickness of the order of 1–3 nm and include a dielectric film manufactured from insulators such as SiO_2 [72], HfO_2 [73], TiO_2 [74] and $TaSi_x$ [75]. Whilst the inclusion of this layer is often deliberate and controlled, thin SiO_2 layers can also be created due to imperfect cleaning and anneal processes during fabrication.

The response of a Pt/SiC Schottky diode in the presence of 800ppm of hydrogen and air is shown in Figure 2.25a [76]. It can be seen that upon exposure to H_2, there is a negative shift in the current-voltage characteristics of the device concurrent with the accepted gas sensing mechanism. It can also be seen in Figure 2.25b, that the magnitude of the device response increases with H_2 concentration, before saturation is observed at concentrations above at 500ppm.

The data in figure 2.26 show the response of the same structure when the catalytic gate metal was swapped from that of Pt to Pd [77]. A greater magnitude of response is observed for the Pd/SiC device in comparison to the Pt/SiC structure, indicating that this structure is significantly more sensitive to hydrogen. This sug-

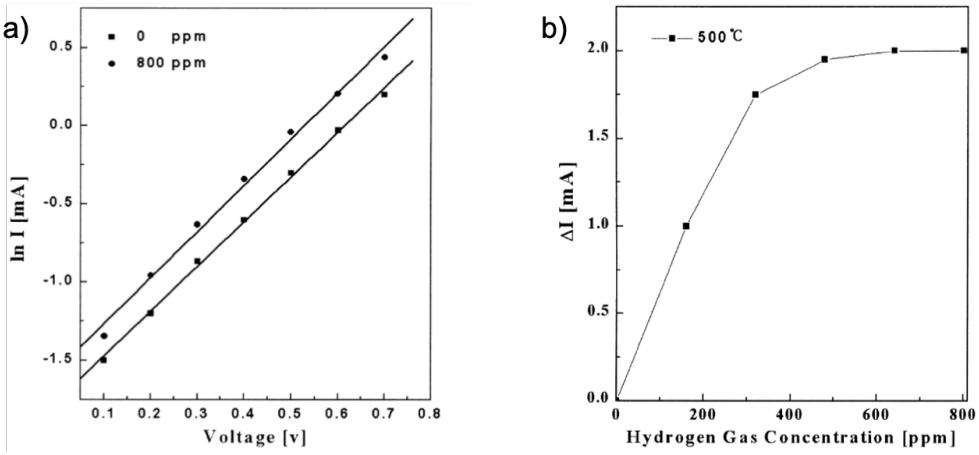

Figure 2.25: a) I-V characteristics of a Pt/SiC Schottky diode in air and 800ppm of hydrogen, b) change in current with hydrogen concentration of at Pt/SiC Schottky diode at 500°C and 3 V forward bias voltage [76]

gests that as well as hydrogen adsorption to the palladium surface, the response may also be influenced by the formation and liberation of hydroxyl ions from the metal surface [78, 79, 80, 81]. In addition to this increased sensitivity, a greater maximum concentration of H_2 can be detected by the Pd/SiC device, as saturation can be observed in the data for concentrations in excess of 800 ppm. This demonstrates that the magnitude of response depends on the choice of gate metal, highlighting he importance of selecting the right materials to construct gas sensors.

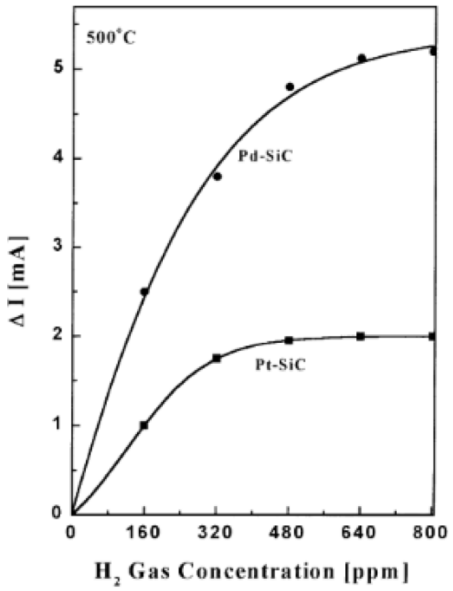

Figure 2.26: Change in current with hydrogen concentration for Pt/SiC and Pd/SiC at 500°C and 3 V forward bias [77]

The data in figure 2.27 show the relative shift in voltage for a $Pt/Ta_2O_5/SiC$ sensor towards varying concentrations under a bias of 1mA at 100 °C and 150 °C

[82]. The Ta_2O_5 layer is very thin, therefore this device acts as a Schottky diode, rather than as a capacitor so the response can be observed as a shift in the voltage when the sensor is operated in constant current mode. Voltage shifts which are proportional to the concentration of the hydrogen gas are observed. It can be seen that the increase in temperature from 100°C to 150°C improves the sensitivity of the device at low concentrations, such as 60ppm, but has little effect at higher concentrations.

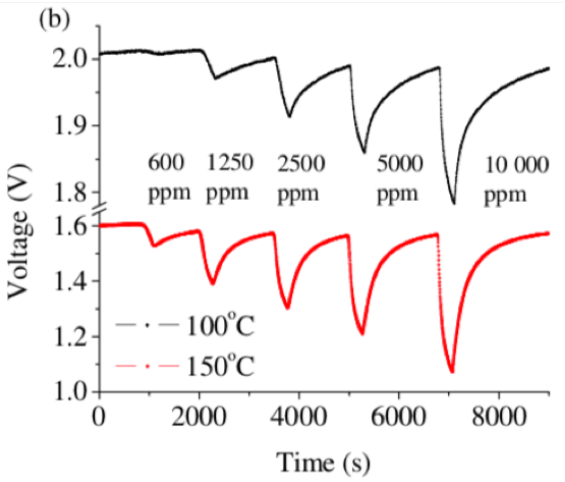

Figure 2.27: Dynamic response of a $Pt/Ta_2O_5/SiC$ sensor towards varying concentrations of H_2 gas at 100°C and 150°C [**DynamicResponsePt/Ta2O5/SiCSchottky**]

The response time of the device is in the order of hundreds of seconds, with the observed recovery time taking significantly longer. The response and recovery time of this device is summarised by the data in Table 2.2. Whilst this structure demonstrates a high level of sensitivity to hydrogen, the protracted response and recovery time makes real-time monitoring of an environment difficult, particularly in automotive applications, where the gas concentrations can change with every rotation of the crankshaft. However, these sensors do not show evidence of saturation, with the voltage returning to the baseline value after recovery.

Examples of devices which can operate as real time combustion monitors have been demonstrated previously with response and recovery times in the order of milliseconds. This fast response allows an accurate picture of a system to be developed. The data in figure 2.28 show a SiC based, Schottky diode, sensor which has been placed in the exhaust manifold of a petrol engine to monitor exhaust output when an engine switches from rich to lean operation [83].

H_2 Concentration (ppm)	Response Time (s)	Recovery Time (s)
600	276	702
1250	303	774
2500	288	711
5000	262	807
10000	264	939

Table 2.2: Response and recovery times of a $Pt/Ta_2O_5/SiC$ sensor with varying concentrations of H_2 [**DynamicResponsePt/Ta2O5/SiCSchottky**]

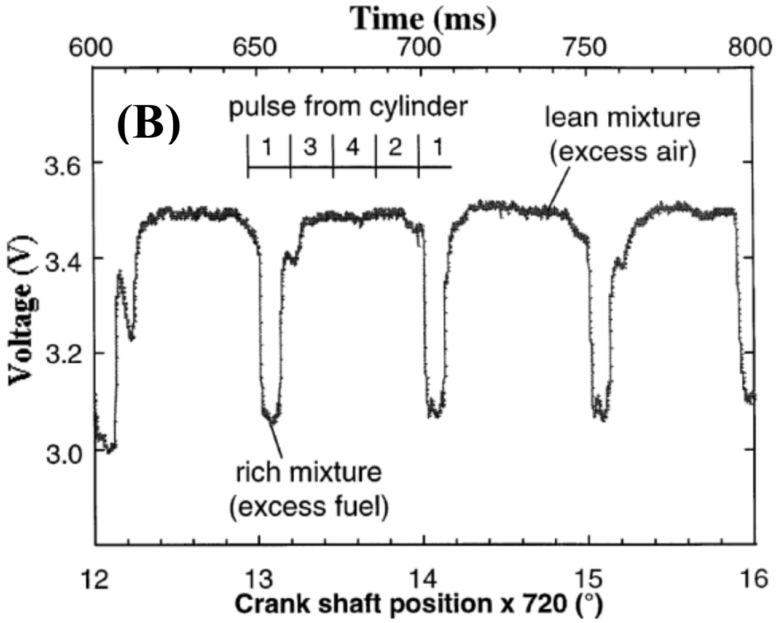

Figure 2.28: Dynamic response of a SiC based Schottky diode sensor placed in the exhaust pipe of a petroleum engine [83]

2.5.2 Metal Oxide Semiconductor Capacitor Sensors

Metal oxide semiconductor capacitors comprise a catalytic gate metal and semiconductor material separated by an insulating layer that has either been deposited or thermally grown onto the semiconductor substrate. Examples of MOS capacitors which are sensitive to H_2 [84, 85, 86],O_2 [87], H_2S [88], NH_3 [85, 89] and hydrocarbons [69] have been demonstrated over the last few decades. When these devices are being interrogated the change in capacitance, usually at the flatband voltage, is monitored to determine the response. The selection of the flatband voltage as the point of measurement is based on the observation from a number of researchers

that the magnitude of response is greatest at the flatband voltage, however the mechanism responsible for this enhanced response is not yet fully understood.

The data in figure 2.29 show the capacitance voltage characteristics of a $Pd/TiO_2/SiC$ capacitor when exposed to increasing hydrogen and oxygen concentrations at 300 °C. It is observable from the data that this device shows a step change in response when exposed to a hydrogen rich environment, before showing a saturation in the characteristics with further increases in the hydrogen concentration.

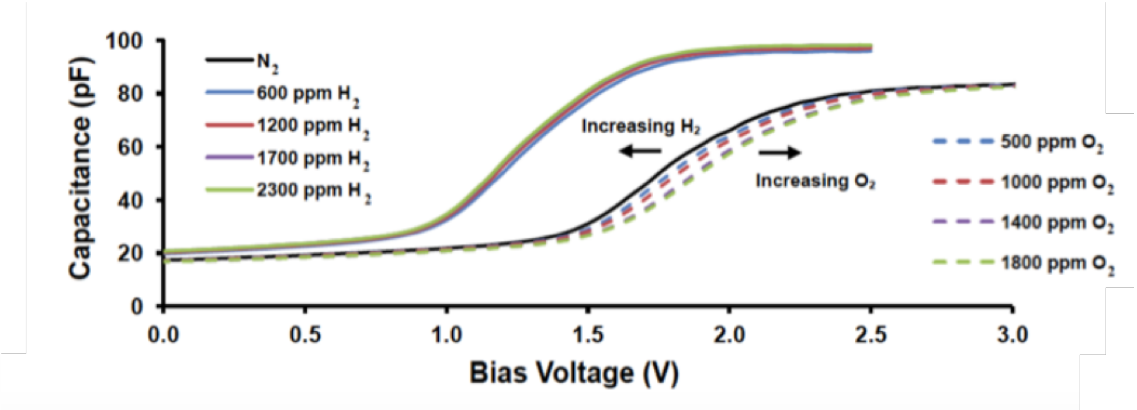

Figure 2.29: Capacitance voltage characteristics of a $Pd/TiO_2/SiC$ MOS capacitor when exposed to varying concentrations of hydrogen and oxygen at 300°C [87]

For capacitors where the I–V characteristics show a significant current flow at low bias (often as a result of a thin SiO_2 layer under the high–κ layer), the leakage current through a MOS capacitor can also be analysed to determine gas response. The data plotted in Figure 2.30 outlines the I-V response of a $Pd/TiO_2/SiC$ capacitor upon exposure to hydrogen, oxygen and hydrogen sulphide. It can be seen from the data that the presence of O_2 causes a significant drop in the device leakage current, whereas H_2 and H_2S result in an increase. This indicates, similar to the capacitance data shown in figure 2.29, that the response for hydrogen rich and oxygen rich ambients is different and that the mechanism responsible for the response has a common origin.

2.5.3 Gas Sensing Mechanism and Response

Metal oxide semiconductor systems have been used as gas sensors in the past for a variety of different analytes. A definitive sensing mechanism is not explicitly known, with a number of theories being suggested, however, in all hypotheses, the gate metal plays an integral part. The gate metal is usually a catalytic noble metal such as platinum, palladium, iridium, or rhodium, capable of causing gas molecules to adsorb and dissociate onto the metal surface. The structural morphology of the gate metal has been demonstrated to have a strong influence on the sensing

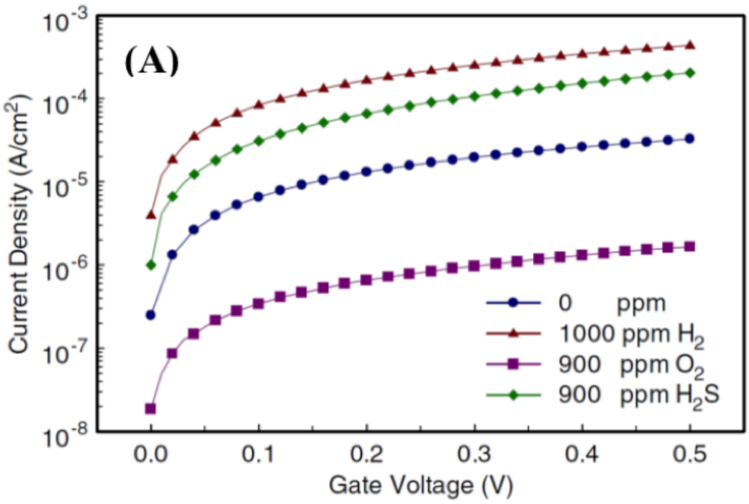

Figure 2.30: Current voltage response of a $Pd/TiO_2/SiC$ capacitor to O_2, H_2 and H_2S at 350°C [88]

mechanism, with porous layers improving the sensitivity to complex analytes [90]. Examples of MOS gas sensors incorporating Pt [86], Pd [91, 92] and Ir [89] have all been observed, and gas adsorption onto rhodium has been studied [93]. There is not a universal gate material to which all of the gases within the exhaust mixture can adsorb, with metals having different affinities for different gases. This selectivity can be exploited as it allows simple discrimination between gases in a mixture. However, this can also be problematic as it requires the need for an array to be used along with sophisticated regression algorithms, if there is more than one target molecule present.

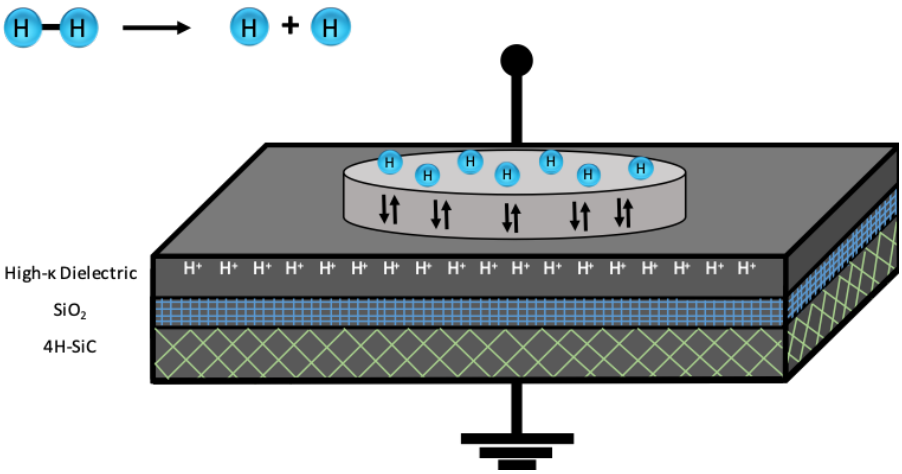

Figure 2.31: Schematic representation Hydrogen Detection by a MOS Gas Sensor

For simple diatomic molecules such as hydrogen, the proposed mechanism relies

on the interaction of the gas molecules with the catalytic metal. Hydrogen molecules come into contact with the catalyst, adsorb to a vacant metal site, and dissociate, forming individual atoms. Due to the small atomic radius of hydrogen, these individual atoms are able to diffuse through the metal layer to the semiconductor-insulator interface and form a charged dipole layer. This polarized layer can give rise to an electric field in the insulator, ultimately altering the number of charge carriers in the semiconductor, thus altering the capacitance output of the device [43, 94, 84]. A schematic of this mechanism is displayed in Figure 2.31, and the shift in a typical C-V curve is shown by the data in Figure 2.32.

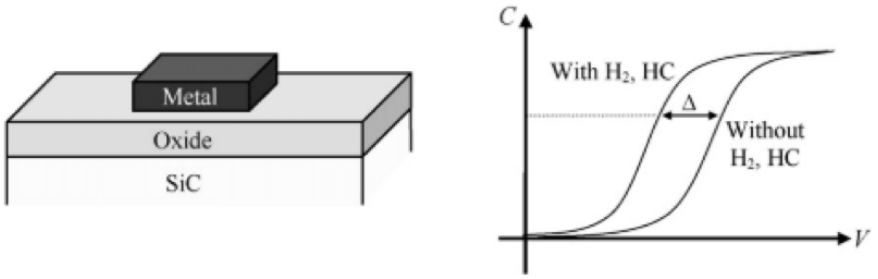

Figure 2.32: Typical response of a MOS capacitor to hydrogen gas [69]

As mentioned previously, capacitance shift is not the only response that can be observed in semiconductor gas sensors. The leakage current through the capacitor can also be monitored to determine the concentration of gaseous analytes. This has been demonstrated for oxygen, hydrogen, and hydrogen sulphide. Here a $Pd/TiO_2/SiO_2/SiC$ device is employed, and the catalytic palladium layer causes decomposition of the H_2S into hydrogen atoms. These hydrogen atoms then diffuse through the metal and form a charged layer on the Pd/TiO_2 interface increasing the leakage current. As expected, the leakage current increases when the concentration of H_2S is increased, as shown by the data in Figure 2.33 [88].

2.5.4 MOS Capacitors as Solvent Sensors

Similar to gases, metal oxide semiconductor capacitors can be used to detect organic solvent vapours. As with gas molecules, there is still ambiguity over the mechanism of interaction between the analytes and the devices. The use of these devices as solvent sensors is relatively uncommon, as silicon carbide based devices are usually used at elevated temperatures. Solvent detection is required at ambient temperatures, due to the volatility of most organic solvents.

One benefit of using the temperature stable SiC based device, is the potential to heat the sensor to remove any adsorbed analytes which will not dissociate, allowing electrical characteristics to return to the baseline value. This will prolong the lifetime

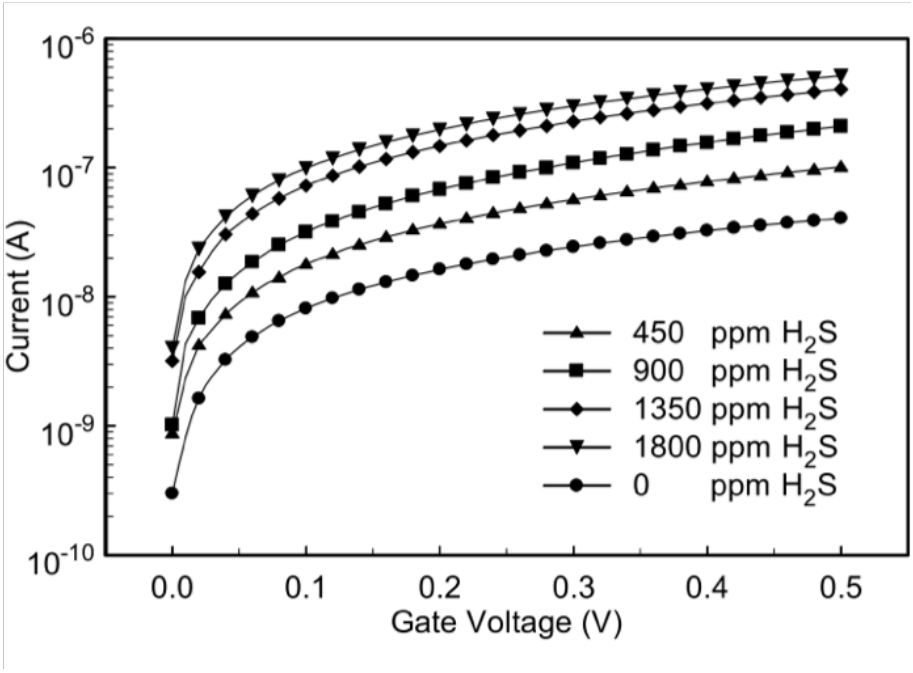

Figure 2.33: Current response to varying H_2S concentrations at 325°C [88]

of the device and prevent sensor drift.

Introducing a MOS capacitor sensor to analytes other then gases, such as solvents, could potentially provide some more useful information on the mechanism of interaction between analytes and the device. Solvents have a range of varying properties, such as boiling point, viscosity, relative permittivity value, and dipole moment among others [95]. Therefore, exposing MOS capacitors to different solvents and observing the changes in electrical characteristics can aid understanding of what is driving the sensor response.

2.5.5 The Langmuir Isotherm, Saturation and Normalisation

The key interaction between gaseous molecules and other analytes with the metal surface can be rationalised by the Langmuir adsorption model. Originally presented by Irving Langmuir in 1916, this model outlines the relationship between surface coverage and gas pressures at a constant temperature [96]. The model relies on the formation of a dynamic equilibrium between an adsorbate (gas molecule) and a vacant adsorption site on the metal, and incorporating the rate constants for the forward and backward reactions, the relationship between surface coverage and gas pressures can be identified [97].

$$\text{Adsorbate} + \text{Empty Site} \rightleftharpoons \text{Adsorbed Complex}$$

$$\mathrm{A}_g + \mathrm{S} \rightleftharpoons \mathrm{A}_{ad}$$

There are certain assumptions that have to be made to satisfy this model, these are:

1. Gas molecules (adsorbate) behave as an ideal molecule.
2. The surface of the metal is homogeneous and made up of a uniform array of sites.
3. The adsorbate forms a monolayer as each site can only hold one molecule.
4. The rate of adsorption and desorption is independent of the number of sites occupied.
5. There is no interaction between molecules once adsorbed.

Consider figure 2.34. If the surface of the metal is taken as a uniform grid, these assumptions can be more easily understood. Each blue square represents a vacant site and each orange circle represents an adsorbed gas molecule. Examining the empty grid (a), it can be seen that the surface is a homogeneous array of uniform sites, each capable of holding only one adsorbed molecule. Looking at the surface which has some molecules adsorbed (b), it is assumed that the next gas molecule that comes into contact with the metal has the same probability of adsorption as all of the previous molecules, regardless of how many are already adsorbed to the surface.

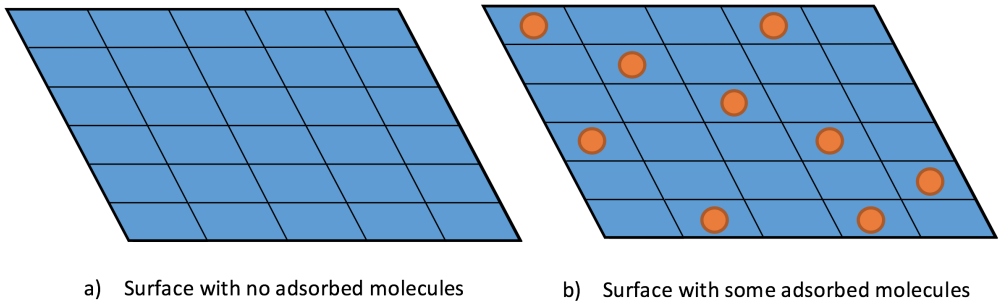

Figure 2.34: Schematic representation of gate metal surface

Accepting these assumptions, an expression of surface coverage can be determined which links the partial pressure of the gas and the rate constants of adsorption and desorption (Equation 2.12). θ represents the number of sites covered with an adsorbate, K is an expression of the combined adsorption and desorption rate constants and P is the partial pressure of the gas being monitored.

$$\theta = \frac{KP}{1 - P} \tag{2.12}$$

In 1997, Vlachos *et al.* conducted a simulation to show the dependence of catalyst coverage on oxygen partial pressure [98]. Figure 2.35 shows adsorbate distribution in the instance of low and high oxygen partial pressure. The lightly coloured area represents the supporting semiconductor (InO_x), the dark circles denote the platinum gate metal and black dots represent adsorbate molecules. The catalytic metal sites in figure 2.35b are more densely populated than those in figure 2.35a; this means the number of covered sites (θ) increases with the partial pressure of the gas, as supported by the isotherm.

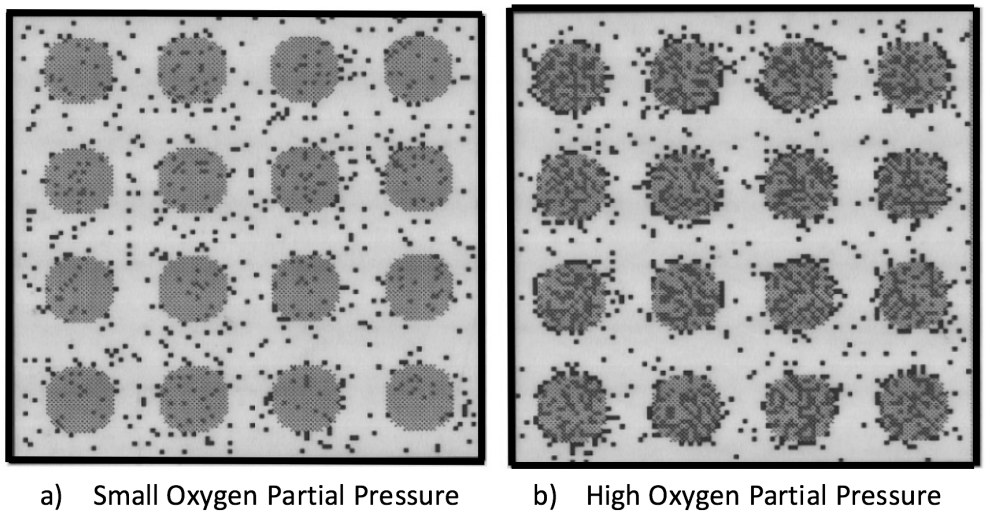

Figure 2.35: Catalyst coverage dependence on oxygen partial pressure [98]

The Langmuir Isotherm allows the definition of the terms saturation and normalisation, which are used later in the thesis to describe the interaction between the metal surface of the device and analytes such as gas molecules or solvents.

Saturation is when the device is exhibiting its maximum electrical response, and there are no changes in characteristics, regardless of whether the concentration of analyte is increased. This saturation is observed beause all available adsorption sites are filled.

Normalisation is the returning of sensor electrical characteristics to the baseline value. This occurs because analytes desorb from the adsorption sites on the metal surface and enter the ambient environment.

2.5.6 Influence of Non-Target Gases

In an ideal scenario, a hydrogen sensor would only come into contact with the desired hydrogen analyte, however, in practice, this is not the case. Devices are usually operated in the presence of a gaseous mixture, meaning other substances can adsorb

to the metal surface. Oxygen adsorption to noble metals is well established, and O_2 molecules compete with hydrogen for adsorption sites on the metal surface, reducing device sensitivity to hydrogen [99]. The removal of adsorbed negative oxygen ions will impart the same electrical effects on the device as the adsorption of positive hydrogen ions [33]. Therefore, in an oxygen containing environment, it is difficult to ascertain which analyte is producing the response [100, 101]. The data in Figure 2.36 shows that oxygen can interfere with hydrogen sulfide detection and shift the device characteristics in comparable ways.

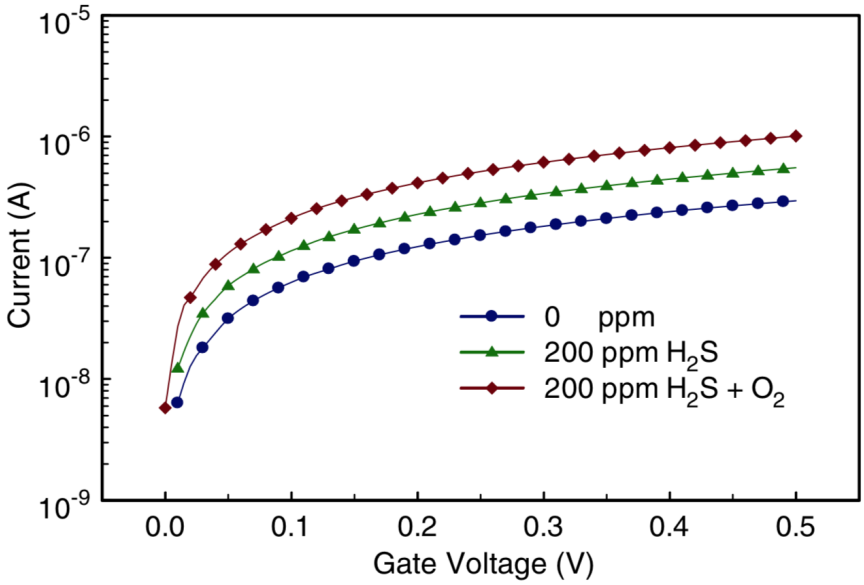

Figure 2.36: Influence of oxygen on detection of H_2S at 325°C [101]

Not only is the hydrogen in competition with oxygen for adsorption sites, but surface reactions between the adsorbed oxygen and gaseous hydrogen can occur, forming hydroxyl ions that leave the metal surface, altering sensor output. Adsorbed oxygen species also influence the sensitivity of different devices. Considering the data in Figure 2.26, this discrepancy in hydrogen sensitivity between Pd/SiC and Pt/SiC can be attributed to the influence of adsorbed oxygen ions on the catalyst surface. The hydroxyl formation energy barrier plays an important role with more energy needed to liberate OH from oxygen and hydrogen adsorbed on Pd compared to Pt, as shown schematically in Figure 2.37) Therefore, adsorbed hydrogen ions are removed more quickly from Pt films, resulting in the lower hydrogen response [94, 102] that is observed in the data. This lack of sensitivity and selectivity to specific analytes is one of the major challenges faced when designing MOS gas sensors.

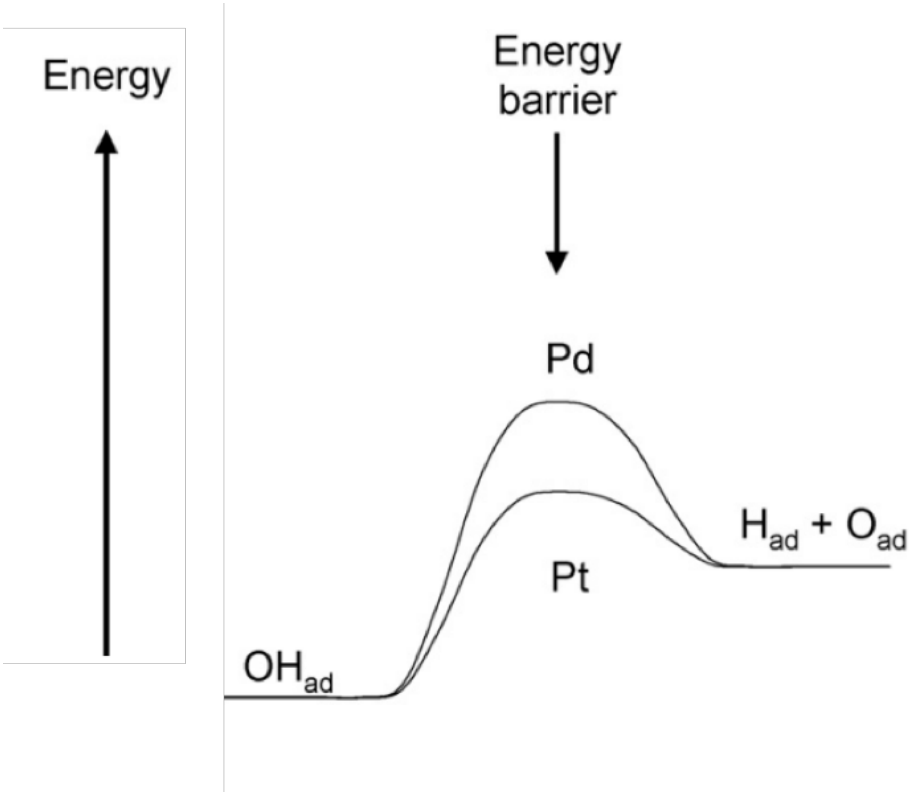

Figure 2.37: Energy diagram for OH formation Pd and Pt

2.5.7 Influence of catalyst porosity

Achieving selectivity and sensitivity to chosen analytes is one of the most challenging aspects of designing gas sensors. As mentioned previously, there is no 'universal' sensor system which can detect and distinguish between every gas contained within a mixture. Therefore it is necessary to optimise the structure of MOS devices to make them receptive to the analyte of choice in the deployed environment. Detection of simple gases such as hydrogen has been demonstrated, however, for more complex gases, the introduction of a porous gate can increase device sensitivity. The porosity of the metal, exposes the bare underlying oxide, allowing direct adsorption to the dielectric. The point at which a gaseous molecule can be in contact with the ambient environment, the gate metal, and the dielectric oxide is known as a 'triple point' and these are employed to increase sensitivity to complex gases, as shown in Figure 2.38 [103, 85]. For example, a device with a porous platinum gate demonstrated increased ammonia sensitivity compared to devices with a continuous gate. The exact mechanism is not known, but the increased sensitivity is attributed to the catalytic activity of the metal-oxide boundaries, which aid the decomposition of ammonia into hydrogen atoms and other derivatives [104].

The influence of triple points on the sensor response is further supported by data generated using a scanning light pulse technique to locally measure the sensitivity

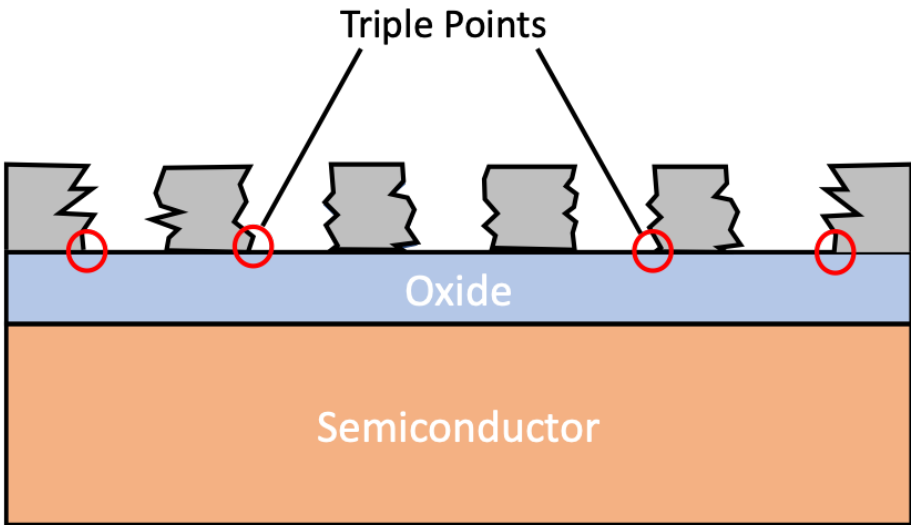

Figure 2.38: Schematic representation of MOS capacitor with porous gate metal giving rise to triple points

of the structure to NH_3 for a capacitor device fabricated with a porous gate. It was found that an increased response was seen towards the edge of the metal where triple points are present (See Figure 2.39). Response decreased towards the middle of the continuous film [94].

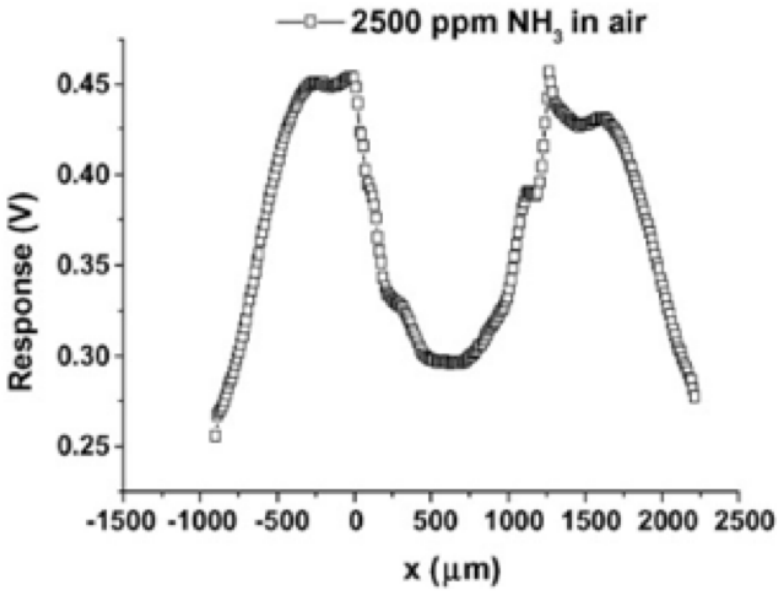

Figure 2.39: Response of a $Pt/SiO_2/SiC$ structure to ammonia in air. The edges of the film are found at 0 and 1500μm

To examine the influence of the concentration of triple points on the sensor response, artificial pores defined using photolithography were produced in a Pt film and exposed to butane. The resulting sensor response as a function of the open

surface area (linked to the porosity of the film) is shown by the data in Figure 2.40 [105]. A SiC device with a multi-layer stacked gate consisting of Pt/Au/Pt was patterned in order to create 3 μm diameter pores, spaced evenly across the metal surface. This device was tested to identify the response to hydrogen, butane, and carbon monoxide. It can be seen in Figure 2.40 that hydrogen response remains relatively stable irrespective of the amount of porosity of the gate metal. This is to be expected, as H_2 sensitivity to MOS devices with Pt gates is established and the small atomic radius of the adsorbed hydrogen ions allows diffusion through a continuous metal layer. Conversely, for larger, more complex gases such as butane and carbon monoxide, the amount of porosity is key to device response. In the absence of any porosity, it can be seen that the device exhibits no response to CO and C_4H_{10}. However, when porosity is introduced, the device begins to show a response to the complex gases. A linear relationship is seen between the amount of porosity and the sensor response to CO, suggesting that as more SiO_2 is uncovered, there are more binding sites available for CO to adsorb, ultimately increasing device response. A similar behaviour is seen with butane, affirming the suggestion that the presence of triple points significantly increases device response to complex gases.

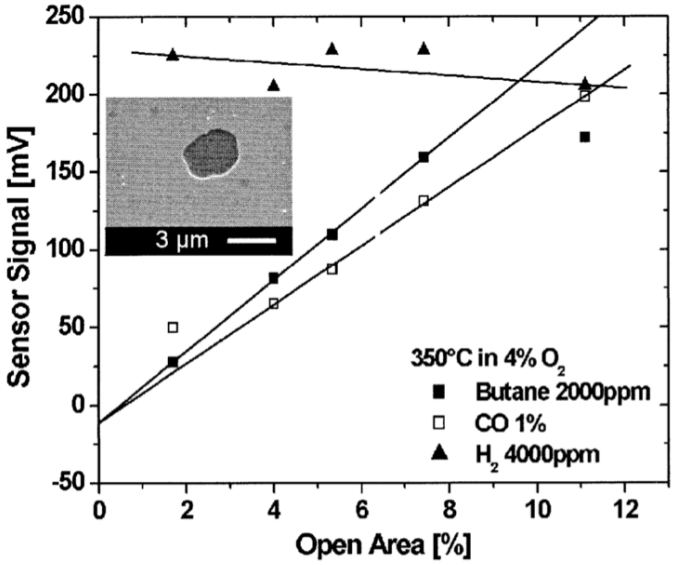

Figure 2.40: Response of a Pt/Au/Pt/SiO_2/SiC structure to hydrogen, carbon monoxide and butane at 350°C [105]

2.6 Conclusion

European legislation has become increasingly tough on automotive diesel engines, with maximum allowable pollutant emissions being continually updated. Whilst helping to monitor the combustion efficiency of the engine, existing automotive gas sensors are not sophisticated enough to accurately monitor pollutants. These sensors have cold-start issues, with data generation only beginning when the engine has heated up as well as selectivity issues, and often exhaust gas treatment systems are required to remove certain gases to leave the desired analyte. In order for engines to comply with these ever-changing laws, the development of a reliable, real-time gas sensor system is required.

Gas sensors capable of withstanding the high temperatures and pressures of an automotive diesel engine have to be made from a resilient material, capable of operating reliably in hazardous environments. The wide bandgap and intrinsic electronic properties of silicon carbide make it an excellent candidate for this application. The development of commercially available wafers, coupled with the existence of a thermally growable silicon oxide allow seamless incorporation into established fabrication processes.

A number of gas sensitive MOS structures have been demonstrated over the last few decades, such as Schottky diodes, MOSFETs and MOS capacitors. The MOS capacitor has been identified as the most promising structure for this application due to its simple fabrication process, increased stability, and easily measurable response to gases. MOS capacitors characteristics experience a shift in the flatband voltage upon exposure to analytes, with hydrogen and oxygen containing gases producing a negative and positive shift respectively.

The magnitude of this sensor response depends on the materials used to make up the device structure. The identity and structural morphology of the catalytic gate metal have proved to be integral to device response, with a porous gate providing increased sensitivity to more complex gases. The identity of the insulating layer also has an effect on analyte selectivity, with different dielectric materials displaying sensitivity to some gases, but not to others. Therefore, in order to improve sensitivity and selectivity to the desired gas species, fine tuning of the sensor system is required.

Bibliography

[1] Klaus. Mollenhauer and Helmut. Tschoke. *Handbook of diesel engines*. Springer, 2010.

[2] Richard Van Basshuysen and Fred Schafer. *Internal combustion engine handbook : basics, components, systems, and perspectives*. SAE International, 2004, p. 811.

[3] Jacques Arnaud, Laurent Chusseau, and Fabrice Philippe. "On classical ideal gases". In: *Entropy* 15 (3 2013), pp. 960–971.

[4] Ibrahim Aslan Resitoglu, Kemal Altinişik, and Ali Keksin. "The pollutant emissions from diesel-engine vehicles and exhaust aftertreatment systems". In: *Clean Technologies Environmental Policies* 17 (June 2014), pp. 15–27.

[5] Usman Asad and Ming Zheng. "Exhaust gas recirculation for advanced diesel combustion cycles". In: *Applied Energy* 123 (June 2014), pp. 242–252.

[6] M.M.Z. Shahadat et al. "Combined effect of EGR and inlet air preheating on engine performance in diesel engine". In: *International Energy Journal* 9 (2 2008).

[7] J. Thangaraja and C. Kannan. "Effect of exhaust gas recirculation on advanced diesel combustion and alternate fuels - A review". In: *Applied Energy* 180 (Oct. 2016), pp. 169–184.

[8] Wenpo Shan and Hua Song. "Catalysts for the selective catalytic reduction of NOx with NH3 at low temperature". In: *Catalysis Science Technology* 5 (9 2015), pp. 4280–4288.

[9] Gesthimani D. Lionta et al. "Selective Catalytic Reduction of NO with Hydrocarbons: Experimental and Simulation Results". In: *Industrial Engineering Chemistry Research* 35 (8 1996). SCR, pp. 2508–2515.

[10] Maroa Semakula and Prof Freddie Inambao. "The Formation, Effects and Control of Oxides of Nitrogen in Diesel Engines". In: *International Journal of Applied Engineering Research* 13 (6 2018), pp. 3200–3209.

[11] P Brijesh and S Sreedhara. “Exhaust emissions and its control methods in compression ignition engines: A review”. In: *International Journal of Automotive Technology* 14 (2 2013), pp. 195–206.

[12] Gurumoorthy S Hebbar. “NOx from Diesel Engine Emission and Control Strategies - A Review”. In: *International Journal of Mechanical Engineering and Robotics Research* 3 (4 2014), p. 471.

[13] A. N. Hayhurst and I. M. Vince. “Production of ‘prompt’ nitric oxide and decomposition of hydrocarbons in flames”. In: *Nature* 266 (5602 Apr. 1977), pp. 524–525.

[14] A.N. Hayhurst and I.M. Vince. “The origin and nature of “prompt” nitric oxide in flames”. In: *Combustion and Flame* 50 (Jan. 1983), pp. 41–57.

[15] C.P. Fenimore. “Formation of nitric oxide in premixed hydrocarbon flames”. In: *Symposium (International) on Combustion* 13 (1 Jan. 1971), pp. 373–380.

[16] Craig T. Bowman. “Kinetics of nitric oxide formation incombustion processes”. In: *International Symposium on Combustion* 14 (1 Jan. 1973), pp. 729–738.

[17] Yu-Ran. Luo. *Comprehensive handbook of chemical bond energies*. Vol. 1. CRC Press, 2007.

[18] S R Turns. *An introduction to combustion: concepts and applications*. Vol. 1. McGraw Hill Education (India) Private Limited, 2000.

[19] Ajinkya B Amritkar and Nilesh Badge. “Effect Of Exhaust Gas Recirculation (EGR) In Internal Combustion Engine”. In: *International Research Journal of Engineering and Technology* (2016).

[20] R Ramamoorthy, P K Dutta, and S A Akbar. “Oxygen sensors: Materials, methods, designs and applications”. In: *Journal of Materials Science* 38 (2003), pp. 4271–4282.

[21] A. S. De Souza Sobrinho and L. C. De Lima. “Monitoring industrial combustion through automotive oxygen sensor”. In: *Journal of Engineering and Applied Sciences* 7 (2 2012), pp. 148–151.

[22] J Riegel, H Neumann, and H M Wiedenmann. “Exhaust gas sensors for automotive emission control”. In: *Solid State Ionics* 152–153 (2002), pp. 783–800.

[23] Hiroyuki Kaneko et al. “Performance of a miniature zirconia oxygen sensor with a Pd–PdO internal reference”. In: *Sensors and Actuators B: Chemical* 108 (1–2 2005), pp. 331–334.

[24] Carlos Lopez Gandara et al. “How to Test Exhaust Gas Sensors? Influence of Gas Testing Systems and Experimental Artifacts in Exhaust Gas Sensors Characterization”. In: *Procedia Engineering* 47 (2012), pp. 1105–1108.

[25] NGK. *Bringing the world’s first high-precision NOx sensor to market — NEWS — NGK INSULATORS, LTD.* 2008. URL: https://www.ngk-insulators.com/en/news/20080611_9229.html.

[26] C O Park et al. “Solid-state electrochemical gas sensors”. In: *Ionics* 15 (3 2009), pp. 261–284.

[27] Jing Gao et al. “Improvement of the NO x selectivity for a planar YSZ sensor”. In: *Sensors and Actuators B: Chemical* 154 (2 2011), pp. 106–110.

[28] Ralf Moos. “A Brief Overview on Automotive Exhaust Gas Sensors Based on Electroceramics”. In: *International Journal of Applied Ceramic Technology* 2 (5 Sept. 2005), pp. 401–413.

[29] Nobuhide Kato, Kunihiko Nakagaki, and Noriyuki Ina. “Thick Film ZrO2 NOx Sensor”. In: Feb. 1996. DOI: 10.4271/96033.

[30] B Jayant Baliga. *Silicon Carbide Power Devices*. World Scientific, 2006.

[31] Gary Lynn Harris. *Properties of silicon carbide*. INSPEC, 1995.

[32] Xu She et al. “Review of Silicon Carbide Power Devices and Their Applications”. In: *IEEE Transactions on Industrial Electronics* 64 (10 Oct. 2017), pp. 8193–8205.

[33] Stephen E. Saddow and Anant (Anant K.) Agarwal. *Advances in silicon carbide processing and applications*. Vol. 2. Artech House, 2004.

[34] G. Brezeanu. “Silicon carbide (SiC): a short history. an analytical aproach for SiC power device design”. In: vol. 2. IEEE, Oct. 2005, pp. 345–348.

[35] Edwin L. Thomas. *Opportunities in Protection Materials Science and Technology for Future Army Applications*. Wiley-Blackwell, Dec. 2012, pp. 145–148.

[36] Alan W. Weimer. *Carbide, Nitride and Boride Materials Synthesis and Processing*. Vol. 1. Springer, 1997.

[37] Simonpietro Di Pierro et al. “Rock-forming moissanite (natural -silicon carbide)”. In: *American Mineralogist* 88 (11-12 Nov. 2003), pp. 1817–1821.

[38] Schubert. E. Fred. *Light-Emitting Diodes*. Vol. 3. E. Fred Schubert, 2018.

[39] H. J. Round. “A Note on Carborundum”. In: WORLD SCIENTIFIC, Mar. 1991, pp. 879–879.

[40] Yu.M. Tairov and V.F. Tsvetkov. "General principles of growing large-size single crystals of various silicon carbide polytypes". In: *Journal of Crystal Growth* 52 (Apr. 1981), pp. 146–150.

[41] M.N. Yoder. "Wide bandgap semiconductor materials and devices". In: *IEEE Transactions on Electron Devices* 43 (10 1996), pp. 1633–1636.

[42] Jose Millan et al. "A Survey of Wide Bandgap Power Semiconductor Devices". In: *IEEE Transactions on Power Electronics* 29 (5 May 2014), pp. 2155–2163.

[43] W. J. Choyke, H. Matsunami, and G. Pensl. *Silicon Carbide : Recent Major Advances*. Vol. 1. Springer Berlin Heidelberg, 2004, p. 844.

[44] F Bechstedt et al. "Polytypism and properties of silicon carbide". In: *physica status solidi (b)* 202 (1 1997), pp. 35–62.

[45] Charles E Ryan et al. "The Conversion of Cubic and Hexagonal Silicon Carbide as a Function of Temperature and Pressure". In: Springer, 1968, pp. 177–197.

[46] Angel L. Ortiz et al. "The prolific polytypism of silicon carbide". In: *Journal of Applied Crystallography* 46 (1 2013), pp. 242–247.

[47] A. Elasser and T.P. Chow. "Silicon carbide benefits and advantages for power electronics circuits and systems". In: *Proceedings of the IEEE* 90 (6 June 2002), pp. 969–986.

[48] Marco Notarianni et al. "Synthesis and applications of carbon nanomaterials for energy generation and storage". In: *Beilstein Journal of Nanotechnology* 7 (Feb. 2016), pp. 149–196.

[49] M C Capizzo, R M Sperandeo-Mineo, and M Zarcone. "Electric conduction in semiconductors: a pedagogical model based on the Monte Carlo method". In: *European Journal of Physics* 29 (3 May 2008), pp. 451–466.

[50] Chris J.H. Wort and Richard S. Balmer. "Diamond as an electronic material". In: *Materials Today* 11 (1-2 Jan. 2008), pp. 22–28.

[51] P G Neudeck, R S Okojie, and Liang-Yu Chen. "High-temperature electronics - a role for wide bandgap semiconductors?" In: *Proceedings of the IEEE* 90 (6 June 2002), pp. 1065–1076.

[52] J.B. Casady and R.W. Johnson. "Status of silicon carbide (SiC) as a wide-bandgap semiconductor for high-temperature applications: A review". In: *Solid-State Electronics* 39 (10 Oct. 1996), pp. 1409–1422.

[53] Robert F Pierret. *Advanced semiconductor fundamentals*. Addison-Wesley Longman Publishing Co., Inc., 1987. ISBN: 0201053381.

[54] Fabrizio Roccaforte et al. “Selective Doping in Silicon Carbide Power Devices”. In: *Materials* 14 (July 2021), p. 3923. DOI: 10.3390/ma14143923.

[55] V. A. Gubanov and C. Y. Fong. “Doping in cubic silicon–carbide”. In: *Applied Physics Letters* 75 (1 June 1999), p. 88.

[56] Magnus Willander et al. “Silicon carbide and diamond for high temperature device applications”. In: *Journal of Materials Science: Materials in Electronics* 17 (1 Jan. 2006), pp. 1–25.

[57] M. E. (Mikhail Efimovich) Levinshteĭn, Sergey L. Rumyantsev, and Michael. Shur. *Properties of advanced semiconductor materials : GaN, AlN, InN, BN, SiC, SiGe*. 1st ed. Wiley, 2001, p. 194.

[58] Jose M. Lujan et al. “An assessment of the real-world driving gaseous emissions from a Euro 6 light-duty diesel vehicle using a portable emissions measurement system (PEMS)”. In: *Atmospheric Environment* 174 (2018), pp. 112–121.

[59] Carl-Mikael. Zetterling. *Process technology for silicon carbide devices*. Institution of Engineering and Technology, 2002.

[60] R. Mahapatra et al. “Energy-band alignment of HfO2SiO2SiC gate dielectric stack”. In: *Applied Physics Letters* 92 (4 Jan. 2008). Low band offset information, p. 042904.

[61] Edward H Nicollian, John R Brews, and Edward H Nicollian. *MOS (metal oxide semiconductor) physics and technology*. Vol. 1987. Wiley New York et al., 1982.

[62] *Dislocations in 4H silicon carbide*. Nov. 2022. DOI: 10.1088/1361-6463/ac8a58.

[63] Filippo Di Giovanni. “Silicon Carbide: Physics, Manufacturing, and Its Role in Large-Scale Vehicle Electrification”. In: *Chips* 2 (3 2023), pp. 209–222. ISSN: 2674-0729. DOI: 10.3390/chips2030013. URL: https://www.mdpi.com/2674-0729/2/3/13.

[64] J P Bergman et al. “Defects in 4H silicon carbide”. In: *Physica B: Condensed Matter* 308-310 (2001). International Conference on Defects in Semiconductors, pp. 675–679. ISSN: 0921-4526. DOI: https://doi.org/10.1016/S0921-4526(01)00790-6. URL: https://www.sciencedirect.com/science/article/pii/S0921452601007906.

[65] Ya-Xun Lin et al. “Electrical deterioration of 4H-SiC MOS capacitors due to bulk and interface traps induced by proton irradiation”. In: *Microelectronics Reliability* 142 (2023), p. 114927. ISSN: 0026-2714. DOI: https://doi.org/10.1016/j.microrel.2023.114927. URL: https://www.sciencedirect.com/science/article/pii/S0026271423000276.

[66] Patrick Fiorenza, Filippo Giannazzo, and Fabrizio Roccaforte. “Characterization of SiO2/4H-SiC Interfaces in 4H-SiC MOSFETs: A Review”. In: *Energies* 12 (12 2019). ISSN: 1996-1073. DOI: 10.3390/en12122310. URL: https://www.mdpi.com/1996-1073/12/12/2310.

[67] Dhar Sarit et al. “Nitrogen and Hydrogen Induced Trap Passivation at the SiO 2 /4H-SiC Interface”. In: *Materials Science Forum - MATER SCI FORUM* 527 (July 2006), pp. 949–954. DOI: 10.4028/www.scientific.net/MSF.527-529.949.

[68] I Lundstrom et al. “A hydrogen sensitive MOS field effect transistor”. In: *Applied Physics Letters* 26 (2 1975), pp. 55–57.

[69] Adrian Trinchi, Sasikaran Kandasamy, and Wojtek Wlodarski. “High temperature field effect hydrogen and hydrocarbon gas sensors based on SiC MOS devices”. In: *Sensors and Actuators B: Chemical* 133 (2 Aug. 2008), pp. 705–716.

[70] J. Kolnik, J. Ivanco, and M. Ozvold. “Metal/thin insulator/silicon schottky diodes with plasma deposited silicon nitride interfacial layer”. In: *Physica Status Solidi (a)* 130 (1 Mar. 1992), pp. 245–251.

[71] Ching-Yuan Wu. “Interfacial layer theory of the Schottky barrier diodes”. In: *Journal of Applied Physics* 51 (1980), p. 3786.

[72] Shinji Nakagomi et al. “Influence of carbon monoxide, water and oxygen on high temperature catalytic metal–oxide–silicon carbide structures”. In: *Sensors and Actuators B: Chemical* 45 (3 Dec. 1997), pp. 183–191.

[73] W.M. Tang, C.H. Leung, and P.T. Lai. “Improved sensing characteristics of MISiC Schottky-diode hydrogen sensor by using HfO2 as gate insulator”. In: *Microelectronics Reliability* 48 (11-12 Nov. 2008), pp. 1780–1785.

[74] S. Kandasamy et al. “Study of Pt/TiO2/SiC schottky diode based gas sensor”. In: vol. 2. IEEE, 2004, pp. 738–741.

[75] Peter Tobias et al. “Studies of the Ambient Dependent Inversion of Catalytic Metal - Oxide - Silicon Carbide Devices Based on 6H- and 4H-SiC Material”. In: *Materials Science Forum* 264-268 (Feb. 1998), pp. 1089–1092.

[76] C.K Kim et al. “A study on a platinum–silicon carbide Schottky diode as a hydrogen gas sensor”. In: *Sensors and Actuators B: Chemical* 66 (1-3 July 2000), pp. 116–118.

[77] C.K Kim et al. “Pd and Pt-SiC Schottky diodes for detection of H2 and CH4 at high temperature”. In: *Sensors and Actuators B: Chemical* 77 (1-2 June 2001), pp. 455–462.

[78] T B Flanagan and W A Oates. “The Palladium-Hydrogen System”. In: *Annual Review of Materials Science* 21 (1 Aug. 1991), pp. 269–304.

[79] Linda L. Jewell and Burtron H. Davis. “Review of absorption and adsorption in the hydrogen–palladium system”. In: *Applied Catalysis A: General* 310 (Aug. 2006), pp. 1–15.

[80] Graeme W. Watson et al. “A Comparison of the Adsorption and Diffusion of Hydrogen on the {111} Surfaces of Ni, Pd, and Pt from Density Functional Theory Calculations”. In: *The Journal of Physical Chemistry B* 105 (21 May 2001), pp. 4889–4894.

[81] Mikael Lofdahl et al. “Difference in hydrogen sensitivity between Pt and Pd field-effect devices”. In: *Journal of Applied Physics* 91 (7 Apr. 2002), pp. 4275–4280.

[82] J. Yu et al. “Hydrogen gas sensing properties of Pt/Ta2O5 Schottky diodes based on Si and SiC substrates”. In: *Sensors and Actuators A: Physical* 172 (1 Dec. 2011), pp. 9–14.

[83] Peter Tobias et al. “Moving gas outlets for the evaluation of fast gas sensors”. In: *Sensors and Actuators B: Chemical* 58 (1–3 1999), pp. 389–393.

[84] Bogdan Ofrim and Gheorghe Brezeanu. “Hydrogen sensor based on MOS capacitor”. In: *UPB Sci. Bull. Ser. C* 75 (2013), pp. 2286–3540.

[85] A. Spetz, M. Armgarth, and I. Lundstrom. “Hydrogen and ammonia response of metal-silicon dioxide-silicon structures with thin platinum gates”. In: *Journal of Applied Physics* 64 (3 Aug. 1988), pp. 1274–1283.

[86] Reza Loloee et al. “Hydrogen monitoring for power plant applications using SiC sensors”. In: *Sensors and Actuators B: Chemical* 129 (1 2008), pp. 200–210.

[87] S K Roy et al. “SiC gas sensor arrays for extreme environments”. In: 2013, pp. 1–4.

[88] M H Weng et al. “Hydrogen sulphide detection in extreme environments”. In: vol. 76. IOP Publishing, 2007, p. 12005.

[89] A Spetz et al. “Structure and ammonia sensitivity of thin platinum or iridium gates in metal-oxide-silicon capacitors”. In: *Thin Solid Films* 177 (1-2 Oct. 1989), pp. 77–93.

[90] V.I Filippov, A.A Terentjev, and S.S Yakimov. “Electrode structure effect on the selectivity of gas sensors”. In: *Sensors and Actuators B: Chemical* 28 (1 July 1995), pp. 55–58.

[91] Seongjeen Kim et al. “Silicon Carbide-Based Hydrogen Gas Sensors for High-Temperature Applications”. In: *Sensors* 13 (10 Oct. 2013), pp. 13575–13583.

[92] Seongjeen Kim. “Hydrogen gas sensors using a thin Ta2O5 dielectric film”. In: *Journal of the Korean Physical Society* 65 (11 2014). Pd Gate Example, pp. 1749–1753.

[93] V V Gorodetskii et al. “Adsorption of hydrogen on rhodium; Comparison with hydrogen adsorption on platinum and iridium”. In: *Surface Science* 108 (2 1981), pp. 225–234.

[94] Ingemar Lundstrom et al. “Twenty-five years of field effect gas sensor research in Linkoping”. In: *Sensors and Actuators B: Chemical* 121 (1 2007), pp. 247–262.

[95] Dariusz Włóka and Marzena Smol. “Evaluation of extraction methods of polycyclic aromatic hydrocarbons (PAHs) from soil and sewage sludge matrix”. In: *Inżynieria i Ochrona Środowiska* 17(4): 683-696 (June 2014).

[96] Irving Langmuir. “The Constitution and Fundamental Properties of Solids and Liquids. Part 1. Solids”. In: *Journal of the American Chemical Society* 38 (11 1916), pp. 2221–2295.

[97] Patiha et al. “The Langmuir isotherm adsorption equation: The monolayer approach”. In: vol. 107. IOP Publishing, Feb. 2016, p. 012067.

[98] D. S. Vlachos, C. A. Papadopoulos, and J. N. Avaritsiotis. “Characterisation of the catalyst-semiconductor interaction mechanism in metal-oxide gas sensors”. In: *Sensors and Actuators B: Chemical* 44.1 (1997), pp. 458–461. DOI: 10.1016/S0925-4005(97)00150-0. URL: http://www.ingentaconnect.com/content/els/09254005/1997/00000044/00000001/art00150%20http://dx.doi.org/10.1016/S0925-4005(97)00150-0.

[99] Gerhard Ertl. “Reactions at surfaces: From atoms to complexity (Nobel lecture)”. In: *Angewandte Chemie International Edition* 47 (19 2008), pp. 3524–3535.

[100] V. Filippov, A. Terentjev, and S. Yakimov. “Oxygen effect on the operation of the MOS-structure-based hydrogen sensor”. In: *Sensors and Actuators B: Chemical* 17 (2 Jan. 1994), pp. 121–124.

[101] Ming Hung Weng et al. “Role of oxygen in high temperature hydrogen sulfide detection using MISiC sensors”. In: *Measurement Science and Technology* 19 (2 2008), p. 24002.

[102] Mikael Löfdahl et al. “Difference in hydrogen sensitivity between Pt and Pd field-effect devices”. In: *Journal of Applied Physics* 91 (7 2002), pp. 4275–4280.

[103] Mikael Lofdahl et al. “Gas response dependence on gate metal morphology of field-effect devices”. In: *Sensors and Actuators B: Chemical* 80 (3 Dec. 2001), pp. 183–192.

[104] A. Spetz, M. Armgarth, and I. Lundstrom. “Optimization of ammonia-sensitive metal-oxide-semiconductor structures with platinum gates”. In: *Sensors and Actuators* 11 (4 May 1987). Porous gate ammonium sensitivity, pp. 349–365.

[105] Jan Schalwig et al. “Response mechanism of SiC-based MOS field-effect gas sensors”. In: *IEEE Sensors Journal* 2 (5 2002), pp. 394–402.

Chapter 3

Material Development and Fabrication Technique Optimisation

3.1 Introduction

The gas sensing properties of metal-oxide-semiconductor capacitor sensors towards a variety of analytes has been well established [1, 2, 3]. Selectivity and sensitivity can be controlled by tuning the identity and morphology of the gate metal and dielectric components of the device. Examples of this include the observed increase in device response towards hydrogen by the replacement of the HfO_2 based dielectric layer with one containing TiO_2 [4]. The incorporation of porosity into gate metal layers has been shown to increase the sensitivity of a gas sensor to a range of gas species, including ammonia [5].

Therefore this chapter aims to identify the optimal fabrication conditions for the realisation of gate metal and dielectric layers in MOS capacitors designed to act as nitrogen oxide gas sensors. Specifically, a study into the deposition conditions for the platinum gate layer was undertaken. The primary focus of this was to control of the level of incorporated porosity, which was analysed using scanning electron microscopy (SEM), supported by image processing. The formation of the tungsten oxide dielectric layer via the deposition of tungsten metal and subsequent oxidation was also studied. The oxidation of the tungsten films was carried out in laboratory air, with conditions such as temperature, oxidation time, and cooling time altered and studied systematically. The properties of the dielectric layer were subsequently analysed using atomic force microscopy (AFM) and Raman spectroscopy to determine the optimal process.

To advance upon previous work which incorporated HfO_2 and TiO_2 as dielec-

tric layers, devices based on zirconium oxide were produced. Zr is located in the same group as Hf and Ti in the periodic table, and therefore is expected to show similar chemical properties. The difference in response for sensors manufactured from HfO_2 and TiO_2 dielectrics to hydrogen and oxygen oxygen rich environments has been demonstrated previously. This suggests that the incorporation of zirconium could produce devices with differing behaviours to those displayed by hafnium and titanium devices. Therefore within this chapter, the fabrication and electronic characterisation of $Pt/ZrO_2/SiO_2$/4H-SiC devices was also performed and compared against hafnium and titanium based devices, prior to gas testing.

3.2 Platinum Gate Metal Study

The role of the gate metal is integral to gas sensing, as it is responsible for the adsorption and dissociation of gaseous analytes to the device. The identity of the metal can be chosen to target a specific analyte or to reduce the response time towards a certain gas. Usually, noble metals are selected, such as platinum, palladium or rhodium due to their well-established catalytic activity, coupled with their chemical inertness and high melting points, which prevents reaction with non-target gases and subsequent degradation over time.

If a metal-oxide-semiconductor system possesses a permeable, catalytically active metal, it can be utilised as sensor of hydrogen, or hydrogen containing gases. The first example of this was demonstrated by Lundstrom *et al.* in 1975 with a transistor incorporating a palladium gate [6, 7]. The mechanism of hydrogen detection involves the adsorption and subsequent dissociation of H_2 at the metal surface to form two hydrogen atoms. According to conventional theory, these individual hydrogen atoms then diffuse through the metal surface forming a charge layer at the metal/insulator interface. Rapid diffusion of hydrogen through noble metal layers is well established, and this allows hydrogen atoms to induce a dipole layer, altering the number of charge carriers in the device. This is detectable as a change in electronic characteristics shown as a shift in capacitance-voltage or current-voltage plots, depending on the measurement taken [8, 9].

Problems arise when targeting gases where the molecule is larger than hydrogen, such as hydrocarbons, ammonia or NOx. The uniform noble metal layer does not allow diffusion of the dissociation products from larger gas molecules to the metal/oxide interface, so an alternative approach is needed. Incorporating porosity into the gate metal layer allows detection of these more complex gases, as the underlying dielectric layer is exposed, forming triple points at which the analyte can be in contact with the oxide, metal and ambient environment simultaneously [5, 10, 11].

3.2.1 Metal Deposition

An effective method for the deposition of materials is physical vapour deposition (PVD), which involves the conversion of the target material into vapour which then condenses onto a substrate forming thin films. Sputter deposition is a controllable form of PVD, which utilises high energy particles and a magnet array to deposit layers of material.

The target material is loaded into the sputtering chamber, along with the substrate, before vacuum pumps reduce the base pressure to around 10^{-6} mbar. Inert argon gas is then released into the chamber and a voltage is applied to the target in order to form a plasma which is concentrated along the generated magnetic field. This plasma consists of argon ions and free electrons, which collide with each other to produce positively charged argon ions. These argon ions are attracted to the negatively charged target material and the subsequent collisions eject atoms (adatoms) from the target surface. These adatoms are then deposited onto the substrate, layer by layer until a desired thickness is reached. For the deposition of metal, a DC current is usually applied in order to ionize the carrier gas, whereas an AC current is used to deposit non-metals. A schematic of the sputtering process for a platinum target is shown in Figure 3.1.

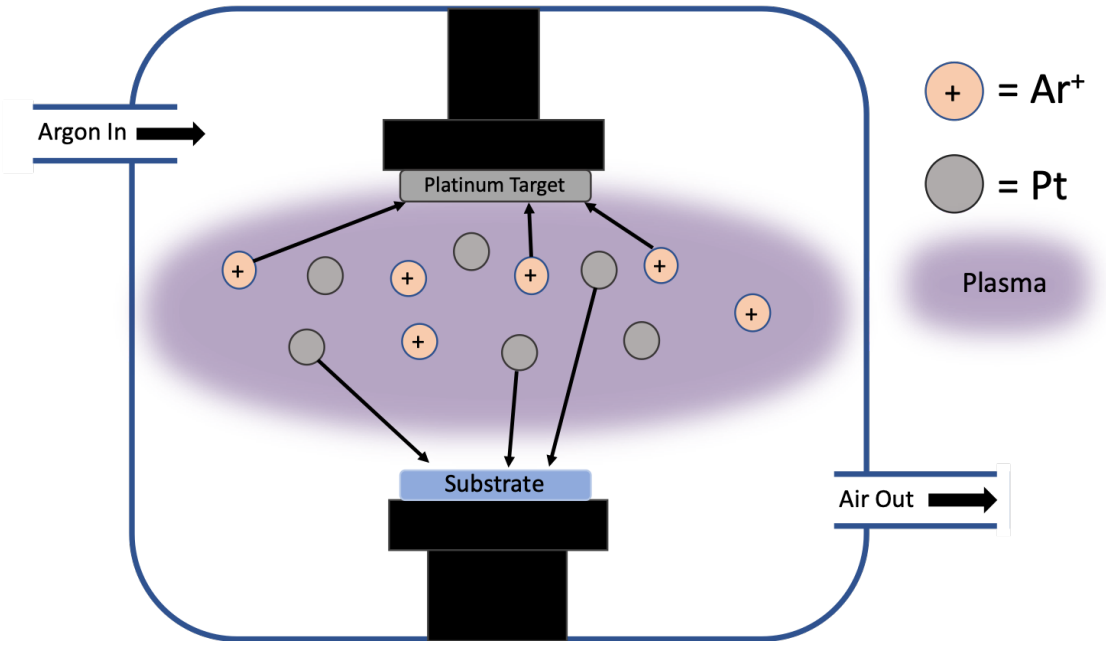

Figure 3.1: Schematic of PVD sputtering of Platinum

The uniformity of the sputtered layers can be controlled by altering the conditions within the deposition chamber. For many applications, a uniform, continuous layer, is usually required, but changes in the argon pressure or applied power can be utilised to control the quality of the deposited layer. For gas sensing applications, a discontinuous gate metal layer can be advantageous in targeting complex analytes,

and efforts have been made to control the level of porosity within these sputter deposited films.

The relationship between sputtering power and rate of deposition is well understood, with an increase in power causing a linear increase in deposition rate. Fundamentally, this can be extrapolated to identify a relationship between sputtering power and the uniformity of deposited films.

It is understood a low rate of deposition favours the formation of uniform films, as the adatoms do not form 'clusters' before impacting the substrate [12]. A balance has to be struck between the rate of deposition and the uniformity of films as the manufacturability of the sensor has to be considered if the deposition rate is very low. A small increase in power initially leads to less uniform films due to the ejected atoms hitting the substrate more quickly and with more disorder. However, a further increase in power can lead to the formation of very crystalline, non-porous, layers. Jhanwar and Chan have reported that high power values of between 150 and 250 W produced films with an increased crystallinity [13, 14]. This is due to the increase in substrate temperature, which arises from the increase in energy transferred to the substrate via the impacting atoms. The extra thermal energy causes re-crystallisation of the adatoms to more energetically favourable and uniform morphologies upon collision with the substrate target [15].

The effect of argon pressure on platinum film porosity was demonstrated in 2013 by Chang *et al.* [16]. Platinum films were deposited at three different pressures and the surface roughness and porosity of the resultant films were determined. Figure 3.2 shows SEM and AFM images of Pt films deposited at 5 mTorr, 60 mTorr and 120 mTorr, and it can be seen that levels of porosity and surface roughness increase with deposition pressure.

This phenomenon can be attributed to an increased number of collisions between argon ions and platinum atoms in the plasma, which cause aggregation of ejected Pt atoms prior to deposition onto the substrate surface. This forms 'islands' of metal atoms on the substrate, preventing uniform deposition and increasing the levels of porosity. The deposition rate also increased with argon pressure. There is a relationship between sputter speed and the uniformity of deposited films [17]. In order to ensure the most uniform film possible, it is advantageous to sputter slowly to ensure that film is built up one atomic layer at a time. Therefore the increase in argon pressure lead to an increased sputter deposition rate and a more porous film.

3.2.2 Platinum Porosity Study

In order to determine the most effective method for incorporating a porous platinum gate metal into the device structure, a series of experiments were performed.

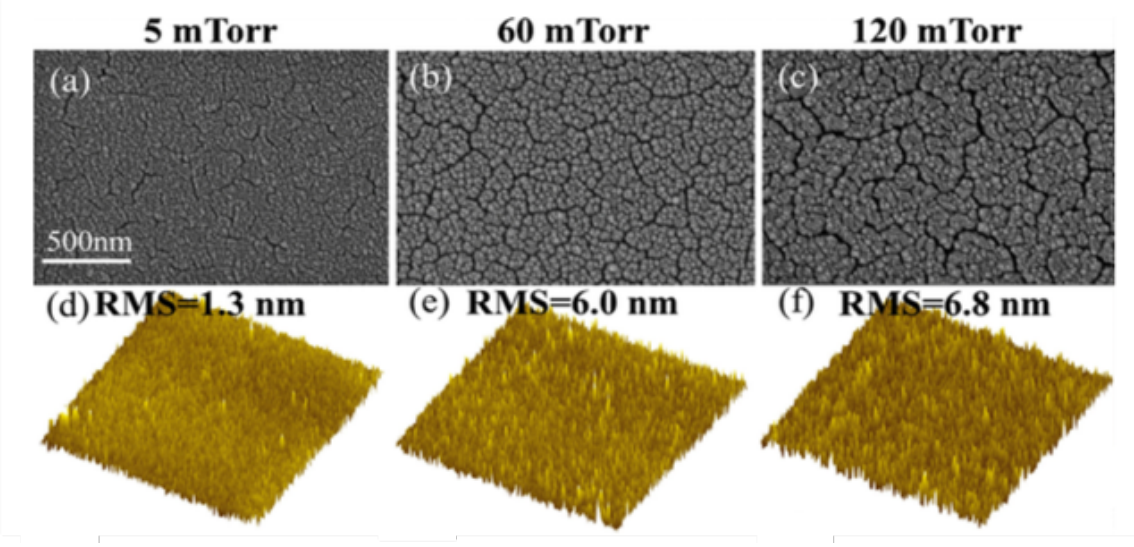

Figure 3.2: SEM and AFM images of three sputtered platinum films at A) 5 mTorr, B) 60 mTorr and C) 120 mTorr

Platinum was deposited by DC sputtering onto oxidised silicon wafers and changes were made to sputtering conditions, as well as post deposition treatment methods. The samples were then analysed and imaged in order to identify the optimum test conditions to provide a desired level of porosity.

6-inch silicon (100) wafers were purchased from University Wafer and subjected to an organic solvent clean using N-methyl-2-pyrollidone (NMP) and isopropyl alcohol (IPA). Further cleaning was carried out using a standard Radio Corporation of America (RCA) process, before oxidation [18]. 25nm of SiO_2 was grown via oxidation in a dry environment for 23 minutes at 1000 °C. The wafers were then cleaved into individual 10x10mm samples for platinum deposition experiments. The Si/SiO_2 substrates were divided into eight different groups and labelled A, B, C, D, E, F, G and H. Substrates A-F had 70nm of platinum deposited onto the surface at six different argon pressures, with a deposition power of 50 W (Table 3.1). Samples G and H had 70nm of platinum deposited at two representative values of power, 50 W and 150 W respectively at a standard chamber pressure. Substrates A-F were imaged using a Hitachi SU70 scanning electron microscope to observe the porosity of the films.

3.2.3 Quantification of Porosity

The porosity of the platinum film was quantified using an open-source image processing software package, Fiji [19]. The SEM images were transformed into grey scale images and two distinct regions were identified. These regions separated uniform platinum from the cracks in the film. Colour manipulation of these two regions allowed a calculation of percentage porosity to be carried out. Figure 3.3 highlights

the two different coloured regions for a sample of platinum deposited at 250 mTorr. The green lines represent cracks in the surface, and therefore the levels of porosity. Fiji was used to calculate the percentage of green pixels in the image, and this was approximated to be the levels of porosity within the film.

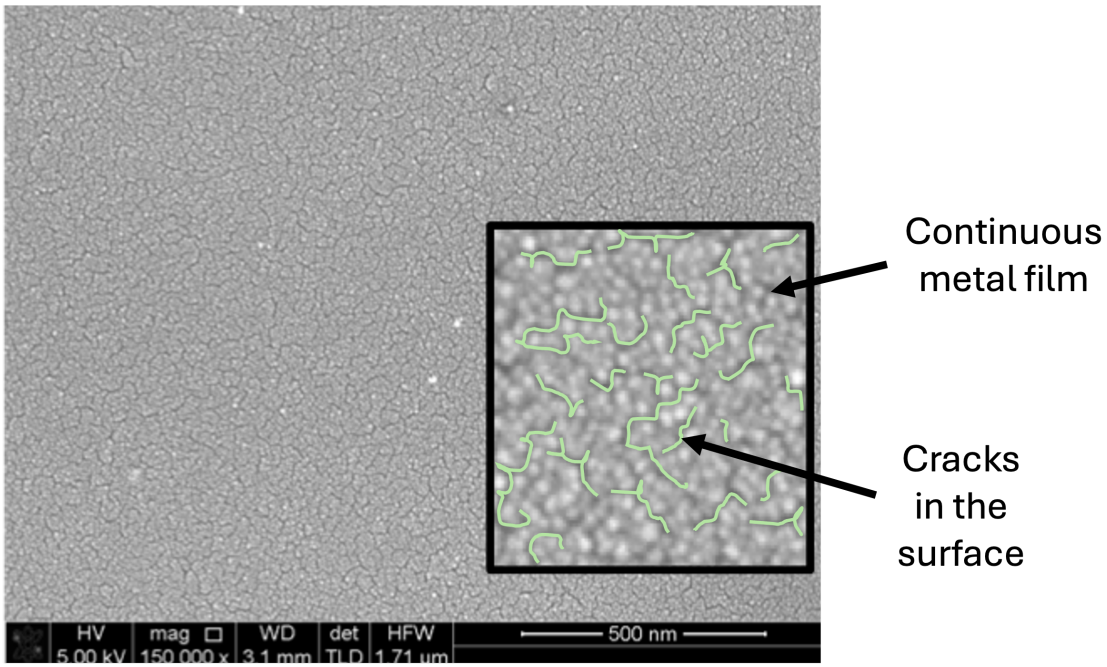

Figure 3.3: Image displaying colour manipulation of SEM image of platinum deposited at 250 mTorr to calculate the levels of porosity

3.2.4 Porosity Results

Figure 3.4 shows the SEM images for the Pt films A-F at 150,000x magnification. The micrographs show a distinct trend between the argon pressure in the chamber and the degree of porosity present. This can be observed from the density of 'cracks' visible in the inset to each of the figures. As the argon pressure is increased, the deposited films become less uniform, and the porosity increases. Sample A is the most porous film and sample F is the most uniform film; these were deposited at chamber pressures of 250 mTorr and 9.8 mTorr respectively. This information is also summarised in Table 3.1, and plotted as a function of argon pressure in the chamber in Figure 3.5.

The data in Figure 3.5 confirms the positive correlation between argon pressure and level of porosity as the chamber pressure is increased from 9.8 mTorr to 250 mTorr, resulting in an increase in porosity of 37.6%. Interestingly, at the lowest argon pressure the minimum amount of porosity in the film is still 47.1%, which suggests that sputter deposited platinum may not be the best choice of gate metal for a device which needs to selectively target hydrogen only. Unwanted, larger, gases

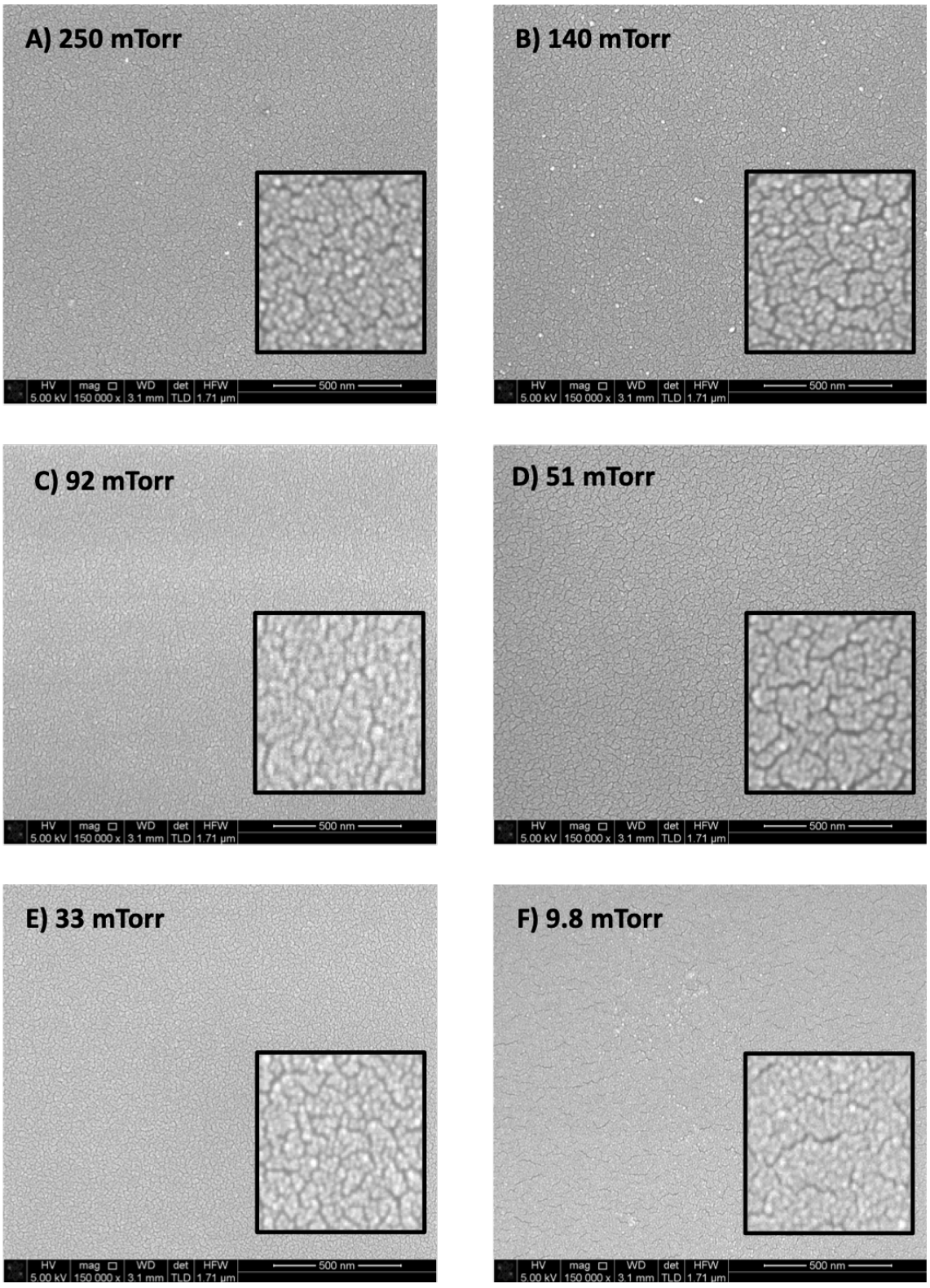

Figure 3.4: SEM images of platinum sputtered at A) 250 mTorr, B) 140 mTorr, C) 92 mTorr, D) 51 mTorr, E) 33 mTorr and F) 9.8 mTorr

within a mixture will be able to interact with the exposed oxide, contributing to the response shown, giving a misleading reading. For the purposes of NOx sensing, porosity is integral, and this deposition tunability allows greater control over testing.

Sample	Argon Pressure (mTorr)	Percentage Porosity (%)
A	250	84.7
B	140	75.4
C	92	67.4
D	51	60.9
E	33	59.2
F	9.8	47.1

Table 3.1: Sputtering pressure and percentage porosity of six deposited platinum films

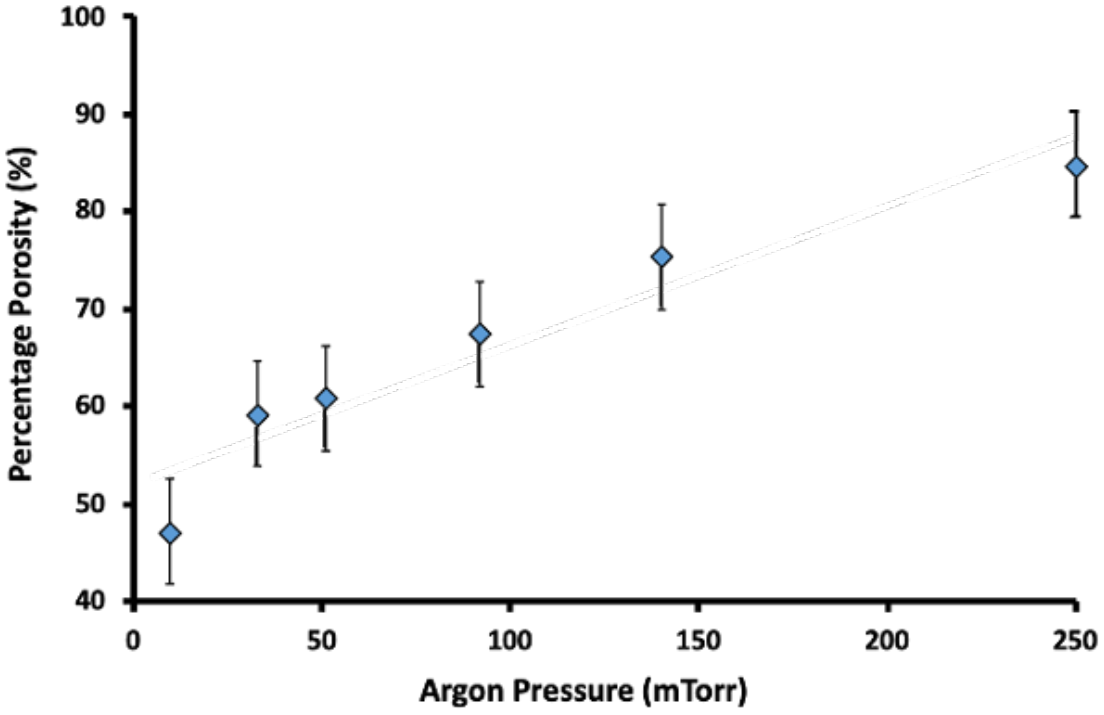

Figure 3.5: Platinum porosity as a function of argon pressure during sputtering

The effect of sputtering power on the amount of porosity incorporated into deposited platinum films was also analysed. Pt layers of identical thickness were deposited at two representative powers of 50 W (Sample G) and 150 W (Sample H). SEM images of samples G and H are shown in Figure 3.6, these were imaged using a Hitachi TM3030 bench-top SEM. Fiji was used again to quantify the amount of porosity in the films and this is outlined in Table 3.2. Energy Dispersive X-ray (EDX) analysis was carried out using the Bruker Quantax 70 system to provide

elemental analysis of the sample surface. EDX highlights the elemental composition of the sample surface which gives a further indication towards the levels of porosity incorporated.

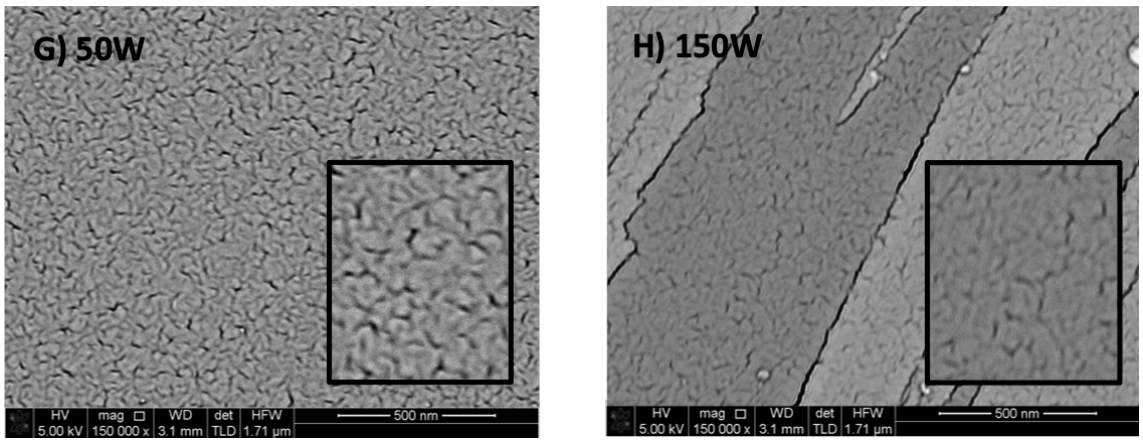

Figure 3.6: SEM images of platinum layers deposited at G) 50 W and H) 150W

Sample	Sputtering Power (W)	Percentage Porosity (%)
G	50	87.3
H	150	62.9

Table 3.2: Sputtering power and percentage porosity of two deposited platinum films

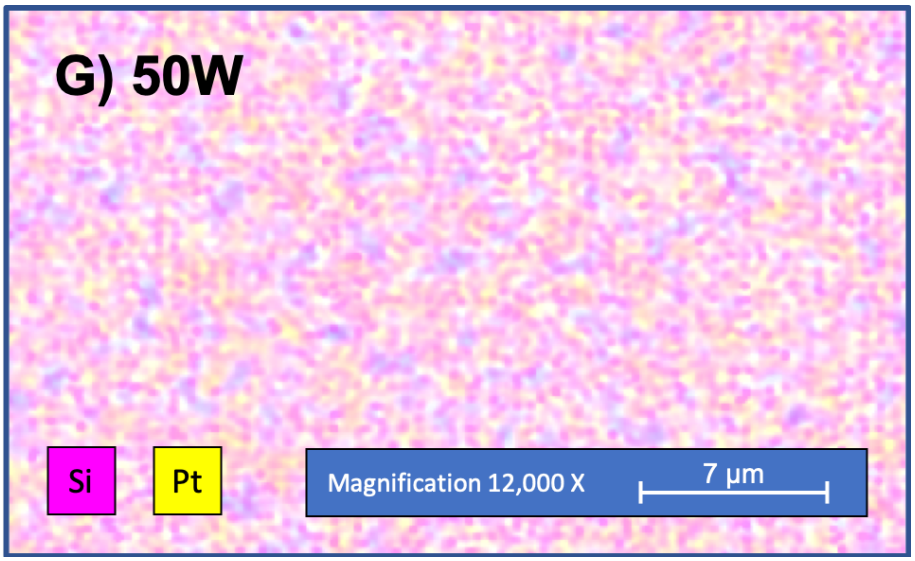

Figure 3.7: EDX analysis of pt film deposited at 50W - Sample G

The data in Table 3.2 show that an an increase in sputtering power reduces the porosity of the deposited film. Deposition at 50 W formed a film with 87.3%

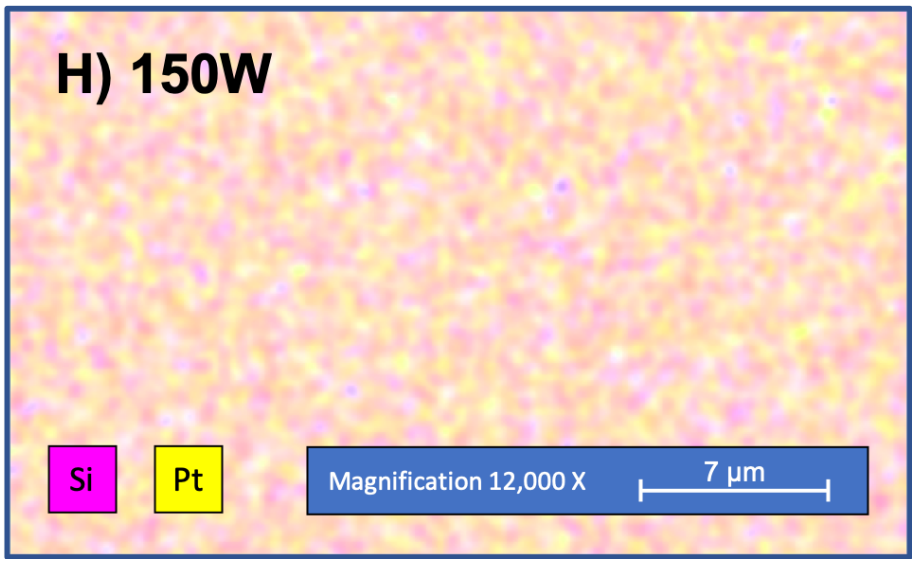

Figure 3.8: EDX analysis of pt film deposited at 150W - Sample H

porosity, whereas the film deposited at 150 W had a reduced level of porosity, 62.9%, due to re-crystallisation as a result of the extra thermal energy in the film during the system. The EDX data support these values. The EDX data for the film shown in Figure 3.7 shows a greater amount of pink, representing the detection of silicon, than yellow, which represents Pt. This indicates that the uniformity of the platinum layer is low and the film is thin, with the EDX probing the underlying SiO_2. In contrast, the sample deposited at 150 W has an appearance that is mainly yellow, suggesting that a more continuous platinum layer has been deposited, with a lower amount of the underlying silicon dioxide film visible.

For gas sensing applications, in order to create gate metal layers which have triple points to which large gas molecules can bind, a less uniform deposition is required. It can be seen from the data in table 3.1 that porosity control can be achieved by modulating the argon pressure, therefore this technique will be used to introduce porosity into Pt layers for the sensors that will be reported in later chapters. A deposition power of 50 W will be used as this allows greater control over sample thickness due to a lower deposition rate. Whilst an argon pressure of 250 mTorr produced a very porous film, these conditions prevented suitable metal coverage, with a patchy sample surface produced. Therefore, considering that deposition at 250 mTorr is unreliable, and the data in Table 3.1 and Figure 3.4, 140 mTorr was selected as optimum argon pressure for all future platinum gate metal depositions.

3.3 Device Fabrication

The substrate used to produce the MOS capacitors was 4H-SiC purchased from Wolfspeed. The substrate had a 2μm epitaxial and an N-type doping concentration

of 3x10^{18} cm^{-1}. The samples were initially cleaned using the organic solvents NMP and IPA before an RCA cleaning process was performed. Dry oxidation of the SiC was performed at 1150 °C in 80 sccm of O_2 for 200 minutes, growing a 25 nm thick layer of SiO_2 on the silicon face. Prior to back contact deposition, the oxide which had formed on the back face of the SiC was removed by a buffered hydrofluoric acid dip. The newly grown SiO_2 layer was protected by hard-baked photoresist to prevent etching. An ohmic contact was then formed on the carbon face by deposition of a metal stack comprising 5 nm of titanium and 100 nm nickel. Annealing of the back contact in vacuum was carried out at 1050 °C for 180 seconds to form nickel silicide. The dielectric layer was then formed by deposition of 50 nm of a chosen metal, followed by oxidation in air at a specified temperature. A study on the optimum oxidation temperature was carried out and the findings from this will be discussed later. Photolithographic patterning of the dielectric surface was performed using S1813 photoresist to realise the individual capacitor structures on the device surface. The gate contact was then formed by deposition of a 5 nm titanium layer for adhesion purposes, followed by 70nm of platinum; the argon pressure was modulated to control the level of incorporated porosity as per section 3.2. Further patterning of the device was performed, followed by a deposition of 300 nm of gold, to produce contacts suitable for bonding to relevant circuitry. Figure 3.9 shows a schematic representation of the fabricated MOS device.

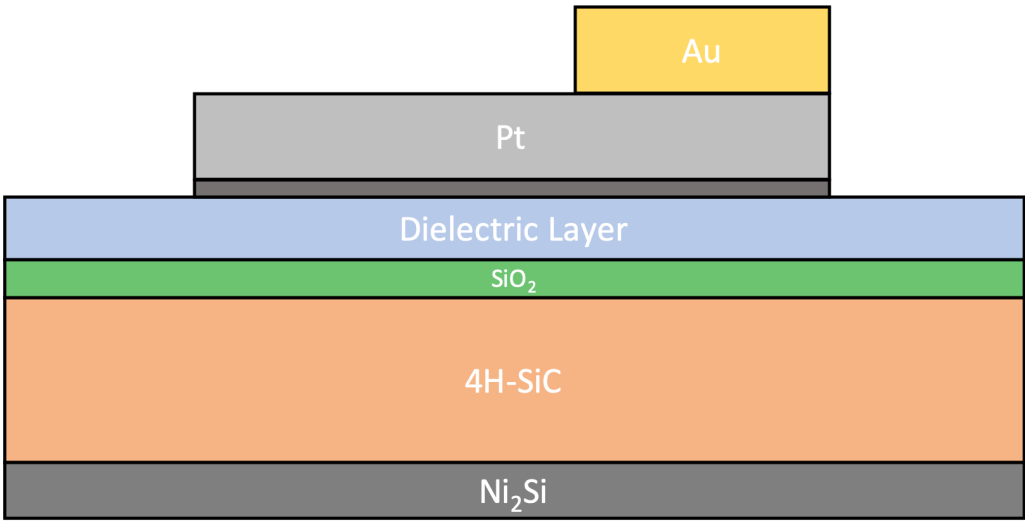

Figure 3.9: Schematic of metal-oxide-semiconductor device

3.4 Device Characterisation and Analytical Techniques

After fabrication of the MOS capacitors, capacitance-voltage (C-V) and conductance-voltage (G-V) characteristics were extracted using a Keithley 4200A-SCS parameter analyser. It is important to test each fabricated device to ensure that each has stable electrical characteristics and identify devices that are suitable for use as a gas sensor. The standard test to extract these parameters involves voltage sweep from depletion to accumulation (-5V to 5V) with an AC excitation frequency of 1 MHz. The sputtered gate metal, with an area of $3.14\text{x}10^{-4}$ cm^{-2}, and the ohmic contact formed on the back of the device were used as the electrical contacts for this test.

3.4.1 MOS Capacitor Voltage Sweeps

MOS capacitors can be subjected to a DC voltage sweep, and parameters such as capacitance (C) and conductance (G) can be monitored to give an insight into device behaviour.

Capacitance-Voltage measurements are used to characterise MOS capacitors, and the capacitance values vary with the voltage applied to the gate. As a standard practice, measurements are carried out at an AC excitation frequency of 1MHz. This high frequency test means that the capacitance values are measured rapidly, allowing majority carriers to be responsible for the observed response. When lower frequencies are used, the behaviour of minority carriers is observable, providing more in depth information into device behaviour.

The applied voltage is periodically increased with a capacitance or conductance value being measured. This provides typical C-V and G-V curves as shown in Figure 3.10. Sweep rates can vary depending on how many data points are to be collected. A usual sweep rate of 0.1V per second is used, but the data in Figure 3.10 was taken at 0.01V per second.

Key parameters from the data can be extracted, such as flatband voltage, maximum capacitance, and maximum conductance. The flatband voltage occurs when the energy bands of the semiconductor are flat, and there is no charge present within the substrate. This is a useful value for calculating gaseous sensitivity.

The maximum conductance refers to the peak value of conductance seen in a G-V sweep, and this is typically observed close to the flatband voltage. This is because the flat energy bands allow the maximum levels of interaction between interface charge states and the semiconductor substrate [21].

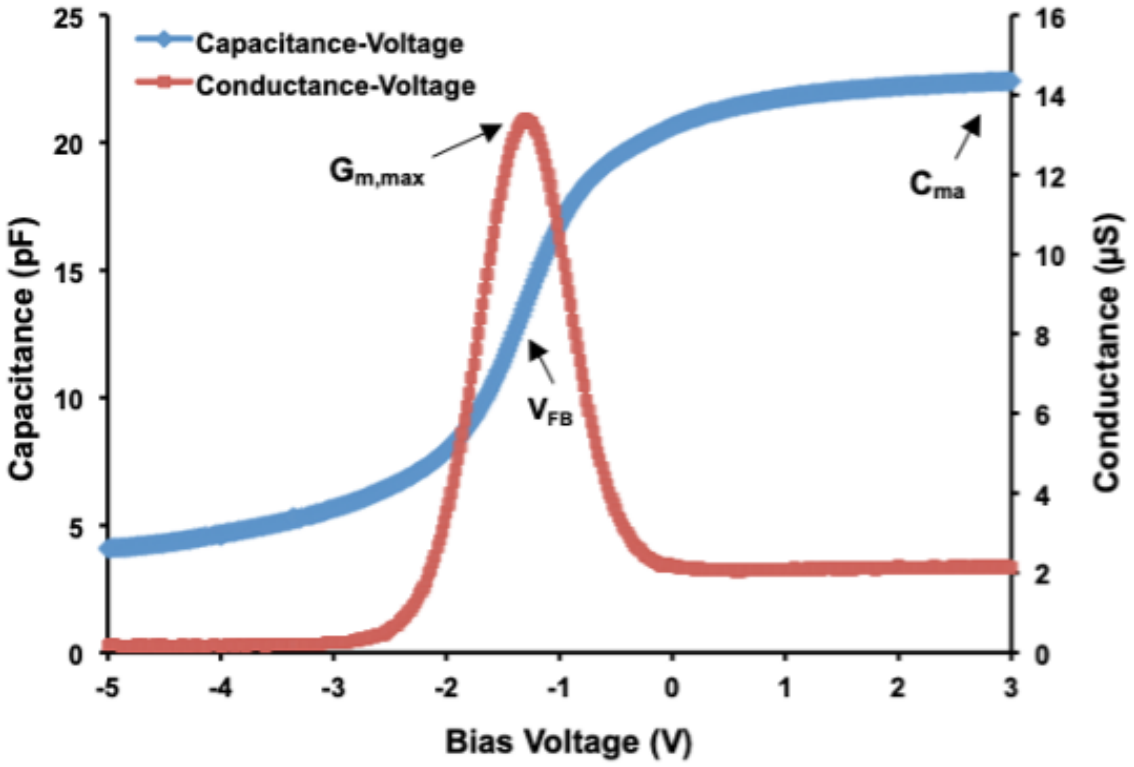

Figure 3.10: A typical set of C-V and G-V characteristics extracted from a Al/SiO_2/Si capacitor and showing key parameters [20]

3.4.2 Series Resistance

The data from the parameter analyser is corrected to remove the effects of series resistance (R_{series}), which arises from the bulk resistance of the SiC substrate and undepleted epitaxial layer [22, 23, 24]. Series resistance can interfere with the characteristics and skew the C-V and G-V data, especially at high measurement frequencies, and R_{series} is calculated using Equation 3.1.

$$R_{series} = \frac{\left(\frac{G_M}{\omega\, C_M}\right)^2}{\left(1 + \left(\frac{G_M}{\omega\, C_M}\right)^2\right) G_M} \tag{3.1}$$

G_M and C_M, are the experimentally measured values of conductance and capacitance, respectively, and ω is the angular frequency at which the measurement was taken. Once R_{series} has been determined, α is used (Equation 3.2) to extract the corrected values of capacitance (C_c) and conductance (G_c) from Equations 3.3 and 3.4.

$$\alpha = G_M - \left({G_M}^2 + \omega^2 {C_M}^2\right) R_{series} \tag{3.2}$$

$$C_C = \frac{\left(G_M{}^2 + \omega^2 C_M{}^2\right) C_M}{\left(\alpha^2 + \omega^2\right) C_M{}^2} \tag{3.3}$$

$$G_C = \frac{\left(G_M{}^2 + \omega^2 C_M{}^2\right) \alpha}{\left(\alpha^2 + \omega^2\right) C_M{}^2} \tag{3.4}$$

The plot in Figure 3.11 shows the C-V and G-V characteristics for an Pt/HfO_2/SiO_2/4H-SiC MOS capacitor prior to, and after, correction for series resistance. The flatband voltage (V_{FB}) and flatband capacitance (C_{FB}) are identified, as well as the value of oxide capacitance (C_{ox}), which after correction has the same value as the capacitance maximum C_{max}.

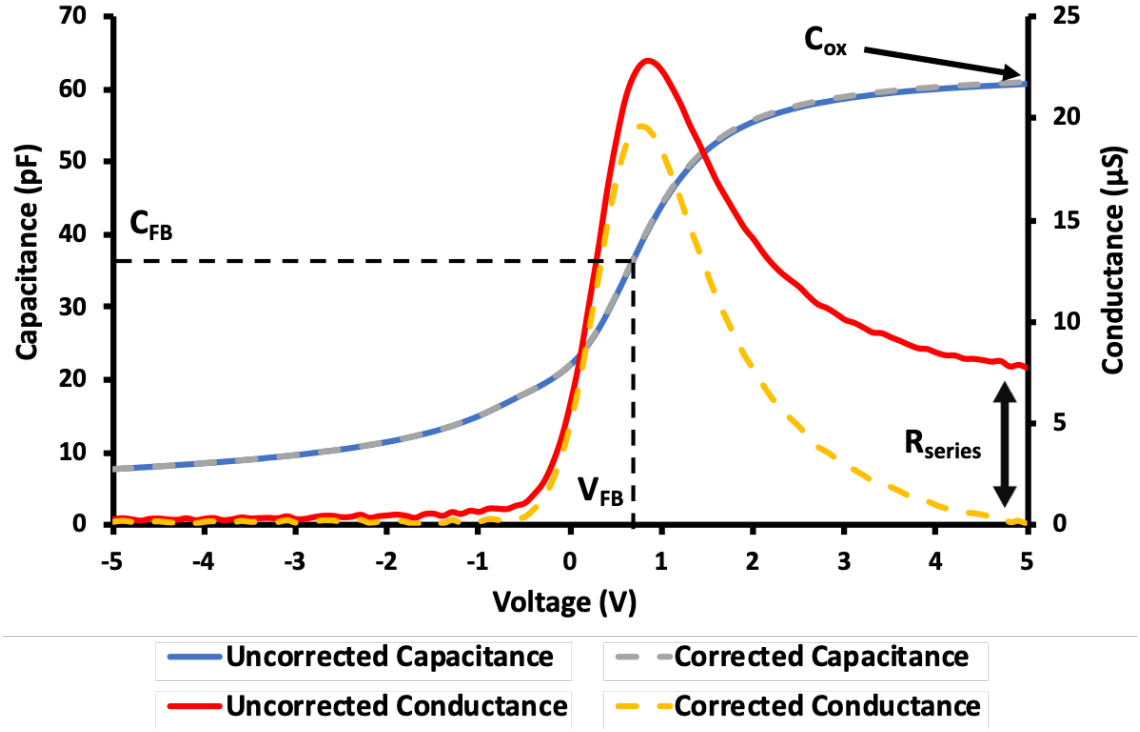

Figure 3.11: Typical C-V and G-V characteristics for an Pt/HfO_2/SiO_2/4H-SiC MOS capacitor outlining the effect of series resistance correction

3.4.3 Flatband Voltage

As outlined previously, the flatband voltage is an important parameter to describe the characteristics of an MOS capacitor. In a gas sensor, variations from this baseline value can be attributed to the influence of external analytes, enabling the detection of gas molecules. Mechanistically, gas molecules can be thought of as altering the charge within the MOS capacitor, which manifests itself as a shift in V_{FB}, through $\Delta V_{FB} = \Delta Q / C_{ox}$. The flatband voltage of a MOS capacitor can be calculated from

Equation 3.5, where ϕ_{ms} is the difference in the metal and semiconductor work functions and Q_f, Q_m and Q_t are values of fixed oxide, mobile and trapped charge respectively.

$$V_{FB} = \phi_{ms} - \frac{Q_f + Q_m + Q_t}{(C_{ox})} \tag{3.5}$$

An ideal MOS capacitor would have no oxide charge, rendering V_{FB} equal to ϕ_{ms}. The work function difference between the metal and the semiconductor can be calculated using Equation 3.6.

$$\phi_{ms} = \phi_m - \left[\chi + \frac{E_g}{2} - \left(\frac{kT}{q} \ln\left(\frac{N_D}{n_i}\right)\right)\right] \tag{3.6}$$

where χ and E_g are the semiconductor electron affinity and band gap respectively, ϕ_m the metal work function, q the electronic charge, N_D the dopant concentration in the semiconductor, n_i the intrinsic carrier concentration, k Boltzmann's constant and T the temperature.

The capacitance at the flatband voltage, the flatband capacitance, C_{FB} can be calculated from Equation 3.7, utilising the values of semiconductor flatband capacitance (C_{FBS}) (Equation 3.8) and the capacitor area (A). This value can be used as a practical method to find V_{FB} from the C-V characteristics.

$$C_{FB} = \left(\frac{C_{FBS}\, C_{ox}}{\frac{C_{ox}}{A} + C_{FBS}}\right) \tag{3.7}$$

$$C_{FBS} = \frac{\epsilon_s\, \epsilon_O}{\lambda_n} \tag{3.8}$$

Where ϵ_s is the semiconductor permittivity, ϵ_0 is the permittivity of free space, and λ_n is the Debye length (outlined in Equation 3.9).

$$\lambda_n = \left(\frac{\epsilon_s\, kT}{q^2\, n_i}\right)^{\frac{1}{2}} \tag{3.9}$$

3.4.4 Interface Trap Density

Trapping states between the semiconductor-oxide interface arise from defects formed during the oxidation process. The density of interface traps (D_{IT}) can be calculated by several methods, two of the most popular being the Hill-Coleman and Terman. The Hill-Coleman method is based on the consideration of a single trapping state located in the middle of the semiconductor bandgap and whilst this is not an accurate description of the interface in silicon carbide MOS capacitors, the ability to make comparative measurements between devices and across a wide range of temperatures

make this a useful technique during the development of new dielectric materials. The density of the trapping states can be estimated from C-V measurements taken at a single frequency, as described by Equation 3.10.

$$D_{IT} = \frac{2}{q\,A}\left[\frac{\left(\frac{G_{max}}{\omega}\right)}{\left(\frac{G_{max}}{\omega\,C_{ox}}\right)^2 + \left(1 - \frac{C_M}{C_{ox}}\right)^2}\right] \tag{3.10}$$

This technique measures the parallel conductance of the capacitor as a function of frequency and voltage. The conductance can be used to estimate the number of traps present via the capture of charge carriers [25].

The Terman method enables the extraction of D_{IT} as a function of energy within the bandgap, which is more suitable for use with silicon carbide MOS structures, where the value of D_{IT} is known to vary exponentially with energy close to the band edges. The experimental measurements require high excitation frequency measurements, which are then compared to an ideal C-V characteristic. This method is known to underestimate the extracted values of D_{IT} in comparison to techniques, however, it is a widely accepted technique in the literature and this enables direct comparison of the characteristics with those available in the literature. The method involves the extraction of the surface potential (ϕ_s) from a comparison between the experimental and theoretical C-V characteristics. Interface traps respond to the applied voltage and cause an elongation of the C-V curve in the depletion region along the voltage axis. The change between the practical and experimental surface potential as a function of gate voltage curves can be used to determine D_{IT} using Equation 3.11 [26].

$$D_{IT} = \frac{C_{ox}}{q^2}\left(\frac{dV_G}{d\phi_s} - 1\right) - \frac{C_s}{q^2} \tag{3.11}$$

3.5 Zirconium Dioxide Incorporation

The use of hafnium dioxide [27, 28, 29, 30] and titanium dioxide [31, 32, 33, 34] as dielectric layers in MOS capacitor based gas sensors has been demonstrated previously. Hafnium and titanium are transition metals and share similar properties due to both elements having the same electronic structure in the outer orbital shells. Both Hf and Ti are easily oxidised to form HfO_2 and TiO_2, by heating to temperatures in excess of 450 °C in air, making them excellent candidates for the dielectric layer of MOS capacitors. When used in gas sensors, hafnium oxide, and titanium dioxide based sensors have previously demonstrated differing response to hydrogen and oxygen. These saturation and normalisation characteristics of these devices also vary. These phenomena are useful as they have been identified as a means to realise

a device array to target specific gaseous concentrations in a mixed environment.

With this in mind, the incorporation of ZrO_2, a metal from the same group as Hf and Ti, as the dielectric layer in the MOS capacitor was studied, in order to test its gas sensing performance. Therefore, a study was carried out to optimise the fabrication process, identify the potential to integrate Zr based sensors with the proposed Ti and Hf based arrays, and compare the behaviour of zirconium based devices to those manufactured from hafnium and titanium.

Samples of 4H-SiC were cleaned, oxidised, and had an ohmic contact deposited using the method outlined in section 3.3. These were then divided into three groups, each of which had 50 nm of hafnium, titanium or zirconium metal deposited on top of the SiO_2 using DC sputtering. These samples were further divided into groups and the oxidation of the metal was undertaken at 450, 550, 650, and 750 °C, for 10 minutes in laboratory air. A 70 nm platinum gate metal contact was then deposited using sputtering on the top surface of the dielectric at 50 W, using an argon pressure of 140 mTorr to maximise the porosity.

3.5.1 Characterisation of Zirconium Oxide Based Devices

Following C-V measurements at 1 MHz, the C_{max}, G_{max} and D_{IT} (using the Terman method) were extracted at E_c–E = 0.2 eV (close to the conduction band), for each sample as a function of oxidation temperature. The overall comparison of these parameters is shown in Figures 3.12, 3.13 and 3.14 for Hf, Ti and Zr respectively. All of the experimental values have been normalised to the results for the capacitors oxidised at 550 °C, which has previously been considered as the optimum oxidation temperature for the realisation of Hf and Ti based sensors. The data for the Hf and Ti devices oxidised at 450 °C have been omitted due to their unstable C-V and G-V characteristics, indicative that the oxidation had not completed as significant un-oxidised metal could still be found in the dielectric.

The data presented in figure 3.12 indicates that 550 °C is the optimum oxidation temperature for Hf based dielectrics. Whilst the properties of the bulk HfO_2 dielectric, namely C_{max} and G_{max} do not show a strong temperature dependence, increasing the temperature to 650 °C results in a 55 % increase in the density of interface traps. This increase suggests a solid state chemical reaction occurs at the HfO_2/SiO_2 interface, similar to that observed in the TiO_2 characteristics shown in figure 3.13. These characteristics match those that have been described previously. The ZrO_2 data shown in figure 3.14 show a more complicated trend with oxidation temperature. As described earlier, oxidation at 450 °C results in incomplete oxidation of the Zr, which can be observed from the low value of C_{max} which arises from the low dielectric constant of the partially oxidised Zr. Increasing the oxidation tem-

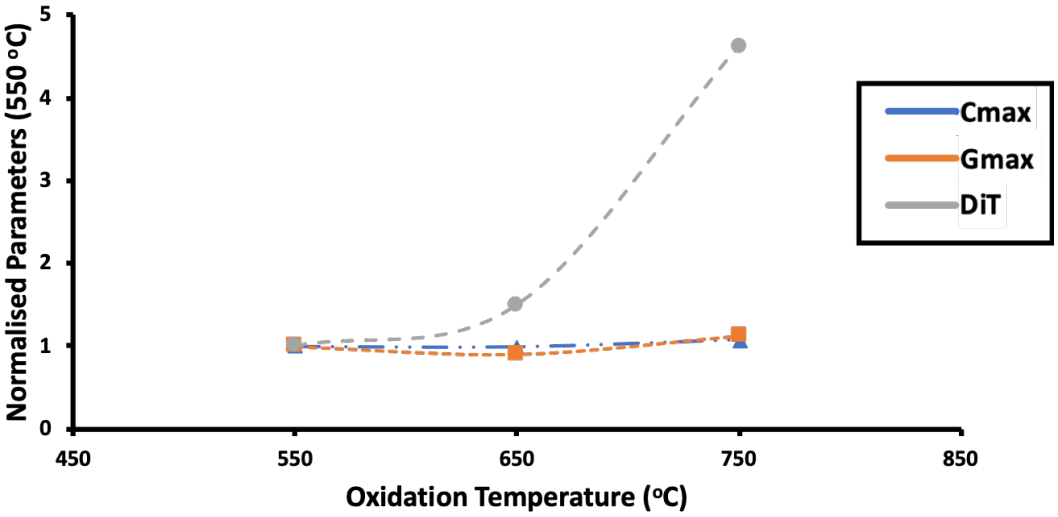

Figure 3.12: Comparison of capacitor performance change with oxidation temperature for a Pt/HfO_2/SiO_2/4H-SiC MOS capacitor

perature above 550 °C does not have an effect on the capacitance, indicating that the Zr is fully oxidised, however, the conductance of the film continues to increase. This may be interpreted as the start of the film undergoing a phase transition to a higher crystallinity, although this would normally be accompanied by an increase in the capacitance, or more likely, an increase in the roughness of the film. Despite the significant decrease in the density of interface traps at 650 °C in comparison to the 550 °C characteristics, 550 °C was selected as the optimum oxidation temperature for the realisation of Zr based gas sensors, because of the stability of the capacitance, low value of conductance and the potential to monolithically integrate the Zr based dielectric with Ti and Hf in a single process.

Further HfO_2, TiO_2 and ZrO_2 devices were fabricated, using 550 °C as the oxidation temperature. C-V and G-V characteristics were extracted over a range of test temperatures up to 300 °C. The data in figure 3.15 show the variation of the flatband voltage, V_{FB}, as a function of test temperature. The data show a similar trend for the three dielectric materials studied here, despite the variation in the magnitude of V_{FB}. As the temperature is raised, the flatband voltage for all three dielectrics decreases up to 150 °C.

This effect is commonly observed in n–type capacitors on SiC and related to the shift in the metal–semiconductor workfunction, ϕ_{ms}, which is defined by Equation 3.12.

$$\phi_{ms} = \phi_m - \left(\chi + \frac{E_g}{2q} + \phi_B\right) \tag{3.12}$$

Where ϕ_B is the energy separation between the intrinsic Fermi Level and the

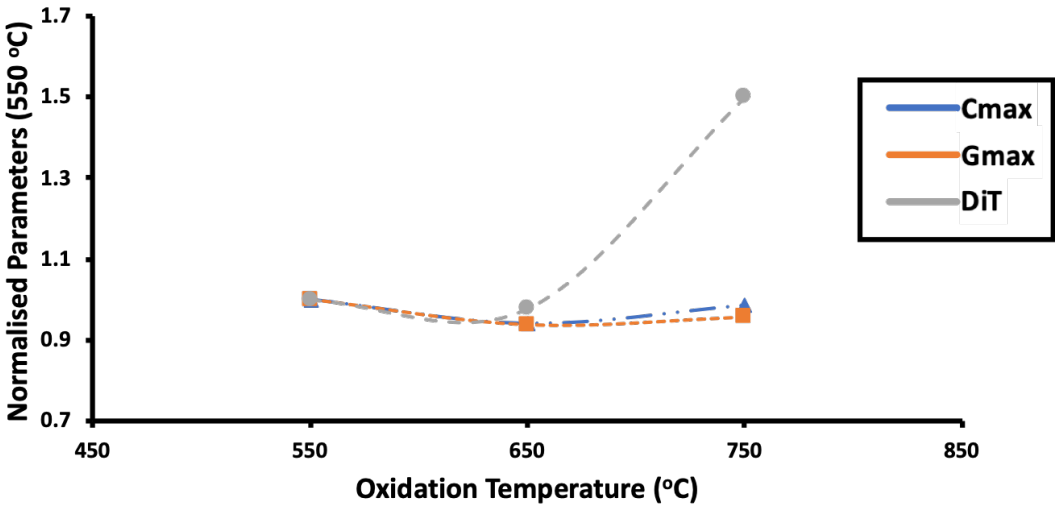

Figure 3.13: Comparison of capacitor performance change with oxidation temperature for a Pt/TiO_2/SiO_2/4H-SiC MOS capacitor

extrinsic Fermi Level in the semiconductor - Equation 3.13.

$$\phi_B = \frac{k_B T}{q} \ln \frac{N_D}{n_i} \tag{3.13}$$

The magnitude of the flatband voltage shift predicted from the change in the intrinsic carrier concentration with temperature, indicates that the characteristics of the TiO_2 dielectric are greater than can be described using the shift in n_i, whereas the characteristics for both the Hf and Zr based dielectrics are smaller. This would suggest that in all cases, the observed characteristics are influenced by changes in the charge trapped within the dielectric. Above 150 °C, the TiO_2 data continues to show a decrease in V_{FB}, in common with data published in the literature (Equation 3.13), however, both the Zr and Hf based devices show that the value fo V_{FB} starts to increase. This non-monotonic behaviour also indicates the existence of a second mechanism in the dielectric. The flatband voltage is conventionally defined by Equation 3.14.

$$V_{FB} = \phi_{ms} - \frac{Q_f + Q_m + Q_{ot}}{C_i} \tag{3.14}$$

Because the temperatures at which the devices are being tested are significantly lower than the fabrication temperature, it is unlikely that the fixed oxide charge values are shifting. Trapped charge in the dielectric film, Q_{ot} is likely to be responsible for the variation of flatband voltage with temperature and the TiO_2 films are trapping charge of a different polarity in comparison to the Hf and Zr based films.

In order to further investigate the contribution of the trapped charge in the oxide film on the capacitor behaviour, capacitance–voltage sweeps were then performed for

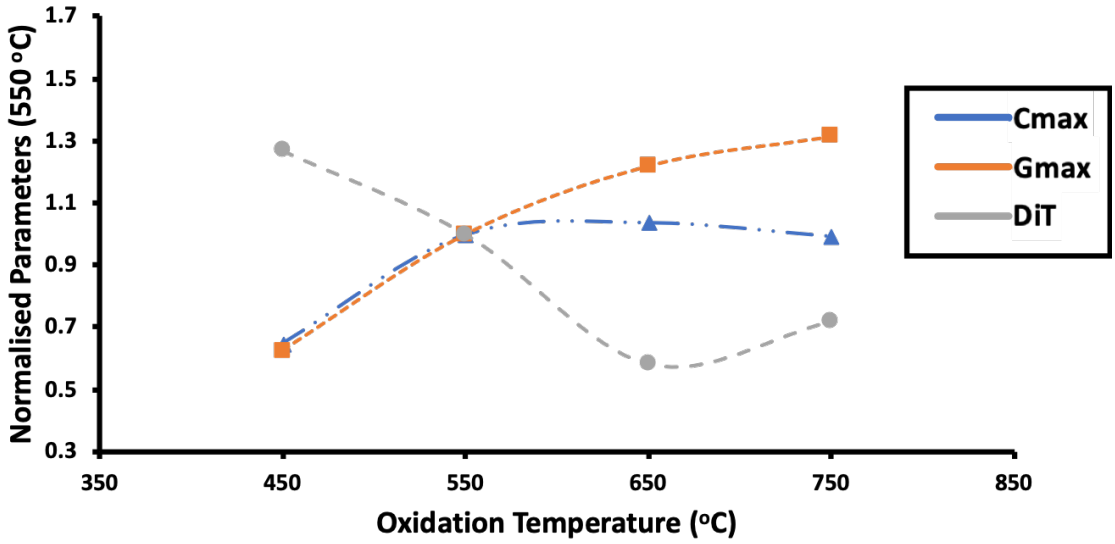

Figure 3.14: Comparison of capacitor performance change with oxidation temperature for a $Pt/ZrO_2/SiO_2/4H\text{-}SiC$ MOS capacitor

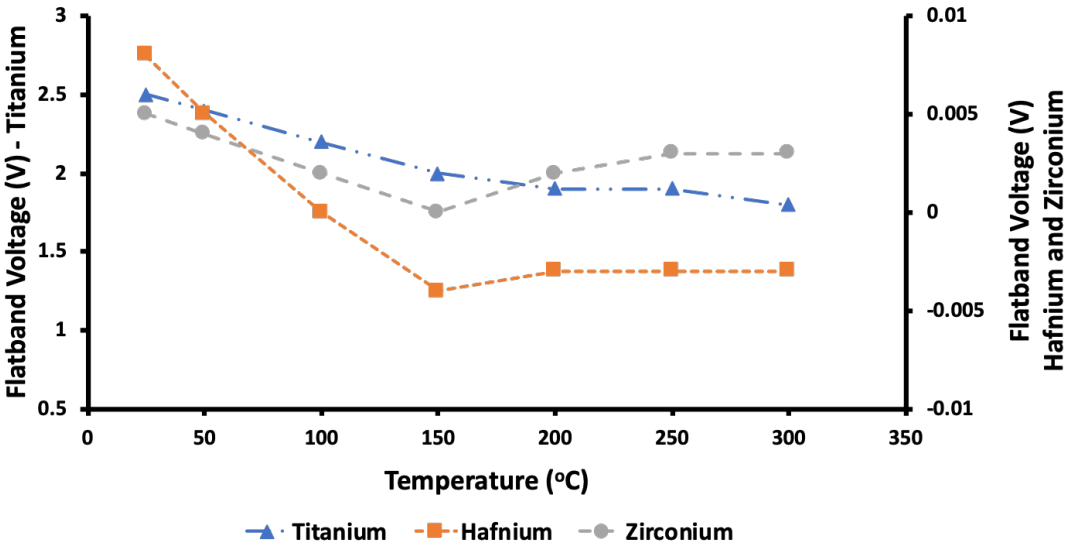

Figure 3.15: Dependence of flatband voltage on test temperature for MOS capacitors containing different dielectric materials

a range of different test frequencies. The data in Figure 3.16 show the dependence of V_{FB} on measurement frequency for the three dielectrics.

The data in figure 3.16 show an increase in the flatband voltage with excitation frequency. The flatband voltage shift for the TiO_2 dielectric is significantly higher than for either the Hf or Zr based films. This would suggest that the TiO_2 contains a larger number of oxide trapping states, which supports the hypothesis relating to the temperature variation, whilst the relatively small variation in flatband voltage for the Zr and Hf based devices indicates that the concentration of oxide traps is lower in these films.

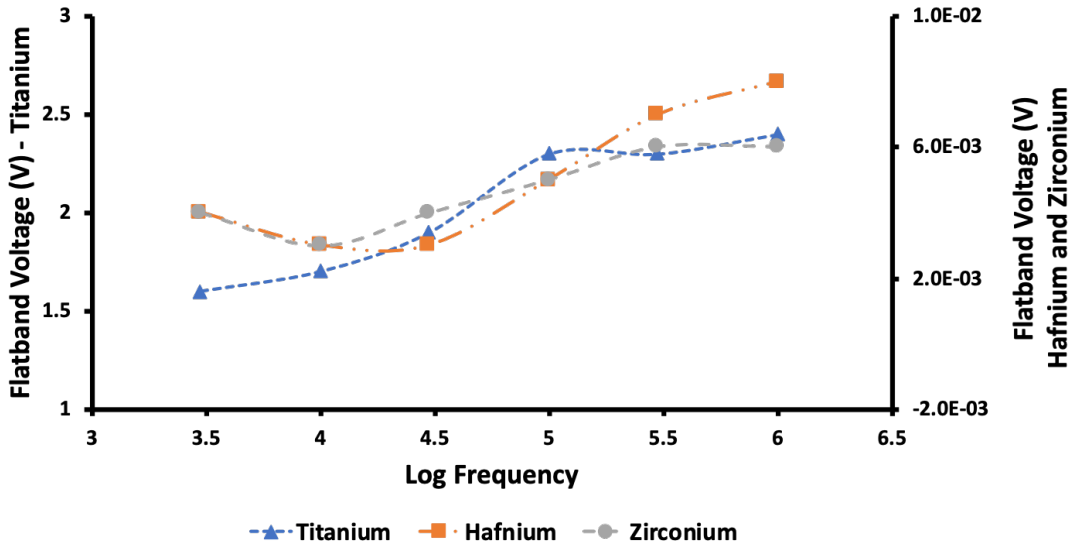

Figure 3.16: Dependence of flatband voltage on test frequency for MOS capacitors containing different dielectric materials

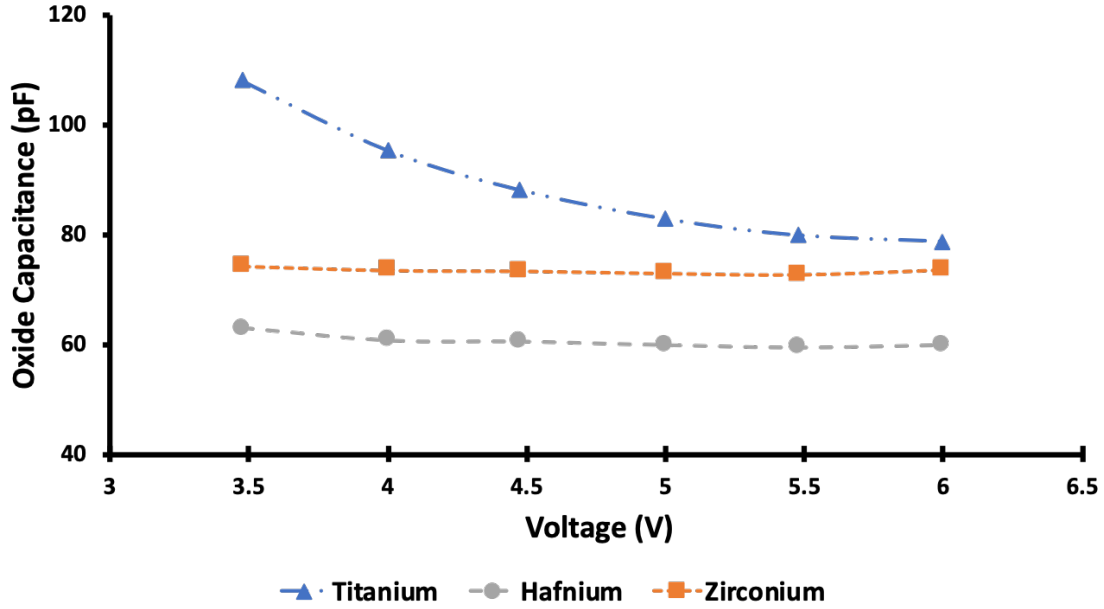

Figure 3.17: Dependence of C_{ox} on test frequency for MOS capacitors containing different dielectric materials

The high concentration of oxide traps in TiO_2 films has been published previously [35]. The current hypothesis is that these additional traps, which are linked to oxygen vacancies in the dielectric are the origin of the enhanced sensitivity of TiO_2 based sensors to hydrogen containing gas species. The ZrO_2 films appear to be similar to the Hf based dielectrics, suggesting that they will be stable for long term operation in hostile environments and that the oxidation of Zr is closer to Hf than to Ti, despite the three elements being listed in the same group in the periodic table.

3.5.2 Raman Spectroscopy

Raman spectroscopy is an analytical technique used to extract information on the chemical structure of samples. A high intensity laser is used to irradiate a sample, and the resultant spectrum of the scattered light is analysed. The Raman scatter spectrum can be used to identify the presence of particular chemical bonds within a material, and therefore be used to confirm whether a metal film has been oxidised.

Raman spectroscopy is a vibrational spectroscopy technique that relies on the scattering of monochromatic light to obtain chemical and structural information about a material. A high intensity laser is used to irradiate a sample, and the resultant pattern of the scattered light is analysed. The Raman scatter pattern can be used to identify the presence of particular chemical bonds within a material, and therefore be used to confirm whether a metal film has been oxidised. During this process, the interaction of scattered photons promotes the bonds in a material to a virtual energy state for a short period of time before returning to their original energy state.

The most common type of scattering is elastic scattering, also known as Rayleigh scattering. This occurs when the molecule relaxes and returns to its original energy level, resulting in the emitted photon having the same energy as the laser. However, inelastic scattering, which is of primary interest in Raman spectroscopy, is less common. In inelastic scattering, the emitted photon has a different energy than the incident photon, leading to an energy gain or loss and a corresponding shift in wavelength. This inelastic scattering is what allows the identification of materials. Figure 3.18 depicts elastic and inelastic scattering.

Raman spectra of tungsten oxide show two distinct peaks that can be used to identify the presence of WO_3. The peak at 717 cm^{-1} corresponds to the asymmetric stretching of the O-W-O bonds and the peak at 806 cm^{-1} represents symmetric stretching, see Figure 3.19 [36]. Pure metal films are not responsive to Raman spectroscopy as there are no vibrational modes that can be excited, therefore, this technique allows confirmation of oxidation by measuring the sample before and after heating in air.

3.6 Tungsten Oxide Study

Previous reports in the literature have identified that Tungsten trioxide (WO_3) has a high selectivity to a range of target gases, which includes nitrogen oxides, methane and carbon monoxide [37, 38, 39]. In order to selectively target the NOx concentration within an automotive exhaust engine, a study was undertaken to examine the possibility of incorporating WO_3 as the dielectric layer in the MOS capacitor,

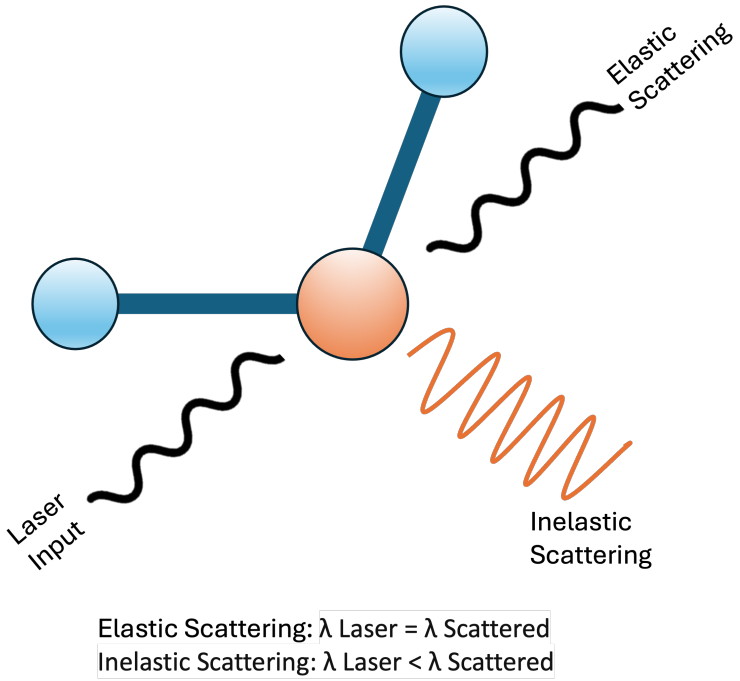

Figure 3.18: Depiction of elastic and inelastic scattering used in Raman spectroscopy

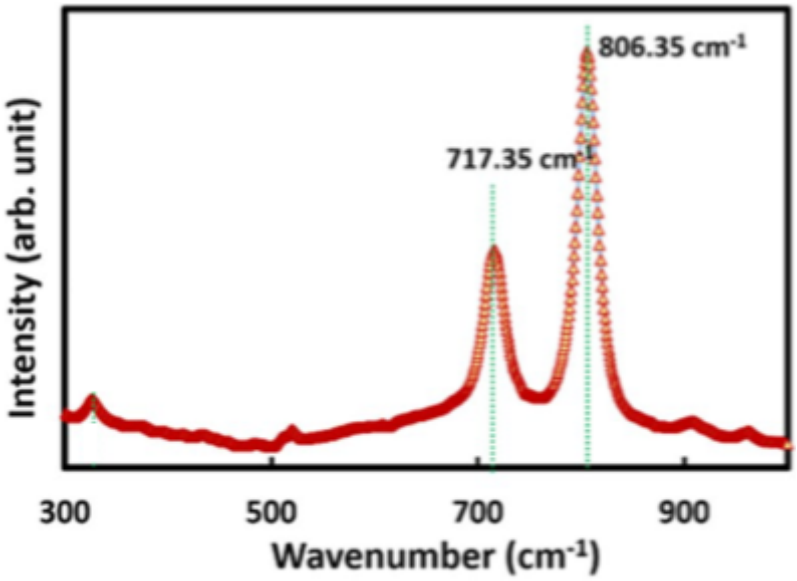

Figure 3.19: Raman spectrum of tungsten oxide grown on tungsten substrate, showing two indicative peaks at 717.35 cm^{-1} and 806.35 cm^{-1} [36]

with the potential to integrate the resulting structure with the Hf, Zr, and Ti based dielectrics described in this chapter. Because tungsten is a transition metal, in principle, the same oxidation process used to oxidise Hf, Ti, and Zr was studied as the initial route to fabrication. As established previously, WO_3 sensitivity alone is not sufficient to selectively detect NOx molecules and functional sensors require modification to the porosity of the platinum gate metal to enable the detection of these

larger gas molecules.

3.6.1 Tungsten Oxide Growth Study

25 nm of SiO_2 was thermally grown on clean 6" silicon wafers, prior to the sputter deposition of 100 nm of tungsten metal. All samples were sputtered simultaneously to ensure that the deposition conditions and hence the metal films were identical. These wafers were then cleaved into 1×1 cm samples and divided into ten groups (labeled as A – J) to study the effect of oxidation conditions on the characteristics of the dielectric film. Initial findings showed that in order to achieve a fully oxidised film, it was necessary to identify the minimum oxidation time, so that WO_3 was formed. An initial starting temperature of 500 °C was chosen because this had demonstrated effective oxidation of hafnium, titanium, and zirconium. The hold time at the maximum temperature during the oxidation and the method for the subsequent cooling was then studied systematically. Raman spectroscopy and AFM imaging were used to identify the formation of WO_3 and to determine the effect of the process conditions on the surface morphology. The data in Table 3.3 summarises the oxidation conditions used in this study.

Sample	**Hold Time (minutes)**	**Temperature (°C)**	**Cooling Method**
A	10	500	Cooled Quickly
B	10	500	Cooled Slowly
C	1200	500	Cooled Quickly
D	0	N/A	N/A

Table 3.3: Oxidation temperature and time of four deposited tungsten films

Sample D was a control sample of tungsten metal and was not oxidised. The samples identified as 'Cooled Quickly' describe samples where at the conclusion of the oxidation time, the sample was removed from the furnace, over a period of five seconds and allowed to naturally cool in ambient air. In contrast, samples denoted as 'Cooled Slowly' were allowed to cool within the furnace once the had the heat source had been removed and reached room temperature in approximately 8 hours.

The data in Figure 3.20 show the Raman spectra for samples denoted A – D.

Comparison of the spectra for samples A, B and C, with the spectra for sample D, shows the successful formation of WO_3. The clearly observed peaks in the spectra at around 720 cm^{-1} and 820 cm^{-1} are present for all samples which had tungsten sputtered onto their surface. The wavenumber of these peaks is in good agreement

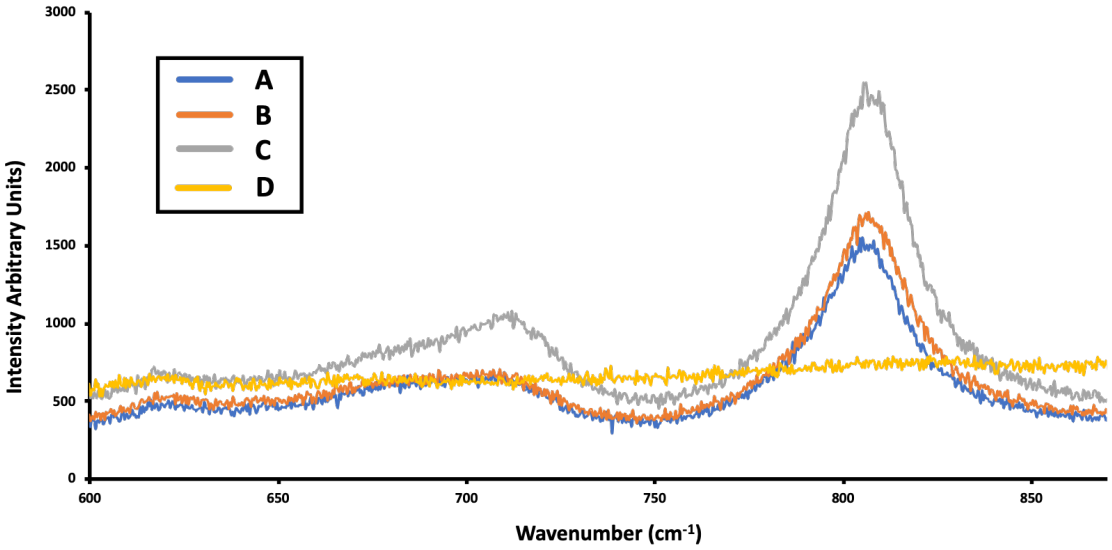

Figure 3.20: Raman spectrum of tungsten oxide samples

with the values for WO_3 reported in the literature [40, 41, 42]. The relative intensity of the Raman peaks is related to the fraction of tungsten oxide present in the sample. It can be observed from the data that there is little variation between sample A which was cooled quickly, and sample B which was cooled slowly both samples having been oxidised for ten minutes at 500 °C. Because of the increased time requirements for the cooling process, method B was not studied further, as the data show that this additional time has no influence on the film. The spectrum for he tungsten film which was oxidised for 1200 minutes (sample C) has a intensity of the Raman peak at 820 cm^{-1} that is approximately 33% higher than samples A and B, which were oxidised with a hold time of 10 minutes. Whilst this enhancement in the Raman intensity appears to be significant, previous characterisation of HfO_2 and TiO_2 films grown using thermal oxidation for similar duration show little electronic variation from oxides grown for 10 minutes. Therefore, for ease of fabrication and with a view to the potential integration of tungsten oxide dielectrics with the Hf, Zr and Ti oxides optimised in the previous section, a 10 minute oxidation process was selected for all further sample fabrication. Figure 3.21 shows AFM images of the surface of samples A – C taken in tapping mode, along with the extracted RMS surface roughness. It can be seen from the data that the extracted roughness values of sample B is 16% higher than for sample A, which arises from the longer duration cooling after the oxidation. The AFM images also show that the two films have a similar morphology. with individual micro-crystallites visible in the image. The increase in roughness indicates that the dielectric is likely to contain a greater concentration of electronic defects. Previous studies have demonstrated that the existence of traps within a dielectric film used to realise MOS based sensors has a significant influence on the sensitivity and response of the gas sensor. However, a compromise between the

potential increase in the sensitivity and the expected increase in the leakage current has to be made, as at high temperatures there will be concerns over the device stability and long term reliability [43, 44]. Because of the minor shift in the surface roughness with the extended cool down time, this further supports the decision to oxidise all future films for 10 minutes.

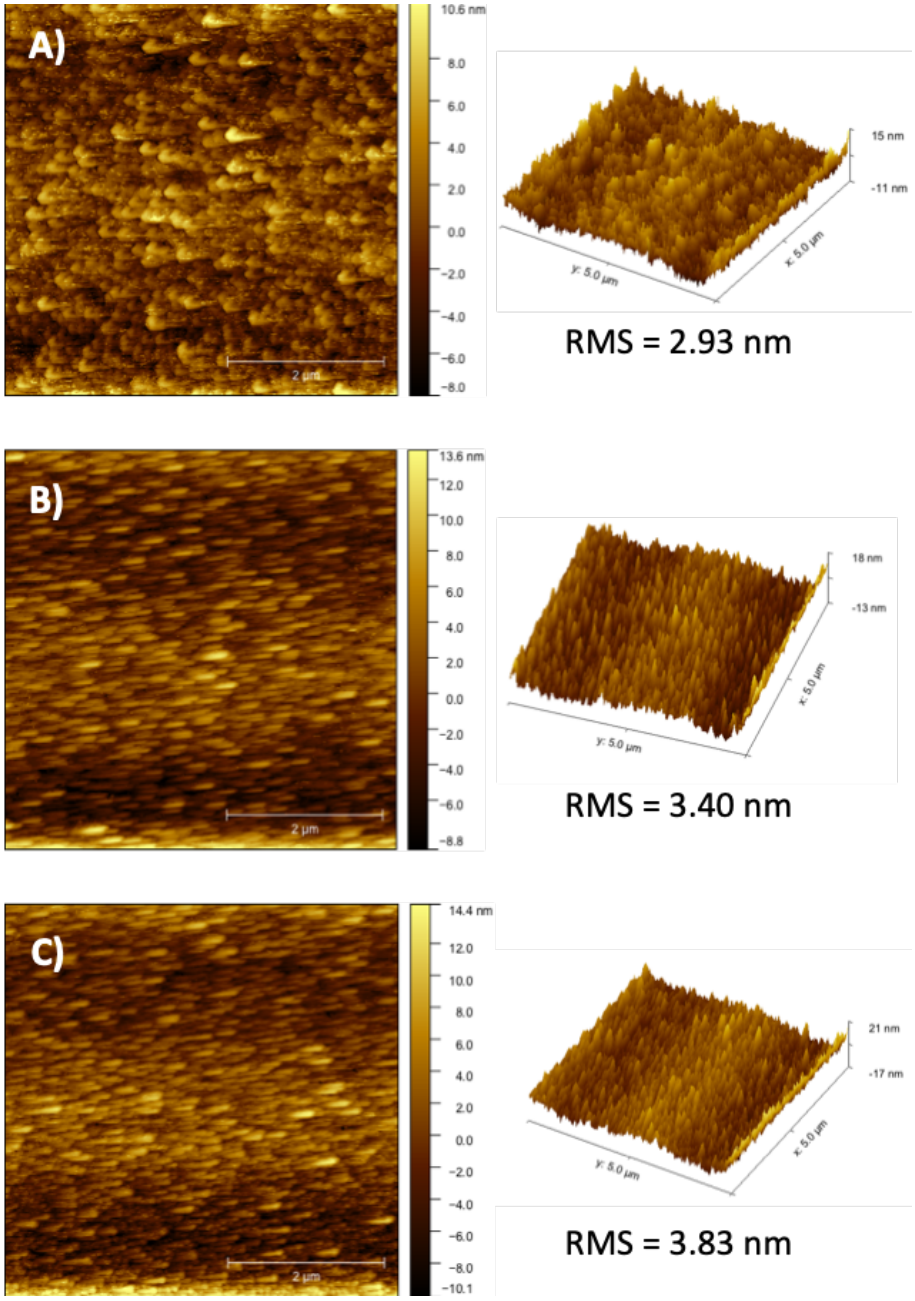

Figure 3.21: AFM images of tungsten oxide samples A-C

The optimisation of the oxidation temperature was performed using samples E – J. The data in Table 3.4 summarises the fabrication conditions, including the oxidation temperature for each sample. The subsequent Raman spectra are shown in Figure 3.22. Note, the Raman spectrum of sample F which was oxidised at 400 °C

has been omitted from the data set. The quality of the sample surface was not of a standard suitable to acquire Raman data, due to scratching and dust contamination. A new sample F, using the same batch of oxidised Si substrate, was fabricated prior to AFM imaging, however, it was not analysed by Raman spectroscopy because the sputter deposition was not performed in the same run as the other samples.

Sample	Temperature (°C)	Time (minutes)
E	300	10
F	400	10
G	500	10
H	600	10
I	700	10
J	800	10

Table 3.4: Oxidation temperature and time of seven deposited tungsten films

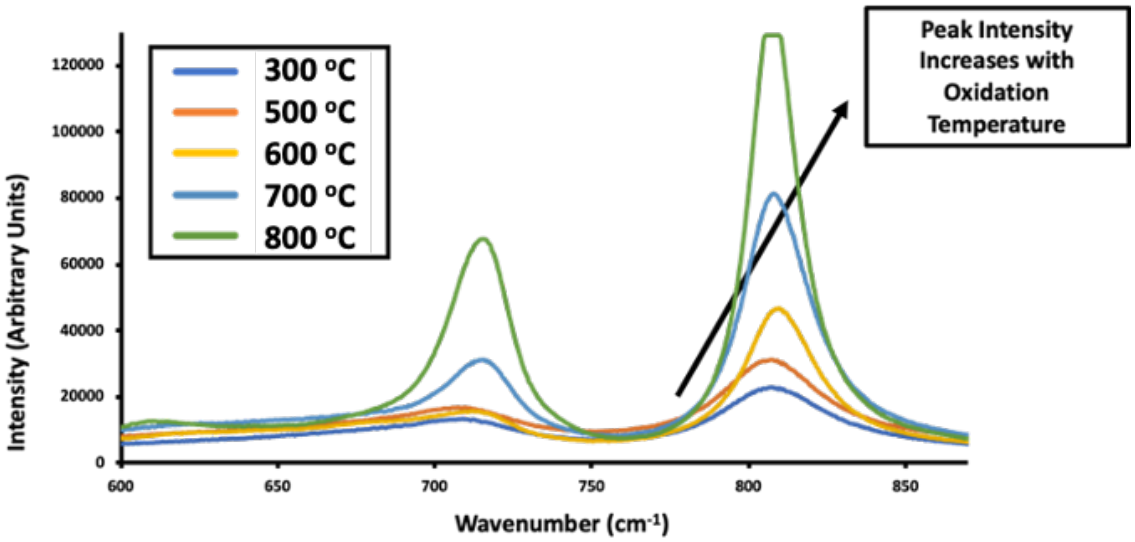

Figure 3.22: Raman spectrum of tungsten samples E-J oxidised for 10 minutes at varying temperatures

The Raman spectra show an increase in the intensity of both peaks that are used to describe the formation to WO_3 with increasing oxidation temperature. This trend is similar to the one observed for oxidation time, where a more intense peak is observed for samples oxidised for longer exposure times. The spectra for the 700 and 800 °C samples show a significant enhancement in the intensity of the peaks in comparison to those samples oxidised at lower temperatures. This suggests

that the tungsten oxide layer that is formed during the high temperature oxidation process is thicker or a more stoichiometric film is realised. The thickness of the WO_3 can be examined by considering surface roughness and amplitude data from AFM images. The data in Figure 3.23 show the RMS roughness of the oxidised samples as a function of oxidation temperature. Increasing the temperature from 300 °C to 500°C there is a linear trend, where the surface roughness of the sample increases with oxidation temperature. The RMS values increase from 1.03 nm to 3.65 nm for samples E – G. However, oxidation at 600 °C causes a major increase to 14 nm in the RMS surface roughness. This significant increase suggests that the extra thermal energy is having an effect on the tungsten oxide growth mechanism, resulting in an alternative surface morphology or the WO_3 film is starting to show evidence of crystalline rather than amorphous characteristics. Imaging of the sample surface was carried out to examine this further. Figure 3.24 shows the AFM images for samples G and H which were oxidised at 500 and 600 °C respectively.

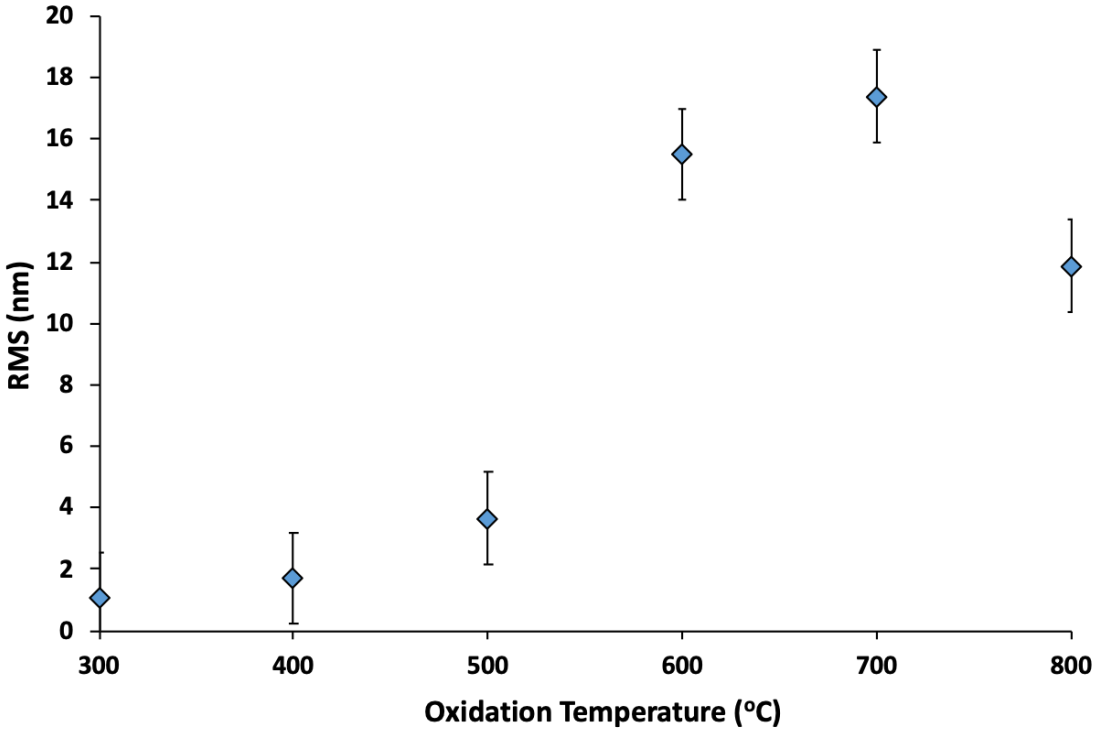

Figure 3.23: Plot of RMS of tungsten oxide samples as a function of oxidation temperature

It can be seen from the figure, that sample G has a relatively uniform surface, with a maximum surface amplitude of 9.3 nm. However, sample H shows evidence of the agglomeration of tungsten oxide particles to form clusters with a maximum height of 54 nm. These clusters are expected to be micro crystalline in nature, based

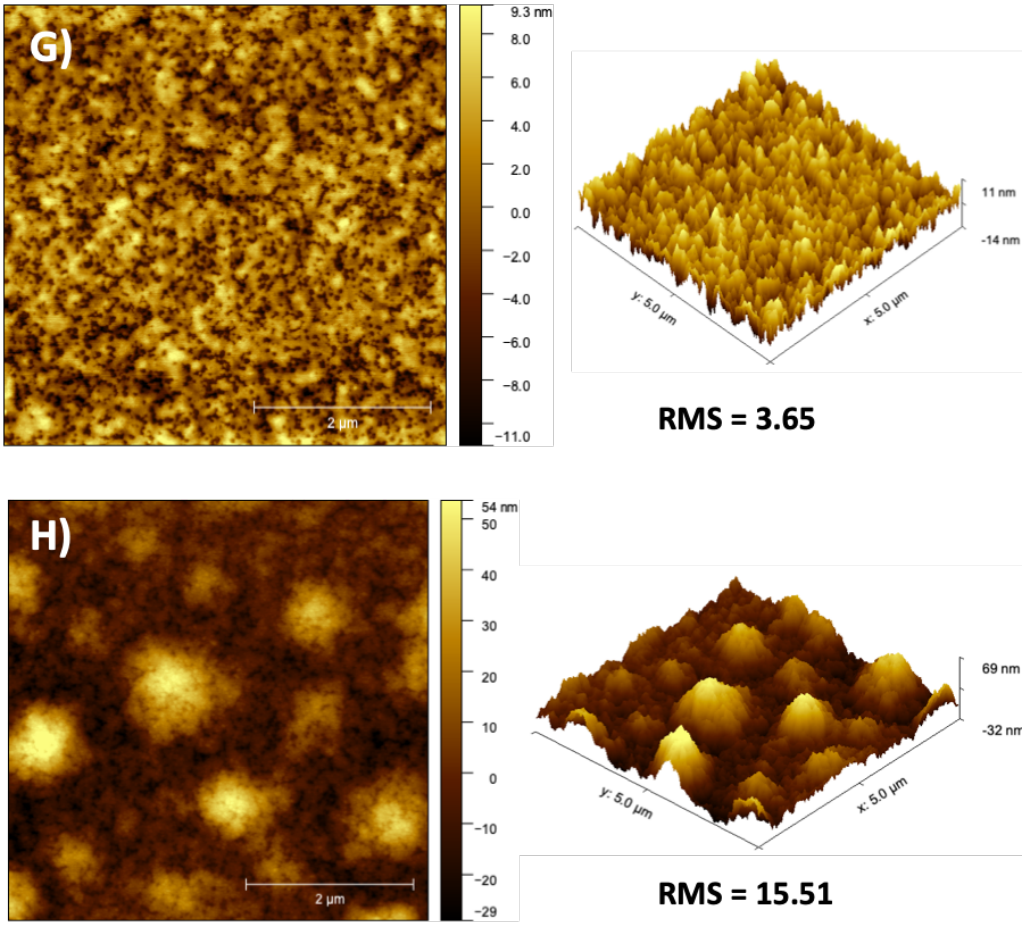

Figure 3.24: AFM images and RMS values of samples G and H

on the enhanced Raman signature for the 600 °C sample, in comparison to those oxidised at lower temperatures. Whilst this enhancement is lower than observed for the 700 and 800 °C oxidation, the 600 °C oxidation shows evidence of the phase change to crystalline material. It is clear from the AFM data that a completely different growth mechanism and surface morphology can be observed from samples oxidised above 600 °C. The same surface morphology is observed for sample I grown at 700 °C, which has a maximum amplitude of 84 nm and an RMS roughness of 17.39 nm. These surface clusters begin to dissipate at 800 °C, forming a more uniform surface with a lower RMS value of 11.86 nm. This data suggests that 500 °C is a suitable oxidation temperature to form a stable, uniform amorphous layer of WO_3. Choosing this temperature, which is similar to the temperature used to oxidise hafnium, titanium, and zirconium, will facilitate the integration of multiple dielectrics to result in array structures, capable of discriminating between different gas species in a mixture.

3.6.2 Incorporation of WO_3 into MOS Capacitors

For use as in sensing in the harsh environment of a diesel engine, the incorporation of high temperature stable SiC as the semiconductor substrate on which to form the capacitor based sensor is essential. Metal oxide semiconductor capacitors, incorporating WO_3 as the dielectric layer were optimised to understand the influence of the process flow for a full sensor on the characteristics of the WO_3 dielectric film. Standard cleaning and SiO_2 growth processes were carried out as described in section 3.3 resulting in a SiO_2 film with a thickness of 25 nm on the silicon face. An ohmic contact was formed on the C-face of SiC using a conventional Ti/Ni metallisation and 1100 °C anneal in a vacuum. A tungsten oxide dielectric was then fabricated on the SiO_2 film and the effect of the oxidation temperature studied. Tungsten oxidation was performed at 500, 600, and 700 °C for ten minutes in normal laboratory air. These temperatures were chosen, taking into consideration the AFM images and RMS data in Figures 3.23 and 3.24, as they provide a range of WO_3 morphologies. The electronic characteristics of these devices were then compared in order to verify the optimum oxidation temperature identified in section 3.6.1. A schematic cross-section a completed $Pt/WO_3/SiO_2/4H\text{-}SiC$ device is shown in Figure 3.25.

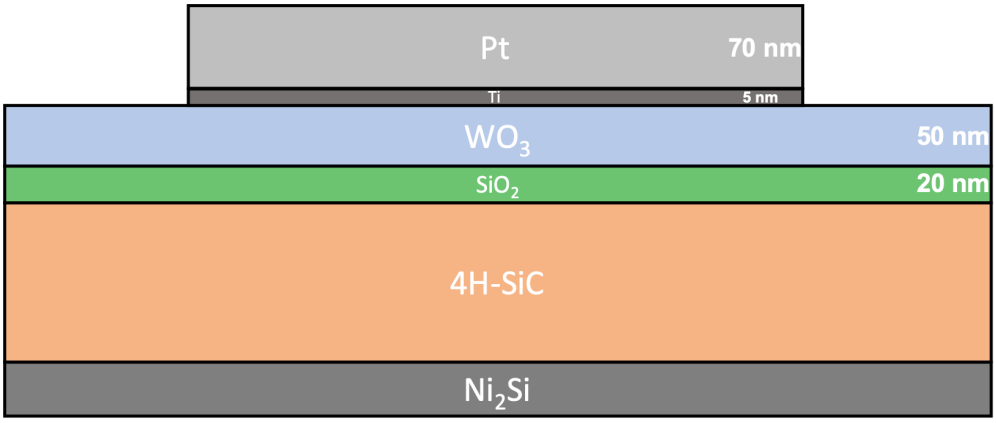

Figure 3.25: Schematic representation of $Pt/WO_3/SiO_2/4H\text{-}SiC$ device

The data shown in Figure 3.26 show the variation in the maximum capacitance, C_{max}, conductance at the flatband voltage, G_{max}, the density of interface traps, D_{IT}, extracted from the 1 MHz C–V data using the Terman method at E_c–E = 0.2 eV.

The data show that there is little change in G_{max} and C_{max}, which after correction is equal to C_{ox}, with oxidation temperature. The most notable information that can be deduced is the relationship between oxidation temperature and the density of interface traps. A linear relationship is observable between oxidation temperature and D_{IT}, with more traps present at higher temperatures.

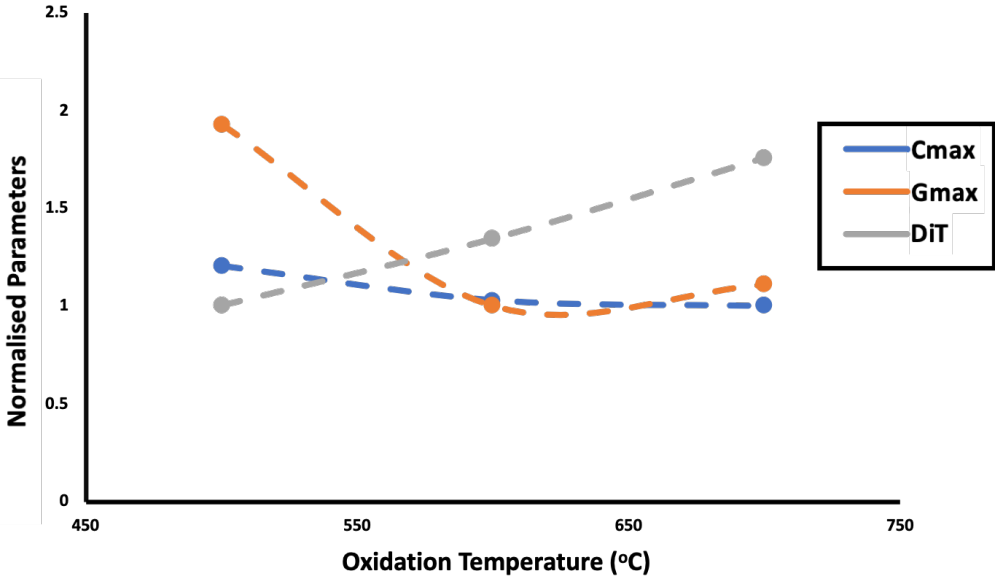

Figure 3.26: Comparison of capacitor electronic characteristics at varying oxidation temperatures for a Pt/WO_3/SiO_2/4H-SiC MOS capacitor

3.7 Conclusion

It has been demonstrated that changing the argon pressure within the sputtering chamber can control the levels of porosity incorporated into platinum films. A linear relationship between argon pressure and percentage porosity was observed when sputtering 70nm platinum layers. The optimum argon pressure which produced a platinum film with 75.4% porosity was 140 mTorr.

Zirconium oxide was incorporated as the oxide layer in MOS capacitor devices. This work was carried out to build upon established devices that use HfO_2 and TiO_2 as the high-κ dielectric layer.

A study into the growth of tungsten oxide films was performed to identify the optimum tungsten oxidation conditions. Raman spectroscopy confirmed that heating tungsten films at 500 °C in air produced WO_3. A comparison between peak intensity and surface roughness extracted from AFM images suggested that 10 minutes was sufficient time to achieve full oxidation.

Mechanistic information about the growth of WO_3 was found from oxidising six films over a temperature range of 300 - 900°C. The intensity of the Raman peaks at 720 and 820 cm^{-1} increased with oxidation temperature suggesting a thicker layer of tungsten oxide is formed. This is supported by the linear trend seen between surface roughness and oxidation temperature. AFM analysis of the oxidised films show a change in morphology when the oxidation temperature is in excess of 500 °C. Prior to this, uniform films were grown with a maximum RMS value of 3.65 nm, but at 600 °C, clusters begin to form on the surface, increasing surface roughness

and amplitude.

Devices were fabricated from tungsten films oxidised at 500, 600 and 700 °C, and critical parameters were extracted. Values of C_{max} and G_{max} were stable independent of oxidation conditions. However, it was observed that the density of interface traps increased linearly with oxidation temperature. This can be related to the morphology of the grown films, as less uniform films, formed under harsh oxidation conditions, contain a greater number of traps.

This work suggests that the optimum oxidation temperature of tungsten is 500 °C, as a uniform film is formed with minimal traps, so this methodology will be taken forward.

Bibliography

[1] Ingemar Lundstrom et al. “Twenty-five years of field effect gas sensor research in Linkoping”. In: *Sensors and Actuators B: Chemical* 121 (1 2007), pp. 247–262.

[2] George F. Fine et al. “Metal Oxide Semi-Conductor Gas Sensors in Environmental Monitoring”. In: *Sensors* 10 (6 June 2010), pp. 5469–5502.

[3] Philip Peterson et al. “Practical Use of Metal Oxide Semiconductor Gas Sensors for Measuring Nitrogen Dioxide and Ozone in Urban Environments”. In: *Sensors* 17 (7 2017), p. 1653.

[4] S K Roy et al. “SiC gas sensor arrays for extreme environments”. In: 2013, pp. 1–4.

[5] A. Spetz, M. Armgarth, and I. Lundstrom. “Optimization of ammonia-sensitive metal-oxide-semiconductor structures with platinum gates”. In: *Sensors and Actuators* 11 (4 May 1987). Porous gate ammonium sensitivity, pp. 349–365.

[6] I Lundstrom et al. “A hydrogen sensitive MOS field effect transistor”. In: *Applied Physics Letters* 26 (2 1975), pp. 55–57.

[7] K. I. Lundstrom, M. S. Shivaraman, and C. M. Svensson. “A hydrogen-sensitive Pd-gate MOS transistor”. In: *Journal of Applied Physics* 46 (9 Sept. 1975), pp. 3876–3881.

[8] T. Ishikawa and R.B. McLellan. “The diffusivity of hydrogen in the noble metals at low temperature”. In: *Acta Metallurgica* 33 (11 Nov. 1985), pp. 1979–1985.

[9] H. Katsuta, R.J. Farraro, and R.B. McLellan. “The diffusivity of Hydrogen in palladium”. In: *Acta Metallurgica* 27 (7 July 1979), pp. 1111–1114.

[10] Hisashi Fukuda et al. “Highly Sensitive MOSFET Gas Sensors with Porous Platinum Gate Electrode”. In: *Japanese Journal of Applied Physics* 37 (Part 1, No. 3B Mar. 1998), pp. 1100–1102.

[11] Toshihiro Yoshizumi and Yuji Miyahara. “Field-Effect Transistors for Gas Sensing”. In: InTech, June 2017. DOI: =.

[12] A. Brewer et al. “Uniform sputter deposition of high-quality epitaxial complex oxide thin films”. In: *Journal of Vacuum Science Technology A: Vacuum, Surfaces, and Films* 35 (6 Nov. 2017), p. 060607.

[13] Prachi Jhanwar et al. “Effect of sputtering power on the growth of Ru films deposited by magnetron sputtering”. In: vol. 1724. 2016, p. 020073.

[14] Kah-Yoong Chan and Bee-San Teo. “Sputtering power and deposition pressure effects on the electrical and structural properties of copper thin films”. In: *Journal of Materials Science* 40 (22 Nov. 2005), pp. 5971–5981.

[15] G P Zhigal’Skii and Brian K Jones. *The physical properties of thin metal films*. CRC Press, 2003.

[16] Ikwhang Chang et al. “Characterization of porous Pt films deposited via sputtering”. In: *Applied Surface Science* 282 (2013), pp. 463–466.

[17] K. Van Dijk et al. “Influence of Ar pressure on r.f. magnetron-sputtered Ca5(PO4)3OH layers”. In: *Surface and Coatings Technology* 76-77 (Nov. 1995), pp. 206–210.

[18] Werner Kern. “The Evolution of Silicon Wafer Cleaning Technology”. In: *Journal of The Electrochemical Society* 137 (6 June 1990), p. 1887.

[19] *Fiji: An open-source platform for biological-image analysis*. July 2012.

[20] Benjamin John Dylan Furnival. “Silicon carbide based gas sensor arrays for deployment within hostile environments”. PhD thesis. University of Newcastle Upon Tyne, 2012.

[21] S.M and K.K Sze NG. “Metal-Insulator-Semiconductor Capacitors”. In: John Wiley Sons, Ltd, 2006, pp. 197–240. ISBN: 9780470068328. DOI: https://doi.org/10.1002/9780470068328.ch4.

[22] Dieter K. Schroder. *Semiconductor Material and Device Characterization: Third Edition*. IEEE Press, 2005.

[23] Rejaiba Omar, Ben Amar Mohamed, and Matoussi Adel. “Effects of series and parallel resistances on the C-V characteristics of silicon-based metal oxide semiconductor (MOS) devices”. In: *European Physical Journal Plus* 130 (4 Apr. 2015), p. 80.

[24] K. Iniewski et al. “Series resistance in a MOS capacitor with a thin gate oxide”. In: *Solid State Electronics* 32 (2 Feb. 1989), pp. 137–140.

[25] W.A. Hill and C.C. Coleman. “A single-frequency approximation for interface-state density determination”. In: *Solid-State Electronics* 23 (9 Sept. 1980), pp. 987–993.

[26] Lewis M Terman. “An investigation of surface states at a silicon/silicon oxide interface employing metal-oxide-silicon diodes”. In: *Solid-State Electronics* 5 (5 1962), pp. 285–299.

[27] W.M. Tang, C.H. Leung, and P.T. Lai. “Improved sensing characteristics of MISiC Schottky-diode hydrogen sensor by using HfO2 as gate insulator”. In: *Microelectronics Reliability* 48 (11-12 Nov. 2008), pp. 1780–1785.

[28] R. Mahapatra et al. “Energy-band alignment of HfO2SiO2SiC gate dielectric stack”. In: *Applied Physics Letters* 92 (4 Jan. 2008). Low band offset information, p. 042904.

[29] Irmak Karaduman and Selim Acar. “The gas sensing properties of hafnium oxide thin films depending on the annealing environment”. In: *Modern Physics Letters B* 31 (30 Oct. 2017), p. 1750284.

[30] Huey-Ing Chen et al. “Hydrogen sensing performance of a Pd/HfO2/GaN metal-oxide-semiconductor (MOS) Schottky diode”. In: *Sensors and Actuators B: Chemical* 262 (June 2018), pp. 852–859.

[31] S. Kandasamy et al. “Study of Pt/TiO2/SiC schottky diode based gas sensor”. In: vol. 2. IEEE, 2004, pp. 738–741.

[32] K Franklin Albertin, M A Valle, and I Pereyra. “Study of MOS capacitors with TiO2 and SiO2/TiO2 gate dielectric”. In: vol. 2. 2007, pp. 89–93.

[33] Adrian Trinchi, Sasikaran Kandasamy, and Wojtek Wlodarski. “High temperature field effect hydrogen and hydrocarbon gas sensors based on SiC MOS devices”. In: *Sensors and Actuators B: Chemical* 133 (2 Aug. 2008), pp. 705–716.

[34] Ming Hung Weng et al. “Role of oxygen in high temperature hydrogen sulfide detection using MISiC sensors”. In: *Measurement Science and Technology* 19 (2 2008), p. 24002.

[35] Bing Miao et al. “Radiation Induced Change in Defect Density in HfO2-Based MIM Capacitors”. In: *IEEE Transactions on Nuclear Science* 56 (5 Oct. 2009), pp. 2916–2924.

[36] Pankaj Kumar, Prashant Sarswat, and Michael Free. “Hybridized Tungsten Oxide Nanostructures for Food Quality Assessment: Fabrication and Performance Evaluation”. In: *Scientific Reports* 8 (June 2018). DOI: 10.1038/s41598-018-21605-5.

[37] Chandra Shekhar Prajapati and Navakanta Bhat. “ppb level detection of NO2 using a WO3 thin film-based sensor: material optimization, device fabrication and packaging”. In: *RSC Advances* 8 (12 Feb. 2018), pp. 6590–6599.

[38] M Penza et al. “Tungsten trioxide (WO3) sputtered thin films for a NOx gas sensor”. In: *Sensors and Actuators B: Chemical* 50 (1 July 1998). Good graph for WO3 NOx sensitivity, pp. 9–18.

[39] M Boulova, A Gaskov, and G Lucazeau. “Tungsten oxide reactivity versus CH4, CO and NO2 molecules studied by Raman spectroscopy”. In: *Sensors and Actuators B: Chemical* 81 (1 2001), pp. 99–106.

[40] M.F. Daniel et al. “Infrared and Raman study of WO3 tungsten trioxides and WO3, xH2O tungsten trioxide tydrates”. In: *Journal of Solid State Chemistry* 67 (2 Apr. 1987), pp. 235–247.

[41] J. Gabrusenoks et al. “Infrared and Raman spectroscopy of WO3 and CdWO4”. In: *Electrochimica Acta* 46 (13-14 Apr. 2001), pp. 2229–2231.

[42] Felicia S Manciu et al. “Spectroscopic analysis of tungsten oxide thin films”. In: *Journal of Materials Research* 25 (12 2010), pp. 2401–2406.

[43] Min Baik et al. “Electrical properties and thermal stability in stack structure of HfO2/Al2O3/InSb by atomic layer deposition”. In: *Scientific Reports* 7 (1 2017).

[44] Y. Lu et al. “Leakage current effects on C-V plots of high- k metal-oxide-semiconductor capacitors”. In: *Journal of Vacuum Science and Technology B: Microelectronics and Nanometer Structures* 27 (1 2009), pp. 352–355.

Chapter 4

The Use of MOS Capacitors as Solvent Sensors

The gas sensing abilities of metal-oxide-semiconductor devices at extreme temperatures have been demonstrated previously, however, little work has been performed to identify their use for solvent detection. Examples of SiC devices used in room temperature applications are minimal, with cheaper silicon based structures usually preferred. A MOS capacitor was fabricated, using platinum as the catalytic gate metal, titanium oxide, and silicon dioxide as the dielectric stack, and 4H-SiC as the substrate. This is a standard structure, with established electronic characteristics, and this chapter demonstrates the use of this device as a room temperature solvent vapour sensor. The novelty of this work arises from the use of high temperature stable SiC. This feature allows the device to be heated to temperatures up to 400°C which can burn off any unwanted poisons adhered to the gate metal surface, effectively resetting the sensor and prolonging its lifetime.

Whilst solvent sensing is a novel and exciting use for SiC based MOS capacitors, the impact of this work can aid the development of these sensors as pollutant gas monitors as it can provide information on how analytes interact with devices. The exact gaseous detection mechanism of these devices is unknown, with a number of different models, based around the formation of a dipole layer, and changes to the metal-semiconductor work function being suggested [1, 2]. Exposing these devices to a different type of analyte and observing the behaviour may provide more information to understand the sensing mechanism. Accepted sensing models rely on the adsorption of analytes to the sensor surface, and the subsequent diffusion through the film, or direct adsorption of charges to exposed areas of oxide; however there is ambiguity about how these charges interact with the oxide-semiconductor interface. The formation of a charged dipole layer at this boundary is one suggestion, another involves the interaction of these charges with oxide defects, but the exact interaction is unknown.

Materials with enhanced catalytic properties and a large number of fermi level states, such as palladium, platinum, or rhodium, are used as the gate metal in MOS capacitor sensors to encourage analyte adsorption [3]. The morphology of this metal layer can be altered depending on the target analyte; a continuous film is suitable for hydrogen sensing, as the diatomic molecule dissociates into its constituent atoms, adsorbs onto the surface, and as a result of its small atomic radius, can diffuse through the metal layer to form a dipole. These diffused species form a dipole layer at the metal-semiconductor interface [4, 5]. For larger molecules such as ammonia or NOx, a porous gate metal is appropriate, as this exposes areas of the underlying oxide to allow direct adsorption and formation of a charge layer. A schematic of this is shown in Figure 4.1.

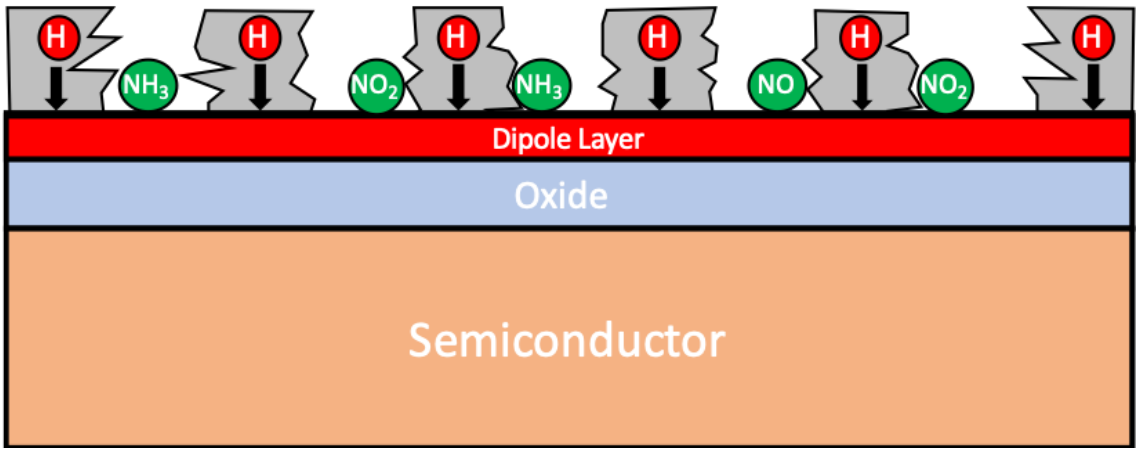

Figure 4.1: Interaction between gaseous analytes and a MOS capacitor with a discontinuous gate metal

The accepted models from the literature indicate that it is the influence of this charged dipole layer which alters the behaviour of the device. The formation of a positive charge layer formed by hydrogen atoms alters the metal work function, lowering the flatband voltage of the device, and subsequently shifting the position of the CV curve towards more negative voltages. Another model is that adsorbed charges diffuse into the oxide layer and passivate trapping states within the bulk of the dielectric or at the oxide-semiconductor interface; adding additional charge to the capacitor, causing a shift of characteristics to higher applied bias [6]. The behaviour of these devices in the presence of alternative, solvent, analytes, may be used to ascertain more information about the device-analyte interaction; and allow the determination of a dominant response mechanism.

Polar solvent molecules have a large dipole moment as a result of the difference in electronegativity of their constituent atoms. Electronegativity, measured on the Pauling scale, is defined as the ability of an atom to attract electron density towards itself within a covalent bond [7, 8]. Fluorine is the most electronegative atom with

a value measuring 4.00 on the Pauling scale. Oxygen and Nitrogen are also very electronegative with values of 3.44 and 3.04 respectively. It is these three atoms that are capable of forming hydrogen bonds when attached to a labile hydrogen within a molecule. The difference in electronegativity of hydrogen (2.2) and a N, O or F atom induces a dipole moment leaving the hydrogen atom with a partial positive charge, capable of electrostatically bonding to a different atom of N, O, or F with a partial negative charge or an atom which possesses a lone pair of electrons.

Non-polar solvents have bonds between atoms with similar values on the Pauling scale, resulting in an even charge distribution within the covalent bond. Solvents in which a hydrogen atom is bonded to a nitrogen or oxygen are knows as protic and are capable of hydrogen bonding and solvents with a lack of this bond are known as aprotic. It has been demonstrated in the past that this property has an influence on the nature of response observed when using epitaxial graphene sensors to detect solvent vapours [9]. The data in Figure 4.2 show the relative resistance response of a graphene based sensor to different vapours as a function of time and it can be seen that a contrasting response occurs for polar protic and polar aprotic solvents. The polar protic ethylene glycol (EG) results in an increase in electrical resistance and conversely, the polar aprotic n-methyl-2-pyrollidone (NMP) and dimethylacetamide (DMAC) caused a decrease in resistance.

The detection and monitoring of solvents within an industrial environment is essential for the maintenance of air quality in order to adhere to health and safety standards, such as EH40/2005 [10]. Table 4.1 shows the long and short-term exposure limits of some common organic solvents. For all chemicals, there are specific short and long term exposure limits and efforts must be taken to ensure that these values are not exceeded. Short term exposure is over a duration of 15 minutes, and long term exposure is 8 hours. Exposure limits vary depending on the solvent, IPA has a short term exposure limit of 500 ppm, however, acetic anhydride is more harmful and has a maximum short term exposure limit of only 2 ppm. Liberal usage of polar solvents is common within an industrial environment, and many of these chemicals can be toxic to humans therefore it is important to monitor and minimise inhalation of vapours. Therefore, a reliable sensor system is required which is capable of monitoring any changes to the concentration of solvent vapours within the ambient.

4.1 Device Fabrication

For this work, a Pt/TiO_2/SiO_2/4H-SiC MOS capacitor was fabricated. 4H-SiC with a 2μm Si face epitaxial layer (N_D=1x10^{17} cm^{-3}) was cleaned using RCA and Piranha procedures, then a 20nm SiO_2 layer was grown at 1150 °C in a dry oxidation process.

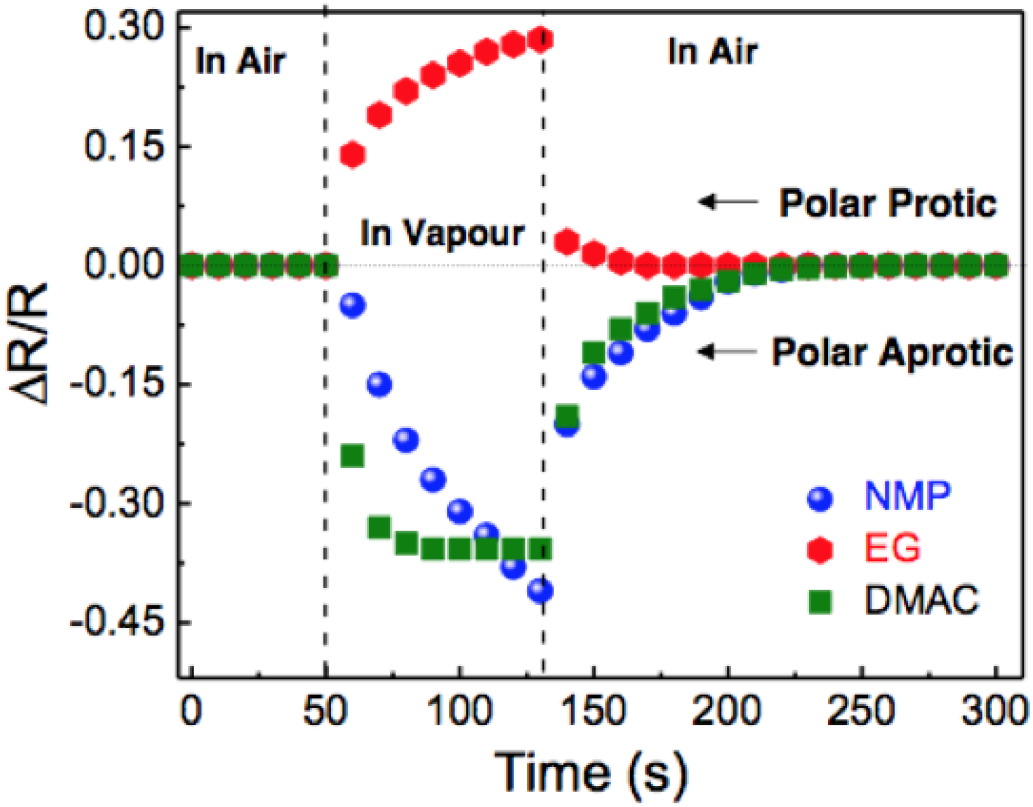

Figure 4.2: Sensing behaviour of a graphene based sensor to EG, NMP and DMAC [9]

Solvent	Long Term Exposure (ppm)	Short Term Exposure (ppm))
Isopropyl Alcohol (IPA)	400	500
Water	N/A	N/A
Ethylene Glycol (EG)	20	40
Acetic Anhydride (AA)	0.5	2
DiMethyl Formamide (DMF)	5	10
N-Methyl-2-Pyrollidone (NMP)	10	20

Table 4.1: Exposure limits of common organic solvents [10]

An Ohmic C-face contact comprising a 5 nm Ti/100 nm Ni metal stack was deposited by e-Beam evaporation and annealed by rapid thermal processing at 1040°C. 50 nm of high-κ TiO_2 dielectric was then formed by e-beam evaporation of titanium metal directly onto SiO_2, followed by annealing in an oxygen environment at 550°C for 10 minutes. Photolithographic patterning of the dielectric layer was performed before deposition of a 70 nm platinum catalytic gate metal. A lift off process was carried out in warm DMF order to realise the individual capacitor structures. The device schematic is shown in Figure 4.3 as an optical micrograph, 3D representation, and

as a cross-section.

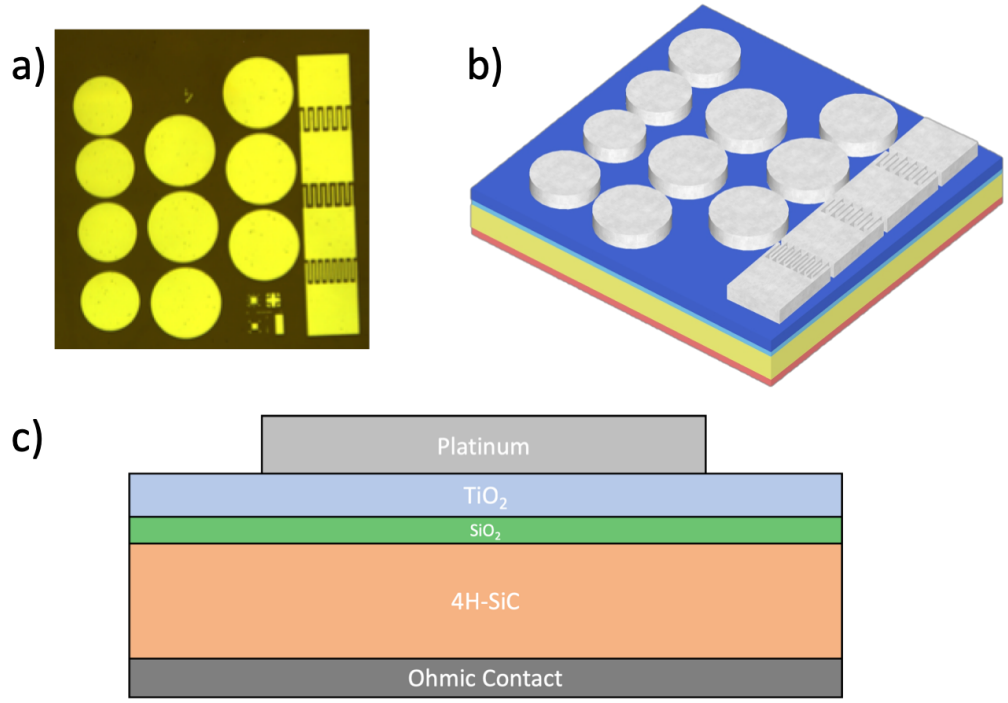

Figure 4.3: Schematic of the $Pt/TiO_2/SiO_2/4H\text{-}SiC$ device as a) optical micrograph, b) 3D representation and c) cross-section

4.2 Device Characterisation

The C-V and G-V profiles of the device were evaluated using an Agilent 4284 LCR meter at a frequency of 100 kHz. A voltage sweep of -5V to 5V was performed displaying a curve with identifiable depletion and accumulation regions with an observable flatband voltage. The test setup was enclosed in a sealed chamber to reduce measurement noise. Before the sensor was exposed to solvent vapours, a baseline sweep was performed which showed the behaviour of the capacitor in the ambient environment of laboratory air at room temperature (Figure 4.4). This is an important step as this data allows determination of the flatband voltage and therefore the sensor response in the presence of an analyte. The response is defined as the percentage change in capacitance relative to the baseline as a result of changes to the ambient environment as shown by Equation 4.1. Where $C_{Baseline}$ is the capacitance measured at flatband voltage in laboratory air and $C_{Measured}$ is the capacitance measured at flatband voltage during exposure to the solvent under test.

$$Response(\%) = \frac{C_{Measured} - C_{Baseline}}{C_{Baseline}} \times 100 \tag{4.1}$$

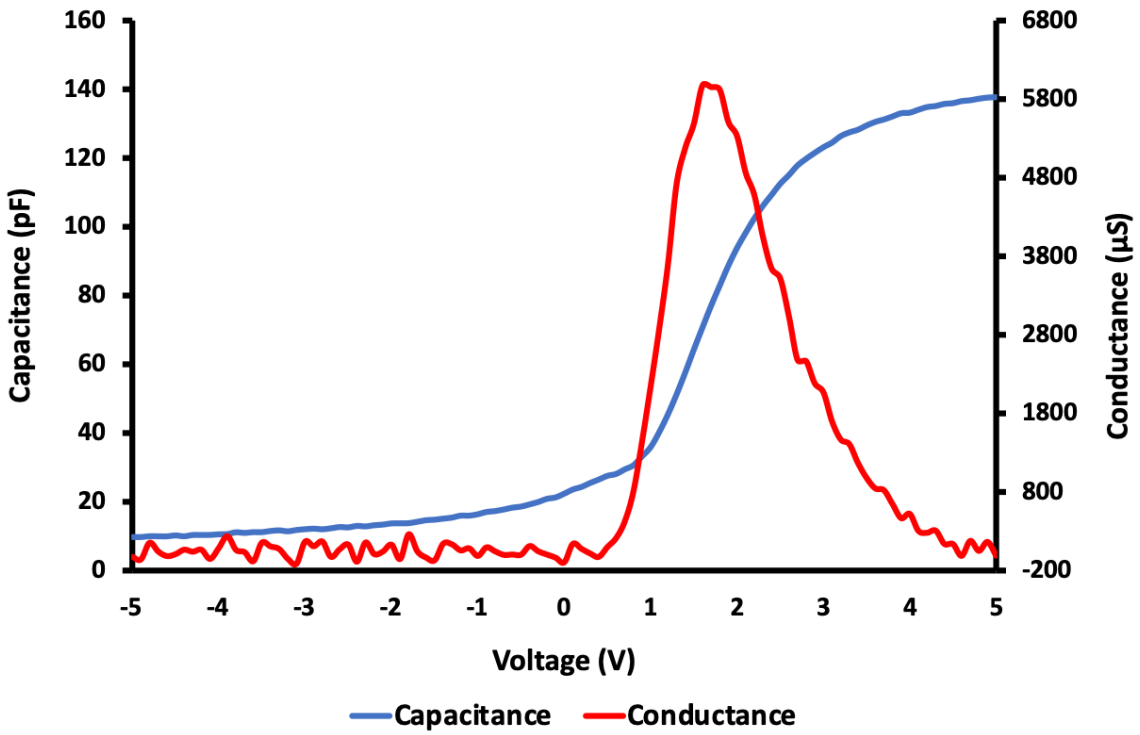

Figure 4.4: C-V (Blue) and G-V (Red) baseline characteristics extracted from a $Pt/TiO_2/Si_2/SiC$ sensor in room temperature laboratory air

It can be seen from the data that the flatband voltage of the device is at 1.8V giving rise to a flatband capacitance of 82.8 pF. The sensor response arises from monitoring changes to the flatband capacitance of the sensor under the influence of different solvents.

4.3 Solvent Testing

For the sensing experiments, the $Pt/TiO_2/SiO_2/SiC$ device was exposed to solvent vapours in an enclosed environment at room temperature: isopropyl alcohol (IPA), water (H_2O), ethylene glycol (EG), acetic anhydride (AA), dimethyl formamide (DMF) and n-methyl-2-pyrollidone (NMP). The chemical structure and relevant properties of these solvents are outline in Table 4.2.

Solvent	Polarity	Dipole Moment (D)	Relative Permittivity	Structure
Isopropyl Alcohol	Polar Protic	1.7	18.2	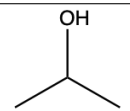
Water	Polar Protic	1.9	80	
Ethylene Glycol	Polar Protic	2.2	37	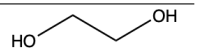
Acetic Anhydride	Polar Aprotic	2.8	21	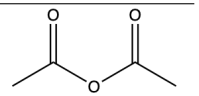
Dimethyl Formamide	Polar Aprotic	3.8	38.2	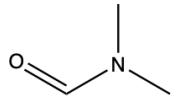
N-Methyl-2-Pyrollidone	Polar Aprotic	4.1	32	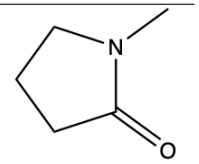

Table 4.2: Classification of polarity, dipole moment, relative permittivity, structures of the tested organic solvents [11]

NMP was used to identify the solvent saturation point of the sensor. C-V and G-V characteristics were taken from the device in normal laboratory air to establish the baseline, using the same method as outlined above. Then three drops of solvent was delivered to a region in close proximity to the sensor, via pipette, and the C-V and G-V characteristics were extracted again. Figure 4.5 shows the change in capacitance at the flatband voltage of the $Pt/TiO_2/SiO_2/4H\text{-}SiC$ device upon exposure to NMP (ΔC), calculated by Equation 4.2. Measurements were taken immediately upon solvent administration (this data is presented at 0 seconds), then at 180, 360, 540, 720, and 900 seconds and the data presented in Figure 4.5 outlines this change in capacitance over time.

$$\Delta C = C_{Measured} - C_{Baseline} \tag{4.2}$$

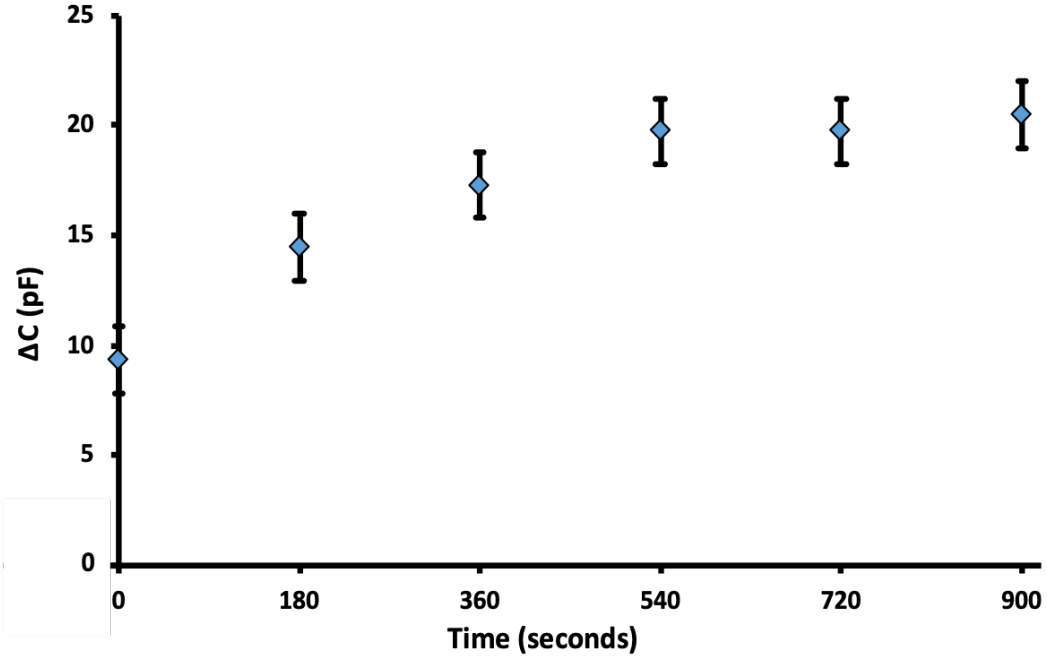

Figure 4.5: Change in $Pt/TiO_2/SiO_2/4H\text{-}SiC$ capacitance at V_{FB} over time in the presence of NMP solvent

It can be seen from the data in Figure 4.5 that a response occurs immediately upon analyte exposure (0 seconds), suggesting a rapid interaction between solvent molecules and the device. The magnitude of response increases over time until saturation is reached after 540 seconds. The data taken at 720 and 900 seconds show no variation from that at 540 seconds within experimental error. This implies that the solvent molecules have fully interacted with the catalytic metal of the sensor and induced a response. In this case, full interaction can be thought of as solvent molecules completely covering the surface of the metal and binding to all available

sites. This saturating behaviour is similar to that seen in gas sensing, as the catalytic gate metal has a finite number of sites available for gases to adsorb [12, 13]. This can be explained by the Langmuir isotherm, which assumes that the metal surface has a uniform array of identical adsorption sites that can only be populated by a single analyte layer. It is also assumed that the rate of adsorption to a particular site does not depend on the state of the neighbouring site [14, 15, 16]. As the saturation point of the metal has been identified as being at 540 seconds, future tests did not exceed this time.

C-V characteristics were measured in the presence of the other solvents. Once $C_{Baseline}$ was found, three drops of solvent were administered and characteristics were taken at 0, 180, 360, and 540 seconds. Figures 4.6 and 4.7 show the capacitance-voltage characteristics of the sensor during exposure to two representative solvents, IPA and NMP, for 540 seconds. The data shows that the solvents induce a voltage shift in the characteristics with respect to the baseline. The magnitude of this response is different depending on the solvent, with NMP causing a greater shift than IPA, but the fundamental shift in characteristics are similar.

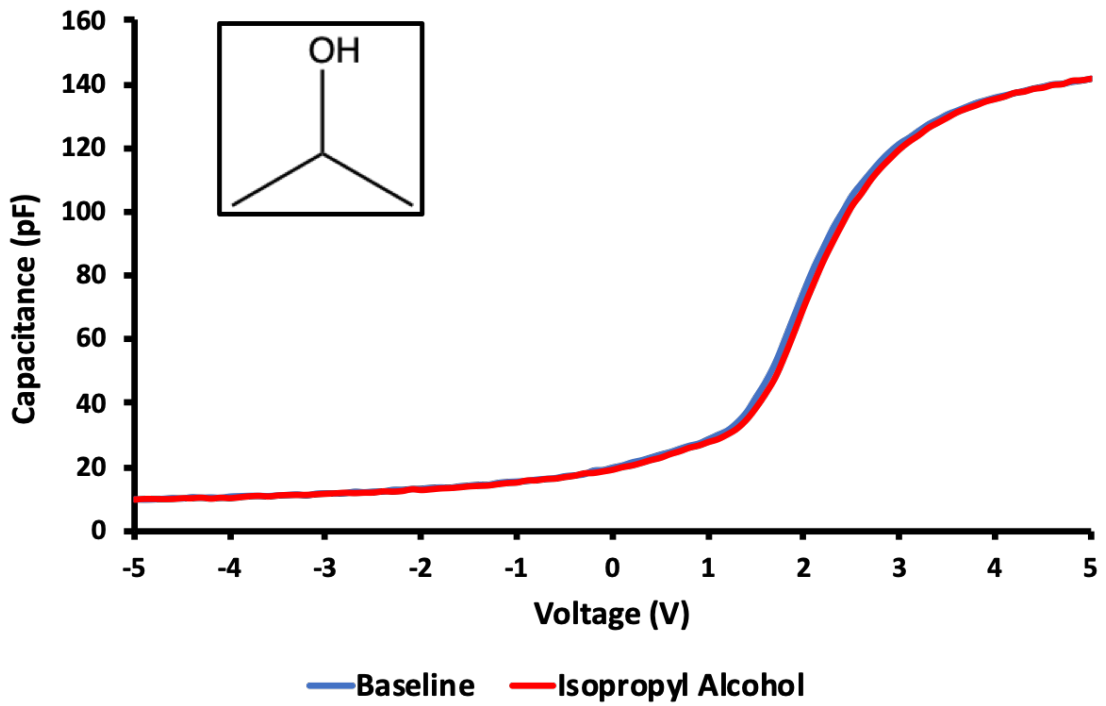

Figure 4.6: C-V characteristics extracted from a $Pt/TiO_2/SiO_2/4H\text{-}SiC$ sensor in the presence of laboratory air (Blue) and IPA solvent (Red)

The plot in Figure 4.8 displays the response of the $Pt/TiO_2/SiO_2/4H\text{-}SiC$ sensor after exposure to NMP and IPA for 180, 360 and 540 seconds.

Figure 4.8 shows that the maximum response (R_{Max}) of the device increases with exposure time for both solvents. The plot also shows that the deceive is more

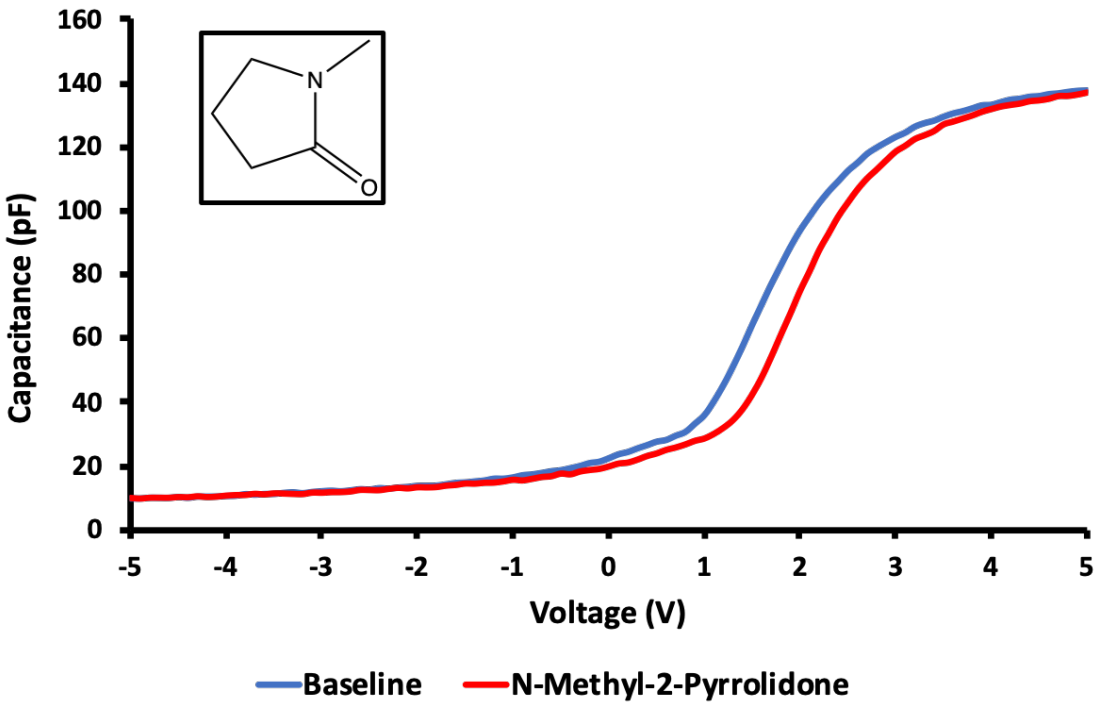

Figure 4.7: C-V characteristics extracted from a Pt/TiO_2/SiO_2/4H-SiC sensor in the presence of laboratory air (Blue) and NMP solvent (Red)

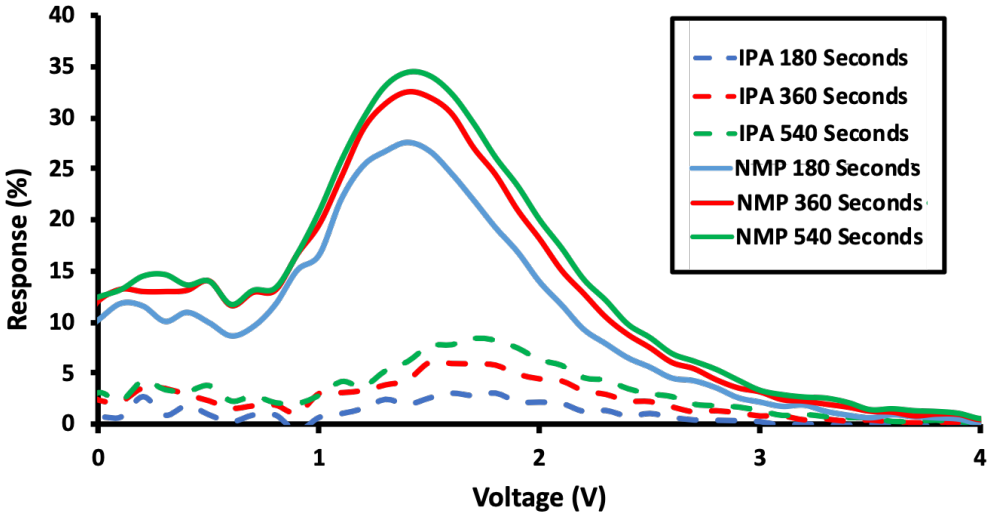

Figure 4.8: Response of the Pt/TiO_2/SiO_2/4H-SiC sensor after exposure to NMP and IPA for 180, 360 and 540 seconds

sensitive to NMP than IPA with an observed R_{Max} of 34.3% and 8.4% respectively. It can also be seen from the data that R_{Max} occurs at different voltage values depending on the solvent tested, 1.7V for IPA and 1.5V for NMP.

Relative to the baseline, all organic vapours induce a positive voltage shift, which is in contrast to the data for the graphene sensors reported above. When identical devices were deployed as high temperature gas sensors, hydrogen containing gases

produced a negative flatband voltage shift and oxygen containing gases produced a positive shift relative to the baseline [17]. The positive shift observed here suggests that the sensing mechanism is similar to that seen when detecting oxygen containing gases. The formation of a charged layer, or the passivation of trapping states is likely to be responsible for the analyte induced changes to the dielectric layer.

The response after exposure to all tested solvents for 540 seconds is shown by the data in Figure 4.9. It can be seen that the magnitude of the response varies with solvent identity, with no two solvents inducing the same level of response. This difference between the induced responses allows, from the data, the unique identification of singular unknown solvent vapours in normal air.

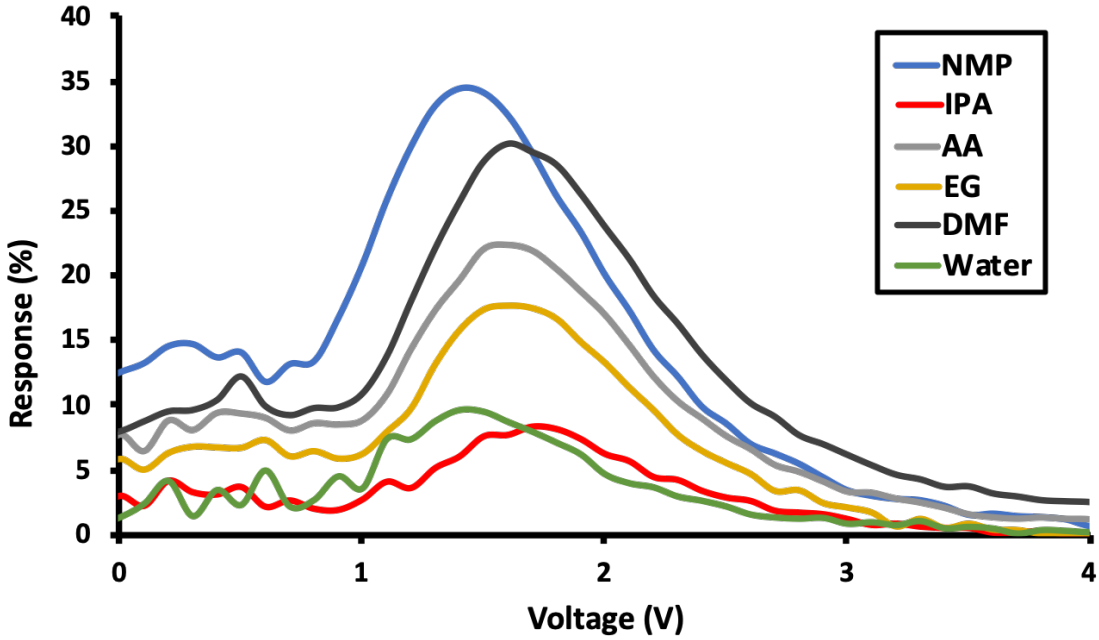

Figure 4.9: Response of the $Pt/TiO_2/SiO_2/4H\text{-}SiC$ sensor after exposure to all tested solvents for 540 seconds

An alternative interpretation of the response is to consider the change in capacitance when the device is biased at the flatband voltage (ΔC_{FB}). The data in table 4.3 show the values of ΔC_{FB} observed when the device was exposed to the different solvents. ΔV_{FB} acquired from the C-V sweep is also outlined.

When examining the data, it is important to find a trend in order to identify the mechanistic implications, as the fundamental properties of the solvent molecules are affecting the characteristics of the device. One hypothesis is that the solvent molecules are creating an additional effective area to the capacitor structure, resulting in increased capacitance, which is often observed when testing capacitors in humid environments. The capacitance can be found if the system is considered to be a parallel plate capacitor as described by Equation 4.3, where ϵ and d are the

Solvent	ΔC_{FB}	ΔV_{FB}
Isopropyl Alcohol	4.91	0.1
Water	5.80	0.1
Ethylene Glycol	10.83	0.2
Acetic Anhydride	14.58	0.2
DiMethyl Formamide	21.54	0.3
N-Methyl-2-Pyrollidone	21.59	0.3

Table 4.3: Change in capacitance at flatband voltage, and change in flatband voltage of a $Pt/TiO_2/SiO_2/4H\text{-}SiC$ sensor upon exposure to varying solvents

permittivity and thickness of the dielectric layer respectively, and A is the area of the capacitor.

$$Capacitance = \epsilon \frac{A}{d} \tag{4.3}$$

The data in Figure 4.10 show the sensor response as a function of the relative permittivity of the solvents, as summarised in Table 4.2 . No obvious correlation can be identified from the data, which suggests that this sensing mechanism is not responsible for the observed capacitance shift.

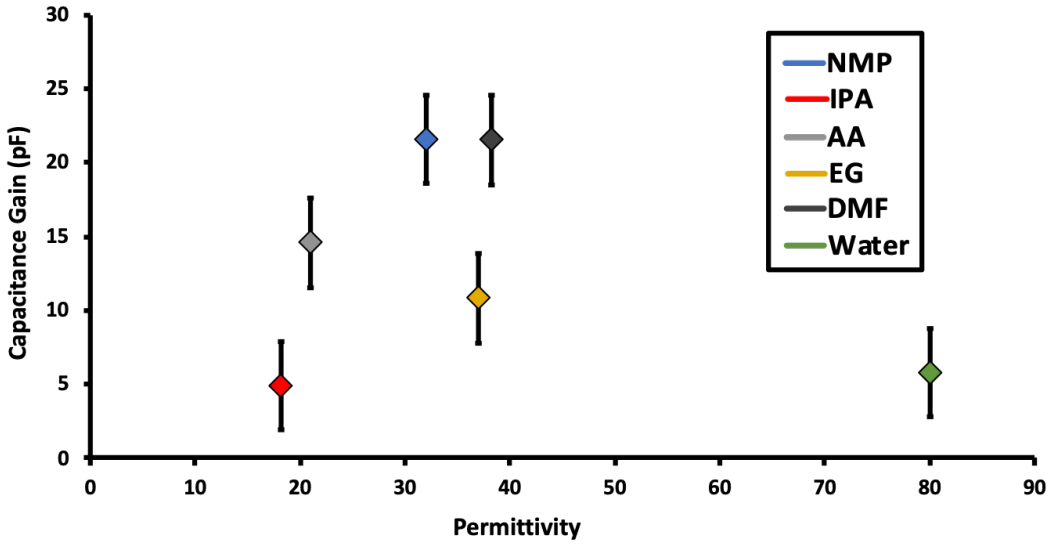

Figure 4.10: Response of the $Pt/TiO_2/SiO_2/4H\text{-}SiC$ sensor to all solvents as a function of relative permittivity

In contrast to the permittivity data, a statistically significant correlation is ob-

served when capacitance gain is plotted as a function of dipole moment, as shown by the data in Figure 4.11. A linear trend can be observed which shows that the sensor produces a greater response to analytes that have a larger dipole moment.

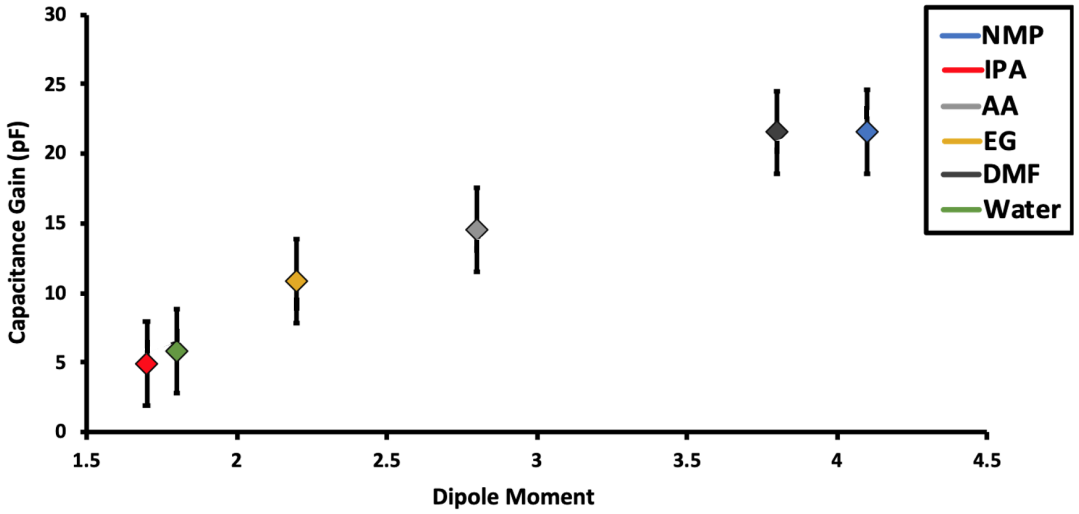

Figure 4.11: Response of the $Pt/TiO_2/SiO_2/4H\text{-}SiC$ sensor to all solvents as a function of dipole moment

Similar behaviour has been observed in resistometric graphene sensors where the dipole moment of the solvent induces a charge in the graphene, resulting in a change in the resistance [9]. In the case of these graphene sensors, the solvent is adsorbed at defects at the surface and this determines the response.

Graphene is a conjugated system consisting of mobile electrons, and this feature makes it a suitable candidate for chemical sensing. Solvent molecules strongly physisorb to the graphene surface and depending on the nature of the molecule, either donate or withdraw electrons from the graphene channel, inducing a measurable response. Polar protic solvents such as isopropyl alcohol, ethylene glycol, and water are electron acceptors and withdraw electrons from the graphene channel, resulting in an increase in resistance. Conversely, polar aprotic solvents like N-methyl-2-pyrollidone, acetic anhydride and DiMethyl formamide are electron donors and increase the electron concentration in the channel, inducing a decrease in resistance [18]. A summary of this behaviour can be seen in Figure 4.12. This relationship is only observed with n-type graphene, for p-type graphene the opposite trend occurs.

Whilst the flatband voltage shift caused upon solvent exposure does not demonstrate an alternating response for protic and aprotic solvents, a similar relationship is observed between the magnitude of sensor response and dipole moment. The data in figure 4.13 shows the change in resistance with respect to the dipole moment of the solvent. Similarly to Figure 4.11, there is a positive correlation observed, with

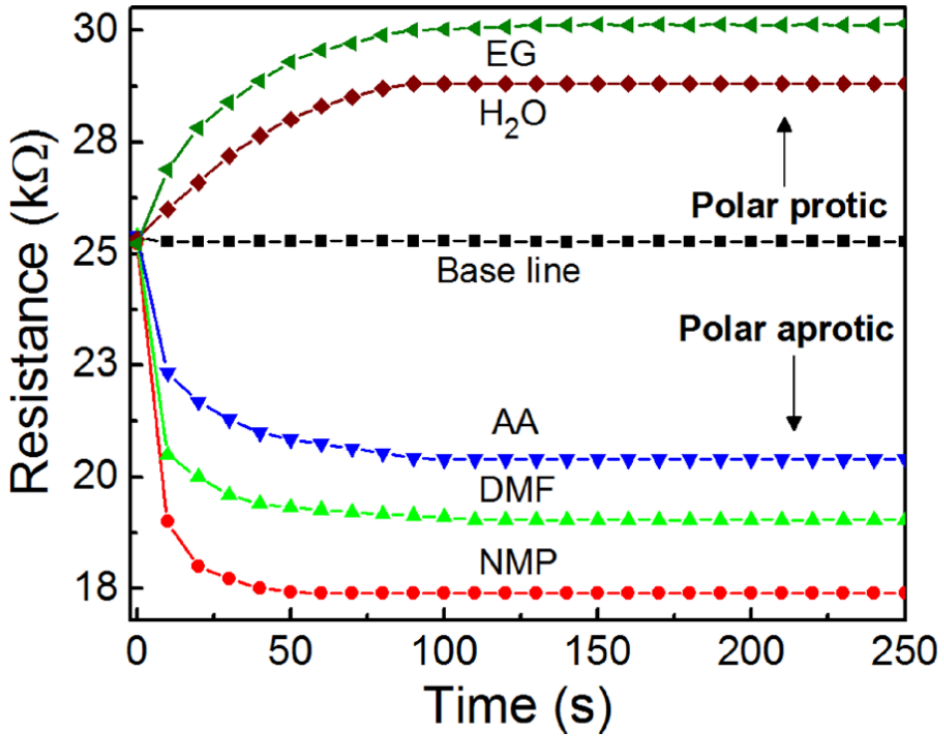

Figure 4.12: Response of resistometric graphene sensor to a number of polar protic and aprotic solvents [18]

NMP contributing to the largest change in resistance.

Hall measurements showed that polar chemicals such as NMP generate high concentrations of induced carriers upon adsorption. This is outlined in the inset of Figure 4.13, which is a plot of the change in carrier density (Δn) as a function of dipole moment. The observed linear relationship validates the hypothesis that the change in carrier concentration determines the sensor response.

For tests carried out on MOS devices, the mechanistic implications are subtle as the structures of graphene sensors and MOS capacitors vary greatly, however, the relationship between the dipole moment of the solvent molecule and induced charges is crucial.

The mechanism proposed to explain the linear relationship between capacitance gain and solvent dipole moment, centres around charged defects within the TiO_2 layer, which are located physically close to the metal/dielectric interface. The solvent molecules induce charges within the device which electrostatically interact with defects, changing the charge state of these defects. This results in additional charge within the structure of the capacitor, which is responsible for the observed shift of the capacitance-voltage profile and increase in capacitance at the flatband voltage. The data in the inset of Figure 4.13 show a linear relationship between solvent dipole moment and the number of induced charges, where molecules with a greater value

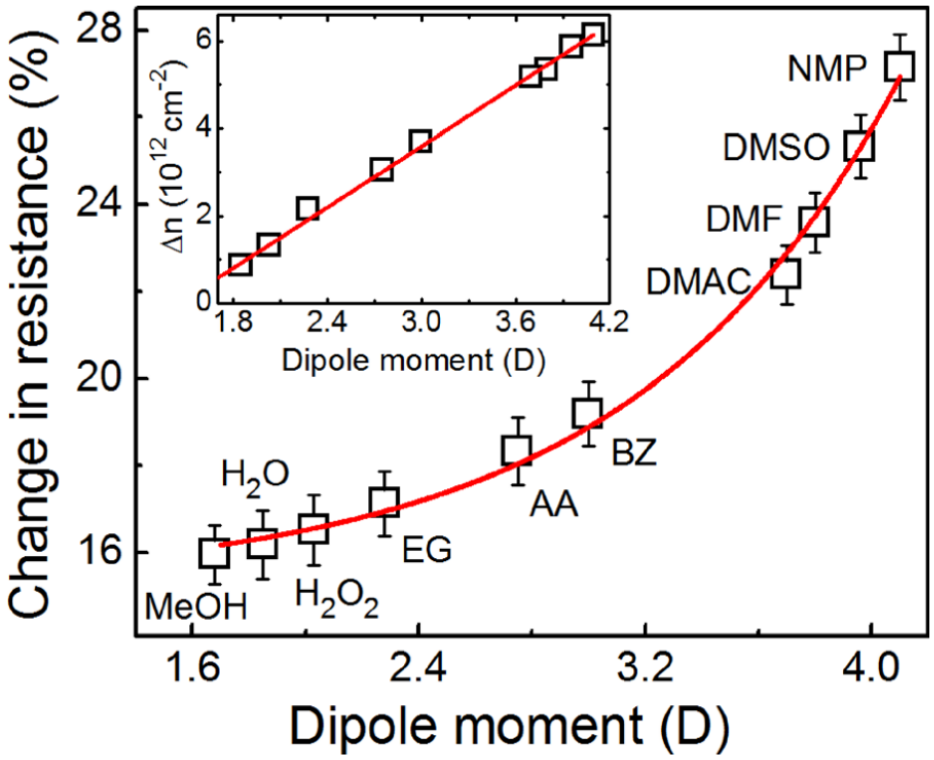

Figure 4.13: Response of the resistometric graphene sensor to a number of solvents as a function of dipole moment. Inset: Change in carrier density with dipole moment [18]

of dipole moment induce a larger number of charge carriers. Therefore solvents such as NMP and DMF cause a greater response from the capacitor as there are more induced charges available to interact with TiO_2 defects. This explains the linear relationship seen in Figure 4.11

The specifics of the interaction between the solvent molecules and the device are as yet unknown, with a variation upon the standard hydrogen gas sensing mechanism suggested. This involves the direct adsorption of the solvent to the platinum surface and diffusion of dissociated species to the metal/insulator interface. There are some issues regarding the application of this theory to the device used in these tests, mainly arising from the uniform, continuous nature of the platinum layer. Whilst direct physisorption of solvents to the catalytic gate metal is likely, the size of the molecules makes diffusion through the metal to the metal/dielectric interface difficult (it is worth noting that the platinum layer will still have a small amount of porosity, so some solvents can adsorb directly). This mechanism is generally accepted for hydrogen containing gases, but requires catalytic or thermal dissociation into individual hydrogen atoms with atomic radii small enough to diffuse through the gate metal [19]. For larger gases, such as NH_3, a porous gate metal is required which

exposes the underlying oxide, allowing direct adsorption to triple points [20]. Triple points are areas in which the analyte is in contact with gate metal, exposed oxide, and ambient air. The volatile nature of solvents prevents thermal decomposition into smaller atoms, therefore whilst there will be adsorption on the catalyst, direct diffusion of charges to the metal/insulator interface is not possible.

In practice, what is likely happening is solvent adsorption directly onto exposed oxide as well as at triple points. Triple points are located at the edges of individually patterned capacitor structures and allow the solvent molecule to contact both the platinum, TiO_2 layer and the ambient environment simultaneously. The dipole moment of these adsorbed solvents are inducing charges which interact with the defects in the TiO_2 layer (Figure 4.14).

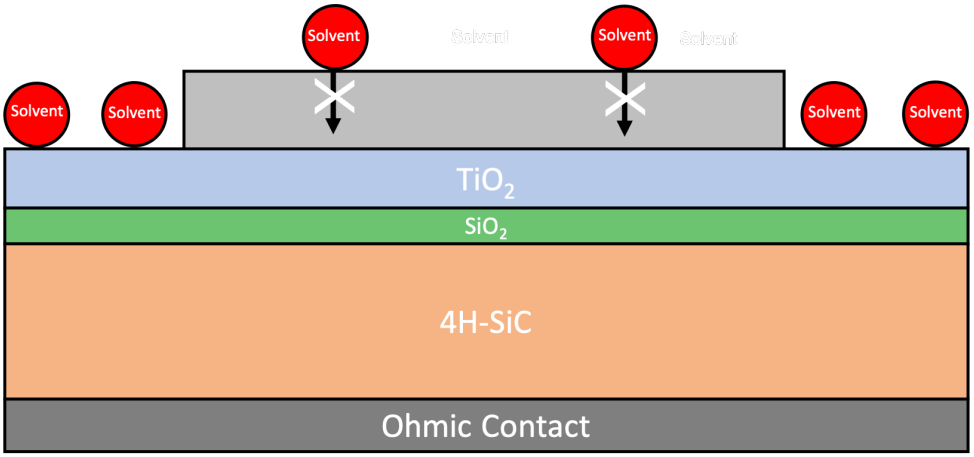

Figure 4.14: Schematic of solvent interaction with $Pt/TiO_2/SiO_2/4H\text{-}SiC$ sensor

The influence of charged defects within TiO_2 dielectric layers has been previously demonstrated in the field of gas sensing [21, 22]. It has been shown that these defects can enable discrimination of gases within a mixture [17]. Often to target a specific gases, it is identity of the catalytic metal which is changed in order to tune selectivity. However previous work by Roy *et al.* demonstrated an array like behaviour from separate sensors comprising TiO_2 and HfO_2 as the dielectric layers and Pt and Pd as the catalytic gate metals. These devices show discriminatory behaviour to hydrogen gas regardless of the gate metal used. Looking at the data in Figure 4.15, it can be seen that the devices with TiO_2 as the dielectric layer have a much greater response that the HfO_2 devices. The surface structure of both devices is identical, and this behaviour is attributed to the defects present within the TiO_2 layer. Analysis of the density of interface traps (D_{IT}) was carried out which showed that upon exposure to hydrogen, there was a qualitative reduction in D_{IT} for the TiO_2 device, and no change for the HfO_2 device ($4.5x10^{11}$ $eV^{-1}cm^{-2}$) [21, 23]. This

suggests that hydrogen atoms are passivating trapping states within the TiO_2 layer and the change in the quantity of trapped charge results in the observed response. It is also worth noting that the sensitivity to O_2 is much greater for the devices which have Pt as the gate metal as opposed to Pd. This, coupled with the influence of the traps in the dielectric layers could lead to simpler, discriminatory devices based around a single catalyst and multiple cheap metal oxides.

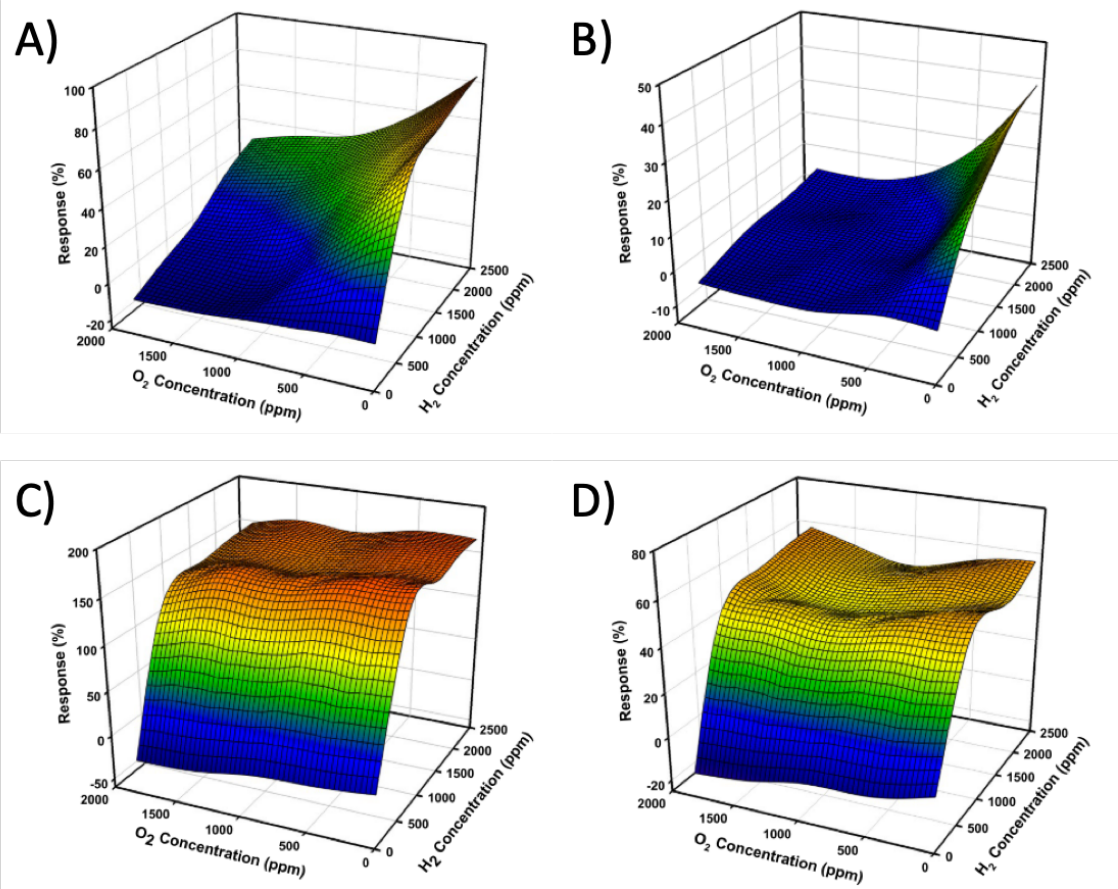

Figure 4.15: The response to mixed oxygen and hydrogen ambients for a A) $Pt/TiO_2/SiO_2/4H\text{-}SiC$, B) $Pt/HfO_2/SiO_2/4H\text{-}SiC$, C) $Pd/TiO_2/SiO_2/4H\text{-}SiC$, D) $Pd/HfO_2/SiO_2/4H\text{-}SiC$ devices [17]

4.3.1 Response Time Analysis

Tests were performed to examine this mechanistic theory. The first of which was to observe the change in device response over the time of exposure, as well as normalisation (i.e. the time taken for the response to return to the baseline). The data in Figure 4.16 show the capacitance shift of the device when biased at V_{FB} upon initial exposure to NMP and after the solvent was removed at 900 seconds. In the presence of the solvent it can be seen that saturation occurs at 540 seconds, as

shown by the data in Figure 4.5. When the solvent is removed, information relating to the interaction between sensor and the solvent can be inferred. After 900 seconds, two distinct regions of the plot are identifiable; region 1 occurs immediately after solvent removal and region 2 after 1620 seconds.

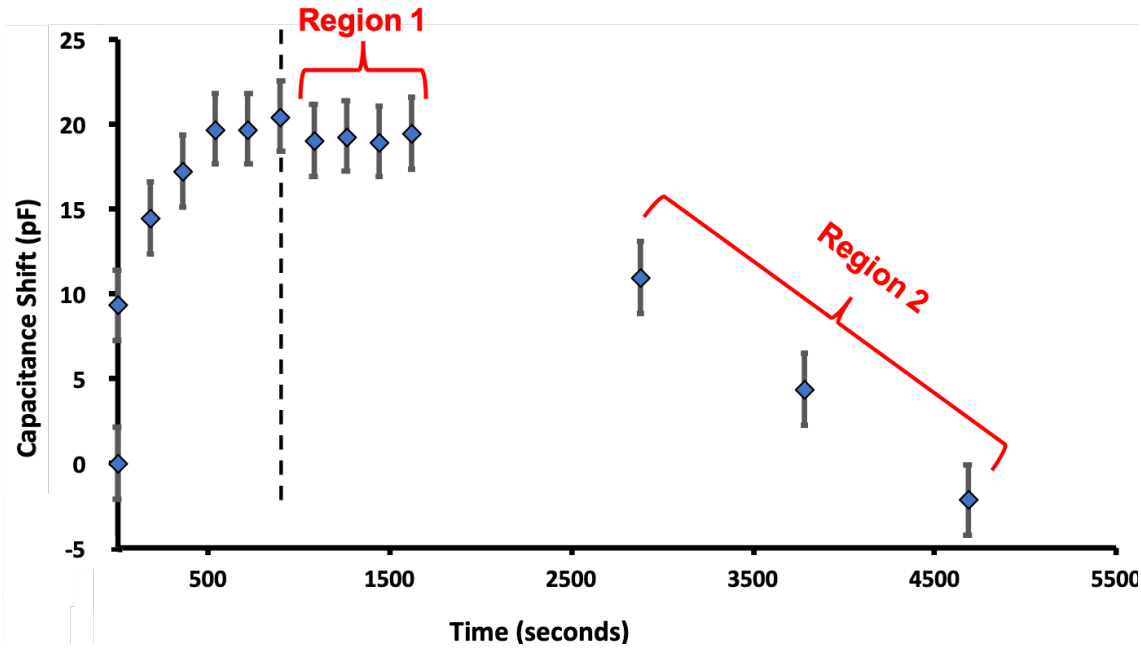

Figure 4.16: Magnitude of the sensor response to NMP as a function of time. Solvent was introduced at 0 seconds and removed at 900 seconds (dashed line)

The immediate drop in capacitance after solvent removal is minor, as shown by the data labeled as Region 1, and is attributed to the solvent molecules that are physisorbed to the metal surface. As discussed previously, it is likely that adsorption will occur, but is not expected to be the dominant response in this type of sensor. The introduction of laboratory air to the sample chamber encourages the immediate dissociation of the NMP, causing a small drop in response at t=1080 seconds, the response then remains constant until 1620 seconds. The response for the data beyond this point (Region 2), indicates that a strong interaction between solvent and the TiO_2 dielectric layer is responsible for slow recovery time. The strong electrostatic interaction between induced charges and electrically charged defects ensures that the response of the device is observable even for a long period after the solvent source is removed. This unique behaviour can be manipulated in potential applications, allowing the device to be introduced to certain environments and then tested remotely. This could be useful if the environment can not support the electronic circuitry required for device interrogation.

The sensor response returns to zero, within the experimental error for times

beyond 5000 seconds, indicating a complete removal of the solvent from the sensor. Due to the temperature stability of silicon carbide, a thermal cycle could be used to speed up the normalisation process. This feature could also prolong device lifetime as the device can be cleaned of poisons by using temperature.

4.3.2 Charge Analysis

To further support the hypothesis that TiO_2 defects are responsible for the response, tests were undertaken to monitor the trap concentration (ΔN_T) during solvent exposure.

The trap density shift in the dielectric layer was determined from the shift in the flatband voltage (V_{FB}) measured at baseline conditions and under the influence of NMP. The flatband capacitance (C_{FB}) for both tests was used to calculate the additional charge (Q) added to the dielectric by the NMP molecules according to Equation 4.4. This shift in charge enables the trap density (N_T)to be determined using Equation 4.5.

$$\Delta V_{FB} = \frac{\Delta Q}{C_{FB}} \tag{4.4}$$

$$N_T = \frac{\Delta Q}{q} \tag{4.5}$$

Test	**V_{FB} (V)**	**C_{FB} (pF)**	**Q (pC)**
Baseline	1.80	81.79	149.04
NMP	1.80	61.21	110.16

Table 4.4: V_{FB}, C_{FB} and Q, extracted from the Pt/TiO_2/SiO_2/4H-SiC sensor under baseline conditions and in the presence of NMP

Under the assumption that this charge originates from single charged trapping states located within the volume found directly underneath the catalytic contact, this equates to a trap density of 2.3x10^{17} cm^{-3}. This is in the region of 1% of the trap concentration found in similar high-k layers grown under the same conditions [24]

4.3.3 Leakage Analysis

Leakage current can be measured laterally (using the interdigitated fingers) and vertically through the device and is a useful tool to extract information about the

dielectric layer. Leakage current values can be used to determine the stability, and breakdown voltage of the device, as well as calculate the trap density within the oxide. These tests were used here to examine changes to the oxide trap density upon exposure to solvents, which can help ascertain a detection mechanism.

Lateral Tests

Leakage current was measured laterally across the interdigitated finger structures patterned onto the device surface (Figure 4.17). Two probes of the Keithley 4200A SCS Parameter Analyser were positioned either side of a set of interdigitated fingers. The voltage was swept from 0 to 5 V and the resultant current was measured. This was carried out in normal laboratory air to determine a baseline, and then again after the device had been exposed to NMP for 540 seconds. The current density was then plotted as a function of electric field for analysis.

As these tests were carried out in a low value of electric field (10 kV/cm), it was expected that trap assisted conduction would be the dominant process. In trap assisted conduction, bulk traps in the insulating layer are lowered to the Fermi level of the gate metal, inducing a tunneling current which is assisted by the traps [25]. It is worth noting that this model does not consider the effect of surface conduction. An alternative path involving conduction across the dielectric surface may be in effect upon solvent adsorption, but no suitable model is available to analyse this.

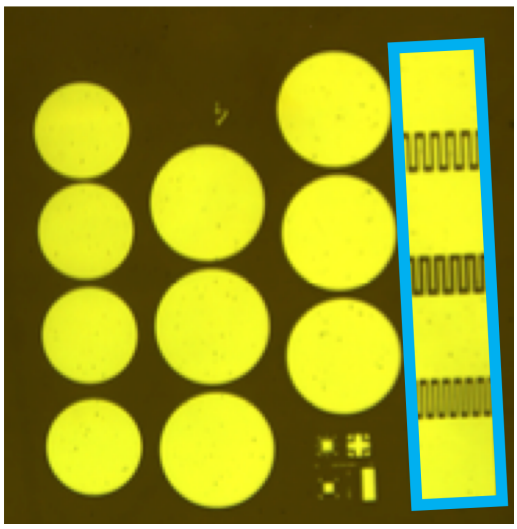

Figure 4.17: Optical micrograph of sensor surface with interdigitated finger structure outlined in blue

If the current between the contacts is dominated by trap assisted conduction, the data would be expected to show a linear trend of J as a function of E as shown by Equation 4.6.

$$J = C\,E\,\exp\left(\frac{q\Phi_A}{k_B T}\right) \tag{4.6}$$

Here, C is related to the density of trapping states in the bulk oxide, E is the value of the electric field and Φ_A is the barrier height of the Pt/TiO_2 junction. However it can be seen from the data in Figure 4.18 that an exponential plot is observed, suggesting that another carrier transport mechanism dominates.

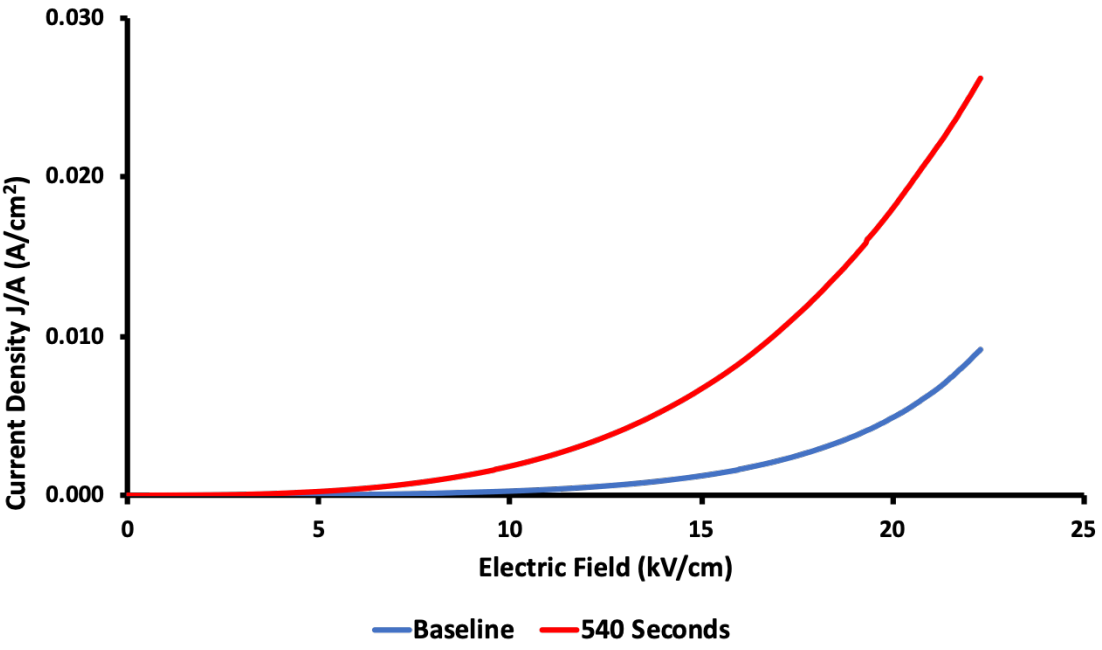

Figure 4.18: Current density vs electric field of Pt/TiO_2/SiO_2/4H-SiC exposed to normal laboratory air and NMP for 540 seconds

The alternative suggested mechanism proposes that surface conduction occurs through the passivation of defects in the oxide. Here, the TiO_2 layer is acting as a two dimensional charge sheet between the interdigitated fingers on the device. The resistance value of this sheet can be determined using Equation 4.7, with R_{sheet} being outlined in Equation 4.8.

$$R = R_{sheet} \times \#\,Squares \tag{4.7}$$

$$R_{sheet} = \frac{1}{n\,e\,\mu} \tag{4.8}$$

Where, n is the sheet carrier concentration, e is electronic charge and μ is mobility. The sheet carrier concentration can then be used to estimate the change in trap concentration upon exposure to NMP.

Vertical Tests

Vertical leakage tests were carried out at higher values of electric field, and the Poole-Frenkel effect is expected to be observable. This mechanism involves the gradual movement of electrons through an insulator due to random thermal fluctuations. These thermal fluctuations provide the electrons with enough energy to be excited from their localised trapping state into the conduction band for a period of time until they relax into an alternate state. The high value of electric field has an effect on the electrons as it reduces the Coulomb potential energy, increasing the probability of thermal excitation into the conduction band [26, 27]. Figures 4.19 and 4.20 show plots of log(Current Density) vs Electric Field and Sensitivity vs Electric Field of a $Pt/TiO_2/SiO_2/4H\text{-}SiC$ device exposed to varying concentrations of NMP, respectively.

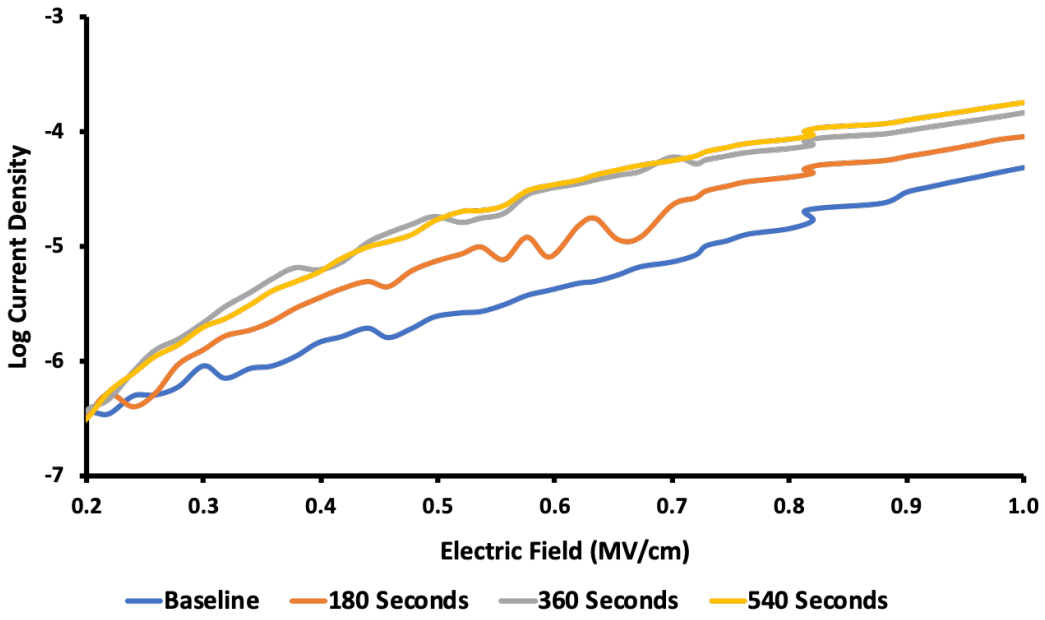

Figure 4.19: Log current density vs electric field of $Pt/TiO_2/SiO_2/4H\text{-}SiC$ exposed to normal laboratory air and NMP for varying time intervals (unusual characteristics at 0.8 MV/cm is due to noise within the testing set up)

4.3.4 Frequency Dispersive Analysis - Gonon Model

Metal insulator metal (MIM) capacitors based on dielectric materials, with a high dielectric constant are known to display non-linear characteristics. A freuency dispersion model of capacitance variation ($\Delta C/C_0$) plotted as a function of electric field, displays these non-linear characteristics - See Figure 4.21. A model to account for this phenomenon was proposed by Gonon in 2007 centred around oxygen defects within the dielectric [28]. This model relates to the formation of percola-

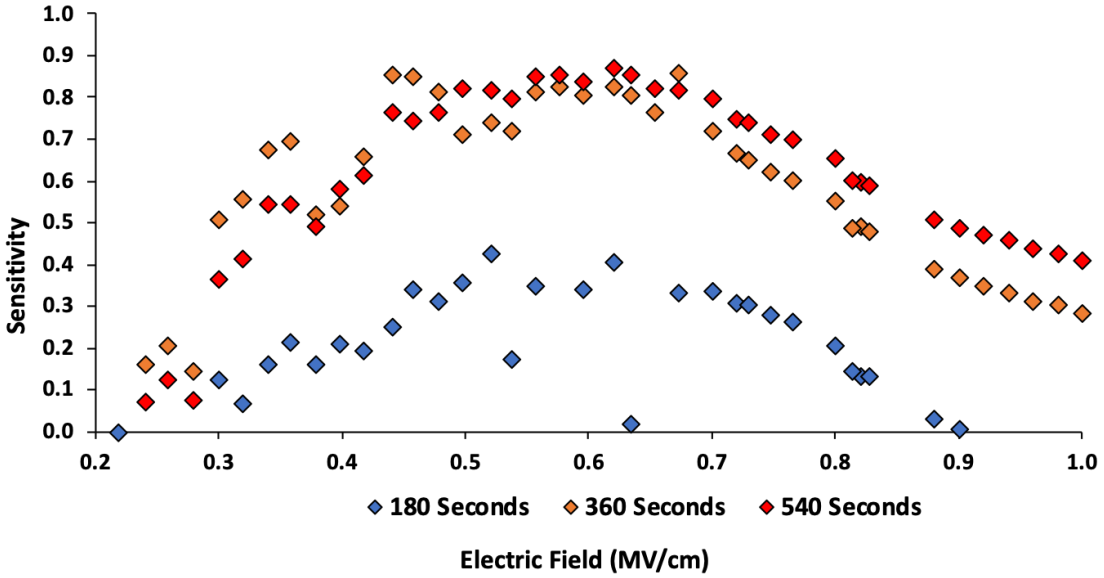

Figure 4.20: Sensitivity vs electric field of $Pt/TiO_2/SiO_2/4H$-SiC exposed to normal laboratory air and NMP for varying time intervals

tion pathways through the dielectric material and the impact that these have on the capacitance. This model is based on an electrode polarisation mechanism that implies the presence and influence of hopping carriers whose mobility is dependent on the experienced electric field. The reduction in capacitance at higher frequencies can be related to the slow response (due to the hopping conduction mechanism) of carriers trapped in the defects that form these percolation pathways. This technique enables the determination of the average hopping distance of a carrier which can be correlated to the trap density.

For this work, the method allows qualitative analysis of the changes in trap concentration (by comparing hopping distance) of the $Pt/TiO_2/SiO_2/4H$-SiC device in the presence of solvent. Using the lateral interdigitated finger structures, which are in effect, a MIM capacitor, the dispersion capacitance at 0V was measured over a range of frequencies in the presence of normal air and NMP.

$\Delta C/C_0$ was calculated from Equation 4.9 where C_f is the capacitance at a given frequency and C_{1MHz} is the capacitance at 1MHz.

$$\frac{\Delta C}{C_0} = \frac{C_f - C_{1MHz}}{C_{1MHz}} \tag{4.9}$$

The density of traps (N_T) can be determined using Equation 4.10, where the value of s is the hopping distance for carriers moving between trapping states. In order to calculate this, it's necessary to first find the frequency factor, n. n can be found by calculating the gradient of a plot of log ($\Delta C/C_0$) as a function of log(frequency) (Figure 4.22).

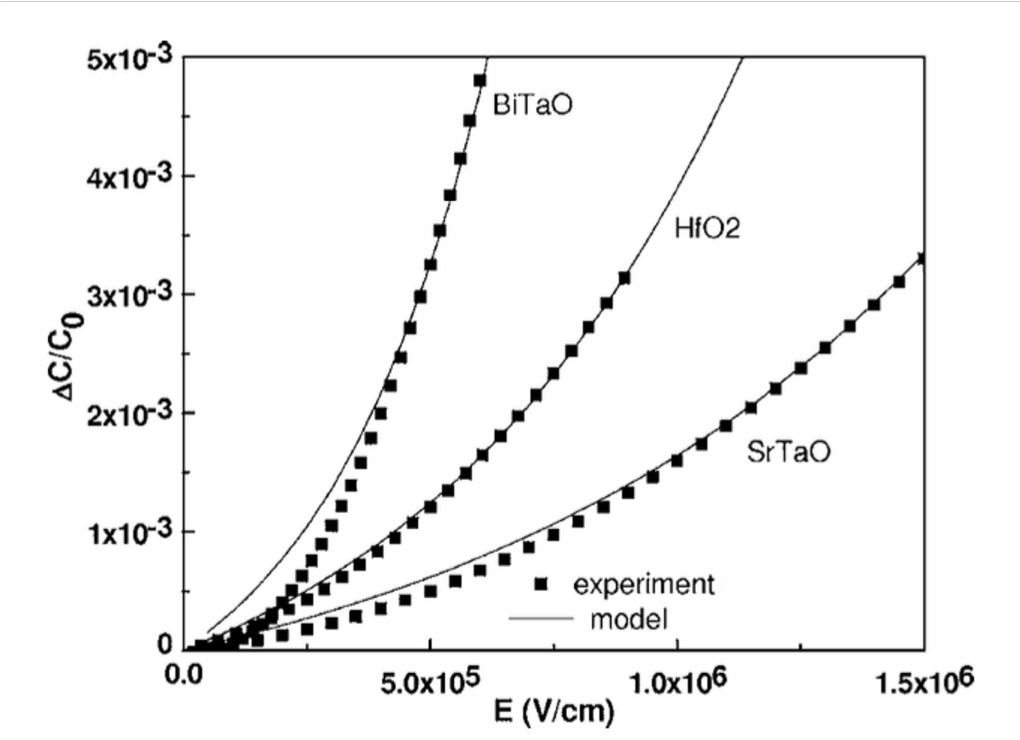

Figure 4.21: Relative variation of capacitance at 10 kHz as a function of electric field for three high dielectric constant oxides - squares represent experimental data and solid lines represent calculated values according to the model

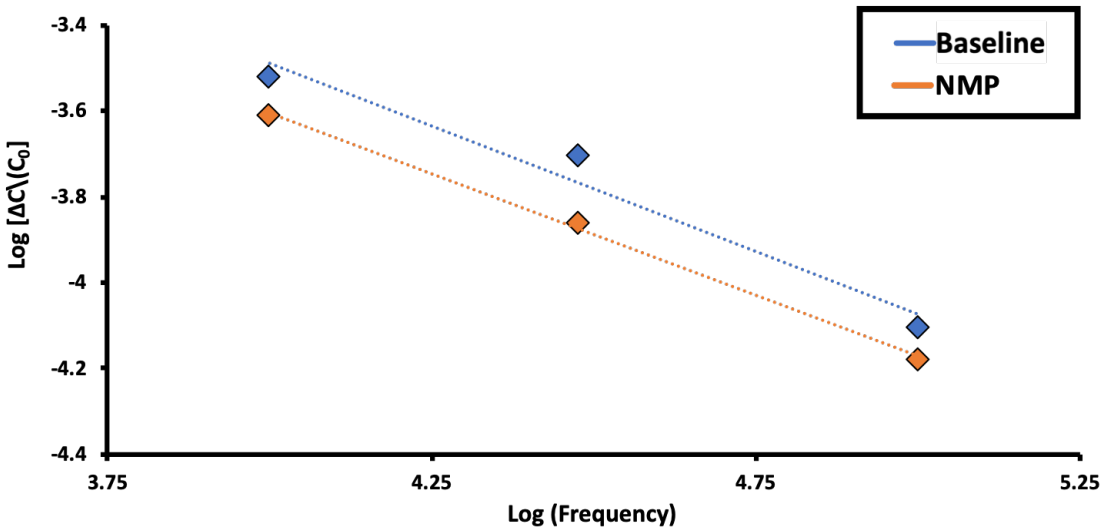

Figure 4.22: Plot of log ($\Delta C/C_0$) vs log(frequency), the slope of which represents 2n

The gradient of a plot of $\Delta C/C_0$ vs log(frequency) (Figure 4.23) can then be used with Equation 4.11 to calculate the hopping distance. Here, q is the electronic charge, k_B Boltzmann's constant, T the temperature and n the frequency factor.

$$N_T = \frac{1}{s^3} \tag{4.10}$$

$$Gradient = \frac{nqs}{k_B T} \tag{4.11}$$

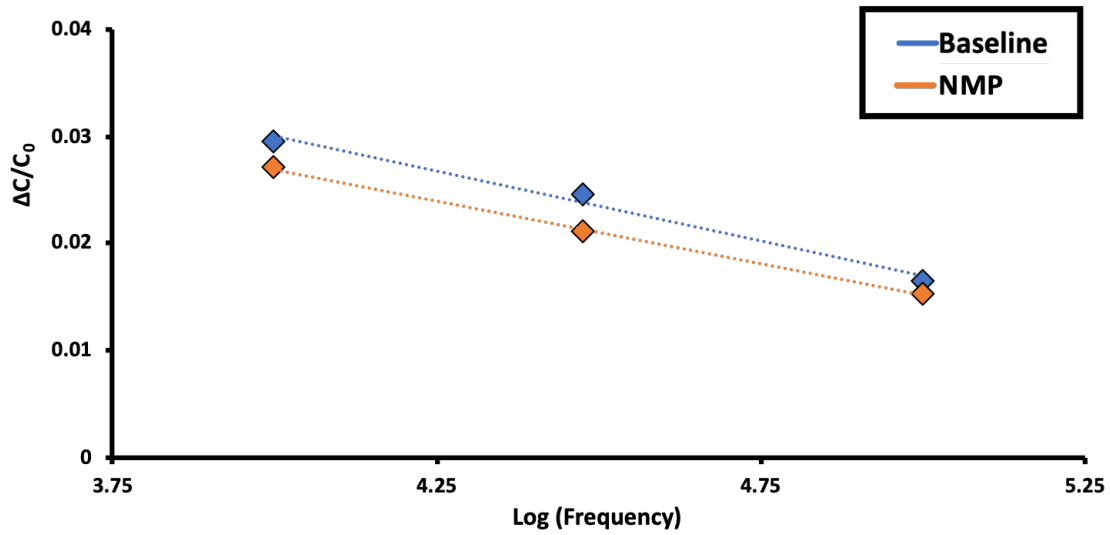

Figure 4.23: Plot of ($\Delta C/C_0$) vs log(frequency), the slope of which represents nqs/K_BT

The concentration of traps in the dielectric layer in normal air (Baseline) and NMP are shown in Table 4.5. Whilst the trap concentration extracted from the structure will not be the true trap concentration due to geometric limitations, the data shows a reduction in the trap concentration of 4.56% on exposure to NMP. Based on the expected trap concentration in TiO_2 grown by the oxidation of Ti, this predicts a change of approximately 1x10^{18} cm^{-3}, which is comparable to that calculated from the flatband shift (2.3x10^{17} cm^{-3}).

Test	**2n**	**s (cm)**	**N_T (cm^{-3})**
Baseline	-0.585	1.36x10^{-6}	3.95x10^{17}
NMP	-0.569	1.38x10^{-6}	3.79x10^{17}

Table 4.5: 2n, s and N_T, extracted from the Pt/TiO_2/SiO_2/4H-SiC sensor under baseline conditions and in the presence of NMP

4.4 Conclusion

It has been demonstrated that a Pt/TiO_2/SiO_2/4H-SiC device can be used effectively as a room temperature solvent sensor. Exposure of the device to a number of representative solvents with varying properties caused an observable positive shift in the capacitance-voltage profile. Response to the varying solvents was monitored as a change in capacitance at the flatband voltage, with a positive correlation observable between the magnitude of response and solvent dipole moment.

This relationship was previously observed in resistometric graphene sensors upon exposure to solvent molecules, with the dominant mechanism centring around defects on the graphene surface. This lead to the hypothesis that the charged defects in the TiO_2 layer could be influential in solvent-device interaction.

The mechanistic theory proposed involves direct interaction between the solvent molecules and the exposed TiO_2 layer; specifically the strong interaction between the dipole moment of the solvent and the charged oxygen defects present toward the surface of the oxide layer. Solvent molecules adsorb to these defects, and induce charges, which causes a shift in the device characteristics.

Tests were carried out to validate this theory and qualitatively monitor the defect concentration throughout the lifetime of solvent interaction. C-V profiles were used to calculate the flatband capacitance, charge value, and subsequently the trap density of the device when exposed to solvent. Under the assumption that charge originates from single trapping states, a trap density of $2.3\text{x}10^{17}$ cm^{-3} was found which is comparable to other dielectric films. Furthermore, vertical and lateral leakage tests were carried out which demonstrated that the solvent acts to change the density of trapping states in the dielectric. This confirms that careful selection of the dielectric film used in the manufacture of silicon carbide MOS sensors has to include consideration of the nature of the defects that are incorporated during the manufacturing process.

Finally, using the model proposed by Gonon, frequency dispersion measurements allowed the calculation of trap density in the presence of laboratory air and NMP. This method, taking into account geometric limitations of the device, showed a reduction in trap concentration of 4.56% upon exposure to NMP, supporting the proposed mechanistic theory.

Whilst demonstrating the use of MOS devices as room temperature solvent sensors, this work has also shed some light on device-analyte interaction. The influence of defects within the dielectric layer has been highlighted and this information will be taken forward and used to optimise the fabrication process for devices to be used as NOx gas sensors.

Bibliography

[1] G Behzadi pour and L Fekri aval. "Highly sensitive work function hydrogen gas sensor based on PdNPs/SiO2/Si structure at room temperature". In: *Results in Physics* 7 (2017), pp. 1993–1999.

[2] Ingemar Lundstrom et al. "Twenty-five years of field effect gas sensor research in Linkoping". In: *Sensors and Actuators B: Chemical* 121 (1 2007), pp. 247–262.

[3] L. Fekri Aval et al. "Comparison of the MOS capacitor hydrogen sensors with different SiO2 film thicknesses and a Ni-gate film in a 4 percent hydrogen–nitrogen mixture". In: *Sensors and Actuators B: Chemical* 216 (Sept. 2015), pp. 367–373.

[4] D. Soderberg and I. Lundtrom. "Surface and interface dipoles on catalytic metal films". In: *Solid State Communications* 35 (2 July 1980), pp. 169–174.

[5] Lars Gunnar Ekedahl, Mats Eriksson, and Ingemar Lundström. "Hydrogen Sensing Mechanisms of Metal-Insulator Interfaces". In: *Accounts of Chemical Research* 31 (5 1998), pp. 249–256.

[6] "Discriminating high k dielectric gas sensors". In: vol. 778-780. Trans Tech Publications, Feb. 2014, pp. 1058–1062.

[7] James L. Reed. "Electronegativity and atomic charge". In: *Journal of Chemical Education* 69 (10 Oct. 1992), p. 785.

[8] Lynne Reed Murphy et al. "Evaluation and Test of Pauling's Electronegativity Scale". In: *The Journal of Physical Chemistry A* 104 (24 June 2000), pp. 5867–5871.

[9] Venkata Karthik Nagareddy et al. "Improved chemical detection and ultrafast recovery using oxygen functionalized epitaxial graphene sensors". In: *IEEE Sensors Journal* 13 (8 2013), pp. 2810–2817.

[10] Health and Safety Executive. "EH40/2005 Workplace exposure limits. Containing the list of workplace exposure limits for use with the Control of Substances Hazardous to Health Regulations 2002 (as amended)." In: 1st ed. Vol. 1. HSE, 2018, p. 63.

[11] Ian M. Smallwood. *Handbook of Organic Solvent Properties*. Elsevier, 2012, pp. 1–306.

[12] Joanne Fearon and Graeme W. Watson. "Hydrogen adsorption and diffusion on Pt {111} and PtSn {111}". In: *Journal of Materials Chemistry* 16 (20 May 2006), p. 1989.

[13] Graeme W. Watson et al. "A Comparison of the Adsorption and Diffusion of Hydrogen on the {111} Surfaces of Ni, Pd, and Pt from Density Functional Theory Calculations". In: *The Journal of Physical Chemistry B* 105 (21 May 2001), pp. 4889–4894.

[14] Nimibofa Ayawei, Augustus Newton Ebelegi, and Donbebe Wankasi. *Modelling and Interpretation of Adsorption Isotherms*. Sept. 2017.

[15] Patiha et al. "The Langmuir isotherm adsorption equation: The monolayer approach". In: vol. 107. IOP Publishing, Feb. 2016, p. 012067.

[16] Reza Loloee et al. "Hydrogen monitoring for power plant applications using SiC sensors". In: *Sensors and Actuators B: Chemical* 129 (1 2008), pp. 200–210.

[17] S K Roy et al. "SiC gas sensor arrays for extreme environments". In: 2013, pp. 1–4.

[18] V K Nagareddy et al. "Detection of polar chemical vapors using epitaxial graphene grown on SiC (0001)". In: *Applied Physics Letters* 102 (17 2013), p. 173103.

[19] Shinji Nakagomi et al. "Electrical characterization of carbon monoxide sensitive high temperature sensor diode based on catalytic metal gate - Insulator - Silicon carbide structure". In: *IEEE Sensors Journal* 2 (5 Oct. 2002), pp. 379–385.

[20] A. Spetz, M. Armgarth, and I. Lundstrom. "Optimization of ammonia-sensitive metal-oxide-semiconductor structures with platinum gates". In: *Sensors and Actuators* 11 (4 May 1987). Porous gate ammonium sensitivity, pp. 349–365.

[21] R. Mahapatra et al. "Leakage current and charge trapping behavior in Ti O2 Si O2 high- gate dielectric stack on 4H-SiC substrate". In: *Journal of Vacuum Science and Technology B: Microelectronics and Nanometer Structures* 25 (1 Jan. 2007), pp. 217–223.

[22] Ming-Hung Weng et al. "Trap-Assisted Gas Sensing Mechanism in Pd-TiO2-SiO2-SiC Capacitors at High Temperatures". In: *IEEE Sensors Journal* 7 (10 Oct. 2007), pp. 1395–1399.

[23] B. J. D. Furnival, N. G. Wright, and A. B. Horsfall. “Discriminating gas concentrations in extreme temperature environments”. In: IEEE, Oct. 2011, pp. 1044–1047.

[24] Bing Miao et al. “Radiation Induced Change in Defect Density in HfO2-Based MIM Capacitors”. In: *IEEE Transactions on Nuclear Science* 56 (5 Oct. 2009), pp. 2916–2924.

[25] P. Fiorenza et al. “From micro to nanotransport properties in Pr2O3 based thin layers”. In: *Journal of Applied Physics* 98 (4 Aug. 2005), p. 044312.

[26] L Colalongo et al. “Numerical analysis of poly-TFTs under off conditions”. In: *Solid-State Electronics* 41 (4 Apr. 1997). Poole Frenkel 1, pp. 627–633.

[27] Fu-Chien Chiu. “A Review on Conduction Mechanisms in Dielectric Films”. In: *Advances in Materials Science and Engineering* 2014 (Feb. 2014), pp. 1–18.

[28] P. Gonon and C. Vallee. “Modeling of nonlinearities in the capacitance-voltage characteristics of high-k metal-insulator-metal capacitors”. In: *Applied Physics Letters* 90 (14 Apr. 2007), p. 142906.

Chapter 5

Incorporation of Novel Dielectric Materials into MOS Capacitor Structures to Optimise Gas Sensitivity

5.1 Introduction

The work in Chapter 3 has allowed the optimisation of fabrication techniques for metal-oxide-semiconductor capacitors to be used as gas sensors in the harsh environment of a diesel engine. The optimum oxidation time and temperatures for the HfO_2, TiO_2, ZrO_2 and WO_3 dielectric layers was determined to be 10 minutes at 550°C for HfO_2, TiO_2 and ZrO_2, and 500°C for WO_3. The optimum sputtering pressure to incorporate porosity of 75.4% into the platinum gate metal layer was found to be 140 mTorr (at a pressure of 50W).

It is important that devices of varying compositions can be produced under similar conditions, as the deployment of a monolithic sensor array into the exhaust system of a vehicle will be the likely conclusion of this work. An integrated array could provide real-time data on the levels of common pollutants within the engine, which could lead to a closed-loop system with modulation of engine performance based on live pollution data. As demonstrated in previous work, different dielectric materials demonstrate varying sensitivity and selectivity to different analyte gases, so the ability to incorporate a number of individual sensors into a monolithic array, will help realise this opportunity.

Pt/HfO_2/SiC, Pt/TiO_2/SiC, Pt/ZrO_2/SiC and Pt/WO_3/SiC devices were fabricated under comparable conditions, and electrically characterised in laboratory air, as well as in the presence of certain analytes.

This chapter details the influence of frequency on electrical characteristics of HfO_2, TiO_2, and ZrO_2 devices.It also demonstrates response data for a $Pt/HfO_2/SiC$ and $Pt/ZrO_2/SiC$ to hydrogen and oxygen gases. For the zirconium based device, this is the first time this has been demonstrated. We have also been able to demonstrate, for the first time, sensitivity of a $Pt/WO_3/SiC$ device to nitric oxide at 573K.

5.2 Device Fabrication

Metal oxide semiconductor capacitors were fabricated from 4H-SiC with a nitrogen dopant concentration of $3x10^{18}$ cm^{-3}. Initial cleaning using the organic solvents NMP and IPA was carried out before an RCA cleaning process was performed. Oxidation (dry) of the SiC was performed at 1150 °C in 80 sccm of O_2 for 200 minutes, growing a 25 nm thick layer of SiO_2 on the silicon face of the wafer. Prior to back contact deposition, any oxide on the back face of the SiC was removed by a buffered hydrofluoric acid dip. The newly grown SiO_2 layer was protected by hard-baked photoresist to prevent etching before an ohmic contact was then formed on the carbon face by deposition of a metal stack comprising 5 nm of titanium and 100 nm nickel. Annealing of the back contact in a vacuum was carried out at 1050 °C for 180 seconds to form nickel silicide. The dielectric layer was then formed by deposition of 50 nm of a chosen metal, followed by oxidation in air at a specified temperature. For Hf, Ti, and Zr, oxidation was carried out in air for 10 minutes at 550 °C. Work from Chapter 3 determined that the optimum oxidation conditions to form WO_3 was heating in air at 500 °C for 10 minutes. Photolithographic patterning of the metal contacts was performed using S1813 photoresist to realise the individual capacitor structures on the device surface.

Platinum was used as the gate metal catalyst and devices were fabricated, incorporating two different morphologies of Pt (continuous and porous). Platinum was chosen as gasses can effectively adsorb to its surface and the introduction of porosity creates triple points which encourage physisorption of gases. An initial 5 nm titanium layer was deposited for adhesion purposes, prior to the sputtering of 70nm of Pt. As outlined in Chapter 3, the continuous platinum layer was deposited at 50 W and with an argon pressure of 9.8 mTorr, and to produce the porous platinum layer, deposition at 50 W and 140 mTorr was carried out. It is anticipated that there is a link between the porosity and gas sensitivity of larger gases, with more porous catalysts resulting in greater flatband voltage shifts. This is due to the increased number of triple points formed, enhancing the sensitivity to complex gaseous molecules [1, 2, 3]. Further patterning of the device was then performed, followed by a deposition of 300 nm of gold, to produce contacts suitable for bonding to relevant circuitry.

This method was used to produce two lots of $Pt/HfO_2/SiC$, $Pt/TiO_2/SiC$, $Pt/ZrO_2/SiC$ and $Pt/WO_3/SiC$ sensors, one set with a porous platinum gate, and one with a continuous platinum gate.

This experimental method was chosen to produce devices under comparable conditions to facilitate the potential of manufacturing monolithically integrated arrays. As demonstrated in previous work, these types of devices have sensitivity to a number of gas species and in order to improve selectivity to target gases from a mixture, a sensor array can be deployed. This is why it is important to make devices with different dielectric layers under similar conditions, as it will simplify the array manufacturing process.

5.3 Device Characteristics

After fabrication, characterisation tests were carried out on the Titanium, Hafnium, and Zirconium devices. The capacitance-voltage (C-V) and conductance-voltage (G-V) characteristics were evaluated over a range of frequencies using an Agilent 4284 LCR meter. Capacitance was measured amid a voltage sweep between -5V to 5V and at frequencies above 100 kHz produced a notable curve detailing depletion and accumulation regions.

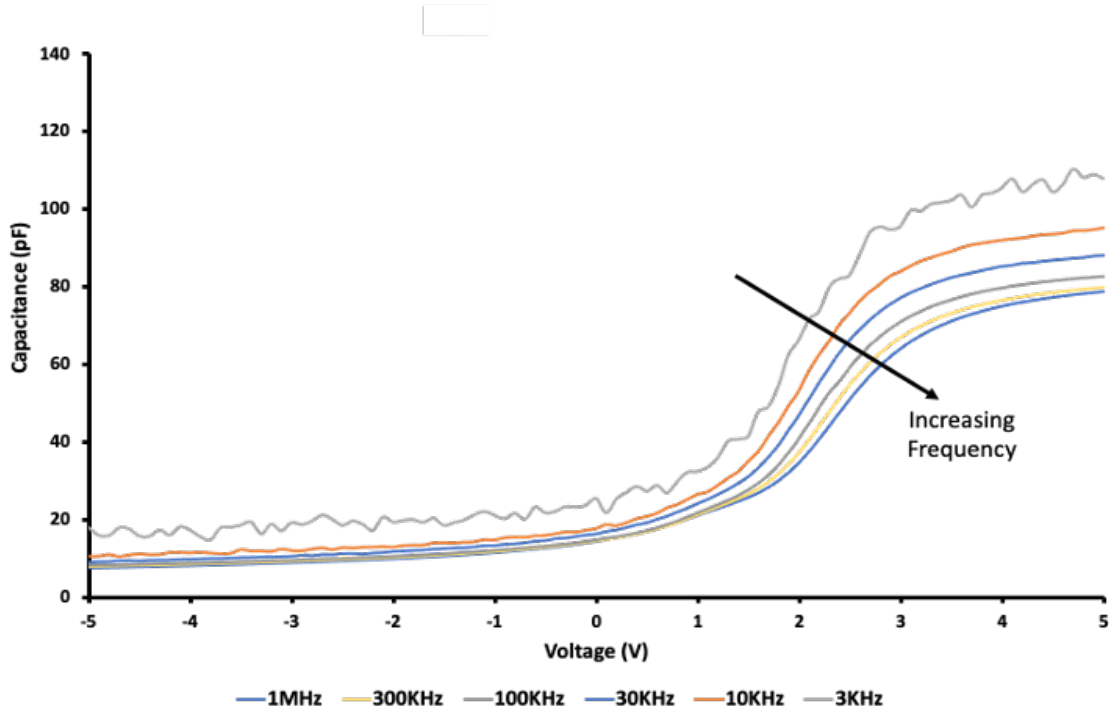

Figure 5.1: C-V characteristics extracted from a $Pt/TiO_2/SiO_2/SiC$ sensor in room temperature laboratory air at varying frequencies

The data in figure 5.1 shows the C-V curve of a TiO_2 based device, and demon-

strates a shift in flatband voltage with increasing frequency. The flatband voltage decreases by 1.2 V when the frequency is changed from 1 MHz to 3 kHz. This behaviour is seen due to the high levels of defects within the oxide layer, which behaves differently at varying frequencies. The frequency changes are causing a change in the TiO_2 oxide capacitance which influences the flatband voltage, as per Equation 5.1. Equation 5.1 outlines the relationship between C_{ox} and V_{FB}, and this is demonstrated in Figure 5.2.

$$V_{FB} = \phi_{ms} - \frac{Q_f + Q_m + Q_t}{(C_{ox})} \tag{5.1}$$

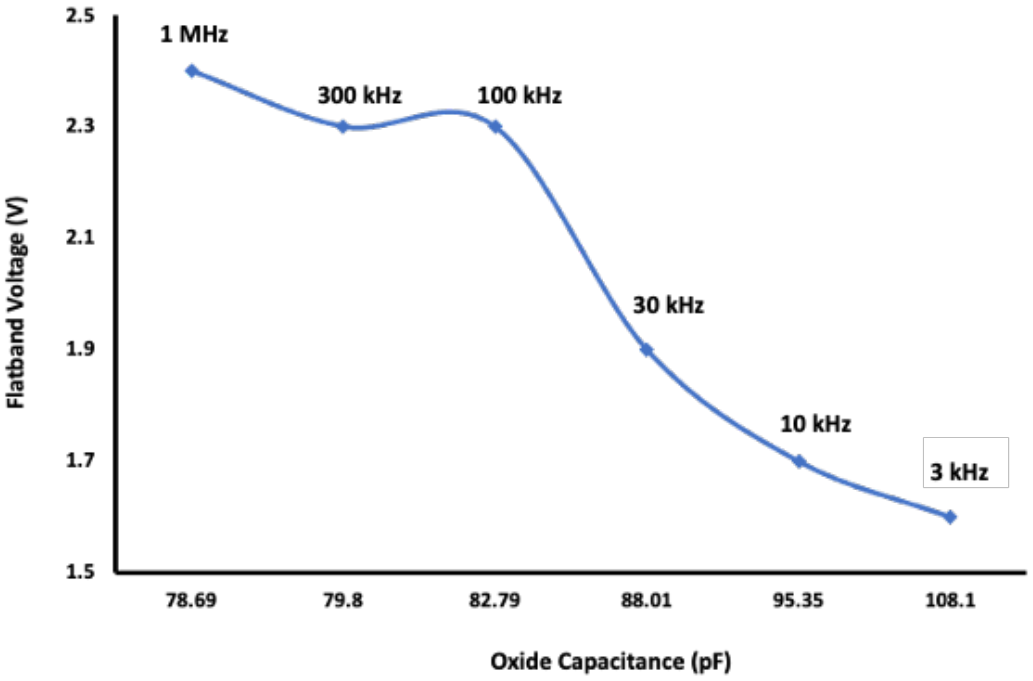

Figure 5.2: Relationship between flatband voltage and oxide capacitance of a $Pt/TiO_2/SiO_2/SiC$ sensor in room temperature laboratory air at varying frequencies

The data in figures 5.3 and 5.4 display the C-V characteristic of a HfO_2 and ZrO_2 device, and it can be seen that there is less of a flatband voltage shift than the titanium device with increasing frequency. This suggests that the hafnium oxide and zirconium oxide dielectric layers have fewer defects in the oxide, meaning lower levels of oxide charge, resulting in a more consistent value of oxide capacitance and flatband voltage.

Figure 5.5 displays the capacitance and conductance characteristics of a WO_3 based device. It is observable that the capacitor has high levels of leakage current, as seen by the increasing levels of conductance at voltages above flatband voltage of 3.6V. Unlike the data in figures 5.1, 5.3 and 5.4, this data set has been not been

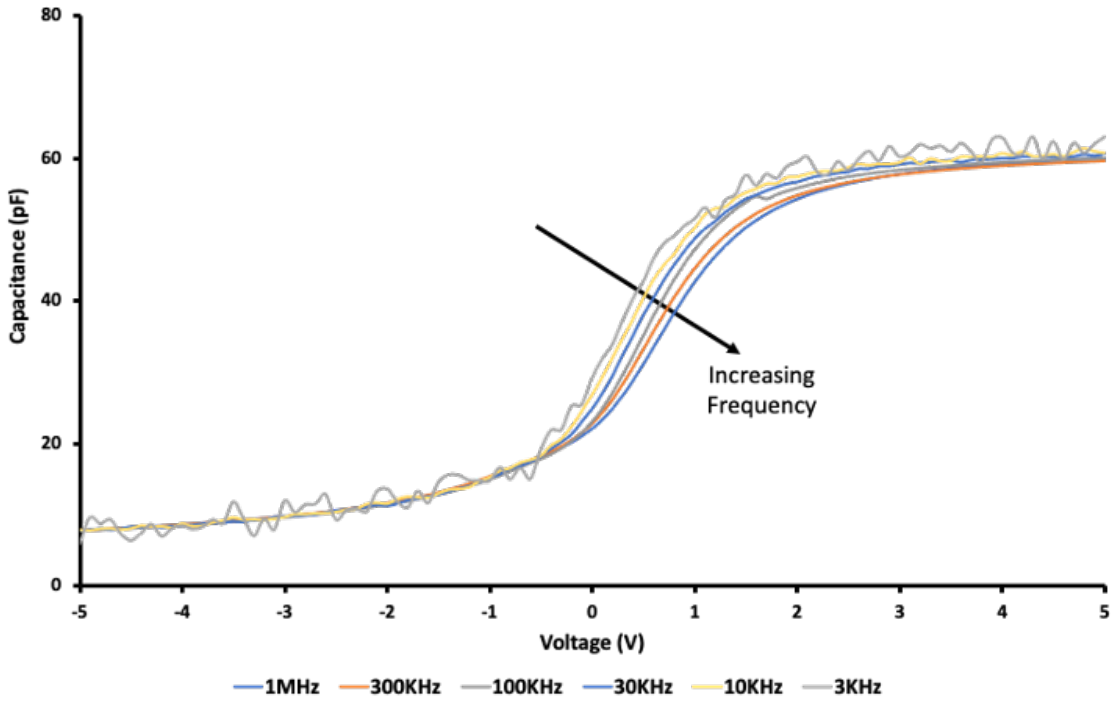

Figure 5.3: C-V characteristics extracted from a $Pt/HfO_2/SiO_2/SiC$ sensor in room temperature laboratory air at varying frequencies

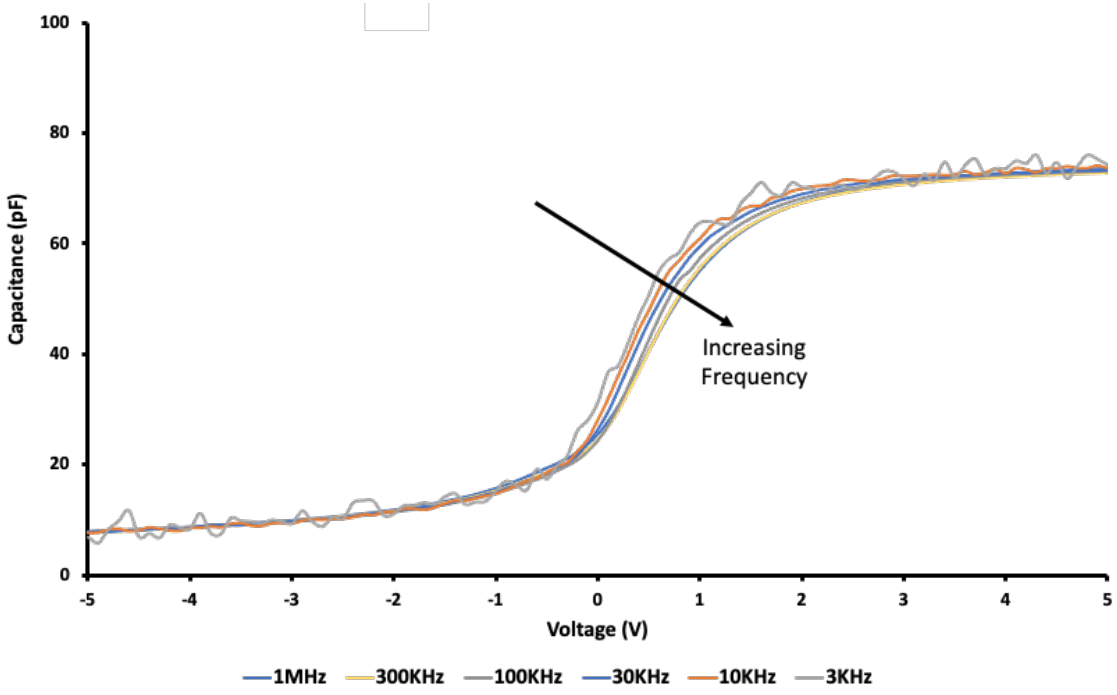

Figure 5.4: C-V characteristics extracted from a $Pt/ZrO_2/SiO_2/SiC$ sensor in room temperature laboratory air at varying frequencies

corrected for series resistance, as due to the high levels of leakage current, this would not be representative of the actual device behaviour.

The values of the series resistance for each dielectric layer has been calculated

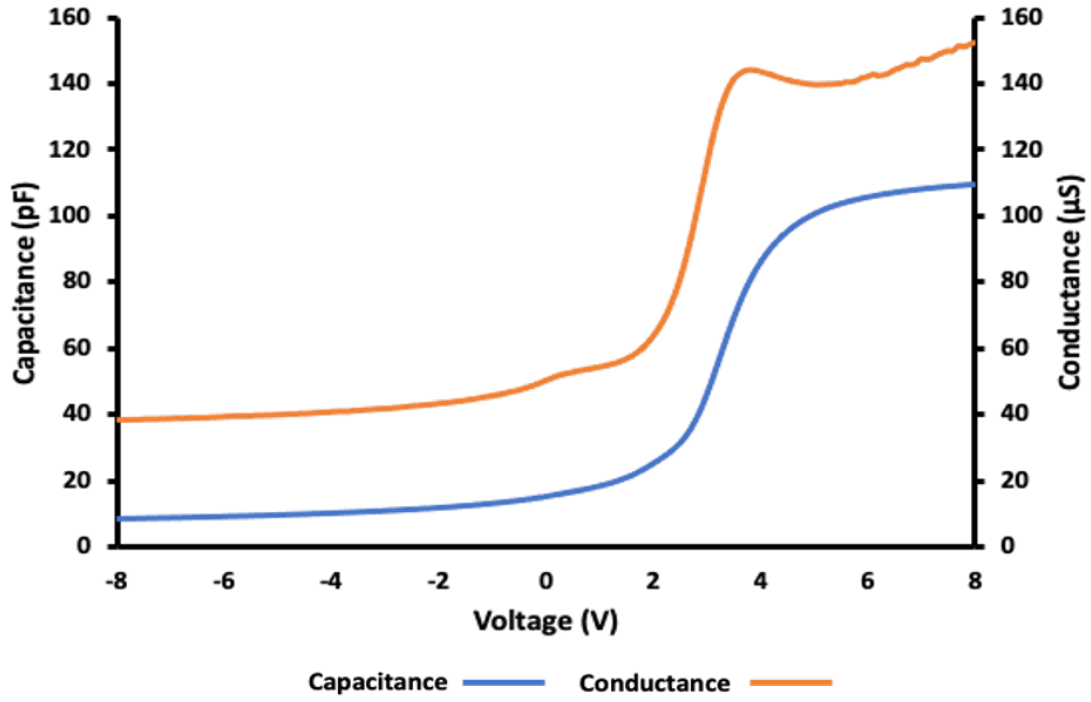

Figure 5.5: C-V and G-V characteristics extracted from a Pt/WO_3/SiO_2/SiC sensor at 300 K and 1 MHz

and the values can be seen in Table 5.1. These values have been extracted during the process of correction for series resistance, and are therefore representative of the levels of leakage current observed within the device.

Dielectric Material	**Resistance (Ω)**
TiO_2	131.7
HfO_2	51.96
ZrO_2	35.11
WO_3	306.9

Table 5.1: Calculated resistance values for varying dielectric materials

This data shows that the leakage current for tungsten can be described in terms of the series resistance extracted from the corrected C-V data. For tungsten oxide, this is 306.9 Ω, which is double that of the titanium oxide material (131.7 Ω), which in turn is double that of hafnium oxide and zirconium oxide, which are broadly similar to each other. The increased series resistance that has to be corrected in the capacitance data is linked to the leakage current through the dielectric film, because it relates to the in-phase voltage drop in the device due to the flow of current through the insulator. The factor of two difference of series resistance between the

titanium oxide device (that is known to have a significant leakage current), and the tungsten oxide layer, suggests an increase in the leakage current for the tungsten oxide device of at least one order of magnitude. This increased leakage current raises concerns about the incorporation of tungsten oxide into a sensor array, as this leakage current could lead to significant self heating of the device, which could lead to dielectric breakdown and sensor failure. The data suggests that zirconium and hafnium oxide are much more stable dielectrics and would function effectively in an array, Titanium dioxide displays higher levels of series resistance than hafnium and zirconium oxide, but the impact of this could be offset by the high thermal stability of the silicon carbide of the device.

5.3.1 Gas Response of Zirconium Based Sensors

The Pt/ZrO_2/SiC device was tested in the presence of varying amounts of hydrogen and oxygen at 573K (as well as in a nitrogen environment to ascertain a baseline) to determine its sensitivity. This is the first report of the assessment of zirconium based MOS devices for gas sensing in extreme environments reported to date. The data in figures 5.6 and 5.7 show the response of a Pt/ZrO_2/SiC sensor with a continuous gate metal layer, to hydrogen and oxygen containing ambients. It can be seen that oxygen produces a positive shift, and hydrogen produces a negative shift, with respect to the flatband voltage; with the magnitude of this shift increasing with gas concentration.

Zirconium oxide was chosen as the dielectric layer for these tests as zirconium is in the same group of the periodic table as titanium and hafnium, and should therefore demonstrate similar gas sensing behaviour. As previously discussed, a potential solution to improving selectivity to certain gases within a multi-gas environment is the utilisation of a sensor array. Target analytes react differently with different dielectric materials, resulting in varying device sensitivity. Introducing ZrO_2 in addition to TiO_2 and HfO_2 increases the opportunity of forming a sensor array. It is therefore important to test the device behaviour in O_2 and H_2 to enable a direct comparison with other dielectric materials and data in the literature.

Traditionally TiO_2 is a defect rich material that impacts the ability of the device to detect gases (a property which can be exploited within an array to improve analyte selectivity) [4, 5]. Hafnium has proven to be a more stable dielectric material with fewer oxide traps, so identical tests were carried out zirconium oxide based devices to benchmark its use as the dielectric later.

Exposure to H_2 negatively shifts the C-V curve along the voltage axis, causing a reduction in the flatband voltage and oxide capacitance. H_2 adsorbs to the device, migrates through to the dielectric layer, and passivates defects within the oxide,

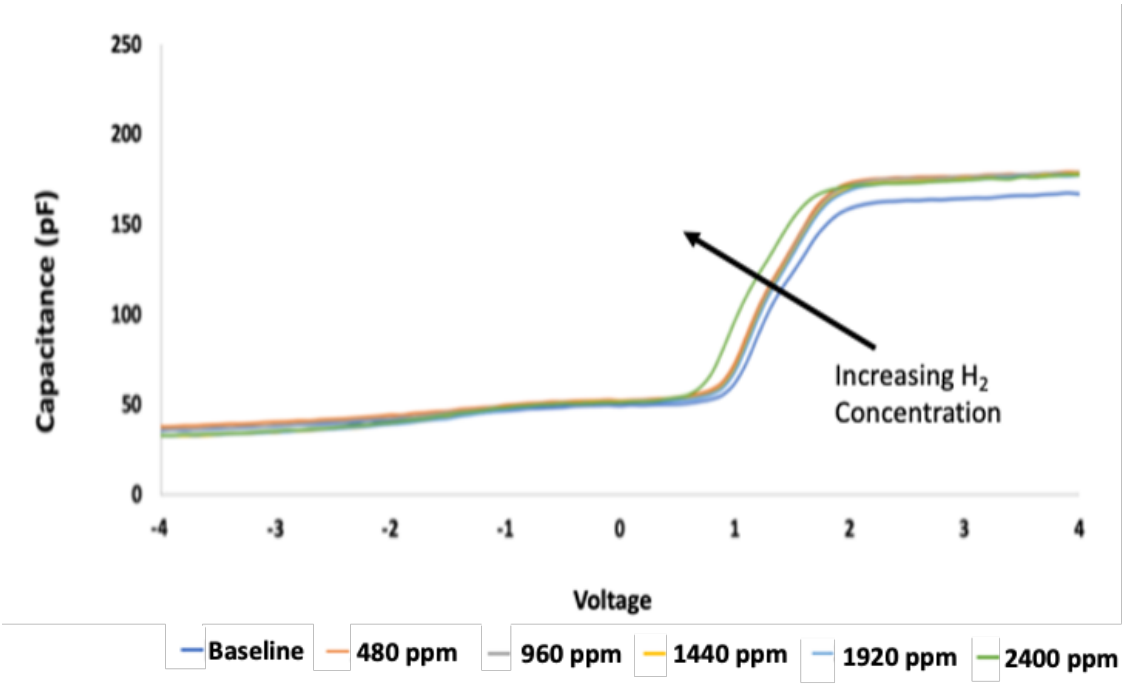

Figure 5.6: C-V characteristics of $Pt/ZrO_2/SiC$ sensor to varying concentrations of hydrogen at 573K

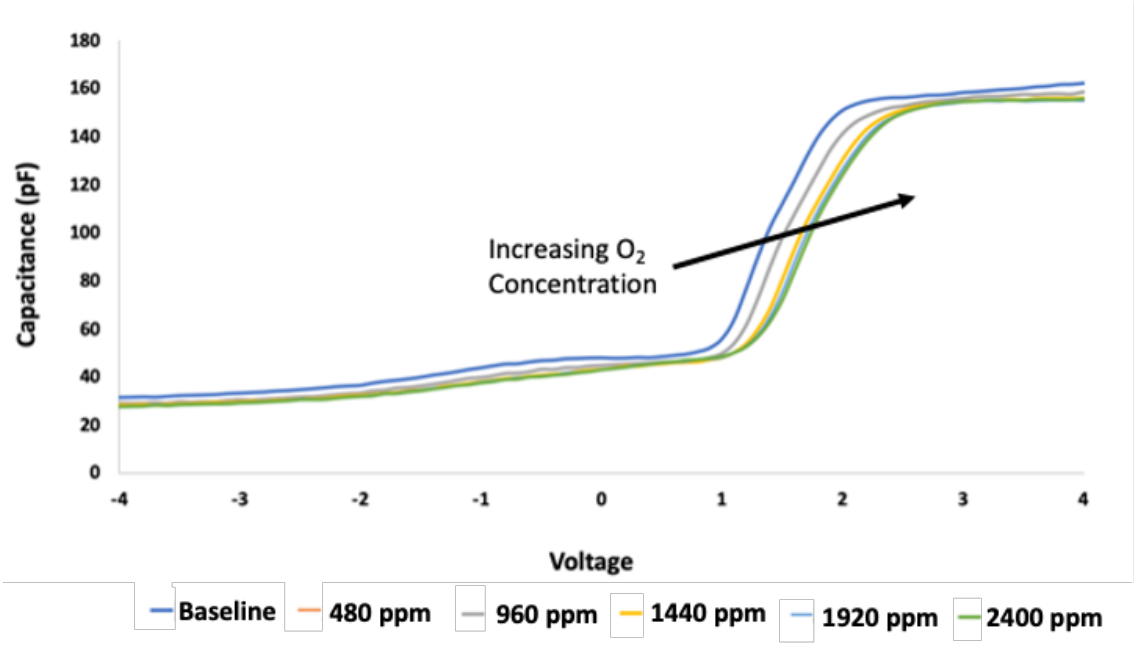

Figure 5.7: C-V characteristics of $Pt/ZrO_2/SiC$ sensor to varying concentrations of oxygen at 573K

resulting in an reduction of V_{FB}. The opposite is observable when the sensor is exposed to O_2 as oxide charge is increased with adsorption and the flatband voltage is increased (as per Equation 5.1). The same response is seen with hafnium and titanium based devices [6, 7].

These tests were repeated and the percentage response was plotted as a function

of bias voltage. Percentage response is defined as the change in capacitance at a certain bias voltage, induced by changes in the atmospheric environment of the device (i.e. influence of gas analytes). This is calculated using Equation 5.2, where $C_{Measured}$ is the capacitance taken during exposure to analyte gas and $C_{Baseline}$ is the capacitance measured in a N_2 atmosphere.

$$\%Response = \frac{C_{Measured} - C_{Baseline}}{C_{Baseline}} \tag{5.2}$$

Figure 5.8 shows the percentage response of the device when exposed to increasing concentrations of hydrogen and oxygen (an anomalous result at 1920 ppm O_2 was omitted from the data set). It can be seen that the data form a bell-shaped curve with a peak for H_2 around 1.1V and a peak for O_2 around 1.4V. This indicates that capacitance can be measured at these voltages in order to determine the response of the sensor to these specific analytes.

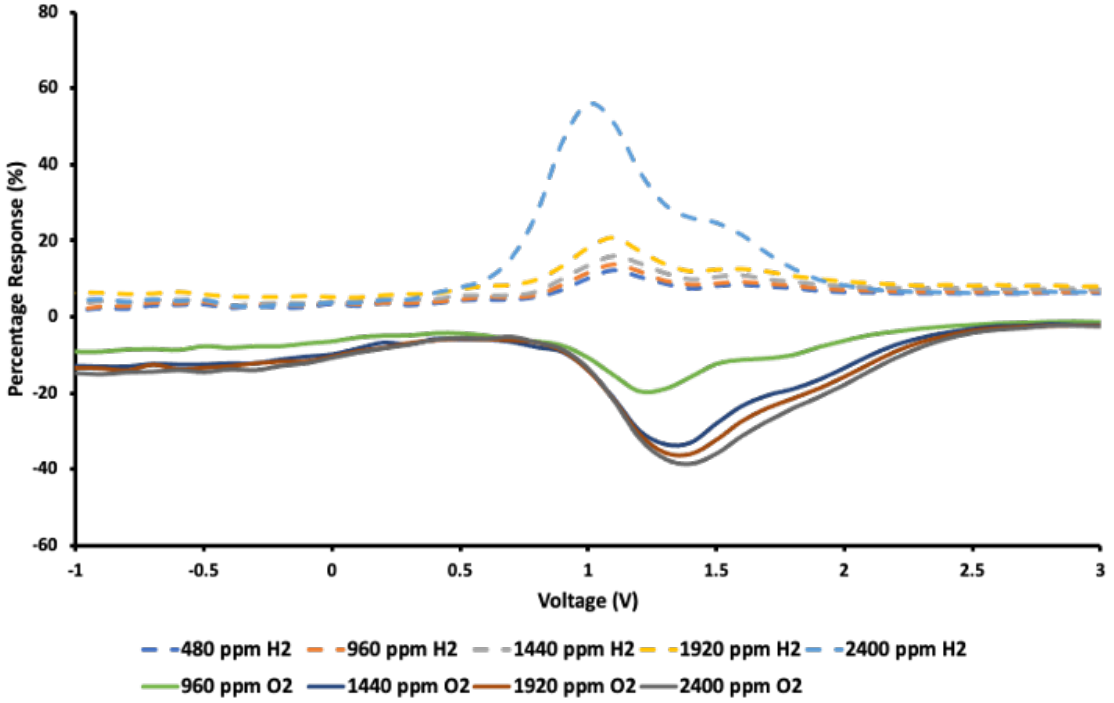

Figure 5.8: Percentage response of $Pt/ZrO_2/SiC$ sensor to varying concentrations of hydrogen and oxygen at 573K

The discrepancy between the voltage values of the hydrogen and oxygen peaks raises an issue when mobilising the sensors in a multi-gas environment. This is due to the voltage value providing maximum sensitivity varying between gases. In order to ensure maximum sensitivity and selectivity to certain gases, an array has been proposed, and in order to exploit this to the fullest extent, the voltage levels must be controllable. The data in Figure 5.8 supports this suggestion as maximum sensitivity is observably different for each gas. If an array is to be used effectively, the

circuitry must allow modulation of voltage levels to improve sensitivity to specific target gases. The most optimum voltage values for each gas can be determined by benchmarking via a voltage sweep. For the sensors tested in Figure 5.8, this would be 1.1V for H_2 and 1.4V for O_2.

Efforts were made to monitor the saturation and normalisation behaviour of the $Pt/ZrO_2/SiC$ device in the presence of oxygen and hydrogen. These are important factors to consider if the devices are to be used in real-time monitoring within the engine environment, as the sensors need to be able to take repeatable, reliable measurements. Hydrogen and oxygen concentrations were increased periodically by 480 ppm (5%) and the capacitance at the baseline flatband voltage was monitored. After 40 minutes, oxygen and hydrogen flows were switched off and the devices were exposed to laboratory air. Figures 5.9 and 5.10 show the hydrogen and oxygen response, respectively.

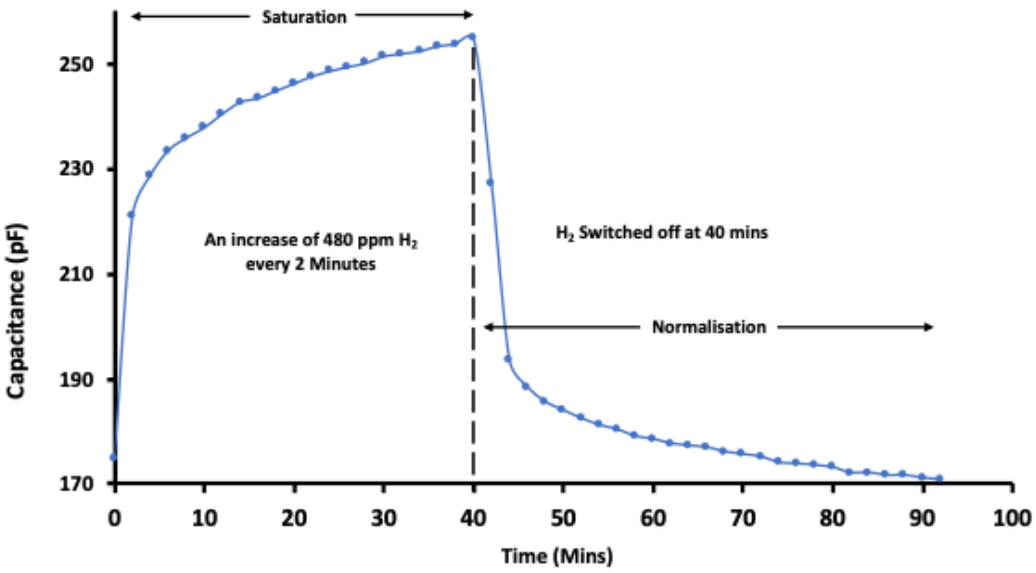

Figure 5.9: Capacitance measured at flatband voltage of a $Pt/ZrO_2/SiC$ sensor exposed to varying concentrations of hydrogen over time and subsequent normalisation upon switch off (573K)

After an initial large increase in capacitance upon exposure to 480 ppm H_2, the device then follows a steady pattern, with a roughly uniform increase in capacitance per 480 ppm of gas. The device responds very quickly to the presence of the analyte gas and 57% of the overall device response is observed when exposed to 960 ppm, after 4 minutes. Once the H_2 is switched off, there is a dramatic drop in capacitance due to the immediate dissociation of hydrogen molecules from the device, prior to steady normalisation back down to the baseline capacitance (within experimental error). Similar devices are often encouraged to return to the baseline capacitance

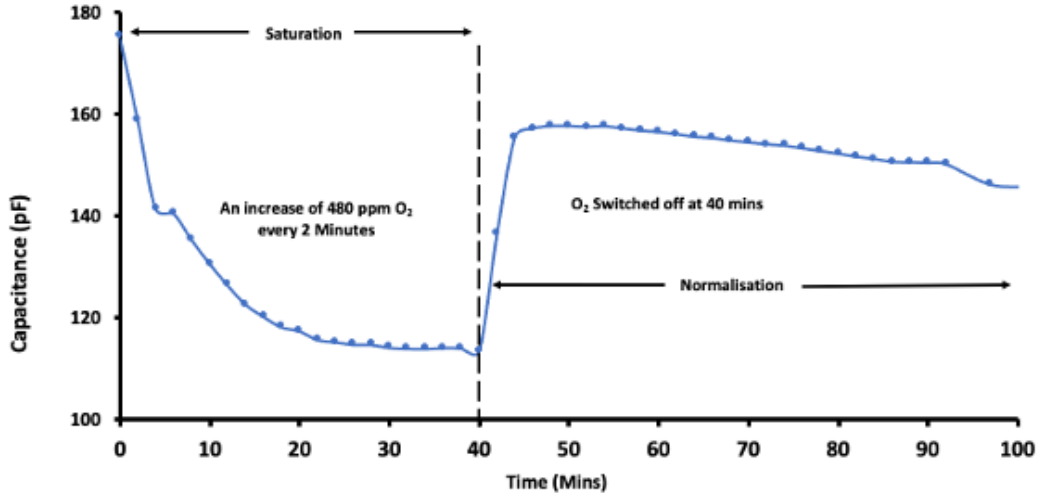

Figure 5.10: Capacitance measured at flatband voltage of a $Pt/ZrO_2/SiC$ sensor exposed to varying concentrations of oxygen over time and subsequent normalisation upon switch off (573k)

value by heating, to discourage dissociation of any gas molecules on the device. Direct heating of the sensors is possible due to the temperature stability of the SiC substrate.

The pattern of capacitance change with increasing levels of hydrogen over the initial 40 minute exposure stage follows the Langmuir isotherm model [8]. This is a model which describes the adsorption of molecules onto a solid surface, and the hydrogen-platinum system has been extensively investigated. The two key assumptions of this model is that the likelihood of an adsorption on any site on the platinum surface is equal and that there is a limited number of adsorption sites, hence saturation is observed once all sites are filled. Comparing this data with the literature, it can be seen that there is a relationship between capacitive response and hydrogen adsorption to platinum. Figure 5.11 shows the adsorption isotherms of dissociative adsorption onto platinum particles with increasing pressures of hydrogen at varying temperatures [9]. The behaviour is analogous to that observed when the $Pt/ZrO_2/SiC$ device was exposed to increasing ppm of hydrogen - 9600 ppm over the initial 40 minute exposure period.

Similar behaviour is observed for the device when it is exposed to O_2, with an initial large drop in capacitance at 480 ppm and 960 ppm of O_2 (54% of the overall response). Saturation is then reached at a steady state with increasing oxygen concentration before the analyte gas is removed from the testing chamber at 9600 ppm (40 minutes). It can be seen that this device doesn't return to the baseline value of capacitance and this sensitivity drift will affect the longevity of the sensors.

The initial, rapid, response of both devices is due to direct physisorption of the

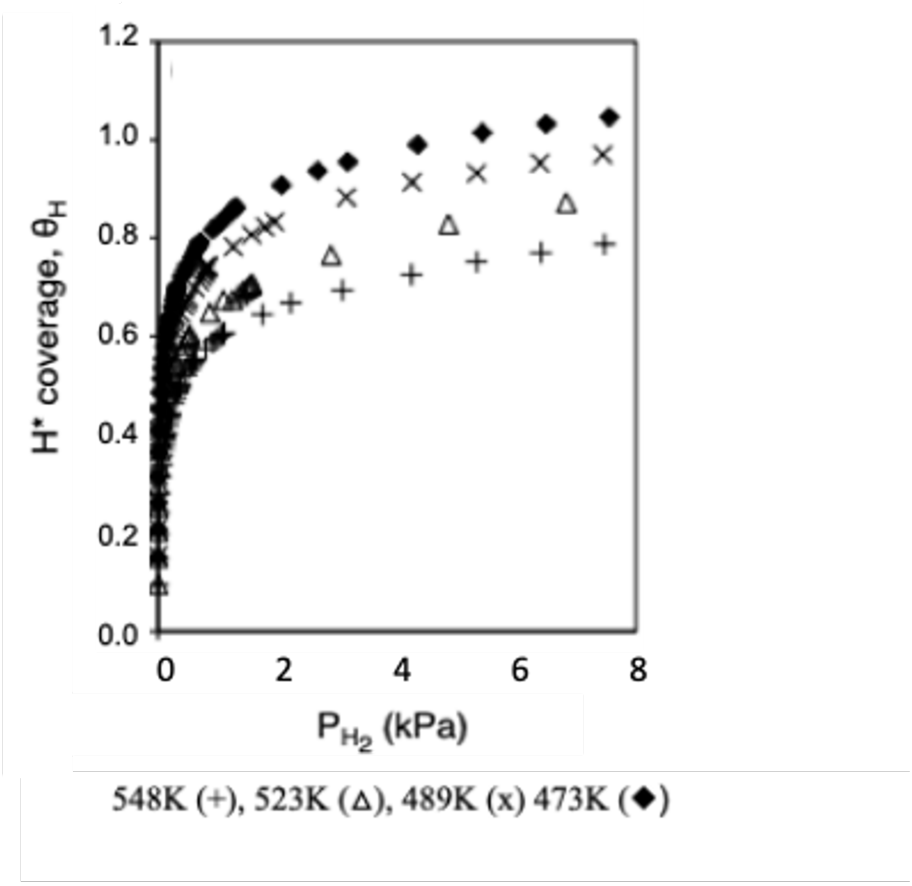

Figure 5.11: Hydrogen coverage of platinum particles with increasing gaseous pressure at varying temperatures [9]

gases to the platinum surface, the subsequent response is due to chemisorption and migration of gases through the platinum layer. The impact of physisorption contributes to 57% and 54% of the total response for hydrogen and oxygen respectively. The same phenomenon is observable when the gas flow was ceased and the device was exposed to laboratory air, the initial rapid changes in capacitance is caused by the dissociation of physisorbed molecules [10, 11, 12, 13].

5.3.2 Temperature Dependent Gas Response

The ambient temperature of the environment in which a gas sensor is operating has an impact on the response. The behaviour of some dielectric materials are temperature dependent and this has proven to be restrictive in certain operating conditions. For example, traditional zirconium oxide based lambda sensors require an elevated temperature to function and are often fitted with a heating element to aid this. This means that detection is not available in colder conditions, for example when the engine is first engaged. Emissions of NOx, CO and hydrocarbons

are greater when the engine is ignited under cold-start conditions, therefore if the sensor is unable to operate in these cooler conditions, detection of some pollutants will be missed. It is therefore important to analyse the behaviour of these sensors under varying temperatures.

The choice to use silicon carbide as the semiconductor substrate for these devices means that sensors can be deployed closer to the combustion site of the diesel engine, meaning that they will be exposed to higher temperatures almost instantly after ignition, which will not rule out the use of ZrO_2 as the dielectric layer.

Tests were carried out to confirm the influence of temperature on a $Pt/ZrO_2/SiC$ device. Figure 5.12 shows the behaviour of a $Pt/ZrO_2/SiC$ device at 300 K in the presence of increasing concentrations of oxygen.

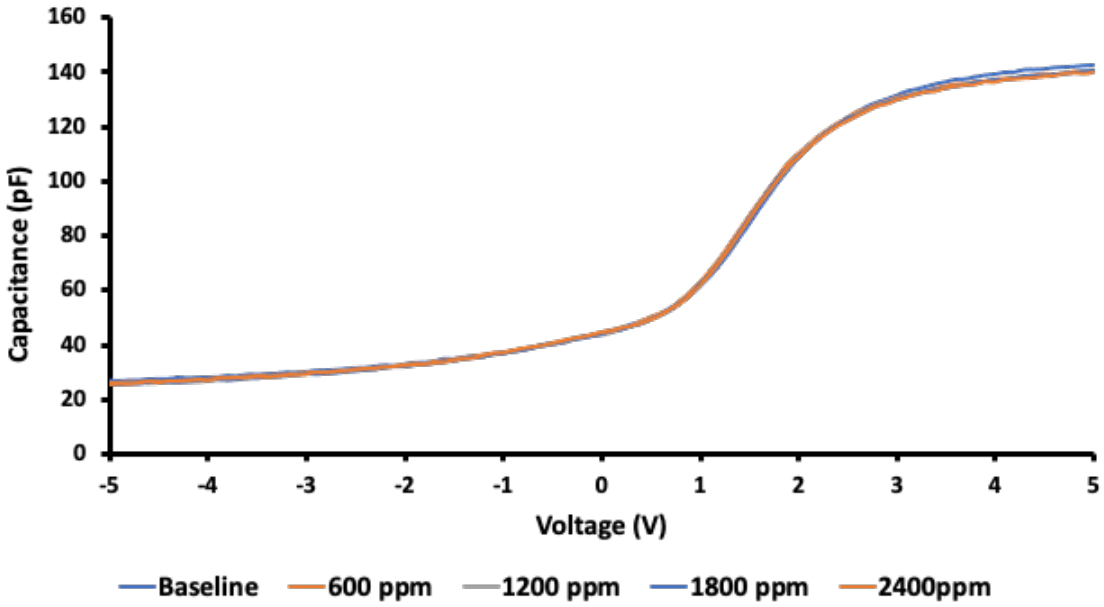

Figure 5.12: Response of $Pt/ZrO_2/SiC$ sensor to oxygen at 300K

At 300 K, it can be seen that there is no observable shift in the capacitance-voltage curve at any concentrations of O_2 as the temperature is not high enough to allow interaction between analyte gases and the dielectric material.

However, it can be seen, that when the temperature is increased to 573K, the device exhibits a measurable response which is proportional to the percentage of oxygen present, as shown by the data in Figure 5.13. Table (5.2) shows the impact that oxygen concentrations have on the flatband voltage of the device. There is a positive shift in the flatband voltage with increasing levels of oxygen and the percentage response can be measured. Previous work in the literature shows that the response time of devices decreases with increasing temperatures, due to faster rates of interaction between gas molecules and the catalytic gate metal [14, 15, 16].

The response of this device at 300 K and 573 K was calculated and plotted as

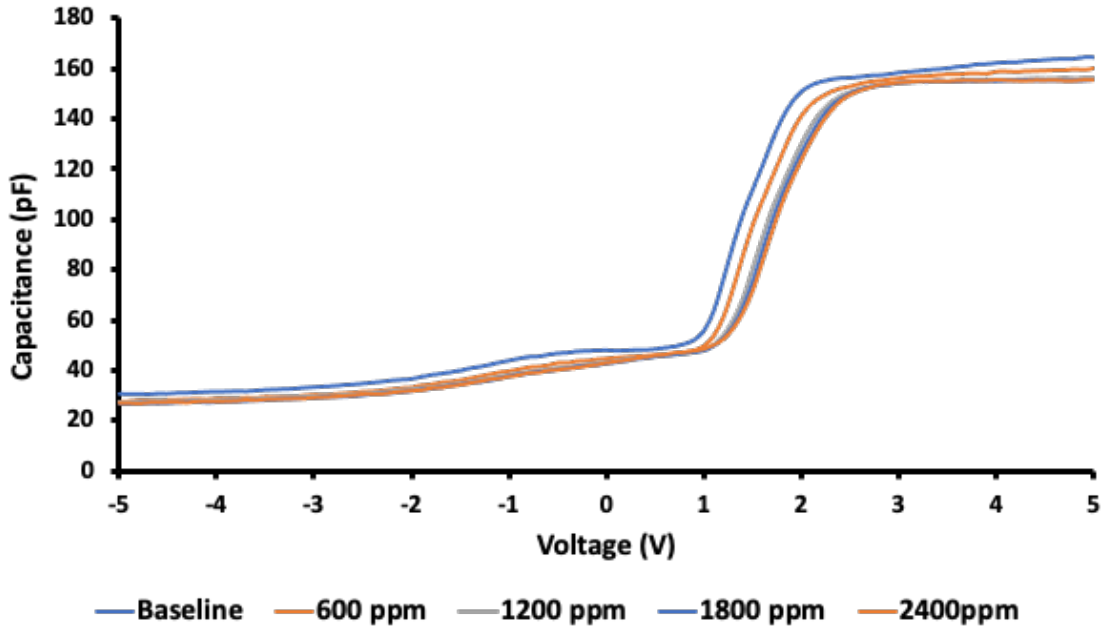

Figure 5.13: Response of $Pt/ZrO_2/SiC$ sensor to oxygen at 573K

a function of bias voltage. Figure 5.14 shows this and, within experimental error, demonstrates that there is no observable response for the tests carried out at 300 K, confirming that the device is not sensitive to oxygen at 300 K. When the temperature is increased to 573 K, the anticipated response is observable with a peak at around 1.4V. Figure 5.15 shows the peak response of the $Pt/ZrO_2/SiC$ device at 300 K and 573 K extracted at 1.4V, confirming that there is no observable response at 300 K, and a positive correlation between response and gas concentration at 573K.

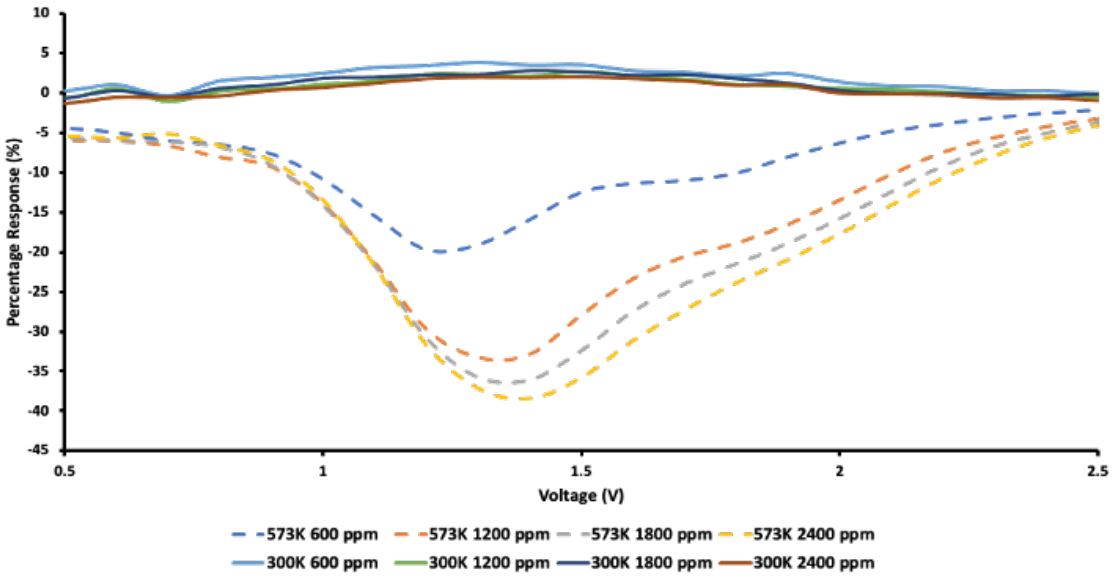

Figure 5.14: Percentage response of $Pt/ZrO_2/SiC$ sensor to varying concentrations of oxygen at 300K and 573K

Oxygen Concentration	Flatband Voltage (V)
Baseline	1.40
600ppm	1.50
1200ppm	1.60
1800ppm	1.65
2400ppm	1.70

Table 5.2: Flatband Voltage of $Pt/ZrO_2/SiC$ device in response to varying oxygen concentrations at 573K

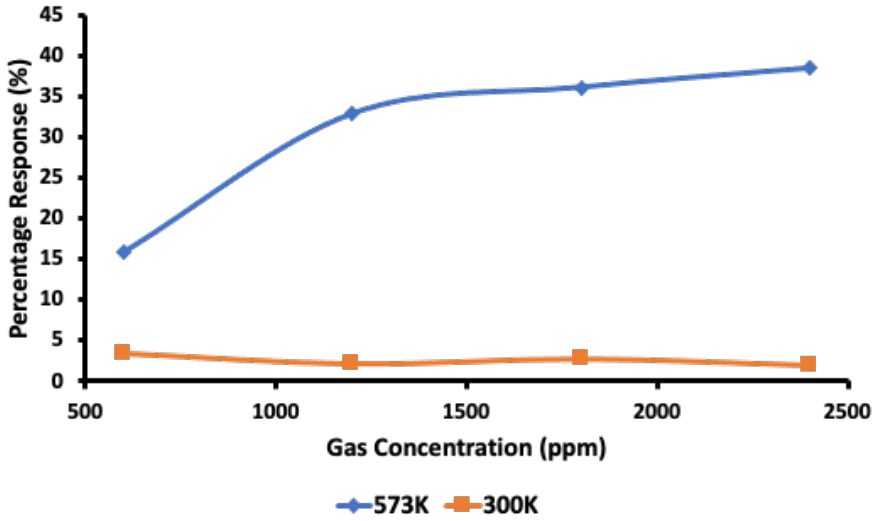

Figure 5.15: Peak response of $Pt/ZrO_2/SiC$ sensor to varying concentrations of oxygen at 300K and 573K, taken at 1.4V

5.3.3 Gaseous Response of Other Dielectrics

Previous work has demonstrated that a $Pt/HfO_2/SiC$ device is responsive to hydrogen, but unresponsive to oxygen. The capacitance-voltage response of the device to 2300 ppm Hydrogen is shown below in Figure 5.16, and the response to varying concentrations of H_2 and O_2 is shown in Figure 5.17. This successful response of the device to 230 ppm of hydrogen is promising for the potential of array manufacturing, as the sensor was created using identical reaction methods as devices based TiO_2 and ZrO_2.

Figure 5.17 shows that the $Pt/HfO_2/SiO_2/SiC$ device is highly selective to hydrogen, and shows no response to oxygen at 575K. This further supports the suggestion that an array device could be used, to improve selectivity. Discrimination between hydrogen and oxygen can be achieved through the use of a $Pt/ZrO_2/SiO_2/SiC$ and

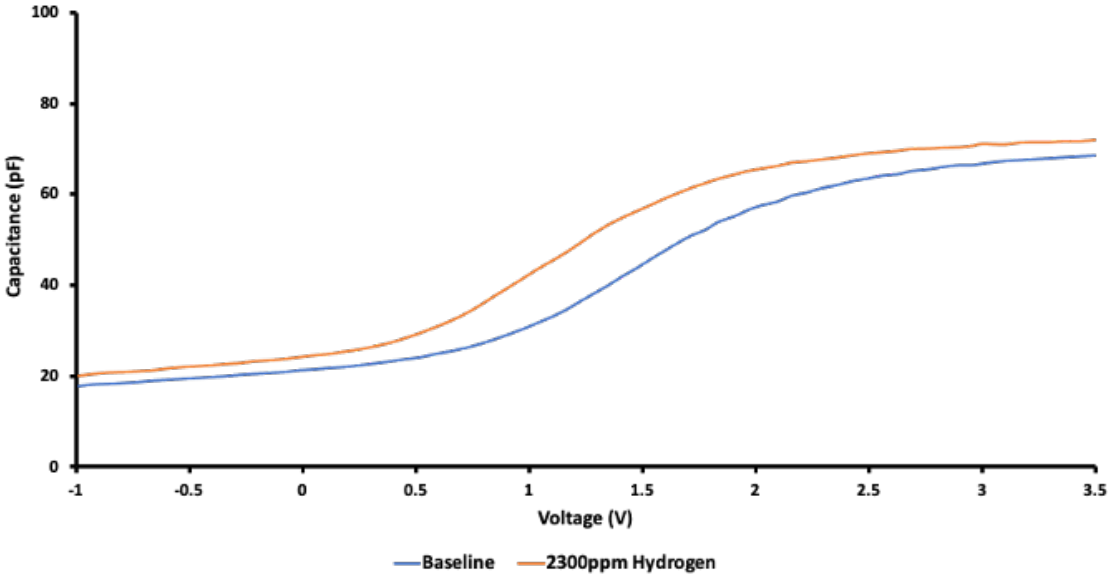

Figure 5.16: C-V Characteristics extracted from a Pt/HfO_2/SiC sensor exposed to 2300ppm H_2 at 573K

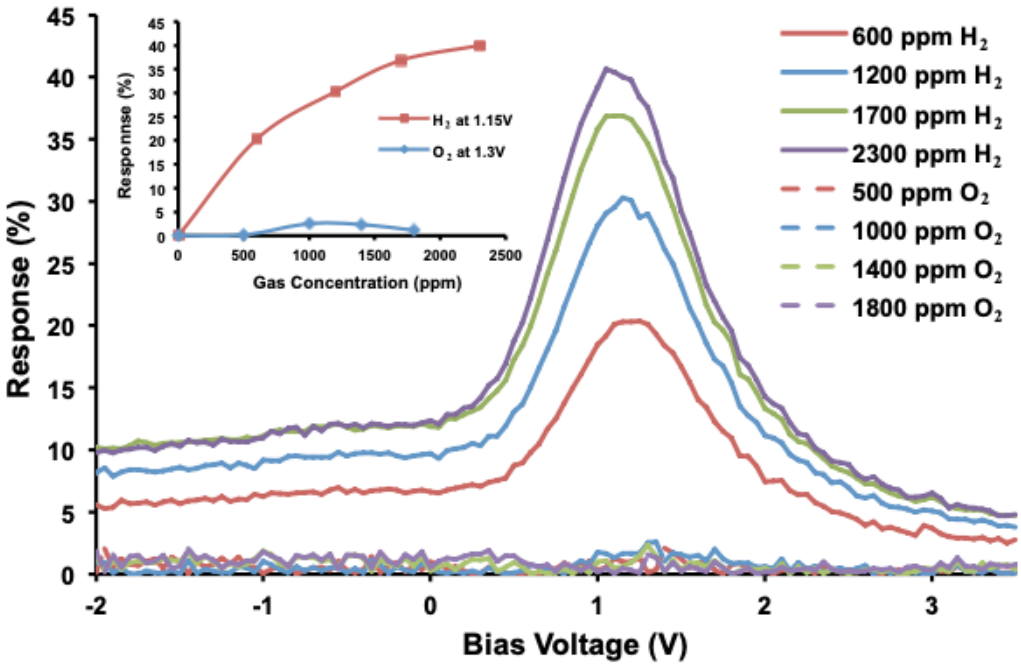

Figure 5.17: Response of the Pt/HfO_2/SiO_2/SiC sensors capacitance to H_2 and O_2 vs. bias voltage at 573K (Inset) Peak response vs. gas concentration [17]

Pt/HfO_2/SiO_2/SiC array at 573K. Further tests need to be carried out to determine selectivity to NOx.

The data presented in this section confirms the potential of utilisation of a sensor array, with varying dielectric materials (HfO_2, TiO_2 and ZrO_2) in hydrogen and oxygen rich environments. The different responses demonstrated by these devices in

varying conditions enable the unique identification of gas concentrations and allow the extraction of the component gases within an ambient. The comparable sensor manufacturing method allows manufacture of a monolithically integrated sensor array reducing the complexity of the circuitry required.

5.3.4 Initial Tungsten Oxide Device Gas Results

$Pt/WO_3/SiO_2/SiC$ devices were fabricated as per the method outlined in Section 5.2. The capacitance voltage characteristics were then extracted in air at 10 kHz at 573 K, and this is shown in Figure 5.18.

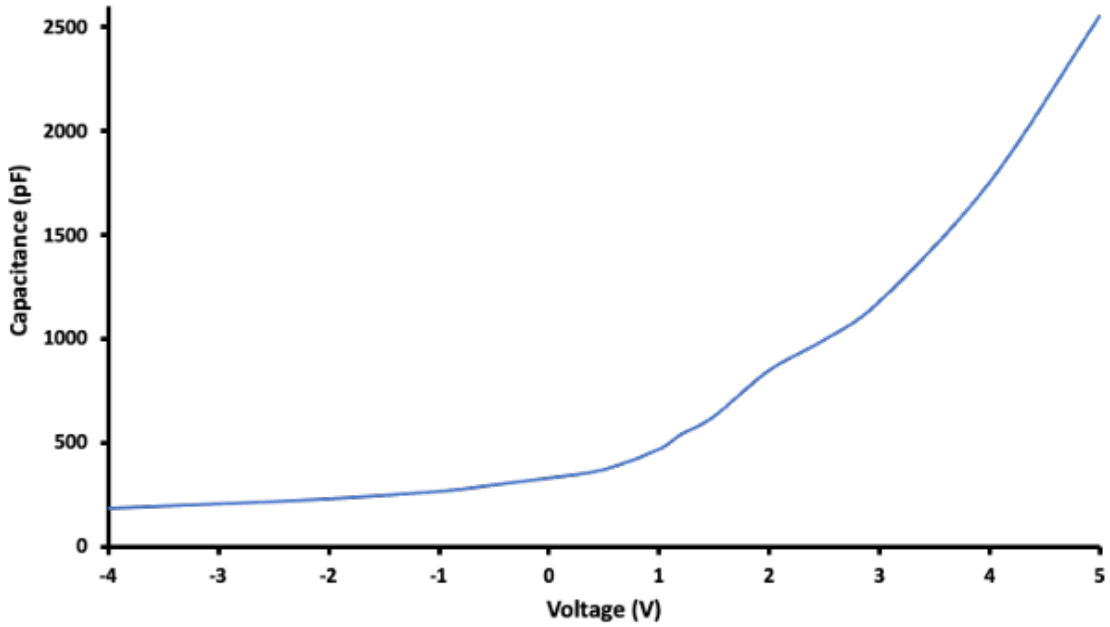

Figure 5.18: C-V characteristics of a $Pt/WO_3/SiO_2/SiC$ device taken in air at 10kHz at 573K

The C-V profile in Figure 5.18 shows that this device is not behaving as a true capacitor and is experiencing large leakage currents. This could be caused by interaction between the WO_3 and SiO_2 layers.

For this device, the flatband voltage appears to be around 2V, which is significantly lower than the flatband voltage of the same device taken at 300 K and 1 MHz (Figure 5.5). This shift as a result of temperature suggests could lead to complications if deployed in extreme environments, as temperature appears to influence the flatband voltage. Further tests are needed to confirm the temperature stability of WO_3 based devices. These tests were written into the experimental plan that was agreed with the University of Mons, but due to the Covid-19 pandemic, were unable to be carried out.

The fabrication process has likely led to an amalgamation of the two oxide layers

forming a, defect heavy, $Si_xW_yO_z$ type material (See Figure 5.19). This material is not an insulator, leading to the high levels of leakage demonstrated.

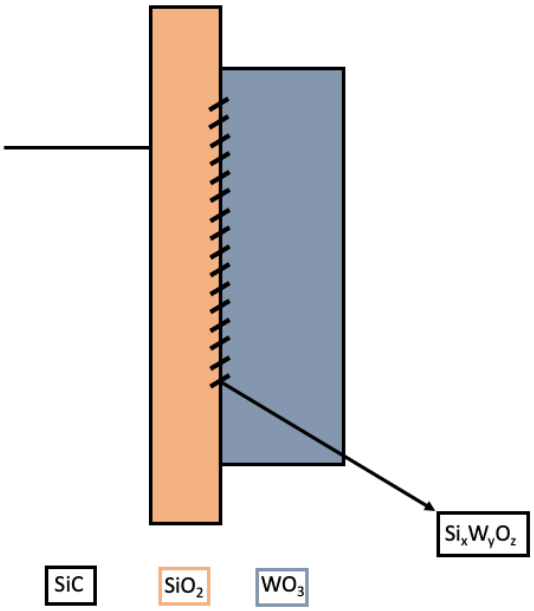

Figure 5.19: Energy band diagrams of SiC/SiO2$_2$/WO$_3$

The same device was then exposed to 20 ppm of NO gas, and a C-V sweep was taken at 10 kHz, see Figure 5.20.

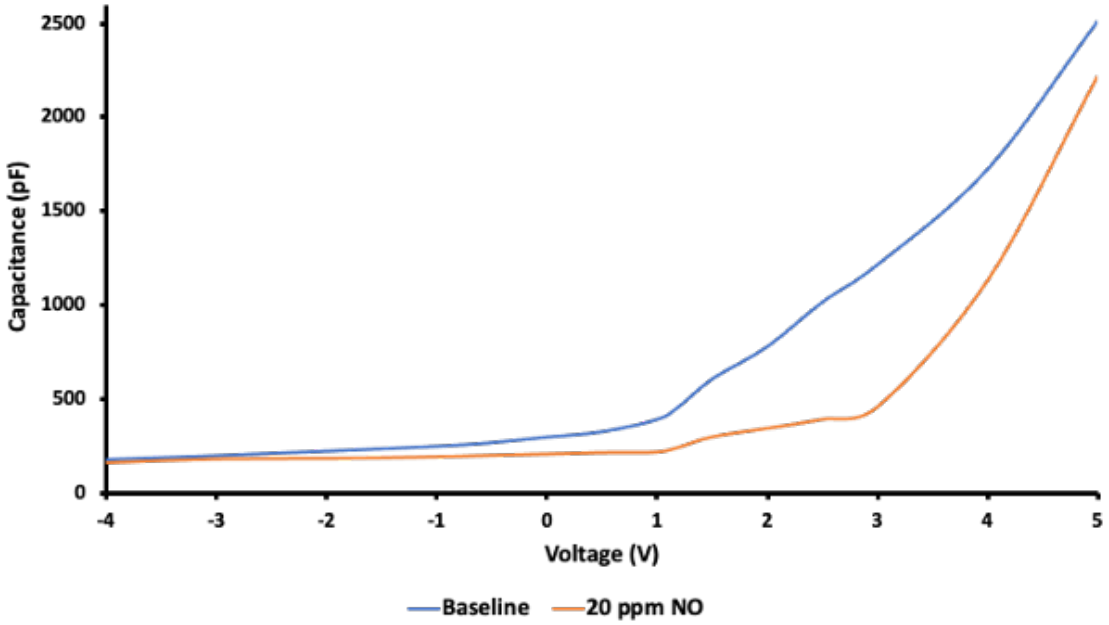

Figure 5.20: C-V characteristics of a Pt/WO_3/SiO_2/SiC device taken when exposed to air and 20 ppm of NO, at 10kHz at 573K

The device does not display a capacitive response, but there is an observable shift in the characteristics when the sensor is in the presence of 20 ppm nitric

oxide gas. This shows that the devices can be used to detect the presence of nitric oxide at moderately high temperatures, but raises questions about the mechanism of sensor-gas interaction. One mechanistic theory is that NOx could be passivating defect states created within the fabrication process, increasing the levels of trapped charge within the system. This could lead to the potential of utilising these devices in an array with previously demonstrated devices, creating a system capable of detecting multiple target gases. In order to do this, a suitable bias voltage would need to be selected in order to observe a response from each device based on varying dielectric materials. It is essential to pick a bias voltage that allows demonstration of sensitivity, and comparing the data in Figures 5.8, 5.17 and 5.20, a reasonable suggestion would be 1.3V as a clear response can be seen at this voltage for devices based on ZrO_2, HfO_2 and WO_3 respectively.

Further work will need to be carried out in order to ascertain the most appropriate interrogation method and circuitry for sensor arrays, due to competing detection mechanisms occurring.

Bibliography

[1] W D Westwood. "Porosity in sputtered platinum films". In: *Journal of Vacuum Science and Technology* 11 (1 1974), pp. 466–471.

[2] A Keffous et al. "40Å Platinum–porous SiC gas sensor: Investigation sensing properties of H2 gas". In: *Physica B: Condensed Matter* 408 (2013), pp. 193–197.

[3] Narendra Singh, Arvind Kumar, and Davinder Kaur. "Hydrogen gas sensing properties of platinum decorated silicon carbide (Pt/SiC) Nanoballs". In: *Sensors and Actuators B: Chemical* 262 (2018), pp. 162–170.

[4] Ming-Hung Weng et al. "Trap-Assisted Gas Sensing Mechanism in Pd-TiO2-SiO2-SiC Capacitors at High Temperatures". In: *IEEE Sensors Journal* 7 (10 Oct. 2007), pp. 1395–1399.

[5] Xu Tian et al. "Gas sensors based on TiO2 nanostructured materials for the detection of hazardous gases: A review". In: *Nano Materials Science* (2021).

[6] Leila Fekri Aval and Smohammad Elahi. "Hydrogen gas detection using MOS capacitor sensor based on palladium nanoparticles-gate". In: *Electronic Materials Letters* 13 (Jan. 2016).

[7] B. J. D. Furnival, N. G. Wright, and A. B. Horsfall. "Discriminating gas concentrations in extreme temperature environments". In: IEEE, Oct. 2011, pp. 1044–1047.

[8] Irving Langmuir. "The Constitution and Fundamental Properties of Solids and Liquids. Part 1. Solids". In: *Journal of the American Chemical Society* 38 (11 1916), pp. 2221–2295.

[9] Monica Garcia-Dieguez, David D Hibbitts, and Enrique Iglesia. "Hydrogen Chemisorption Isotherms on Platinum Particles at Catalytic Temperatures: Langmuir and Two-Dimensional Gas Models Revisited". In: *The Journal of Physical Chemistry C* 123 (13 Apr. 2019), pp. 8447–8462.

[10] Graeme W. Watson et al. “A Comparison of the Adsorption and Diffusion of Hydrogen on the {111} Surfaces of Ni, Pd, and Pt from Density Functional Theory Calculations”. In: *The Journal of Physical Chemistry B* 105 (21 May 2001), pp. 4889–4894.

[11] R Lewis and R Gomer. “Adsorption of hydrogen on platinum”. In: *Surface Science* 17 (2 1969), pp. 333–345.

[12] R Lewis and R Gomer. “Adsorption of oxygen on platinum”. In: *Surface Science* 12 (2 1968), pp. 157–176.

[13] T Zambelli et al. “Complex pathways in dissociative adsorption of oxygen on platinum”. In: *Nature* 390 (6659 1997), pp. 495–497.

[14] A Lloyd Spetz et al. “High Temperature Sensors Based on Metal–Insulator–Silicon Carbide Devices”. In: *physica status solidi (a)* 162 (1 July 1997), pp. 493–511.

[15] P Tobias et al. “Millisecond response time measurements of high temperature gas sensors”. In: Nov. 2004, 770–771 vol.2.

[16] Gheorghe Brezeanu et al. *High temperature sensors based on silicon carbide (SiC) devices*. Oct. 2015, pp. 3–10.

[17] B.J.D Furnival. “Silicon Carbide Based Gas Sensor Arrays For Deployment Within Hostile Environments”. In: (2012).

Chapter 6

Conclusion

This work has demonstrated the fabrication of silicon carbide based metal oxide semiconductor devices, with varying identities of dielectric oxide layers and platinum gate metal morphology.

Previous work has shown the use of hafnium oxide and titanium oxide-based devices as suitable sensors for simple diatomic gas molecules such as hydrogen and oxygen. In order to encourage the detection of more complex analytes found in the harsh environment of a diesel engine, changes to the dielectric oxide layer and gate metal are required. Work in Chapter 3 determined optimal device fabrication conditions.

Complex gases require the presence of triple points on the device surface, and these exist due to porosity within the gate metal layer. Therefore an investigation was carried out to determine the optimum sputtering conditions required to deposit platinum films with the required level of porosity. This work has confirmed that there is a direct and proportional relationship between the argon pressure in the PVD sputter chamber, and the observed levels of porosity in the platinum films, with higher pressures producing more porous layers.

Six, 70nm layers of platinum were deposited on 10x10 mm oxidised silicon wafers via DC sputtering, under varying pressures of argon in the sputtering chamber. A linear relationship was seen between sputtering pressure and porosity, and a pressure of 140 mTorr was determined as optimal for producing layers of platinum with good sample coverage and levels of porosity.

The sputtering power was also manipulated to observe the impact on porosity levels. Deposition at higher powers produces more uniform and therefore less porous films due to the increased thermal energy of the system. This energy leads to recrystallisation of the platinum films to more uniform layers - sputtering was carried out at 50 W and 150 W to confirm this. As a result of this work, the optimal platinum sputtering conditions were identified to be an argon pressure of 140 mTorr of and a power of 50 W.

In order to target nitrogen oxides, a tungsten dioxide dielectric layer was incorporated into the metal-oxide-semiconductor structures, and work was undertaken to find the optimal conditions for the growth of these WO_3 films. Raman spectroscopy was used to validate the conversion of tungsten films into WO_3 upon heating in air. Analysis of peak intensity and surface roughness, extrapolated from Atomic Force Microscopy (AFM) images, indicated that a duration of 10 minutes sufficed for complete oxidation.

In-depth mechanistic insights into the growth of WO_3 were established by oxidising six films across a temperature range spanning 300 to 900°C. The Raman peaks at 720 and 820 cm^{-1} exhibited an amplified intensity with increasing oxidation temperature, signifying the formation of a tungsten oxide layer. This observation was substantiated by a observable linear correlation between surface roughness and oxidation temperature. AFM analysis of the oxidised films revealed a distinct change in morphology when the oxidation temperature surpassed 500°C. Prior to this threshold, uniform films with a maximum Root Mean Square (RMS) value of 3.65 nm were produced. However, at 600°C, the emergence of surface clusters resulted in an elevation of surface roughness and amplitude (RMS of 16 nm).

Using films oxidised at 500, 600, and 700°C, devices were fabricated, and critical parameters were extracted. Notably, values of C_{max} and G_{max} remained consistent regardless of oxidation conditions. Conversely, a noteworthy observation was made regarding the linear escalation in the density of interface traps with rising oxidation temperature. This phenomenon was associated with the morphology of the grown films, as harsh oxidation conditions yielding less uniform films appeared to have a greater number of traps.

The implications of this study confirmed an optimal oxidation temperature of 500° for tungsten. At this temperature, a uniform film is generated with minimal trap density, suggesting the practicality of adopting this methodology for future applications in tungsten oxide film fabrication.

More detail into the mechanistic behaviour of metal oxide semiconductor devices was determined in Chapter 4, with devices being used to detect a range of organic solvents.

It was demonstrated that a $Pt/TiO_2/SiO_2/4H\text{-}SiC$ device can be used as an effective solvent sensor at room temperature. This device was exposed to isopropyl alcohol, water, ethylene glycol, acetic anhydride, di-methyl formamide, and n-methyl-2-pyrollidone in an enclosed environment at room temperature, and electrical characteristics were monitored. All of the solvents produced a change in capacitance at the flatband voltage, but the magnitude of this change varied depending on solvent identity.

A positive correlation was observed between the magnitude of response and

the dipole moment of the organic solvent, a trend previously seen in resistometric graphene sensors when exposed to solvents.

This led to the hypothesis that charged defects within the TiO_2 layer might play a significant role in influencing the interaction between the solvent and the device. The proposed mechanistic theory suggests a direct interaction between solvent molecules and the exposed dielectric layer, particularly emphasising the strong interaction between the dipole moment of the solvent and the charged oxygen defects located near the surface of the oxide layer. Solvent molecules adsorb to these defects, inducing charges, thereby causing a shift in the device characteristics.

To substantiate this theory and qualitatively monitor defect concentration over the course of solvent interaction, tests were conducted. C-V profiles were employed to calculate the flatband capacitance, charge value, and subsequently, the trap density of the device when exposed to the solvent. Assuming that charge originates from single trapping states, a trap density of $2.3x10^{17}$ cm^{-3} was determined, comparable to other dielectric films. Additionally, vertical and lateral leakage tests were performed, demonstrating that the solvent alters the density of trapping states in the dielectric. This underscores the importance of careful dielectric film selection in the manufacturing of silicon carbide MOS sensors, considering the nature of defects introduced during the manufacturing process.

Furthermore, utilising Gonon's model, frequency dispersion measurements enabled the calculation of trap density in the presence of laboratory air and NMP. Accounting for the geometric limitations of the device, this method revealed a 4.56 % reduction in trap concentration upon exposure to NMP, providing support for the proposed mechanistic theory.

Work in chapter 5 demonstrated fabrication of a $Pt/ZrO_2/SiO_2$/4H-SiC device, and its subsequent use as a hydrogen and oxygen sensor. This device was fabricated using identical conditions to hafnium and titanium oxide based devices and it was exposed to varying levels of oxygen and hydrogen at 573 K. Oxygen induced a positive shift in relation to the baseline, and hydrogen produced a negative shift, both proportional to the amount of gas present.

We then tested the saturation and normalisation behaviour of the Pt/ZrO_2/SiC device when exposed to oxygen and hydrogen. These aspects are crucial for the practical application of the devices in real-time monitoring within engine environments, requiring sensors to produce repeatable and reliable measurements. Periodic increases in hydrogen and oxygen concentrations by 480 ppm (5 %) were implemented, and the capacitance at the baseline flatband voltage was continuously monitored. Following a 40 minute exposure, the flows of oxygen and hydrogen were ceased, and the devices were subsequently exposed to laboratory air.

The Pt/ZrO_2/SiC device exhibits an initial substantial increase in capacitance

upon exposure to 480 ppm H_2, followed by a consistent, roughly uniform increase in capacitance per 480 ppm of gas. The device shows rapid response to the analyte gas, with 57 % of the overall response observed at 960 ppm within 4 minutes. Upon switching off H_2, there is a sharp drop in capacitance due to hydrogen molecule dissociation, followed by steady normalisation back to baseline capacitance.

The pattern of capacitance change with increasing hydrogen levels aligns with the Langmuir isotherm model, indicating saturation on the platinum surface. Similar behavior is observed for the device exposed to O_2, with an initial drop in capacitance at 480 ppm and 960 ppm (54 % of the overall response). Unlike H_2 exposure, the device does not return to baseline capacitance after exposure to 9600 ppm of O_2, indicating sensitivity drift that may affect sensor longevity.

The initial rapid response of both devices results from the direct physisorption of gases to the platinum surface, while subsequent responses involve chemisorption and gas migration through the platinum layer. Physisorption contributes to 57 % and 54 % of the total response for hydrogen and oxygen, respectively. The same phenomenon occurs when gas flow ceases, and the device is exposed to laboratory air, with initial rapid capacitance changes caused by the dissociation of physisorbed molecules.

We also tested the impact of temperature on zirconium oxide based devices, this is an important variable to consider, as diesel engines do not instantly reach high temperatures, and there is a period where combustion occurs in a 'cold start' environment. Therefore if thermal energy from the combustion engine is required to activate the gas sensors, there will a period where pollutants are being produced, but not detected.

In order to examine this, we exposed a Pt/ZrO_2/SiO_2/4H-SiC device to increasing levels of oxygen at 300 K and at 573 K. At 300 K there is no observable shift in the capacitance voltage curve at any concentrations of oxygen, confirming that the device is not able to act as a sensor at 300 K. We then increased the testing temperature to 573 K, and the device exhibited a measurable response which is proportional to the oxygen concentration in the testing chamber. This confirms that elevated temperatures are needed to activate zirconium oxide based devices, therefore a heating element could need to be considered in the final sensor architecture.

The final test that we were able to carry out in this work (due to limitations cause by Covid-19) was the exposure of a Pt/WO_3/SiO_2/4H-SiC device to nitric oxide (NO) at 573 K. Initially, the C-V characteristics of this device were benchmarked, and it was observable that this device was not behaving like a true capacitor, and demonstrated very high levels of leakage current. A theory as to why this occurred is that during fabrication, there was an interaction between WO_3 and SiO_2 layers, leading to an amalgamated, defect rich, $Si_xW_yO_z$ layer. Due to limitations in time,

we were unable to re-fabricate these devices to mitigate this effect.

The device with high levels of leakage current was used to test the device response to nitric oxide. The sensor was exposed to 20 ppm of NO gas, and a C-V sweep was taken at 10 kHz. As before, the device is not displaying a capacitive response, but it can be seen that there is a clear shift in the position of the curve along the voltage axis, which confirms that the device is responsive to NO. This response does raise queries about the sensor-gas interaction mechanism, and the system could operate by passivation of defect states by NO molecules, increasing the levels of trapped charge. Further investigation into WO_3 based sensors would be needed to ascertain more mechanistic information about analyte-device interaction

6.1 Experimental Plans Impacted by the Covid-19 Pandemic

An extensive experimental plan was agreed with the University of Mons to fully expose all devices to conditions that would closely resemble the environment of a diesel combustion engine, and observe their behaviour.

Two sets of four sensors were fabricated, Pt/HfO_2/SiC, Pt/TiO_2/SiC, Pt/ZrO_2/SiC and Pt/WO_3/SiC, one of which had a continuous platinum gate, and the other a porous gate morphology. Barring the platinum deposition technique, the devices were produced under identical conditions (with the exception of WO_3 oxidation, which was carried out at 50°C lower than other dielectrics).

An experimental plan was agreed with the laboratory in Mons as outlined below:

1. Initial electrical characterisation to ensure that no damage had occurred to the devices in transit.

2. Testing of the sensors to a series of industrially relevant gases - O_2, N_2, H_2, CO, NO, NO_2 and NH_3. The repeatability and reproducibility of sensor behaviour is important, so the tests will be carried out three times.

3. The influence of non-target gases on device sensitivity will be tested with the introduction of small amounts of SO_2 and unburned exhaust gases.

4. The long term behaviour of the sensors will be tested. Devices will be exposed to ambient air and exhaust gases for prolonged periods, and will be periodically tested to monitor potential flatband drift, leakage currents or breakage.

5. Device saturation and normalisation will be tested in detail to determine if substrate heating is required to return the sensors to baseline characteristics.

As a result of the Covid-19 pandemic, only two tests were able to be carried out at the laboratory in Mons - a capacitance-voltage sweep (-4-5V) of the Pt/WO_3/SiC (porous platinum) at 10 kHz and 573 K and exposure of this device to 20 ppm of NO at the same frequency and temperature.

6.2 Further Work

Another set of Pt/WO_3/SiO_2/4H-SiC devices should be fabricated and tested to ensure that they are exhibiting a true capacitive response. These devices should then be tested under varying concentrations of NO, to confirm that flatland voltage shift can be used to extrapolate the concentration of gas present within the system.

The sensors should then be exposed to a series of industrially relevant gases such as CO, NO_2 and NH_3 as these will all likely be present in the exhaust system. It is also important to understand the impact of non-target analyses such as SO_2 and unburned hydrocarbons which would interact with the sensors and pollute the system, altering response.

The long term behaviour of the sensors should be tested via exposure to ambient air and exhaust gases for prolonged periods at ambient and elevated temperatures. Periodic testing should be carried out to ensure that there is no drift in the flatland voltage, or any observable leakage or breakage. Also, saturation and normalisation of devices should be repeatedly tested to determine whether substrate heating is required to return the sensors to baseline characteristics, to ready them for re-use.

Ultimately, the likely conclusion of this work is the utilisation of a sensor array to target multiple gaseous analyses. The incorporation of varying dielectric layers into the metal-organic-semiconductor capacitor system has demonstrated that there is the potential to specifically target certain gases by tuning device structure. Therefore future work should focus on the fabrication and testing of a monolithically integrated sensor containing varying dielectrics to target specific analytes within the diesel combustion engine.